ISBN 978-82-326-1800-2 (printed version)
ISBN 978-82-326-1801-9 (electronic version)
ISSN 1503-8181

Doctoral Thesis

Mats Jørgen Thorsen

Doctoral theses at NTNU, 2016:231

NTNU
Norwegian University of Science and Technology

Doctoral theses at NTNU, 2016:231

NTNU

NTNU
Norwegian University of Science and Technology
Faculty of Engineering Science and Technology
Department of Marine Technology

NTNU
Norwegian University of Science and Technology

Doctoral theses at NTNU, 2016:231

Mats Jørgen Thorsen

Time domain analysis of vortex-induced vibrations

Mats Jørgen Thorsen

Time domain analysis of vortex-induced vibrations

Thesis for the degree of Philosophiae Doctor

Trondheim, September 2016

Norwegian University of Science and Technology
Faculty of Engineering
Science and Technology
Department of MarineTechnology

NTNU
Norwegian University of
Science and Technology

NTNU
Norwegian University of Science and Technology

Thesis for the degree of Philosophiae Doctor

Faculty of Engineering
Science and Technology
Department of MarineTechnology

ISBN 978-82-326-1800-2 (printed version)
ISBN 978-82-326-1801-9 (electronic version)
ISSN 1503-8181

Doctoral theses at NTNU, 2016:231

Printed by Skipnes Kommunikasjon as

Abstract

This thesis deals with the development of a new empirical model of the hydrodynamic loads associated with vortex-induced vibrations (VIV) of slender circular cylinders. The most commonly used VIV analysis tools operate in the frequency domain, and are unable to account for non-linear structural effects. In addition, these methods cannot handle time varying flows, and interaction with other loads is difficult to account for.

To dispose of the limitations associated with frequency domain analyses, a new method for time domain simulation of VIV is proposed in this work. Different load formulations are explored, and the final version consists of the well-known Morison's equation for inertia and drag forces, plus an additional term that models the effect of vortex shedding. A key component is a synchronization model which simulates how the vortex shedding reacts to structure motion to obtain lock-in. To evaluate the hydrodynamic load model, numerical simulations of a rigid cylinder subjected to an incoming flow and forced cross-flow oscillations are performed. Comparison with published experimental results shows that the proposed model reproduces the basic behavior of the fluctuating lift force.

To predict VIV of flexible cylinders, the hydrodynamic load model is combined with a finite element structural model. A linear beam model is utilized to simulate VIV of a riser in uniform and sheared stationary flow. Fatigue damage is calculated based on rainflow counting and Miner-Palmgren summation, and comparison with experimental data shows reasonable agreement. The uncertainties associated with VIV fatigue damage are however significant, and safety factors are necessary in some cases to obtain conservative results.

The proposed model has no restrictions on the time variability of the incoming flow, and through comparison with experimental data, it is demonstrated that the model accurately predicts the unstable VIV of a flexible cylinder subjected to a sinusoidal oscillating flow at two different KC-numbers. In the high KC-number case, the VIV response is intermittent, with vibrations continuously building up and dying out. It is also shown that multi-mode response occurs in oscillating flow when the reduced velocity is above a certain level, and the cylinder mass ratio is found to be important for the mode participation.

Finally, the hydrodynamic load model is implemented in a non-linear finite element program for dynamic analysis of slender structures. This is used to simulate VIV of a truncated model scale steel catenary riser in two different conditions: uniform stationary flow and oscillating relative flow caused by prescribed top-end motion. The predicted strains show good agreement with experiments, although some discrepancies are seen.

Acknowledgements

First of all, I wish to thank my supervisors, Prof. Svein Sævik and Prof. Carl Martin Larsen. They have provided excellent guidance during this work, and their office doors have always been open. They have been positive, enthusiastic and supportive, but, as true scientists, they have also been skeptical and critical at some points. I have truly enjoyed our discussions, both regarding VIV and other things.

Thanks to Philippe Mainçon for generous help and interesting discussions in the initial part of this work. Thanks also goes to the VIV-team at MARINTEK: Halvor Lie, Elizabeth Passano, Shixiao Fu, Jie Wu and Decao Yin, who have been very kind and helpful. They have provided help with experimental data, given advice along the way and shown interest in my work. For this I am very grateful. Also, thanks to Jungao Wang for sharing his knowledge about the oscillating flow experiments carried out at Shanghai Jiao Tong University.

Thanks to all my friends and colleagues at the Department of Marine Technology for making this rather long study a fun and pleasant experience. A special thanks goes to Vegard Longva for help with LaTeX and SIMLA. Also, thanks to Jan Vidar Ulveseter and Tor Huse Knudsen for joining me in VIV research.

Statoil is gratefully acknowledged for permission to use and publish experimental results from the oscillating flow experiments performed at the Shanghai Jiao Tong University. I would also like to thank the Norwegian Deepwater Programme (NDP), Riser and Mooring Project for permission to use and publish data from the Riser High Mode VIV tests.

Thanks to my parents, Sissel and Ole Kristian, and my sister, Hege for always supporting me. Thanks to my beautiful wife Solfrid for encouragement and understanding, and thanks to my wonderful daughters, Mia and Sara for getting me up in the morning.

List of publications

The following original research papers are included as part of this thesis:

I) M.J. Thorsen, S. Sævik and C.M. Larsen. A simplified method for time domain simulation of cross-flow vortex induced vibrations, *Journal of Fluids and Structures*, Vol. 49, pp. 135 – 148, 2014.

II) M.J. Thorsen, S. Sævik and C.M. Larsen. Fatigue damage from time domain simulation of combined in-line and cross-flow vortex-induced vibrations, *Marine Structures*, Vol. 41, pp. 200 – 222, 2015.

III) M.J. Thorsen, S. Sævik and C.M. Larsen. Time domain simulation of vortex-induced vibrations in stationary and oscillating flows, *Journal of Fluids and Structures*, Vol. 61, pp. 1 – 19, 2016.

IV) M.J. Thorsen, S. Sævik and C.M. Larsen. Non-linear time domain analysis of cross-flow vortex-induced vibrations, *Submitted for journal publication*, 2016.

This PhD work also resulted in the following conference papers which are not regarded as part of the thesis:

i) M.J. Thorsen, S. Sævik and C.M. Larsen. Time domain simulation of cross-flow and in-line vortex-induced vibrations, *Proceedings of EURODYN 2014*, Porto, Portugal, 2014.

ii) M.J. Thorsen, S. Sævik and C.M. Larsen. Time domain simulation of vortex-induced vibrations based on phase-coupled oscillator synchronization, *Proceedings of the ASME 2015 34th International Conference on Ocean, Offshore and Arctic Engineering*, St. Johns, Canada, 2015.

iii) T.H. Knudsen, S. Sævik and M.J. Thorsen. Numerical analysis of combined VIV and slug flow in time domain, *Proceedings of the ASME 2016 35th International Conference on Ocean, Offshore and Arctic Engineering*, Busan, South Korea, 2016.

Contents

Chapter 1

Introduction

1.1 Background and motivation

Slender cylindrical structures with circular cross section, such as risers, pipelines, mooring lines and power cables, may experience vortex-induced vibrations (VIV) when exposed to incoming currents [1, 2]. These vibrations occur as a result of the oscillating drag and lift forces caused by flow separation and vortex shedding. When VIV occurs, the material is subjected to cyclic bending stresses, causing crack growth over time, which eventually may lead to fracture. To ensure safe operation, engineers need to predict the time varying stresses and the associated fatigue damage caused by VIV. In addition, the vibrations lead to an increase in the mean drag forces, referred to as drag amplification [3], causing enlarged static displacements and tensile forces.

Figure 1.1: Vortex-induced vibration of riser [4].

VIV is an example of fluid-structure interaction. The vortex shedding triggers the vibration, while the cylinder motion alters the flow, thus affecting the fluid forces. This mix of fluid and structural mechanics makes VIV an interesting topic from an academic point of view. In addition, the flow around circular cylinders is complicated as a result of unsteady separation and turbulence. VIV appears in a long list of engineering applications, and as a result of the combined interest from academia and the industry, the phenomenon has been subjected to extensive research, as illustrated in several review articles [5–7]. The oil and gas industry is continuously setting new records in water depth, and presently the world's deepest production and drilling platform is at approximately 2 450 meters water depth [8]. Because wave loads decrease quickly with depth, current loads (i.e. vortex shedding) may be the most important fatigue design issue for risers in such deep waters.

The flow around a circular cylinder is governed by the Navier-Stokes equation, which for practical cases can only be solved numerically, at a high computational cost. Therefore, much of the research on the topic has been experimental. Based on the knowledge gained from experiments, several researchers have proposed different empirical models to predict VIV. In the industry, the most common VIV prediction programs are SHEAR7 [9], VIVANA [10] and VIVA [11]. Although these programs differ in several ways, they all operate in the frequency domain, and use hydrodynamic coefficients that depend on dimensionless frequency and amplitude parameters. This means that the structure needs to be linearized, and stationary flow conditions are required.

Due to the linearization, cases involving non-linear structural effects cannot be handled using frequency domain methods. This is not a problem for cases involving simple geometries and environmental conditions, such as a vertical riser in uniform incoming flow. However, other cases may include important non-linear effects, such as time varying boundary conditions (e.g. seabed contact), large displacements, tension variations, stick-slip behavior in flexible pipes and coupling between lateral and axial vibrations. Another issue with working in the frequency domain is that the response at each frequency is considered individually, and interaction between different frequencies is difficult to account for. This may be a problem for structures in sheared current, because a frequency domain procedure will find several possible response frequencies, and it is difficult to say if these frequencies will act simultaneously, consecutively, or in some alternative fashion [12]. Furthermore, it is difficult to account for interaction with other dynamic loads.

To account for non-linear effects, time-varying flows, interaction between different frequencies and other external loads, one can perform a step-by-step time integration of the equation of motion, i.e. time domain analysis. With the available finite element technology and modern computers, this is not a problem, and time domain simulation of risers subjected to wave loads based on Morison's equation is standard engineering procedure. However, because VIV is analyzed in frequency domain, this must be done separately, and the fatigue contributions from waves and current (VIV) are then added together [13]. This is unphysical, as the influence from waves on the vortex shedding is disregarded. To capture potentially important interaction effects, waves and current should be considered

simultaneously, in one single time domain simulation. Replacing two different simulations with one would also simplify the calculation procedure.

An important feature of VIV is synchronization, or lock-in. For a stationary cylinder, the vortex shedding frequency increases linearly with the flow velocity. However, cylinder vibration influences the vortex shedding in such a way that it deviates from the linear relationship and synchronizes with the cylinder motion (i.e. their frequencies become equal). Most existing VIV prediction methods rely on empirical force coefficients which are obtained at a constant flow velocity, vibration frequency and amplitude. Such experiments only provide information on how the fluid force behaves under given constant conditions. As a result of this, traditional VIV prediction tools distinguish between lock-in and non-lock-in states, but they are unable to describe the process of moving from one state to the other. It seems reasonable to believe that, to successfully predict VIV in oscillating flows, it is necessary to realistically model the synchronization process.

1.2 Objectives

The purpose of this work is to develop a simplified empirical model of the hydrodynamic loads relevant for vortex-induced vibrations, which can be applied in a time domain simulation. The model should be easy to use, computationally efficient, and provide reasonably accurate results. Furthermore, the model should be suited for both stationary and time-varying flows. It is also important that the model contains as few empirical parameters as possible, and the necessary parameters should be related to the actual physics in a clear way. Too many parameters will make the model difficult to use and understand, and it can also be hard to find suitable parameter values.

This thesis focuses on cross-flow VIV, but combined in-line and cross-flow vibrations are considered in paper II. Prediction of pure in-line VIV (occurring at low reduced velocities) is considered outside the scope of this work. The overall objective will be completed through a number of subgoals, as stated below:

- Propose a hydrodynamic damping model sufficiently accurate to represent the negative energy transfer during VIV. To be applicable in a time domain simulation, the damping formulation should be independent of frequency.

- Develop a time domain description of the hydrodynamic force associated with vortex shedding. This requires a model of how the vortex shedding reacts to cylinder motion, i.e. a synchronization model.

- Test and validate the proposed hydrodynamic load model against published experimental results in terms of added mass, lift coefficient in phase with cylinder velocity (excitation) and mean drag.

- Implement the hydrodynamic load model in a finite element program for structural analysis.
- Perform VIV simulations using the combined structural and hydrodynamic model. Different structures will be considered (straight and curved risers) and different flow conditions shall be tested (uniform, sheared, stationary, oscillating). The accuracy will be documented through comparison with experiments.
- Investigate the accuracy of the model with respect to fatigue damage prediction, the associated uncertainties and the importance of higher harmonics.

1.3 Thesis organization

This thesis is written as a collection of articles, which are appended in full-length after the main section. These articles represent the actual research contribution from this work, while the main section is meant to provide an overview of vortex-induced vibrations and previous research in the field, as well as a summary of the present work. The remaining part of the thesis is organized as follows:

Ch. 2 Contains a review of some of the previous work on vortex shedding and vortex-induced vibrations. This chapter also serves as an introduction to the topic.

Ch. 3 Provides an extended summary of the four research papers. This should give the reader an overview, but it is recommended to study the full-length papers to get a thorough understanding of the work.

Ch. 4 Presents conclusions and suggestions for future work. A list of original contributions is given, and the limitations of this research are discussed.

Chapter 2

Fundamentals of vortex-induced vibrations

This chapter has two objectives. First of all, it provides a literature survey of some of the previous work on vortex-induced vibrations. As the topic has been subjected to extensive research for more than half a century, the present chapter will reflect only a small fraction of the total available literature. The second objective is to provide some basic understanding to readers who are not already familiar with vortex-induced vibrations.

2.1 Flow around a circular cylinder in steady flow

This section is based on the book by Sumer and Fredsøe [14]. Consider a smooth stationary circular cylinder, positioned in a steady incoming flow. When fluid is in contact with a solid body, the no-slip condition must be satisfied at all times, meaning that the flow velocity is zero at the cylinder surface. This causes the formation of a thin boundary layer, characterized by a large velocity gradient in the radial direction. Viscous shear forces develop as a result of such velocity gradients. The Reynolds number[1] gives the ratio of the inertial forces to the viscous forces, which is defined as:

$$\mathrm{Re} = \frac{UD}{\nu}, \tag{2.1}$$

where U is the velocity of the incoming undisturbed flow, D is the cylinder diameter and ν is the kinematic viscosity of the fluid. When Re is very low (creeping flow), viscous forces dominate. In this flow regime, no separation occurs, and the flow remains attached to the cylinder all the way around.

When $\mathrm{Re} \approx 5$, the flow begins to separate from the cylinder and forms a free shear layer, as shown in figure 2.1. The shear layers roll up into vortices which for $5 < \mathrm{Re} < 40$ remain stable behind the cylinder. For $\mathrm{Re} \approx 40$, an instability occurs, causing one vortex to grow larger than the other. The larger vortex draws the other one across the wake, which cuts the large vortex free from the boundary layer. The large vortex is then convected downstream by the flow, and a new vortex starts to form in its place. The previously smaller vortex eventually grows large enough to draw the new vortex across the

[1] Osborne Reynolds (1842 - 1912), British engineer and scientist.

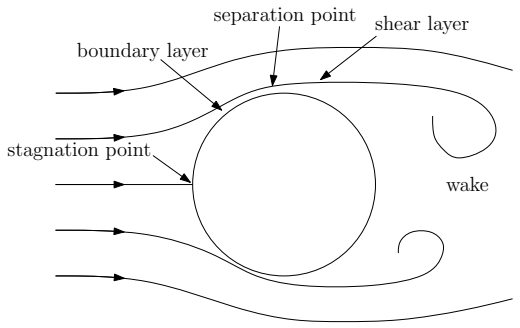

Figure 2.1: Flow around a stationary circular cylinder.

wake, and the process repeats itself [15]. This alternating vortex shedding causes the appearance of two rows of vortices, often referred to as a von Kármán[2] vortex street. For $40 < \mathrm{Re} < 200$, the vortex street is laminar and two-dimensional, meaning that the vortex shedding is correlated along the length of the cylinder [16]. As the Reynolds number is increased above 200, transition to turbulence occurs in the wake [17] and when Re reaches 300, the wake is completely turbulent. The vortex shedding becomes three-dimensional, and vortices are shed in distinct cells in the spanwise direction. For $300 < \mathrm{Re} < 3 \times 10^5$ (known as the subcritical regime) the boundary layer remains laminar. For higher Reynolds numbers, transition to turbulence in the boundary layer starts to occur. In the range $3 \times 10^5 < \mathrm{Re} < 3.5 \times 10^5$ (called the critical flow regime), the boundary layer becomes turbulent at the separation point, but surprisingly only at one side of the cylinder. The flow at the other separation point remains laminar, causing an asymmetry in the flow and a non-zero mean lift force. If the Reynolds number is increased further, the boundary layer separation is turbulent on both sides of the cylinder. For $3.5 \times 10^5 < \mathrm{Re} < 1.5 \times 10^6$ (the supercritical regime), the boundary layer is not yet completely turbulent, and the transition point is located somewhere between the stagnation point and the separation point. When $1.5 \times 10^6 < \mathrm{Re} < 4.5 \times 10^6$ (the upper-transitional regime), the boundary layer at one side of the cylinder is completely turbulent, while the other side is still partly laminar. When $\mathrm{Re} > 4.5 \times 10^6$ (the transcritical regime), the boundary layer is turbulent everywhere.

Vortex shedding will occur behind cylinders of any size, provided that the Reynolds number is larger than approximately 40. Figure 2.2 shows a satellite photo of Alexander Selkirk Island, located in the southern Pacific Ocean, showing vortex formation in wind driven clouds. The diameter of the island is about 1.5 km, which means the Reynolds number may easily be larger than 1×10^8. When comparing cylinders of different size and/or flows with different velocity, a helpful dimensionless number is the Strouhal[3] number:

[2]Theodore von Kármán (1881 - 1963), Hungarian-American engineer and scientist.
[3]Vincenc Strouhal (1850 - 1922), Czech physicist.

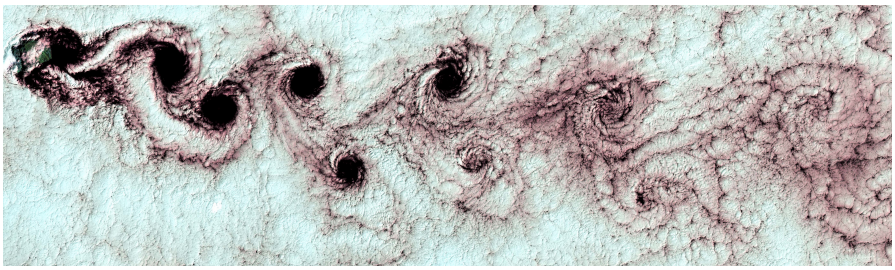

Figure 2.2: Satellite image showing vortex shedding in the clouds around Alexander Selkirk Island in the southern Pacific Ocean [18].

$$\mathrm{St} = \frac{f_s D}{U}. \tag{2.2}$$

Here, f_s is the vortex shedding frequency for the stationary cylinder, which is also referred to as the Strouhal frequency. A practical consequence of equation (2.2), is that the vortex shedding frequency for a fixed cylinder of arbitrary diameter and incoming flow velocity may easily be predicted, provided that the Strouhal number is known. Although the Strouhal number varies with Reynolds number and the surface roughness of the cylinder [19], it is virtually constant over a wide range of Re. For instance, in the entire subcritical range, $\mathrm{St} \approx 0.2$ [20]. For a smooth cylinder in the critical and supercritical regime, St increases to about 0.45. When Re is increased into the transcritical range, the Strouhal number drops again to around 0.25-0.3. Note that the vortex shedding process is not always consistent with a narrow-banded spectrum and a well-defined dominating frequency, but may consist of several frequency components [21]. In the sub- and supercritical regime, the frequency spectrum is narrow-banded, corresponding to a well-organized, regular vortex shedding. However, as Re is increased into the upper-transitional range, the vortex shedding becomes irregular and disordered. When Re goes into the transcritical range, the narrow-banded regular vortex shedding is established again.

The flow around the cylinder causes varying fluid pressure and shear stress, and the resulting fluid force acting on the cylinder can be found by integrating the contributions around the circumference. The force component in the direction of the flow is called drag, or in-line fluid force (see figure 2.3). The force component normal to the flow is called lift, or cross-flow fluid force. The forces are commonly expressed as dimensionless drag and lift coefficients, defined as:

$$C_x = \frac{F_x}{\frac{1}{2}\rho D U^2} \qquad \text{and} \qquad C_y = \frac{F_y}{\frac{1}{2}\rho D U^2}. \tag{2.3}$$

Here, x and y denotes the in-line and cross-flow direction respectively, while ρ is the fluid density. C_x is the drag coefficient and F_x is the in-line fluid force per unit length, while C_y is the lift coefficient and F_y the cross-flow fluid force per unit length. The drag coefficient has a significant mean value, which is denoted $\bar{C}_x$. This is mainly due to the low pressure behind the cylinder (i.e. in the wake region). Because the width of the wake depends on the Reynolds number and surface roughness, so does $\bar{C}_x$. For a smooth cylinder, $\bar{C}_x = 1.2$ in the subcritical regime. In the supercritical regime, the separation points move to the rear of the cylinder, causing a narrower wake and a large drop in $\bar{C}_x$ called the drag crisis. There is also a fluctuating component of the drag force, which oscillates at a frequency of $2f_s$, i.e. twice the vortex shedding frequency. The fluctuating drag force is small compared to the mean drag and the fluctuating lift [22].

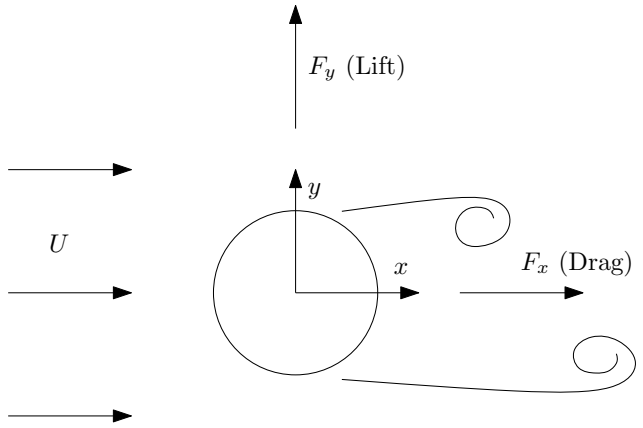

Figure 2.3: Cylinder with incoming flow, showing the lift and drag forces and coordinate system.

The mean value of the lift is zero due to symmetry (except in the critical flow regime), however the instantaneous fluctuating lift is significant and oscillates with the same frequency as the vortex shedding. The root-mean-square of the lift coefficient, $(\overline{C_y^2})^{1/2}$, varies strongly with the Reynolds number. In the upper end of the subcritical range, $(\overline{C_y^2})^{1/2}$ is relatively large and around 0.5 [23]. It drops considerably in the critical and supercritical range, which is related to the changes in the separation point and the correlation length. The lift force is only approximately sinusoidal, and the amplitude can vary from one period to another [24].

The influence of cylinder surface roughness on the vortex shedding frequency was investigated by Achenbach and Heinecke [19]. They used cylinders with various degrees of surface roughness and observed a clear effect on the Strouhal number. Compared with a smooth cylinder, transition to turbulence occurs at a lower Reynolds number. For cylinders with $k_s/D > 3 \times 10^{-3}$ (k_s/D is the equivalent sand-grain roughness), the critical, supercritical and upper transitional flow regime merge into a narrow region, and the flow

switches directly to transcritical as Re is increased. This causes the previously described drag crisis to become less pronounced. Furthermore, the mean drag coefficient in the transcritical range becomes higher as the surface roughness is increased. Zhou et al. [25] measured the lift and drag forces on circular cylinders over the range $6 \times 10^3 < \mathrm{Re} < 8 \times 10^4$, and found that the surface roughness has an effect on both the lift and drag coefficient.

2.2 Forced oscillation of cylinders in steady flow

Bishop and Hassan [26] were the first researchers to measure the fluid forces on a circular cylinder oscillating in the cross-flow direction with different (controlled) amplitudes and frequencies. They found that, when the driving frequency of the cylinder is sufficiently far from f_s, the lift force oscillates at the expected Strouhal frequency. However, when the driving frequency approaches f_s, the force becomes synchronized with the cylinder motion, meaning that the lift force starts oscillating with the driving frequency of the cylinder, and the Strouhal frequency disappears. Interestingly, this synchronization occurs over a range of oscillation frequencies.

An important consequence of synchronization is that the spanwise correlation is much greater for a vibrating cylinder than a stationary cylinder. The spanwise correlation is quantified in terms of the correlation length, which is defined by the integral

$$L_{\mathrm{corr}} = \int_0^\infty R(z)dz, \tag{2.4}$$

where $R(z)$ is the correlation coefficient for e.g. the fluctuating pressure along the cylinder. This can be found experimentally as:

$$R(z) = \frac{\overline{p'(\zeta)p'(\zeta+z)}}{\sqrt{\overline{p'^2(\zeta)}}\sqrt{\overline{p'^2(\zeta+z)}}}, \tag{2.5}$$

where ζ is the spanwise location (treated as a variable in the expression above), z is the separation between two measurement points, and p' is the fluctuating fluid pressure, or some other relevant unsteady quantity. Novak and Tanaka [27] have shown experimentally that the correlation length increases from about $3.5D$ to more than $40D$ when the cylinder is vibrating, and the large increase begins at vibration amplitudes as small as 5 % of the diameter. The increased correlation means a larger net force along the cylinder, which is important for the resulting amplitude of a freely vibrating cylinder.

Sarpkaya [28] did experiments with forced cross-flow vibrations, and measured the mean drag and fluctuating lift force. He found that the mean drag coefficient increases significantly when the cylinder is oscillating, and proposed an approximate expression based on the projected area of the cylinder:

$$\bar{C}_x = \bar{C}_{x,0}\Big(1 + 2\frac{y_0}{D}\Big), \tag{2.6}$$

where $\bar{C}_{x,0}$ is the drag coefficient for the stationary cylinder and y_0 is the cross-flow oscillation amplitude. Sarpkaya decomposed the lift force into a component in phase with the cylinder velocity (excitation/damping) and a component in phase with the cylinder acceleration (added mass). He then showed how the data could be used to predict the vibration amplitude of an elastically mounted freely vibrating cylinder.

Williamson and Roshko [29] also performed experiments with forced cross-flow oscillations, and used flow visualization to construct a map of the different vortex shedding regimes. They found several distinct vortex modes, such as 2S, 2P and P+S. 2S means two single vortices are shed every cycle, which is the von Kármán vortex street found for stationary cylinders. 2P means two pairs of vortices each cycle, while in the P+S regime, one pair and a single vortex is shed every cycle. They noticed that the sudden change in the lift force phase occurring around the Strouhal frequency is caused by a transition from the 2S to the 2P mode.

Gopalkrishnan [30] studied both sinusoidal and beating oscillation in the cross-flow direction. His contour plots of fluid excitation, added mass and mean drag coefficients have been widely used for prediction of VIV. Moe and Wu [31] also did experiments with forced cross-flow oscillation, but made the cylinder spring supported in the in-line direction. They found that the range of synchronization was wider when the cylinder vibrated in the in-line direction. In addition, the in-line motion caused a lift force component oscillating at three times the cross-flow motion frequency.

Morse and Williamson [32] did pure cross-flow forced oscillation experiments, measuring the fluid forces and using particle image velocimetry (PIV) for flow visualization. They used a very high resolution in the amplitude-frequency plane, enabling them to clearly identify the boundaries between different vortex modes. A new mode called $2P_O$ was discovered, with two pairs of vortices formed during each cycle, where the second vortex in each pair is much weaker than the other. Two sets of experiments were performed, one at $\mathrm{Re} = 4\ 000$ and one at $\mathrm{Re} = 12\ 000$. The results were similar, except that the region where energy is transferred from the fluid to the cylinder (also known as the excitation region) is stretched towards higher amplitude when the Reynolds number is increased.

Aronsen [33] measured the forces on a cylinder with pure in-line motion and presented plots of the in-line excitation coefficient, added mass and mean drag as a function of vibration amplitude and frequency. He also performed forced oscillation tests with combined cross-flow and in-line oscillation, and found that the hydrodynamic forces are strongly dependent on the phase difference between the cross-flow and in-line motion. In addition, he found a significant higher harmonic component in the lift force at three times the cross-flow oscillation frequency. Dahl [34] established a large database for combined

in-line and cross-flow vibrations. He confirmed the existence of the 3rd harmonic lift force, and found that it increases almost linearly with the in-line vibration amplitude.

In most of the work done on forced oscillations, the cylinder motion was purely sinusoidal. However, when VIV is observed on flexible cylinders, the motion is not perfectly sinusoidal, but may include amplitude variations and multiple frequency components. This motivated the research by Aglen [35] and Yin [36] who did forced vibration experiments with realistic cylinder trajectories. More specifically, the prescribed motion used in their experiments were taken directly from VIV tests of flexible cylinders. These studies showed that the true trajectory of the cylinder may cause hydrodynamic forces significantly different than observed in experiments with sinusoidal motion.

To summarize, some of the most important effects of cylinder oscillation are:

1. The vortex shedding synchronizes with the motion (i.e. the frequencies become equal) if the frequency of motion is close to the natural Strouhal frequency.
2. The spanwise correlation of the flow increases greatly, even for small vibration amplitudes.
3. The mean drag is amplified.
4. The synchronization range and the hydrodynamic coefficients are affected by in-line vibration.
5. In-line vibration causes a third harmonic component in the lift force.
6. Realistic cylinder trajectories (from flexible cylinder tests) give different hydrodynamic forces than harmonic motion.

2.3 VIV of elastically mounted rigid cylinders

If a rigid cylinder in a flow is mounted on springs or other types of elastic support, it will respond to the vortex shedding forces by oscillating. This oscillating motion is referred to as vortex-induced vibrations, or VIV. Depending on the supporting structure, the cylinder can be restrained to move only in the cross-flow or in-line direction, or it can move in both. These different set ups are shown in figure 2.4. If the supporting structure acts as a linear spring and damper, the equation of motion for the cross-flow displacement $y(t)$ is:

$$m\ddot{y} + c\dot{y} + ky = F_y, \tag{2.7}$$

where m is the cylinder mass, c is the structural damping coefficient and k is the spring stiffness. In general, the fluid force term F_y may be decomposed into a component in

phase with the cylinder velocity and a component in phase with the cylinder acceleration. The first will act as excitation or damping, meaning that it will supply or extract energy from the oscillation. The component in phase with the cylinder acceleration does not contribute to the energy transfer, but acts as an inertia force, and may therefore be expressed as an added mass. Denoting the added mass by m_a, the natural frequency of the oscillating system can be written as:

$$\omega_n = \sqrt{\frac{k}{m + m_a}}. \tag{2.8}$$

The added mass is strongly dependent on the non-dimensional oscillation frequency, $\hat{f} = f_{\text{osc}} D/U$ and the amplitude ratio, y_0/D. This causes the natural frequency to change, which means it is possible to have resonance over a range of excitation frequencies, or flow velocities. This was verified experimentally by Vikestad et al. [37], who showed that the vibration frequency is truly a natural frequency when the measured added mass is taken into account.

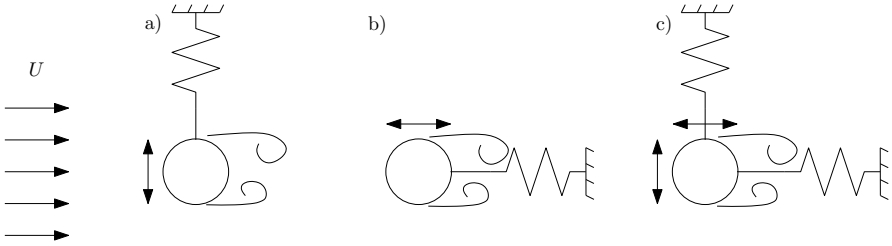

Figure 2.4: Typical VIV experiments with rigid cylinders: a) Cross-flow, b) In-line, c) Combined in-line and cross-flow.

The experiment by Feng [38] serves as a good illustration of pure cross-flow VIV. He studied how the vortex shedding frequency, vibration frequency and amplitude of a spring mounted cylinder varied as a function of the reduced velocity, $V_r = U/(Df_n)$, where f_n is the natural frequency of the cylinder. The experiment was conducted in air, which means the added mass was negligible compared to the actual mass of the cylinder. As a result of this, the natural frequency of the cylinder was virtually constant. He found that for low flow velocities, the cylinder did not vibrate, and the vortex shedding frequency followed the Strouhal relationship, $f_s = \mathrm{St}U/D$. When the reduced velocity is increased to 5, the vortex shedding frequency coincides with the natural frequency of the cylinder, and the cylinder starts to vibrate. Interestingly, when V_r is increased above 5, the vortex shedding frequency no longer follows the Strouhal relationship. Instead, it locks on to the natural frequency of the cylinder, and remains constant until $V_r \approx 7$. This is a result of the synchronization between the vortex shedding and the cylinder motion, which was

discussed in section 2.2. When V_r is increased beyond 7, the vortices are no longer able to lock on to the natural frequency of the cylinder. The cylinder oscillation ceases, and the vortex shedding starts to follow the Strouhal relationship again. Regarding the vibration amplitude of the cylinder, this is large when the frequency is close to f_n, i.e. for $5 < V_r < 7$.

An important difference between air and water is the density. For water, this is so high that the added mass of the cylinder contributes significantly to the total oscillating mass. This affects the natural frequency of the cylinder, causing an extension of the synchronization range. The mass ratio is defined as $m^* = m/(0.25\rho\pi D^2)$, which is the ratio between the cylinder mass and the mass of the displaced fluid. Khalak and Williamson [39] did experiments with pure cross-flow VIV and found that the synchronization range is significantly larger when m^* is reduced. They also show that the peak amplitude is independent of m^*, but varies with $m^*\zeta$, where ζ is the structural damping ratio. Govardhan and Williamson [40] found that for mass ratios below a critical value $m^*_{crit} = 0.54$, the synchronization region extends to infinitely high frequency, and large amplitude vibrations persists for all flow velocities. The resulting frequency and amplitude of a spring mounted cylinder with cross-flow motion is illustrated in figure 2.5, which also shows the effect of changing the mass ratio.

VIV of a rigid cylinder with two degrees of freedom (2-DOF, see figure 2.4c) was studied by Sarpkaya [41] who found that the cylinder response was influenced by the ratio between the in-line and cross-flow natural frequency. Jauvtis and Williamson [42] also did experiments with two degrees of freedom, and focused on the importance of the mass ratio. They found that the in-line motion affects the cross-flow motion very little for mass ratios higher than 6. However, for lower m^* , the maximum cross-flow amplitude increases significantly. The observed high-amplitude oscillations were associated with a new wake mode named 3T, where a triplet of vortices are formed each half cycle. Dahl et al. [43] did similar 2-DOF experiments, and varied the ratio between the in-line and cross-flow natural frequency. From this study it is apparent that changing the frequency ratio causes a change in the cylinder trajectory, which in turn alters the flow and corresponding forces.

Because the Reynolds number is important for the flow around a stationary cylinder, it also influences the VIV response of elastically mounted rigid cylinders. Based on a compilation of experiments, Govardhan and Williamson [44] found that the maximum cross-flow amplitude could be expressed as $(y_0/D)_{\max} = \log(0.41\mathrm{Re}^{0.36})$ in the range $500 < \mathrm{Re} < 33\,000$. Blevins and Coughran [45] did experiments with Re up to $150\,000$, and their results show a similar trend, meaning that the maximum cross-flow amplitude increases as a function of the Reynolds number. Dahl et al. [46] did 2-DOF experiments at supercritical Reynolds numbers between $320\,000$ and $710\,000$ using a roughened cylinder. Their results show that the maximum amplitude for the rough cylinder at supercritical Re is reduced compared to a smooth cylinder in the subcritical range. Raghavan and Bernitsas [47] also investigated the Reynolds number effect on VIV, and found that the

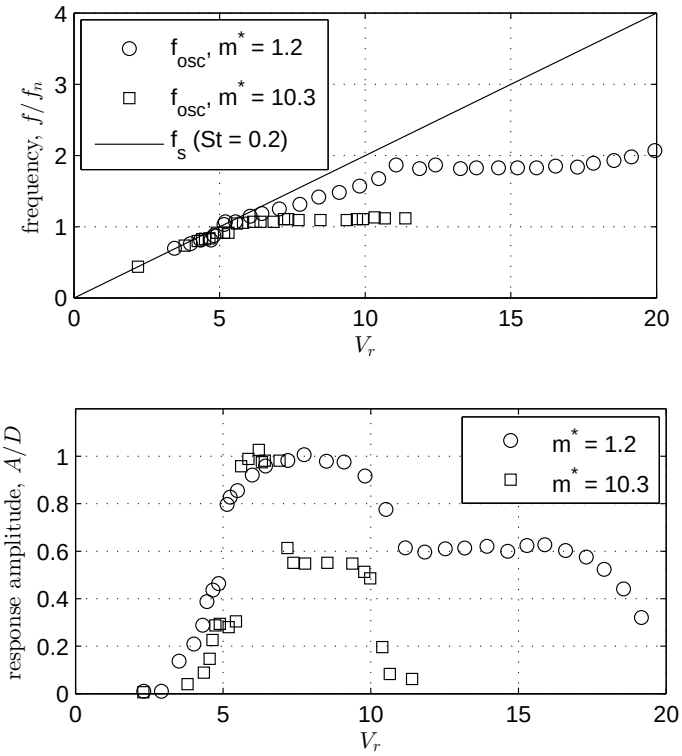

Figure 2.5: Frequency and amplitude for cross-flow VIV of rigid cylinder with different mass ratio according to Govardhan and Williamson [40]. The frequency is normalized with respect to the natural frequency in still-water. The Strouhal frequency $f_s = \mathrm{St}U/D$ is shown for reference.

synchronization range and the maximum amplitude increases with Re. The experiments were conducted in the subcritical range, and they observed amplitudes as high as $y_0/D = 1.9$ for $\mathrm{Re} \approx 1 \times 10^5$.

Although it is well known that the surface roughness of the cylinder has an effect on the fluid flow, there has been a limited amount of research on how the surface roughness affects the VIV response of elastically mounted rigid cylinders. Kiu et al. [48] ran experiments with an elastically mounted rigid cylinder in the subcritical range of Reynolds numbers, and found that the maximum response amplitude and the mean drag coefficient decreased with increasing roughness. They also found that the onset of lock-in was delayed for the rougher cylinders, and the width of the lock-in range was reduced. In another

study, Yin et al. [49] made a compilation of several experiments with different Reynolds number and surface roughness, and confirmed the importance of the surface roughness in the critical and post-critical regime.

The behavior of elastically mounted rigid cylinders subjected to a constant incoming flow can be summarized as follows:

1. The vortex shedding may lock on to the natural frequency of the cylinder, causing large amplitude vibrations over a wide range of reduced velocities.
2. The maximum vibration amplitude depends on the combined structural mass and damping parameter, $m^*\zeta$.
3. The width of the synchronization range increases with decreasing mass ratio.
4. For low mass ratio cylinders, in-line vibrations have an effect on the cross-flow response.
5. Reynolds number and surface roughness has an effect on the maximum vibration amplitude and the lock-in range.

2.4 VIV of flexible cylinders

A starting point for understanding the behavior of flexible cylinders is the dynamic equilibrium equation. As illustrated in figure 2.6, vertical equilibrium of a small segment of length dz yields the following equation:

$$T\frac{\partial^2 u}{\partial z^2} + \frac{\partial Q}{\partial z} + q(z,t) = m\frac{\partial^2 u}{\partial t^2}. \tag{2.9}$$

Here, u is the lateral displacement of the cylinder, T is the tension, Q is the internal shear force, q is the external lateral load and m is the mass per unit length of the cylinder. The shear force can be expressed through the bending moment M, which in turn is related to the bending stiffness EI and the curvature of the cylinder:

$$Q = \frac{\partial M}{\partial z} = \frac{\partial}{\partial z}(-EI\frac{\partial^2 u}{\partial z^2}). \tag{2.10}$$

Assuming EI is constant, the dynamic equilibrium equation for the cylinder is obtained by inserting equation (2.10) into equation (2.9):

$$m\frac{\partial^2 u}{\partial t^2} - T\frac{\partial^2 u}{\partial z^2} + EI\frac{\partial^4 u}{\partial z^4} = q(z,t). \tag{2.11}$$

Note that equation (2.11) is only valid for small displacements, and shear deformations are neglected. If the tension T is constant, it can be shown from the above equation, that when the cylinder vibrates freely, i.e. when $q(z,t) = 0$, the solution for the lateral displacement can be written as:

$$u(z,t) = \psi(z)Y(t) = u_0 \sin\left(\frac{n\pi z}{L}\right)\sin\omega_n t, \qquad \text{where} \qquad n = 1, 2, ... \tag{2.12}$$

Here it has been assumed that the cylinder is pinned, meaning that the displacement and curvature are zero in both ends. The first part of the solution, which describes the spatial variation of the displacement, is called the mode-shape. The first 5 mode-shapes, i.e. for $n = 1-5$ are shown in figure 2.7. For each mode, there is an associated natural frequency, given as:

$$\omega_n = \frac{n\pi}{L}\sqrt{\frac{T}{m} + \left(\frac{n\pi}{L}\right)^2 \frac{EI}{m}}. \tag{2.13}$$

From equation (2.13) it is seen that the natural frequency increases with n, meaning that mode 1 has the lowest natural frequency. Both the tension and the bending stiffness contributes to the natural frequency, and the bending stiffness becomes more important when n is large.

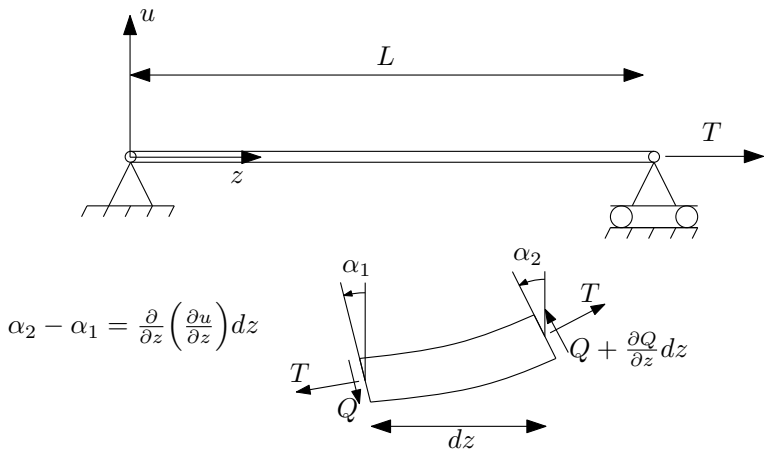

Figure 2.6: Flexible cylinder and internal forces acting on a small segment dz in a displaced configuration.

To illustrate how a flexible cylinder behaves when subjected to VIV, consider a cylinder in a uniform incoming flow. Because there is an infinite number of natural frequencies, the vortex shedding may in principle lock on to any of these. Now, assume the flow

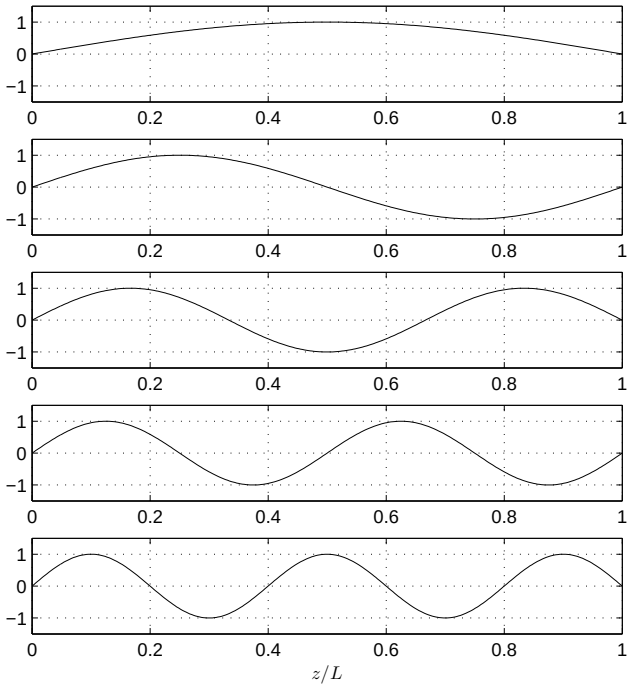

Figure 2.7: The first 5 mode-shapes for a straight and uniform flexible cylinder with pinned ends.

velocity increases slowly from zero. At first, the vortex shedding frequency follows the Strouhal relationship, and the cylinder vibrates very little. When the flow velocity is sufficiently high, the vortex shedding frequency comes close to the first natural frequency, ω_1, and locks on to this. Large amplitude vibrations in mode 1 will then quickly develop. As the flow velocity increases further, the vortex shedding are no longer able to synchronize with ω_1, but ω_2 may possibly be within the synchronization range. If this is so, the vortex shedding frequency will jump to a value close to ω_2, and excite mode 2 vibrations. In this way, the vortex shedding may always find a new natural frequency to lock on to when the flow velocity is increased, and large amplitude vibrations may therefore continue to exist for all higher velocities. Figure 2.8 illustrates how the vortex shedding frequency increases as a function of flow velocity, and shows how the natural frequencies of the structure may fall within the synchronization range.

The above description is of course simplified and incomplete, as it only takes into consideration the natural frequencies of the cylinder and the possible vortex shedding

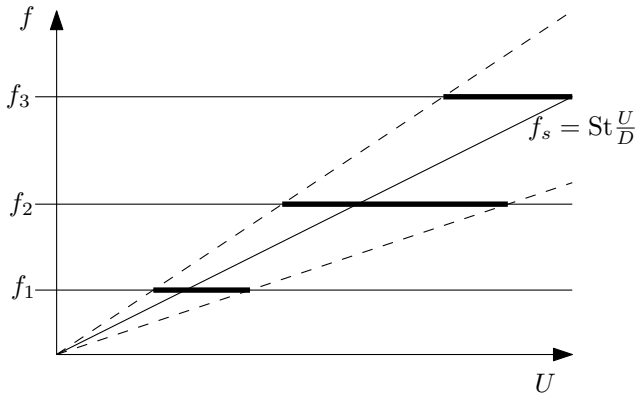

Figure 2.8: Vortex shedding frequency versus flow velocity. The dashed lines indicate the boundaries of the synchronization range. The horizontal lines are natural frequencies of the cylinder, and the bold lines indicate regions where lock-in is possible.

frequencies. The actual VIV behavior of elastic cylinders is more complicated for several reasons. Vandiver [2] gives a thorough discussion of VIV of long flexible cylinders in ocean currents, with focus on various important dimensionless parameters. He shows that when the variation in flow velocity over the cylinder length is large, the response is irregular and contains multiple frequencies. He presents two dimensionless parameters which can be used to judge whether or not single-frequency lock-in is likely to occur: the shear fraction, $\Delta U/U_{\max}$, and the number of natural frequencies within the excitation bandwidth, N_s. He also shows that the mass ratio has a strong effect on the range of reduced velocities where lock-in can occur. This effect is also seen for elastically mounted rigid cylinders, which has already been addressed in section 2.3. Vandiver also discusses how the response amplitude under lock-in conditions may be predicted using the reduced damping parameter, S_G, which is the damping ratio (including both structural and hydrodynamic damping) divided by the mass ratio. He also introduces the parameter $n\zeta_n$, which is the product between the mode number and the modal damping ratio, and shows that this parameter is useful in determining whether standing or traveling waves will dominate the response. In a more recent paper, Vandiver [50] has proposed a dimensionless damping parameter, $c^* = 2c\omega/\rho U^2$, where c is the structural damping per unit length and ω is the response frequency. This parameter captures the dynamic equilibrium between the lift and structural damping force, and can be used to characterize VIV for all reduced velocities in the synchronization range.

VIV of flexible cylinders are mainly of concern due to fatigue. For illustration purposes, assume that the in-line and cross-flow displacements of a cylinder can be expressed as:

$$x(z,t) = x_0 \sin\left(\frac{n\pi z}{L}\right) \sin(2\omega t), \tag{2.14}$$

$$y(z,t) = y_0 \sin\left(\frac{m\pi z}{L}\right) \sin(\omega t - \theta). \tag{2.15}$$

The in-line frequency is usually twice the cross-flow, due to the nature of the oscillating lift and drag forces. By assuming that the displacements are small, the maximum bending stresses in the two orthogonal directions may be found as:

$$\sigma_x = \frac{1}{2} E D x_0 \Big(\frac{n\pi}{L}\Big)^2 \qquad \text{and} \qquad \sigma_y = \frac{1}{2} E D y_0 \Big(\frac{m\pi}{L}\Big)^2, \tag{2.16}$$

where E is the Young's modulus of the cylinder material. The in-line mode is usually higher than the cross-flow, i.e. $n > m$, because the in-line frequency is twice the cross-flow. For a tension-dominated structure, the natural frequencies increase linearly with the mode number, which means that it is reasonable to assume (for illustration purposes) that $n = 2m$. Then, with reference to equation (2.16), the in-line bending stress may become equally important compared to the cross-flow stress, even though the in-line amplitude x_0 is much smaller than y_0. This was demonstrated by Baarholm et al. [51], based on data from a large-scale model test of a tensioned steel riser. The riser model was 90 m long, and was exposed to a linear shear flow, increasing from zero current velocity at the lower end to a maximum at the top. It was found that the in-line induced fatigue damage was larger than the cross-flow damage for the lowest flow velocities, where the riser was tension-dominated. For higher flow velocities, the bending stiffness becomes important and cross-flow fatigue damage is largest.

Trim et al. [52] presented results from the Norwegian Deepwater Programme (NDP) Riser High Mode VIV tests, where a 38 m long riser was exposed to uniform and sheared flow. These tests confirmed that the in-line fatigue damage was of the same order of magnitude as the cross-flow fatigue damage. Different configurations of helical strakes were also tested, and it was found that VIV could be effectively suppressed. However, the suppression effectiveness dropped rapidly when the coverage was reduced. Modarres-Sadeghi et al. [53] used data from the NDP High Mode VIV tests to show that the response is essentially stationary (a single, constant dominating frequency) in some time intervals, and chaotic (broad-banded response) in others. These different response types are observed in uniform as well as sheared flow.

Chaplin et al. [54] performed experiments with a vertical tensioned riser in a stepped current. In these tests, the lower 45 % of the riser was exposed to a uniform incoming current, while the upper part was in still water. The observed VIV response generally contained several modes. Some cases were stationary with almost constant amplitude for each mode, while other cases showed highly modulated amplitudes and a time varying dominant mode. The drag coefficient was found to increase with the vibration amplitude, and reached values 120 % higher than that of a stationary cylinder.

As previously mentioned, the lift force contains a significant higher harmonic component at three times the fundamental frequency when the cylinder vibrates in the in-line direction. This is important for flexible cylinders, because the 3rd harmonic may coincide with a natural frequency, causing significant high frequency stresses. Vandiver et al. [55] investigated the fatigue damage caused by the fundamental frequency and the higher harmonics based on field experiments in uniform and sheared flow. The experiments were designed to investigate VIV at mode numbers higher than 10. In both sets of experiments, the existence of higher harmonic vibrations was confirmed. In some cases, the contribution to the total r.m.s. of stress from the higher harmonics was more than 50 %, which has a large impact on the fatigue damage. The effect of higher harmonic forces on fatigue life of risers was also studied by Modarres-Sadeghi et al. [56]. Based on data from the NDP High Mode VIV tests, they confirmed a significant decrease in fatigue life when higher harmonic components were considered.

Free spanning pipelines typically vibrate at low modes, and pure in-line VIV can be dominating. Compared to risers, free spanning pipelines behave differently, due to the lower L/D and tension, making the bending stiffness more important. For long spans, the sag due to gravity may be significant, which can cause the mode 1 natural frequency in the vertical direction to be higher than the mode 2 natural frequency. Because the natural frequencies and modes in the lateral direction are less affected by the sag, unexpected behavior such as simultaneous mode 1 vibrations in the cross-flow and in-line direction can be observed, even though the in-line vibration frequency is twice the cross-flow frequency. A large number of free spanning pipeline model tests and analyses were carried out in connection with the Ormen Lange field development, as described in Refs. [57–59].

The effect of Reynolds number and surface roughness has previously been discussed, and applies to the flexible cylinder case as well. Swithenbank et al. [60] made a compilation of experiments with flexible cylinders with Reynolds number ranging from $1\,600$ to $240\,000$. Their results show that the dominating non-dimensional vibration frequency $\hat{f} = f_{\text{osc}}D/U$ and the maximum y_0/D and x_0/D depend on the Reynolds number. The maximum vibration amplitude is found to increase with Re over the subcritical range, which is consistent with observations of elastically mounted rigid cylinders. Allen and Henning [61] performed experiments with a flexible cylinder at critical and supercritical Reynolds numbers, with different levels of surface roughness. They found that, for a smooth cylinder, VIV was essentially eliminated when Re was increased above 3.5×10^5. However, as the surface roughness was increased, the VIV response increased as well.

Some of the most important features of flexible cylinder VIV are summarized below:

1. Flexible cylinders have an infinite number of natural frequencies, and may experience lock-in and high amplitude vibrations for almost any flow velocity above a certain threshold.

2. Variation in flow velocity over the cylinder length may cause multi-frequency re-

sponse.

3. The response may consist of standing or traveling waves, or a combination of both.
4. Flexible cylinder VIV includes cross-flow and in-line vibrations. The cross-flow displacements are usually larger (except for the lowest flow velocities), but the fatigue damage caused by the in-line vibrations should not be neglected.
5. Higher harmonic stresses may contribute significantly to the total fatigue damage.

2.5 VIV in time varying flows

To illustrate the difference between VIV in steady and oscillating flows, consider a rigid cylinder with a cross-flow degree of freedom exposed to a sinusoidal incoming flow, $U(t) = U_m \sin(2\pi f_w t)$. For illustrative purposes, assume the Strouhal relation is still valid, meaning that the vortex shedding frequency will vary with time as:

$$f_s(t) = \mathrm{St}\frac{U_m}{D}|\sin(2\pi f_w t)|. \tag{2.17}$$

The vortex shedding can only synchronize with the natural frequency of the cylinder when f_s is close to f_n, which means that excitation (i.e. positive energy transfer) is only possible at certain time intervals, as indicated in figure 2.9. Outside these intervals, the fluid force on the cylinder will mainly be damping. As the situation continuously changes from excitation to damping, the VIV response is expected to be more irregular than in the case of steady flow. Another complicating fact is that previously shed vortices are present in the incoming flow.

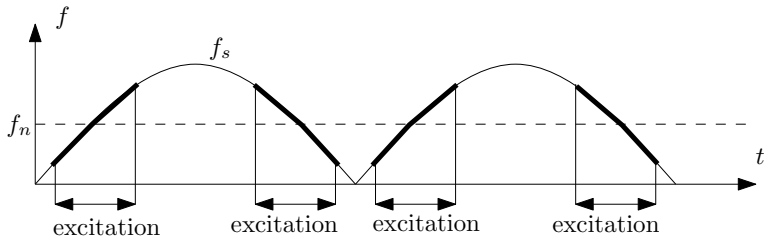

Figure 2.9: Vortex shedding frequency for a cylinder in a sinusoidal flow based on the Strouhal number and the instantaneous incoming flow velocity. The dashed line indicates the natural frequency of the cylinder, f_n.

An important dimensionless parameter in oscillating flows is the Keulegan–Carpenter number [62]:

$$\mathrm{KC} = \frac{U_m T_w}{D}, \tag{2.18}$$

where $T_w = 1/f_w$ is the period of the oscillating flow. For sinusoidal flow, the relative amplitude of motion is $A_m = U_m T_w / 2\pi$, which means that equation (2.18) can be reformulated as:

$$\mathrm{KC} = \frac{2\pi A_m}{D}. \tag{2.19}$$

From equation (2.19), it is understood that KC is a measure of the distance the flow travels before it reverses, in terms of the cylinder diameter. For vortex shedding to occur, KC must be larger than 7 [14].

Sumer and Fredsøe [63] carried out experiments with a 1-DOF elastically mounted rigid cylinder in a sinusoidal oscillating flow. Their experiments covered the range $5 \leq \mathrm{KC} \leq 100$, as well as stationary current for comparison, and the reduced velocity $V_r = U_m/(f_n D)$ was varied from 0 to 16. When plotting the resulting amplitude as a function of V_r, they found that the response in oscillating flow was very different from that in stationary flow, except for the cases where KC was very large. In general, lock-in did not occur once, but several times, causing multiple peaks in the amplitude response.

Maull and Kaye [64] did experiments with a cylinder in waves. Some of their tests had simultaneous in-line and cross-flow response, and in others the cylinder was restrained in the in-line direction. They found that the cross-flow response was the same whether the cylinder was free or fixed in the in-line direction. However, the in-line motion in their tests was small, as the wave frequency did not coincide with the natural frequency of the cylinder. Lipsett and Williamson [65] performed tests with a 2-DOF cylinder in an oscillating flow, and studied how the trajectory varied with KC and the frequency of the flow. In some of their tests the in-line motion was large enough to influence the transverse force and response.

Kozakiewicz et al. [66] studied the 1-DOF cross-flow response of a cylinder in irregular oscillating flow. They investigated the effect of bandwidth in the incoming flow velocity spectrum, and compared the results with regular oscillating flow. They found that the response is different from the regular oscillating flow case in several ways. Firstly, the amplitude as a function of reduced velocity does not contain multiple peaks, but remains almost constant over a wide range. Secondly, the VIV response in irregular flow is significantly lower, and decreases when the bandwidth is increased. However, for the smallest reduced velocities, the motion of the cylinder is larger than in regular oscillating flow.

The behavior of long flexible cylinders in sinusoidal oscillating flow has been studied by Fu et al. [67]. They observed that for higher KC numbers, the VIV response was intermittent, with vibrations building up and dying out for each half-cycle of the oscillating flow. A hysteresis effect was also seen, meaning that for a given instantaneous flow

velocity, the response was largest during flow deceleration. Wang et al. [68] performed large-scale model tests of a truncated steel catenary riser (SCR) in a relative oscillating flow which was generated by forced in-plane motions of the riser top end. The observed cross-flow vibrations depended strongly on the KC number, and tension variations were found to cause differences in the VIV response during lifting and lowering of the riser. Flexible cylinder VIV in unsteady flow has also been studied by Liao [69], who proposed an equivalent reduced damping parameter based on quasi-steady considerations which can be used to predict the VIV response. More recently, Resvanis [70] proposed an unsteady flow parameter, γ, which measures how much the flow velocity changes during one vibration cycle. For very small values of γ, the VIV response approaches steady state conditions. For very high values of γ, VIV is unlikely to occur, because the cylinder does not have time to react. For intermediate γ-values, the cylinder will vibrate, but the amplitude depends on the specific duration of excitation.

2.6 Existing methods for VIV prediction

The goal of any VIV prediction method is to compute the vibrations of a given flexible structure exposed to a given incoming flow. This task can be divided into two sub-problems: (1) Find the fluid forces acting on the structure, and (2) compute the structural response (i.e. displacements, velocities and accelerations) as a result of the fluid forces. The second task can be solved using the basic principles of structural mechanics: equilibrium, continuity and the material law. The structure can be discretized as finite elements (FEM, see e.g. Ref. [71]), resulting in an equation of motion for the structure, which may be solved using different approaches such as the frequency response method or time integration [72]. If FEM is used, a slender structure can be modeled as beam elements, resulting in a relatively low number of structural degrees of freedom. This means that the equation of motion for the structure can be solved at a low computational cost, at least if the material behavior is linear. As the finite element technology available for slender structures can be considered mature, and the computational cost is low, sub-problem 2 is not a research problem. The fluid dynamic part of the problem is however a challenge, and although various VIV prediction methods may use different structural models, the important difference is how the fluid forces are calculated. Over the years, a large number of methods have been proposed, see for example Refs. [73, 74]. In the following, a short description of some of the most popular methods is given.

2.6.1 Computational fluid mechanics

The fluid forces acting on a structure can be found by integrating the fluid pressure and shear stresses around the surface. These are coupled to the fluid velocity field through

the Navier-Stokes[4, 5] equation, which is basically Newton's[6] second law for the fluid [75]. Combined with the law of mass conservation, it is possible to calculate the entire flow field around the structure. This is the basis for the scientific discipline known as computational fluid dynamics (CFD).

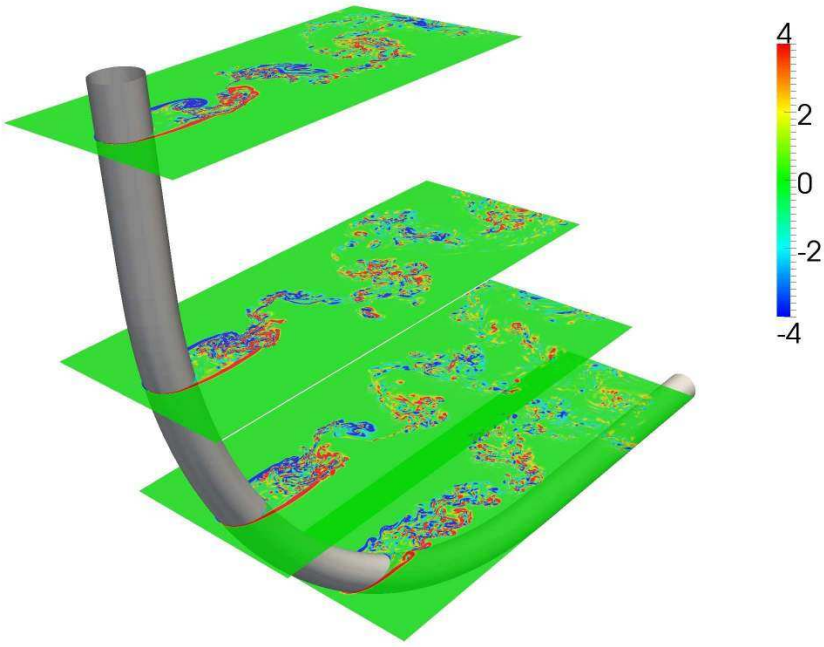

Figure 2.10: Example of CFD results, from Gallardo [76]. The color indicate vorticity.

Several numerical methods exists, which differ in how the fluid domain is discretized and in how turbulence is modeled. Some of the most popular discretization methods are the finite volume method and the finite element method, while available turbulence models include the Reynolds-averaged Navier-Stokes (RANS) and large eddy simulation (LES) to name a few. It is also possible to solve the Navier-Stokes equations directly without any turbulence model, which means that the entire range of space and time scales must be resolved. This procedure is called direct numerical simulation (DNS) and generally requires a very fine mesh and small time steps [77].

There has been several attempts to apply CFD methods for simulation of VIV. For example, four different CFD codes participated in a blind prediction study of a riser in a

[4]Claude-Louis Navier (1785 - 1836), French engineer and physicist.
[5]Sir George Gabriel Stokes (1819 - 1903), British mathematician and physicist.
[6]Sir Isaac Newton (1642 - 1727), English physicist and mathematician.

stepped current [73]. All of these considered 2-dimensional flow at multiple planes along the riser, and were less accurate than the semi-empirical methods. From this, it can be concluded that a 3-dimensional model of the fluid flow is necessary to obtain high-quality results. Bourget et al. [78] used 3-dimensional direct numerical simulation to simulate VIV of a long slender cylinder in shear flow at Reynolds numbers up to 1100. Such analyses provide a highly detailed and realistic picture of both the flow and the structural response. The required computational resources are however extremely large.

2.6.2 Semi-empirical methods

The first class of semi-empirical methods to be described here are the frequency domain tools, such as VIVA [11], SHEAR7 [9] and VIVANA [10], which are popular within the offshore industry. Although there are a number of differences between these methods, they have two important things in common. First of all, they operate in the frequency domain, and secondly, they use hydrodynamic coefficients for excitation, damping and added mass. The coefficients are typically obtained from experiments with forced oscillations of rigid cylinders.

As an example of how the frequency domain semi-empirical methods work, a short description of the VIVANA analysis procedure is given here. The structure is represented by finite elements, using beam elements with stiffness matrix contribution from tension and bending stiffness. The analysis follows these steps:

1. Static non-linear analysis to find the mean position of the structure due to weight, buoyancy and current.

2. Eigenvalue analysis to find modeshapes and natural frequencies based on the still-water added mass.

3. Identification of response frequencies when accounting for variation in added mass. An iteration procedure is necessary as the added mass is frequency dependent (but assumed to be independent of amplitude).

4. Because several response frequencies may be a part of the solution, the different frequencies are ranked according to an energy criterion.

5. The response at all possible frequencies are found using the frequency response method. The excitation forces are based on Gopalkrishnan's curves [30], with some modifications. Damping outside the excitation zones are based on Venugopal's damping model [79].

6. Fatigue damage is calculated based on assumptions regarding amplitude variations and combinations of response at selected discrete frequencies.

A different class of semi-empirical methods are those that operate in time domain, meaning that they simulate step-by-step forward in time how the structural response and fluid forces evolve. ABAVIV [80, 81] is one such method. In this method, the vibration amplitude and frequency must be estimated from the predicted response as the simulation progresses to decide if lock-in will occur or not. Outside lock-in, the lift force oscillates with the Strouhal frequency and a random phase angle. When lock-in occurs at some point along the riser, the lift force is gradually transitioned to be in phase with the cylinder velocity at that point. Another time domain method was proposed by Lie [82], which uses hydrodynamic coefficients from experiments that depends on the vibration frequency and amplitude. These quantities must therefore be estimated for every time step as the simulation progresses. A completely different time domain approach was developed by Mainçon [83]. He used a dataset of hydrodynamic force measurements obtained from oscillating rigid cylinders to train an artificial neural network in predicting the forces. He showed that the neural network combined with a finite element model of a flexible cylinder was capable of predicting the VIV response with a high degree of realism in some cases. Some stability issues were however also observed, perhaps caused by the limited amount of training data.

Another type of semi-empirical model is the wake-oscillator, which has been studied by a large number of researchers (see e.g. Ref. [74]). Here, the fluctuating lift force from vortex shedding is described by a forced van der Pol[7] equation:

$$\ddot{q} + \epsilon\Omega_f(q^2 - 1)\dot{q} + \Omega_f^2 q = F, \tag{2.20}$$

where $q(t)$ is a dimensionless wake variable, $\Omega_f = 2\pi \mathrm{St} U/D$ is the Strouhal angular frequency and ϵ is an empirical damping parameter. The relationship between equation (2.20) and the lift force due to the vortex shedding is given as $F_y = 0.25\rho D U^2 C_{L_0} q$, where C_{L_0} is the reference lift coefficient found on a stationary cylinder. An important property of equation (2.20) is that in the absence of forcing (i.e. when $F = 0$) it describes a self-sustained limit-cycle oscillation with a frequency Ω_f. This is seen from the fact that the second term is essentially a negative damping force when $q < 1$, which causes the amplitude to increase. If q becomes large, the damping will become positive, and the amplitude will drop until stable oscillations develop. Hence, the van der Pol equation reproduces the basic behavior of the oscillating lift force. The coupling between the structure motion and the lift force is through the forcing term F. Facchinetti et al. [84] studied how different coupling terms affect the performance, and considered displacement coupling ($f = Ay$), velocity coupling ($f = A\dot{y}$) and acceleration coupling ($f = A\ddot{y}$). Here, $f = F/(D\Omega_f^2)$ and A is an empirical coupling parameter. They found that acceleration coupling was the best alternative, as it succeeded in modeling many features of VIV qualitatively, and in some cases also quantitatively. The wake oscillator models have later been refined by sev-

[7] Balthasar van der Pol (1889 - 1959), Dutch physicist.

eral researchers, for instance Srinil and Zanganeh [85], who considered combined in-line and cross-flow VIV.

Chapter 3

Extended summary of papers

This chapter contains an extended summary of the research papers, such that the reader may get an overview of the work without reading through the full papers. The main contribution of this PhD work has been the development of a new simplified hydrodynamic load model, which was first presented in paper I. Since then, the model has constantly been evolving, and several changes and improvements have been introduced in papers II-IV. Paper I, III and IV focus on cross-flow VIV only, while paper II considers in-line vibrations as well.

Paper I: A simplified method for time domain simulation of cross-flow vortex induced vibrations

The starting point for developing the hydrodynamic load model was the assumption that the force on a cross-section of the cylinder consists of three components: lift, damping and added mass (here, the use of the word 'lift' is used to describe the force component resulting from the shedding of vortices. In paper II-IV, this force component is more appropriately referred to as 'excitation force' or 'vortex shedding force'). A damping formulation was proposed, consisting of a linear and a quadratic damping term, where the quadratic term increases linearly with the vibration amplitude of the cylinder section. The damping coefficients were found by minimizing the difference between the proposed model and the damping model by Venugopal [79]. The reason why Venugopal's model was not used directly is that it contains frequency-dependent terms, and is therefore not suited for time domain simulation.

The magnitude of the lift force is given by a dimensionless coefficient, $C_{l,0}$, which was assumed to be a function of the cross-flow vibration amplitude to diameter ratio, A/D. The values of $C_{l,0}$ for different A/D were found by matching the resulting energy transfer (power in from vortex shedding minus power out from damping) to the excitation coefficient used in VIVANA. The fluctuations of the lift force is taken into account through an instantaneous phase angle, ϕ_l, which goes from 0 to 2π through one oscillation cycle. How this phase angle develops as a function of time was described by a synchronization model. Assuming that the time derivative of the lift force phase (i.e. the instantaneous frequency of the lift force) is a function of the phase difference between the cross-flow cylinder velocity and the lift force itself, it was possible to derive the synchronization

model based on data from VIVANA. Note that data from forced vibration experiments could have been used instead, and the present formulation is completely independent of VIVANA. The resulting synchronization model is seen in figure 3.1. The instantaneous phase of the cross-flow cylinder velocity is denoted $\phi_{\dot{y}}$, and the instantaneous frequency of the lift force (normalized by the Strouhal frequency) is taken as a function of $\phi_{\dot{y}} - \phi_l$.

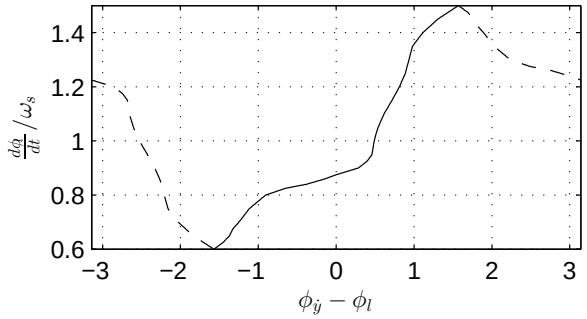

Figure 3.1: Synchronization model.

The proposed hydrodynamic load model was tested through numerical simulations and comparison with published experimental results. The first test was to simulate the hydrodynamic force on a rigid cylinder undergoing forced sinusoidal cross-flow motion. This was done using different frequencies and amplitudes, and for each simulation, the resulting time series was post-processed to obtain the cross-flow force component in phase with the cylinder velocity and acceleration. Comparison with the experimental results of Gopalkrishnan [30] showed that the model captured the main features, such as positive power transfer within a specific range of non-dimensional frequencies and below a certain amplitude. The predicted component in phase with the cylinder acceleration (i.e. the added mass force) was also in good agreement with experiments, although there were some minor discrepancies.

Next, the load model was combined with a 1-DOF dynamic equilibrium equation to simulate cross-flow VIV of a spring supported rigid cylinder. Time domain simulations of the cylinder response were performed, and the resulting vibration amplitude and frequency were found for different reduced velocities. This was done for two different cylinders, one with a mass ratio of 1.2 and another with mass ratio 10.3. Comparison with the experiments by Govardhan and Williamson [40] showed good overall agreement, and the model successfully predicted that large-amplitude vibrations persists for a longer range of velocities for the low-mass cylinder.

Finally, the hydrodynamic load model was combined with a linear beam finite element model to simulate VIV of a flexible tensioned cylinder exposed to a linear shear flow. The High Mode VIV-tests performed by the Norwegian Deepwater Programme (NDP) [52]

were used for comparison. A typical simulation result is shown in figure 3.2. Simulations were run for incoming flow velocities ranging from 0.3 m/s to 2.4 m/s, and the results were compared to the NDP experiments in terms of dominating frequency, mode of vibration and maximum r.m.s. displacement. The comparison showed good agreement, except for a slight overestimation of the frequency and mode, which suggests that the synchronization model can be improved.

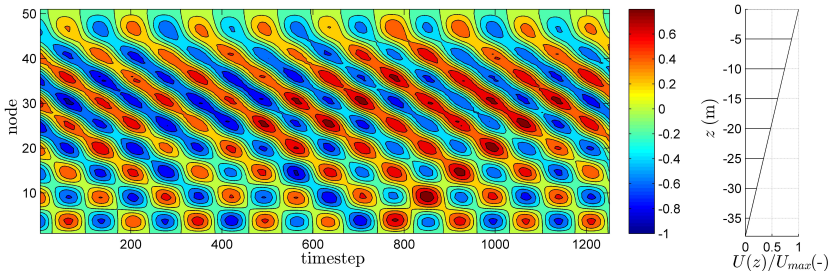

Figure 3.2: Simulated cross-flow response of flexible cylinder. The incoming current profile is shown to the right.

Paper II: Fatigue damage from time domain simulation of combined in-line and cross-flow vortex-induced vibrations

This paper deals with combined in-line and cross-flow VIV. The cross-flow hydrodynamic force model is essentially the same as in paper I, except for the introduction of a Reynolds number dependent factor in the vortex shedding frequency calculation. Based on experimental data, this factor was however found to be almost constant and approximately 0.85, so the actual effect is a slight reduction of the vortex shedding frequency in general. This solved the problem of overestimating the vibration frequency which was seen in paper I.

The in-line hydrodynamic force model was based on simplified physical considerations. The starting point for developing the in-line force model was the approximation that the vortex shedding force acts perpendicular to the instantaneous *relative* velocity between the fluid and the cylinder. Hence, cross-flow motion gives rise to an in-line fluctuating component, as illustrated in figure 3.3.

A synchronization model for the oscillating in-line hydrodynamic force was also introduced. Here, the frequency was assumed to be approximately 2 times the frequency of the cross-flow vortex shedding force, but a small deviation was allowed such that the in-line force may synchronize with the in-line motion of the cylinder. The in-line synchronization model works in the same way as the cross-flow synchronization model, meaning that the instantaneous frequency of the in-line vortex shedding force is a function of the

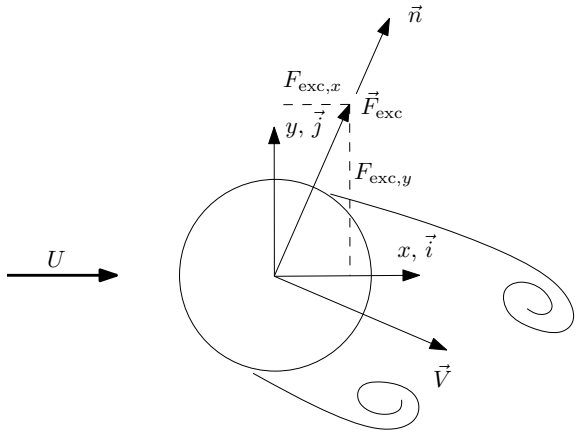

Figure 3.3: Vortex shedding force with in-line and cross-flow components.

phase difference between the in-line velocity of the cylinder and the force itself. Hydrodynamic damping was modeled the same way as for the cross-flow direction, i.e. by fitting the damping coefficients to Venugopal's [79] in-line damping model.

The combined in-line and cross-flow hydrodynamic load model was then linked to a linear beam finite element model to simulate the NDP High-Mode VIV tests [52]. Fatigue damage was computed using rainflow counting and Miner-Palmgren summation. This was done with the experimental data as well, and the fatigue damage rates were compared. The maximum predicted fatigue damage for all cases (22 in uniform flow and 22 in shear flow) were compared to the experimental results as shown in figure 3.4. The comparison shows that the model predicts the maximum fatigue damage for cross-flow and in-line VIV with a reasonable level of realism, although safety factors must be applied to achieve conservative predictions in some cases.

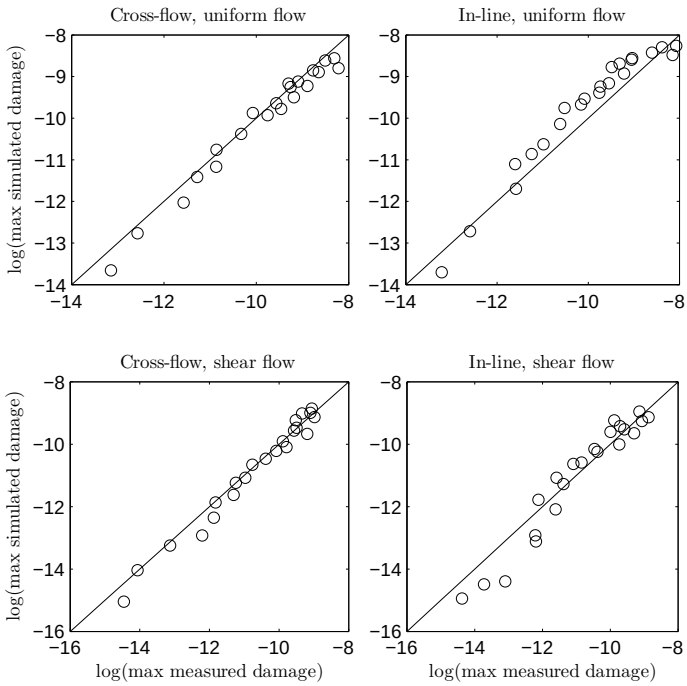

Figure 3.4: Simulated versus measured maximum fatigue damage rate (in-line and cross-flow) for the NDP tests.

Paper III: Time domain simulation of vortex-induced vibrations in stationary and oscillating flows

The research presented in this paper had two main goals. The first one was to improve the hydrodynamic force model with respect to the prediction accuracy for stationary flows. The motivation behind this goal was observations made in paper II, where the predicted cross-flow vibration amplitude was generally too high in uniform flow and too low in sheared flow. The improvements consisted of two changes in the model. The first was a new damping formulation, where the linear damping term was dropped. An amplitude dependent damping coefficient was found from experiments with a cylinder oscillating in still water, and it was shown that the derived damping model also gave accurate results for a cylinder vibrating in a current at high and low reduced velocity. The second improvement to the model was to optimize the excitation force coefficient C_v (this was denoted $C_{l,0}$ in paper I) through a series of simulations and comparison with the NDP High Mode

VIV test data.

The second goal of this paper was to investigate how the model performed at predicting cross-flow VIV in oscillating flows. An important point is that no modifications were introduced in the hydrodynamic load model, meaning that the formulation and the parameters were the same as in the stationary flow simulations. The hydrodynamic force model and a linear beam finite element model were used to simulate the cross-flow VIV of a flexible cylinder subjected to a sinusoidal oscillating flow. The simulated cylinder was identical to the one tested by Fu et al. [67], which made direct comparison possible. The maximum reduced velocity was varied between 4 and 6.5, where the higher value corresponds to the point where the vibration amplitude is expected to be at its largest. The KC number for the oscillating flow is important, as it describes the distance traveled between each flow reversal. The model was tested at a moderate value of $\mathrm{KC} = 31.4$ and a high value of $\mathrm{KC} = 178$. Figure 3.5 shows simulation results at $V_r = 4.0$ and $\mathrm{KC} = 178$ compared to the experiment. The other cases show similar agreement, indicating that the model is able to predict VIV in oscillating flows.

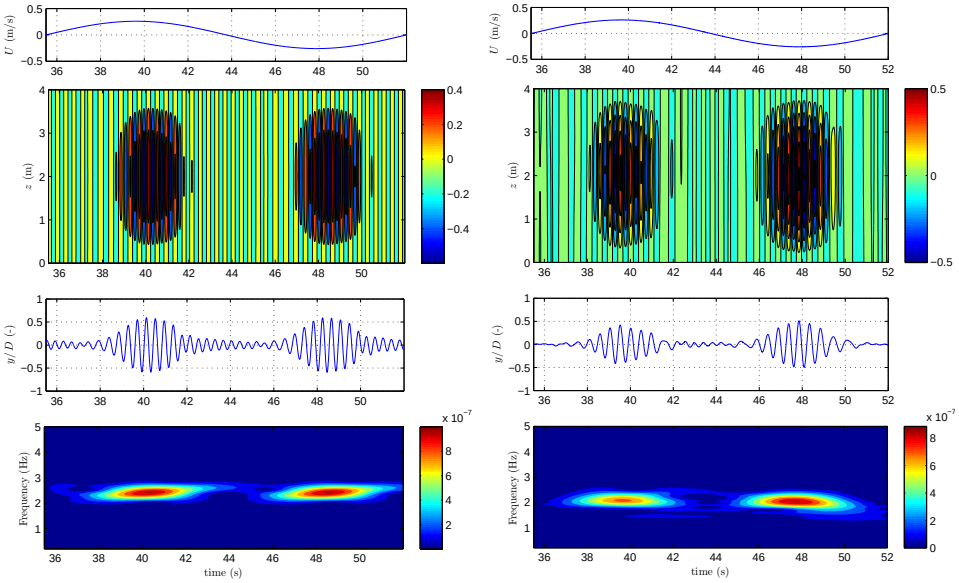

(a) Simulation (b) Experiment

Figure 3.5: Comparison between simulation and experiment with flexible cylinder in oscillating flow.

Furthermore, the model was used to investigate the effect of increasing the reduced velocity for the oscillating flow case, and also how the mass ratio affects the mode participation when multiple modes may be excited. The results from a simulation with high

reduced velocity and low mass ratio showed significant contributions from mode 1-4, and the dominating mode changed continuously as the flow velocity caused the vortex shedding to lock on to different natural frequencies. When this simulation was performed with a high mass ratio cylinder, the result was a nearly single mode response at mode 3, indicating that the high mass ratio cylinder is more resistant to changes in the vibration state. It is therefore concluded that, in oscillating flows, mass ratio is important in determining the mode participation at high reduced velocities.

Paper IV:Non-linear time domain analysis of cross-flow vortex-induced vibrations

The purpose of this paper was to develop a general tool for simulating the non-linear dynamic response of risers and other slender structures due to ocean currents in combination with prescribed motions and other loads. Drag forces should be included, and it was therefore natural to use Morison's equation as a starting point. Here, the drag force on a cylinder cross-section is computed based on the instantaneous relative velocity between the fluid and the cylinder. The drag term in Morison's equation causes damping of vibrations, which means that it cannot be combined with the damping models used in paper I-III. A new hydrodynamic load model was therefore proposed, consisting of the original Morison's equation with inertia and drag forces, plus an additional term describing the vortex shedding force. The vortex shedding force was modeled similarly as in the previous papers, except for the synchronization model which was reformulated as a sine function for simplicity and numerical efficiency. Also, the vortex shedding force coefficient C_v was independent of vibration amplitude, which is in contrast to the previous papers. The final hydrodynamic force model is then given as:

$$\begin{aligned}\mathbf{F} = C_M\rho\frac{\pi D^2}{4}\dot{\mathbf{u}}_n - (C_M-1)\rho\frac{\pi D^2}{4}\ddot{\mathbf{x}}_n + \frac{1}{2}\rho D C_D|\mathbf{v}_n|\mathbf{v}_n \\ + \frac{1}{2}\rho D C_v|\mathbf{v}_n|(\mathbf{j}_3\times\mathbf{v}_n)\cos\phi_{\text{exc}}.\end{aligned} \tag{3.1}$$

The predictive capabilities of the new hydrodynamic load model was tested through comparison with experimental results. Energy transfer was quantified through the lift coefficient in phase with the cylinder velocity, and numerical simulations of a rigid cylinder oscillating with various amplitudes and frequencies were performed. It was demonstrated that the model gives positive power transfer inside the synchronization range and below a certain amplitude, and it was shown that the maximum amplitude of the positive excitation zone can be changed by varying C_v. The effective added mass predicted by the model consists of the original added mass term in Morison's equation and the part of the vortex shedding force which is in phase with the cylinder acceleration. It was shown that the

model predicts positive and negative added mass for the correct values of non-dimensional frequency. The predicted added mass for a spring-mounted rigid cylinder was found by simulations, and comparison with experiments by Vikestad [86] showed very good agreement over the most important range of reduced velocities. Simulations also show that the model predicts drag amplification, i.e. an increased mean drag force when the cylinder is vibrating.

The hydrodynamic force model was implemented into an existing program for non-linear finite element analysis of slender structures, SIMLA [87]. The dynamic analysis was based on the incremental equation of motion, which was solved in time domain using the HHT-α method [88]. To test and demonstrate the applicability of the model, it was utilized to simulate VIV of a truncated model scale steel catenary riser in two different conditions: In the first case, the riser was exposed to a stationary uniform incoming current, while in the second case there were no current, but the top-end of the riser was oscillating, creating a relative oscillatory flow. These cases were tested experimentally by Wang et al. [89], and the simulations were compared to these tests. In the stationary flow case, the response was almost steady state with a single dominating frequency. The magnitude and frequency of the bending strain were accurately predicted, but the mode of vibration was slightly over-predicted (7 peaks along the riser span in the simulation compared to 6 peaks in the test). In the second case, the relative oscillating flow caused an irregular response, as seen in figure 3.6. The frequency content and the r.m.s. of strain were quite accurately captured, although the actual response appears somewhat more irregular than predicted.

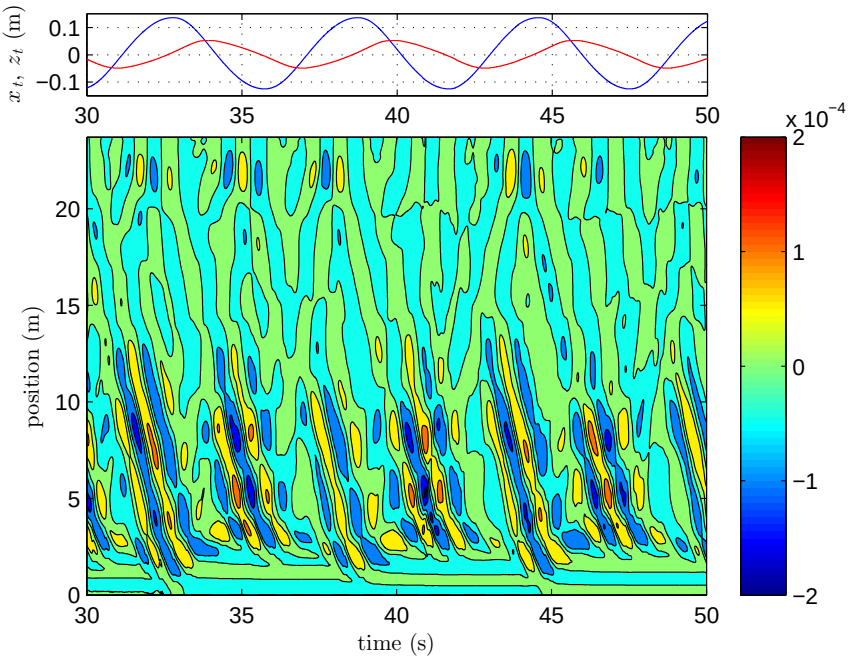

Figure 3.6: Simulation of VIV due to oscillation of riser top end.

Chapter 4

Conclusions and future work

This thesis has dealt with prediction of vortex-induced vibrations of elastic cylinders. The overall goal has been to develop a computationally efficient model, which is simple to use and sufficiently accurate for engineering purposes. The model has been formulated in time domain, which means that simulations including non-linear effects can be performed. Hence, this work should be of particular interest to engineers working with design of slender structures subjected to ocean currents.

4.1 Original contributions

The list below summarizes all the original contributions in this thesis:

1. A cross-flow hydrodynamic damping model was proposed in paper I. The formulation is independent of frequency and therefore suitable for time domain simulations.

2. A model of the cross-flow vortex shedding force (lift) was proposed in paper I, including a synchronization model which describes the behavior of the instantaneous frequency of the force.

3. It was demonstrated that the hydrodynamic force model in paper I provides realistic results for the lift coefficient in phase with the cylinder velocity (excitation) and acceleration (added mass), for a rigid cylinder with a prescribed cross-flow oscillating motion.

4. Through simulations and comparison with experimental work, it was also shown that the model in paper I provides realistic predictions of VIV for a spring mounted rigid cylinder (1-DOF) as well as an elastic cylinder in sheared flow.

5. A model for the in-line hydrodynamic force was proposed in paper II, which is similar to the cross-flow force model. This includes an in-line synchronization model based on the assumption that the frequency of the oscillating drag force is approximately two times the frequency of the lift force.

6. It was shown that the model in paper II gives realistic estimates of the in-line and cross-flow fatigue damage for a flexible cylinder in uniform and sheared flow. Safety factors are necessary in some cases to ensure conservative results.

7. The cross-flow damping model was modified in paper III by dropping the linear damping term. This gave excellent agreement with tests performed in still-water and in a current, outside the synchronization range.

8. The cross-flow vortex shedding force was modified in paper III by introducing a new curve for the amplitude dependent coefficient C_v. The new curve was found by minimizing the prediction error associated with VIV in stationary flow.

9. It was demonstrated that the force model in paper III is able to predict cross-flow VIV of an elastic cylinder in oscillating flow for different reduced velocities and KC numbers.

10. Simulations showed that multi-mode response may occur for elastic cylinders in oscillating flow at high reduced velocities. Mass ratio was identified as an important parameter in determining the mode participation in oscillating flows.

11. A hydrodynamic force model based on Morison's equation plus an additional term for the vortex shedding force was presented in paper IV. A sinusoidal synchronization model was introduced for efficiency in the numerical calculation.

12. It was shown that the vortex shedding force coefficient, C_v, could be taken as independent of amplitude, without significant loss of accuracy. The Reynolds number dependency must however be taken into account.

13. It was demonstrated that the load model proposed in paper IV gives reasonable results in terms of power transfer (damping/excitation), added mass and mean drag for a rigid cylinder undergoing forced cross-flow oscillation.

14. The load model introduced in paper IV was implemented in a non-linear finite element program for analysis of slender structures (SIMLA).

15. A SIMLA model was established to simulate cross-flow VIV of a catenary riser in two conditions: uniform current and top-end oscillations in still water. In the latter case, VIV is a result of the relative oscillating flow caused by the movement of the riser through the fluid. Comparison with experiments showed good agreement in both cases, although some discrepancies were seen.

4.2 Conclusions

The main contribution of this work is a new mathematical model of the hydrodynamic forces acting on a vibrating circular cylinder in a fluid flow. The proposed model is empirical, and relies on hydrodynamic coefficients which must be obtained from experimental data. The formulation has changed slightly during the course of this work, but the basis

has remained the same: that the total hydrodynamic force can be described as a sum of inertia, damping and vortex shedding forces. It is well known that the vortex shedding will synchronize with the cylinder motion if the frequency of motion is close to the vortex shedding frequency for a stationary cylinder (i.e. the Strouhal frequency). To simulate this, a synchronization model was formulated, which effectively captures how the vortex shedding may slow down or speed up to synchronize with the motion of the cylinder. Similar formulations have previously been used for modeling synchronization in completely different scientific fields [90], but to the author's knowledge, this is the first time such a synchronization model has been used in connection with VIV.

The proposed hydrodynamic force model is formulated in time domain, which means that it can be utilized in a step-by-step time integration procedure for solving the dynamic equilibrium equation for an elastic structure. This is in contrast to the commonly used frequency domain tools which require a linearized structural model and stationary conditions. In a time domain simulation, the stiffness, damping and mass matrices are allowed to vary with time, which means that any type of structural nonlinearity may be included. The external loads may include multiple frequencies simultaneously, and the load frequency can vary with time. The hydrodynamic model makes no use of concepts such as dimensionless frequency or reduced velocity, which means the flow velocity is allowed to vary with time, making it possible to simulate VIV in oscillating flows. This was successfully demonstrated in paper III and IV.

When a cylinder is subjected to vortex shedding, the hydrodynamic added mass varies strongly with the dimensionless frequency (or reduced velocity) as well as amplitude ratio. There are different ways of dealing with this in analysis methods. For instance, in VIVANA [10], all the hydrodynamic force in phase with the cylinder acceleration is treated as added mass, which is placed on the left-hand side of the dynamic equilibrium equation, together with the structural mass. This results in a dynamic system that is always at resonance. Another alternative is to keep all the hydrodynamic force on the right-hand side of the system, as an external force. This will typically be done in a coupled CFD and structural analysis, resulting in a dynamic system that is not necessarily at resonance. The model proposed in this thesis does something in between, as the total hydrodynamic force contains two terms which influence the effective added mass. Firstly, there is a constant added mass term associated with cylinder acceleration, which is moved to the left-hand side of the dynamic equilibrium equation together with the structural mass. Secondly, the vortex shedding force is generally not in phase with the cylinder velocity or acceleration, but somewhere in between (there is a phase difference which is determined by the synchronization model). Hence, the vortex shedding force will contribute to the effective added mass, and this contribution will vary depending on the dimensionless vibration frequency and amplitude. This was clearly demonstrated in paper IV. It should be emphasized that the different alternatives for modeling added mass are not in conflict, they simply represent different options for describing the same physics. However, an advantage with the present formulation is that the iteration procedure which is needed in frequency

domain to obtain consistency between added mass and vibration frequency is avoided. Splitting the total added mass into two contributions is however not a new idea, and the wake oscillator models (see e.g. Ref. [84]) use a similar approach.

In the fourth and final paper of this thesis, a new hydrodynamic load model was introduced, consisting of the well-known Morison's equation plus an additional term describing the vortex shedding force. The main reason for changing the formulation was the desire to include drag forces. One may then ask, why not keep the model as it was in e.g. paper III and simply add a static drag force in the direction of the flow? This would work fine for cases with constant current velocity, and with no dynamic motion except VIV. However, in general, the relative flow may be a combination of incoming current plus prescribed motions (as in the case with top-end oscillation), or large amplitude motion caused by other external loads. Therefore, the drag and the vortex shedding force should be computed based on the instantaneous relative flow velocity. This was achieved using Morison's equation plus the additional vortex shedding term.

To summarize, the final version of the hydrodynamic force model contains the traditional inertia and drag coefficients, C_M and C_D, plus the vortex shedding force coefficient C_v. In addition, the synchronization model, as formulated in the final paper, contains two empirical parameters: $\hat{f}_0$ which determines the center frequency of the vortex shedding force, and $\Delta\hat{f}$ which gives the range of synchronization. Hence the total hydrodynamic load model contains 5 empirical parameters, which in general may depend on the Reynolds number, the cylinder surface roughness, the KC number (if the flow is oscillating), and possibly also the actual shape of the cylinder trajectory (e.g. in-line amplitude and phase angle). Hence, the model parameters are associated with significant uncertainties, which have not been fully addressed in this work. Instead of focusing on the specific choice of parameters, the major achievement of this work has been to demonstrate that a model based on these parameters can be very useful.

4.3 Limitations

There are several limitations to the proposed hydrodynamic load model. First of all, it only applies to circular cylinders. As already stated, the model is an approximation of the real physics, which relies on empirical coefficients. Therefore, experimental data for the actual Reynolds number and cylinder surface roughness should be available. Although this has not been investigated, it is possible that the optimal coefficients depend on the specific cylinder trajectory. However, the results presented in this thesis suggests that this is of minor importance.

This work has focused on cross-flow VIV and the associated forces. A model of the in-line hydrodynamic forces was presented in paper II, but this is not compatible with the final formulation (i.e. paper IV). In addition, the model in paper II was only valid for combined cross-flow and in-line VIV, and not applicable in cases with pure in-line VIV.

Data from VIV tests usually include significant higher harmonic components. It has been noted that the formulation presented in paper IV gives rise to *some* higher harmonics if in-line vibrations at double the cross-flow frequency are present. However, a proper in-line hydrodynamic force model must be in place before it is possible to say if the arising higher harmonics are close to observations.

In reality, VIV is not a regular stationary vibration. Particularly for high mode vibrations, amplitude modulations and change in frequency may happen, and riser VIV has been described as a chaotic phenomenon. In its present form, the proposed model does not capture this behavior, as simulations with constant incoming flow velocity show an approximately steady state vibration.

4.4 Suggestions for future work

Before the proposed hydrodynamic load model can be applied in actual engineering design, more work is necessary to establish guidelines on what coefficients to use. A large database of test results should be compiled, and comparison with simulations could be performed to find the best combination of model parameters. Such a study should ideally take into account the Reynolds number and surface roughness dependency, and possibly KC number as well. Because VIV is a complicated phenomenon and the model is an approximation, uncertainties will always be present. These should be treated appropriately using statistical methods, similar to what Fontaine et al. [91] have done.

In its final form (paper IV), the present model can only predict cross-flow VIV. Future work should also look at how the fluctuating drag forces can be modeled, with the goal of establishing a model which is able to predict pure in-line VIV as well as combined in-line and cross-flow VIV. When the in-line motions are in place, it may also be possible to model the higher harmonics as previously discussed. However, the understanding of the higher harmonic components is presently limited, and successful modeling may require a substantial amount of research.

As the proposed model is able to predict VIV in oscillating flows, it is tempting to think that it is equally suited for simulating VIV caused by waves. This is however not necessarily true, as the flow may be quite different due to e.g. the elliptic orbit of the fluid particles and the free surface. This needs to be investigated in the future.

References

[1] Blevins RD. Flow-Induced Vibration. 2 ed.; Van Nostrand Reinhold; 1990.

[2] Vandiver JK. Dimensionless parameters important to the prediction of vortex-induced vibration of long, flexible cylinders in ocean currents. Journal of Fluids and Structures 1993;7(5):423 – 455.

[3] Jhingran VG. Drag amplification and fatigue damage in vortex-induced vibrations. Ph.D. thesis; Massachusetts Institute of Technology; 2008.

[4] Lundby L. Havromsteknologi. NTNU; 2013.

[5] Bearman PW. Vortex shedding from oscillating bluff bodies. Annual Review of Fluid Mechanics 1984;16(1):195–222.

[6] Sarpkaya T. A critical review of the intrinsic nature of vortex-induced vibrations. Journal of Fluids and Structures 2004;19(4):389 – 447.

[7] Williamson C, Govardhan R. Vortex-induced vibrations. Annual Review of Fluid Mechanics 2004;36(1):413–455.

[8] Shell Perdido project. `http://www.shell.com/about-us/major-projects/perdido.html`; Accessed 15.04.2016.

[9] Vandiver JK, Li L. SHEAR7 V4.4 Program Theoretical Manual. Department of Ocean Engineering, Massaccusetts Institute of Technology; 2005.

[10] Larsen CM, Lie H, Passano E, Yttervik R, Wu J, Baarholm G. VIVANA - Theory Manual, Version 3.7. MARINTEK; 2009.

[11] Triantafyllou M, Triantafyllou G, Tein Y, Ambrose BD, et al. Pragmatic riser VIV analysis. In: Offshore Technology Conference. 1999,.

[12] Larsen CM, Zhao Z, Lie H. Frequency components of vortex induced vibrations in sheared current. In: ASME 2012 31st International Conference on Ocean, Offshore and Arctic Engineering. American Society of Mechanical Engineers; 2012, p. 493–501.

[13] Det Norske Veritas, Recommended Practice DNV-RP-F204 Riser Fatigue. 2010.

[14] Sumer BM, Fredsøe J. Hydrodynamics around cylindrical structures; vol. 12. World Scientific Publishing Company; 1997.

[15] Gerrard J. The mechanics of the formation region of vortices behind bluff bodies. Journal of Fluid Mechanics 1966;25(02):401–413.

[16] Williamson C. Oblique and parallel modes of vortex shedding in the wake of a circular cylinder at low Reynolds numbers. Journal of Fluid Mechanics 1989;206:579–627.

[17] Bloor MS. The transition to turbulence in the wake of a circular cylinder. Journal of Fluid Mechanics 1964;19(02):290–304.

[18] NASA Earth Observatory. `http://earthobservatory.nasa.gov/IOTD/view.php?id=2613`; Accessed 15.04.2016.

[19] Achenbach E, Heinecke E. On vortex shedding from smooth and rough cylinders in the range of Reynolds numbers 6×10^3 to 5×10^6. Journal of Fluid Mechanics 1981;109:239–251.

[20] Roshko A. Experiments on the flow past a circular cylinder at very high Reynolds number. Journal of Fluid Mechanics 1961;10(03):345–356.

[21] Schewe G. On the force fluctuations acting on a circular cylinder in crossflow from subcritical up to transcritical Reynolds numbers. Journal of Fluid Mechanics 1983;133:265–285.

[22] Hallam M, Heaf N, Wootton LR. Dynamics of marine structures: Methods of calculating the dynamic response of fixed structures subject to wave and current action. Tech. Rep.; CIRIA Underwater Engineering Group; 1977.

[23] Norberg C. Fluctuating lift on a circular cylinder: review and new measurements. Journal of Fluids and Structures 2003;17(1):57–96.

[24] Bishop R, Hassan A. The lift and drag forces on a circular cylinder in a flowing fluid. Proceedings of the Royal Society of London Series A Mathematical and Physical Sciences 1964;277(1368):32–50.

[25] Zhou B, Wang X, Gho WM, Tan SK. Force and flow characteristics of a circular cylinder with uniform surface roughness at subcritical reynolds numbers. Applied Ocean Research 2015;49:20–26.

[26] Bishop R, Hassan A. The lift and drag forces on a circular cylinder oscillating in a flowing fluid. Proceedings of the Royal Society of London Series A Mathematical and Physical Sciences 1964;277(1368):51–75.

[27] Novak M, Tanaka H. Pressure correlations on a vibrating cylinder. In: Proc. 4th Int. Conf. Wind Effects on Building and Structures, Heathrow. 1975, p. 227–232.

[28] Sarpkaya T. Fluid forces on oscillating cylinders. Journal of the Waterway, Port, Coastal and Ocean Division 1978;104(3):275–290.

[29] Williamson C, Roshko A. Vortex formation in the wake of an oscillating cylinder. Journal of Fluids and Structures 1988;2(4):355–381.

[30] Gopalkrishnan R. Vortex-induced forces on oscillating bluff cylinders. Ph.D. thesis; Massachusetts Institute of Technology; 1993.

[31] Moe G, Wu ZJ. The lift force on a cylinder vibrating in a current. Journal of Offshore Mechanics and Arctic Engineering 1990;112(4):297–303.

[32] Morse T, Williamson C. Prediction of vortex-induced vibration response by employing controlled motion. Journal of Fluid Mechanics 2009;634:5–39.

[33] Aronsen KH. An experimental investigation of in-line and combined in-line and cross-flow vortex induced vibrations. Ph.D. thesis; Norwegian University of Science and Technology; 2007.

[34] Dahl JM. Vortex-induced vibration of a circular cylinder with combined in-line and cross-flow motion. Ph.D. thesis; Massachusetts Institute of Technology; 2008.

[35] Aglen I. VIV in free spanning pipelines. Ph.D. thesis; Norwegian University of Science and Technology; 2013.

[36] Yin D. Experimental and numerical analysis of combined in-line and cross-flow vortex induced vibration. Ph.D. thesis; Norwegian University of Science and Technology; 2013.

[37] Vikestad K, Vandiver J, Larsen C. Added mass and oscillation frequency for a circular cylinder subjected to vortex-induced vibrations and external disturbance. Journal of Fluids and Structures 2000;14(7):1071–1088.

[38] Feng C. The measurement of vortex induced effects in flow past stationary and oscillating circular and D-section cylinders. M.Sc. Thesis. University of British Columbia,; 1968.

[39] Khalak A, Williamson C. Motions, forces and mode transitions in vortex-induced vibrations at low mass-damping. Journal of Fluids and Structures 1999;13(7):813–851.

[40] Govardhan R, Williamson C. Modes of vortex formation and frequency response of a freely vibrating cylinder. Journal of Fluid Mechanics 2000;420:85–130.

[41] Sarpkaya T. Hydrodynamic damping, flow-induced oscillations, and biharmonic response. Journal of offshore Mechanics and Arctic engineering 1995;117(4):232–238.

[42] Jauvtis N, Williamson C. The effect of two degrees of freedom on vortex-induced vibration at low mass and damping. Journal of Fluid Mechanics 2004;509:23–62.

[43] Dahl J, Hover F, Triantafyllou M. Two-degree-of-freedom vortex-induced vibrations using a force assisted apparatus. Journal of Fluids and Structures 2006;22(6):807–818.

[44] Govardhan R, Williamson C. Defining the 'modified Griffin plot' in vortex-induced vibration: revealing the effect of Reynolds number using controlled damping. Journal of Fluid Mechanics 2006;561:147–180.

[45] Blevins RD, Coughran CS. Experimental investigation of vortex-induced vibration in one and two dimensions with variable mass, damping, and Reynolds number. Journal of Fluids Engineering 2009;131(10).

[46] Dahl J, Hover F, Triantafyllou M, Oakley O. Dual resonance in vortex-induced vibrations at subcritical and supercritical Reynolds numbers. Journal of Fluid Mechanics 2010;643:395–424.

[47] Raghavan K, Bernitsas M. Experimental investigation of Reynolds number effect on vortex induced vibration of rigid circular cylinder on elastic supports. Ocean Engineering 2011;38(5):719–731.

[48] Kiu K, Stappenbelt B, Thiagarajan K. Effects of uniform surface roughness on vortex-induced vibration of towed vertical cylinders. Journal of Sound and Vibration 2011;330(20):4753 – 4763.

[49] Yin D, Wu J, Lie H, Baarholm RJ, Larsen CM, et al. VIV Prediction of Steel Catenary Riser–A Reynolds Number Sensitivity Study. In: The Twenty-fifth International Offshore and Polar Engineering Conference. International Society of Offshore and Polar Engineers; 2015,.

[50] Vandiver JK. Damping parameters for flow-induced vibration. Journal of Fluids and Structures 2012;35:105–119.

[51] Baarholm GS, Larsen CM, Lie H. On fatigue damage accumulation from in-line and cross-flow vortex-induced vibrations on risers. Journal of Fluids and Structures 2006;22(1):109–127.

[52] Trim A, Braaten H, Lie H, Tognarelli M. Experimental investigation of vortex-induced vibration of long marine risers. Journal of Fluids and Structures 2005;21(3):335–361.

[53] Modarres-Sadeghi Y, Chasparis F, Triantafyllou M, Tognarelli M, Beynet P. Chaotic response is a generic feature of vortex-induced vibrations of flexible risers. Journal of Sound and Vibration 2011;330(11):2565–2579.

[54] Chaplin J, Bearman P, Huera Huarte F, Pattenden R. Laboratory measurements of vortex-induced vibrations of a vertical tension riser in a stepped current. Journal of Fluids and Structures 2005;21(1):3–24.

[55] Vandiver JK, Swithenbank SB, Jaiswal V, Jhingran V. Fatigue damage from high mode number vortex-induced vibration. In: 25th International Conference on Offshore Mechanics and Arctic Engineering. American Society of Mechanical Engineers; 2006, p. 803–811.

[56] Modarres-Sadeghi Y, Mukundan H, Dahl J, Hover F, Triantafyllou M. The effect of higher harmonic forces on fatigue life of marine risers. Journal of Sound and Vibration 2010;329(1):43–55.

[57] Søreide T, Paulsen G, Nielsen FG. Parameter study of long free spans. In: The Eleventh International Offshore and Polar Engineering Conference. International Society of Offshore and Polar Engineers; 2001,.

[58] Nielsen FG, Søreide TH, Kvarme SO. Viv response of long free spanning pipelines. In: ASME 2002 21st International Conference on Offshore Mechanics and Arctic Engineering. American Society of Mechanical Engineers; 2002, p. 121–129.

[59] Passano E, Larsen CM, Wu J. VIV of free spanning pipelines: Comparison of response from semi-empirical code to model tests. In: ASME 2010 29th International Conference on Ocean, Offshore and Arctic Engineering. American Society of Mechanical Engineers; 2010, p. 567–577.

[60] Swithenbank SB, Vandiver JK, Larsen CM, Lie H. Reynolds number dependence of flexible cylinder VIV response data. In: ASME 2008 27th International Conference on Offshore Mechanics and Arctic Engineering. American Society of Mechanical Engineers; 2008, p. 503–511.

[61] Allen D, Henning D. Surface roughness effects on vortex-induced vibration of cylindrical structures at critical and supercritical reynolds numbers. In: Offshore Technology Conference. Offshore Technology Conference; 2001,.

[62] Keulegan GH, Carpenter LH. Forces on cylinders and plates in an oscillating fluid. US Department of Commerce, National Bureau of Standards; 1956.

[63] Sumer B, Fredsoe J. Transverse vibrations of an elastically mounted cylinder exposed to an oscillating flow. Journal of Offshore Mechanics and Arctic Engineering 1988;110(4):387–394.

[64] Maull D, Kaye D. Oscillations of a flexible cylinder in waves. In: Proc. Int. Conf. on Behaviour of Offshore Structures (BOSS '88). 1988,.

[65] Lipsett A, Williamson I. Response of a cylinder in oscillatory flow. Journal of fluids and structures 1994;8(7):681–709.

[66] Kozakiewicz A, Sumer BM, Fredsøe J. Cross-flow vibrations of cylinder in irregular oscillatory flow. Journal of waterway, port, coastal, and ocean engineering 1994;120(6):515–534.

[67] Fu S, Wang J, Baarholm R, Wu J, Larsen C. Features of vortex-induced vibration in oscillatory flow. Journal of Offshore Mechanics and Arctic Engineering 2014;136(1).

[68] Wang J, Fu S, Baarholm R, Wu J, Larsen CM. Out-of-plane vortex-induced vibration of a steel catenary riser caused by vessel motions. Ocean Engineering 2015;109:389–400.

[69] Liao JC. Vortex-induced vibration of slender structures in unsteady flow. Ph.D. thesis; Massachusetts Institute of Technology; 2001.

[70] Resvanis TL. Vortex-induced vibration of flexible cylinders in time-varying flows. Ph.D. thesis; Massachusetts Institute of Technology; 2014.

[71] Hughes TJ. The finite element method: linear static and dynamic finite element analysis. Courier Corporation; 2012.

[72] Langen I, Sigbjørnsson R. Dynamisk analyse av konstruksjoner. Tapir; 1979.

[73] Chaplin J, Bearman P, Cheng Y, Fontaine E, Graham J, Herfjord K, et al. Blind predictions of laboratory measurements of vortex-induced vibrations of a tension riser. Journal of Fluids and Structures 2005;21(1):25–40.

[74] Gabbai R, Benaroya H. An overview of modeling and experiments of vortex-induced vibration of circular cylinders. Journal of Sound and Vibration 2005;282(3):575–616.

[75] White FM. Fluid Mechanics. 6 ed.; McGraw-Hill; 2008.

[76] Gallardo Canabes JP. Numerical studies of viscous flow around bluff bodies. Ph.D. thesis; Norwegian University of Science and Technology; 2015.

[77] Versteeg HK, Malalasekera W. An Introduction to Computational Fluid Dynamics: The Finite Volume Method. 2 ed.; Pearson Education; 2007.

[78] Bourguet R, Karniadakis GE, Triantafyllou MS. Vortex-induced vibrations of a long flexible cylinder in shear flow. Journal of Fluid Mechanics 2011;677:342–382.

[79] Venugopal M. Damping and response prediction of a flexible cylinder in a current. Ph.D. thesis; Massachusetts Institute of Technology; 1996.

[80] Finn L, Lambrakos K, Maher J. Time domain prediction of riser VIV. In: Proceedings of the Fourth International Conference on Advances in Riser Technologies. 1999,.

[81] Cheng Y, Lambrakos KF. Time domain computation of riser VIV from vessel motions. In: 25th International Conference on Offshore Mechanics and Arctic Engineering. American Society of Mechanical Engineers; 2006, p. 829–838.

[82] Lie H. A time domain model for simulation of vortex induced vibrations on a cable. In: Proc. Sixth Int. Conf. on Flow Induced Vibrations. London, UK; 1995, p. 455–466.

[83] Mainçon P. A Wiener-Laguerre model of VIV forces given recent cylinder velocities. Mathematical Problems in Engineering 2011;2011.

[84] Facchinetti ML, de Langre E, Biolley F. Coupling of structure and wake oscillators in vortex-induced vibrations. Journal of Fluids and Structures 2004;19(2):123–140.

[85] Srinil N, Zanganeh H. Modelling of coupled cross-flow/in-line vortex-induced vibrations using double duffing and van der pol oscillators. Ocean Engineering 2012;53:83–97.

[86] Vikestad K. Multi-frequency response of a cylinder subjected to vortex shedding and support motions. Ph.D. thesis; Norwegian University of Science and Technology, Department of Marine Technology; Trondheim, Norway; 1998.

[87] Sævik S. SIMLA Theory Manual; 2008.

[88] Hilber HM, Hughes TJ, Taylor RL. Improved numerical dissipation for time integration algorithms in structural dynamics. Earthquake Engineering & Structural Dynamics 1977;5(3):283–292.

[89] Wang J, Fu S, Baarholm R, Wu J, Larsen CM. Fatigue damage of a steel catenary riser from vortex-induced vibration caused by vessel motions. Marine Structures 2014;39:131–156.

[90] Ermentrout GB, Rinzel J. Beyond a pacemaker's entrainment limit: phase walk-through. American Journal of Physiology - Regulatory, Integrative and Comparative Physiology 1984;246(1):102–106.

[91] Fontaine E, Rosen J, Marcollo H, Vandiver J, Triantafyllou M, Resvanis T, et al. Using model test data to assess VIV factor of safety for SCR and TTR in GOM. In: ASME 2013 32nd International Conference on Ocean, Offshore and Arctic Engineering. American Society of Mechanical Engineers; 2013,.

Appended papers

Paper I

A simplified method for time domain simulation of cross-flow vortex-induced vibrations

Mats J. Thorsen, Svein Sævik and Carl M. Larsen

Department of Marine Technology, Norwegian University of Science and Technology, Trondheim, Norway

Journal of Fluids and Structures, Vol. 49, 2014, pp. 135 – 148

Abstract

A new method for time domain simulation of cross-flow vortex-induced vibrations of slender circular cylindrical structures is developed. A model for the synchronization between the lift force and structure motion is derived from already established data for the cross-flow excitation coefficient. The proposed model is tested by numerical simulations, and the results are compared to experimental observations. When a sinusoidal cross-flow motion is given as input to the algorithm, the generated force time series are generally in good agreement with experimental measurements of cross-flow force in phase with cylinder velocity and acceleration. The model is also utilized in combination with time integration of the equation of motion to simulate the cross-flow vibration of a rigid cylinder. The resulting amplitude and frequency of motion as functions of reduced velocity are compared to published experimental results. In combination with the finite element method, the model is used to simulate cross-flow vibrations of a flexible cylinder in shear flow. Comparison with experiments shows that the model is capable of reproducing important quantities such as frequency, mode and amplitude, although some discrepancies are seen. This must be expected due to the complexity of the problem and the simple form of the present method.

Keywords: Vortex-induced vibrations; Simulation; Time-domain; Synchronization

1 Introduction

Slender structures such as marine risers and mooring lines are subjected to vortex-induced vibrations (VIV) when placed in a current flowing around the structure. The vibrations are a result of the oscillating fluid forces arising from the shedding of vortices. Such vibrations may lead to rapid accumulation of fatigue damage, and it is therefore important for the safety of offshore operations such as drilling and hydrocarbon production to be able to predict the time varying stresses caused by VIV.

The topic of VIV has been subjected to extensive research during the second half of the 20th century, and much of the work has been reviewed by Bearman [1], Sarpkaya [2], Williamson and Govardhan [3] and Wu et al. [4]. Studies have traditionally focused on the cross-flow oscillations and fundamental frequency response, however in more recent publications, authors have focused on cylinders free to oscillate in both transverse and in-line directions [5, 6] and higher order force and vibration components [7, 8]. It has also been recognized that the VIV response of risers can be chaotic, meaning that it is non-periodic with a broad band spectrum [9].

When it comes to prediction of VIV for slender structures there is a large number of available methods, which according to Lie et al. [10] can be divided into three classes: Computational fluid dynamics (CFD), wake oscillator models and semi-empirical models. As demonstrated by Bourguet et al. [11], CFD methods are promising, but generally complicated and computationally demanding. Wake oscillator models, as described by e.g. Facchinetti et al. [12] use a Van der Pol oscillator to describe the wake. Results obtained using this model show a qualitative agreement with experimental observations, but it is difficult to find a set of parameters such that the model conforms to both free and forced vibrations [13].

The most commonly used prediction tool in design of marine risers are the semi-empirical models, such as SHEAR7 [14] and VIVANA [15]. The basis for these programs is the use of databases for hydrodynamic forces, e.g. added mass, damping and excitation (lift) coefficients. The formulation restrict these methods to stationary, harmonic response in the frequency domain, hence only linear structural behavior is allowed, and interaction between different response frequencies is difficult to account for. Also, these tools are unable to predict VIV caused by unsteady flows such as waves, and cross-flow and in-line motion is considered separately, neglecting the interaction between the two.

Semi-empirical time domain methods for simulation of riser VIV have been developed by Lie [16] and Finn et al. [17]. A challenge with these methods is the need to estimate the vibration frequency of the riser for every time step, based on the previous time history. Recently, Mainçon [18] proposed a totally new method for time domain prediction of VIV. He applied an artificial neural network in order to predict the instantaneous hydrodynamic force based on a compressed form of the recent velocity history. The results obtained in the study were promising, but in some cases the model adopted a non-physical pattern of vibration, indicating that the algorithm has stability issues.

In this paper, an alternative method for time domain prediction of VIV is presented. The most important element is the proposed synchronization model, which effectively simulates how the lift force changes its instantaneous frequency to obtain lock-in. Another key component is a new damping model, based on the model by Venugopal [19], but put in an alternative form to avoid frequency dependence. Combined with a finite element model of the structure, the hydrodynamic force model makes a powerful tool for time domain simulation of VIV, and it is shown through numerical investigation that the method produces results very similar to those observed in various types of experiments. The formulation includes no restrictions on the time variation of the incoming current velocity, and therefore enables the study of VIV in waves and other unsteady flows, although this has presently not been investigated. The formulation also has potential for incorporating the interaction between cross-flow and in-line hydrodynamic forces and motion, as well as drag amplification and higher order frequency components. However, these issues will not be addressed further in the present research. In this initial stage of development, focus will be on cross-flow response in stationary flow.

2 Hydrodynamic force model

2.1 Hydrodynamic forces on circular cylinders

A cylinder placed in a flowing fluid will experience forces in the direction of the flow as well as perpendicular to the flow. The force component in the direction of the flow is called drag, while the perpendicular component is usually termed lift. For a single cylinder positioned in an otherwise undisturbed flow, the mean of the lift force is zero, while the drag force oscillates around a non-zero mean value. The case with a fixed cylinder in uniform incoming flow was thoroughly studied by Bishop and Hassan [20] and many others since then, see e.g. [21] for a comprehensive review. In summary, the lift forces are a result of the fluctuating pressure which in turn is related to the vortex shedding process. It is found to vary almost sinusoidally with the same frequency as the vortex shedding frequency, $f_s = \mathrm{St}\, U/D$, where St is the Strouhal number, U is the incoming undisturbed fluid velocity and D is the cylinder diameter. Stochastic variations in amplitude and frequency are seen, hence the forces are only approximately sinusoidal. The drag force has a significant non-zero mean value, while the fluctuating part oscillates at twice the vortex shedding frequency with a small amplitude, only around 10 % of the lift force [22]. The drag and lift force are usually expressed in terms of the non-dimensional coefficients $C_d = F_d/(\frac{1}{2}\rho DU^2)$ and $C_l = F_l/(\frac{1}{2}\rho DU^2)$ where ρ is the fluid density and F_d and F_l are the drag and lift force per unit length. The mean value and the amplitude of the coefficients are found mainly as functions of the Reynolds number and the cylinder's surface roughness, while the turbulence level in the incoming flow and specific experimental conditions such as aspect ratio, end terminations and blockage effects have some influence on measurements as well. Curves for the coefficients and the Strouhal number have been

established through extensive research (see e.g. [23]), though it should be mentioned that values for the lift coefficient from various researchers show significant scatter.

The complexity of the problem increases considerably when the cylinder is allowed to oscillate. This subject has perhaps been studied even more than the stationary cylinder case, and typical experiments consist of freely oscillating spring supported cylinders [24, 25] and cylinders forced to move in specified patterns [26, 27]. The last category of experiments has served two purposes: To increase the understanding of the vortex-shedding process as well as to create a database of force coefficients which can be used in prediction tools. The reason why the moving cylinder case is more challenging to predict than the fixed case is that the cylinder motion disturbs the flow. The most important effect is possibly that the frequency of the vortex shedding may adjust itself, and synchronize with the frequency of the cylinder motion. This is referred to as *lock-in*, as the vortex frequency "locks on" to the frequency of oscillation. The fact that the vortex shedding frequency can adjust, makes large amplitude motions possible over a relatively long range of current velocities. Another effect of the cylinder motion is a significant increase in the mean drag force [28].

2.2 Model assumptions and simplifications

Consider a circular cylinder positioned in a flowing fluid, while moving in the in-line and cross-flow direction in an arbitrary fashion, as shown in figure 1. A coordinate system (x, y, z) is defined such that the x-axis points in the direction of the incoming flow and the y-axis in the orthogonal direction in the plane of the cylinder. The z-axis is pointing out of the plane in the longitudinal direction of the cylinder and creates a right handed coordinate system. The unit base vectors are $\vec{i}$, $\vec{j}$ and $\vec{k}$. Let the origin be positioned at the static equilibrium position of the cylinder, such that x and y corresponds to the in-line and cross-flow displacement of the cylinder respectively. Due to the combination of incoming current and cylinder motion, the relative velocity between fluid and structure changes both magnitude and direction continuously. Given the velocity of the cylinder, the relative fluid velocity vector may be expressed as:

$$\vec{V} = (U - \dot{x})\vec{i} - \dot{y}\vec{j}. \tag{1}$$

The force exerted by the fluid on the cylinder cross section is assumed to consist of three components: Lift, damping and added mass. The lift force is a result of the pressure field associated with vortex shedding, while the damping force comes from fluid resistance as the cylinder moves through the fluid. The added mass force is due to the pressure field related to cylinder acceleration. A model for the damping force has been proposed by Venugopal [19], based on a survey of available results and measurements of damping of flexible cylinders in still water and uniform flow. Most of the data which the model is based on is for a Reynolds number around 10 000. He gives two different expressions for

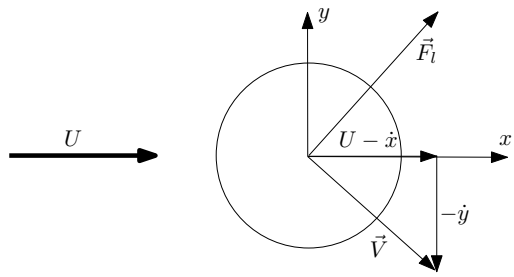

Figure 1: Moving cylinder in incoming flow. Coordinate system, relative velocity and lift force are shown.

the damping coefficient, one valid for low reduced velocity ($V_r = U/(fD)$, where f is the vibration frequency) and one for high reduced velocity:

$$c_{\text{low}} = \frac{\omega \pi \rho D^2}{2}\left[\frac{2\sqrt{2}}{\sqrt{\text{Re}_\omega}} + 0.25(\frac{A}{D})^2\right] + \frac{1}{2}\rho D U C_{vl}, \tag{2}$$

$$c_{\text{high}} = \frac{1}{2}C_{vh}\frac{\rho U^2}{\omega}, \tag{3}$$

where $\text{Re}_\omega = \omega D^2/\nu$ and ν is the kinematic viscosity of the fluid. C_{vl} and C_{vh} is set to 0.36 and 0.4 respectively, based on measurements. The angular frequency of motion is given by ω, while A is the oscillation amplitude. These expressions are not suitable for time domain simulations, as the damping coefficient is a function of oscillation frequency. Therefore, an alternative damping model is suggested here, which is independent of frequency and hence suitable for the present application. The proposed cross-flow damping model contains a linear and non-linear term as follows:

$$F_{\text{damp},y} = -\frac{1}{2}\rho D C_1 U \dot{y} - \frac{1}{2}\rho A C_2 |\dot{y}|\dot{y}. \tag{4}$$

The coefficients C_1 and C_2 are constants, and are chosen such that the energy extracted per cycle is approximately the same as in Venugopal's low reduced velocity model. The energy transfer is conveniently expressed as a non-dimensional excitation coefficient:

$$C_e = \lim_{T\to\infty}\frac{2}{T}\int_0^T C_y(t)\cos(\omega t)dt, \tag{5}$$

where $C_y(t)$ is the dimensionless cross-flow force, and the cross flow velocity is $\omega A\cos(\omega t)$. Inserting the damping force from equation (4) into equation (5) gives the excitation coefficient due to damping only:

$$C_e = -C_1 \frac{\omega A}{U} - C_2 \frac{8\omega^2 A^3}{3\pi D U^2}. \tag{6}$$

Repeating this calculation using Venugopal's expression for low reduced velocity gives:

$$C_e = -c_{\text{low}} \frac{2\omega A}{\rho D U^2}. \tag{7}$$

Ideally, the two different damping models should produce the same excitation coefficient for all combinations of amplitudes, A/D and non-dimensional frequencies, $\hat{f} = fD/U$ in the low reduced velocity regime ($\hat{f} > 0.2$). This means that equation (6) and (7) can be set equal to each other, and an infinite number of such equations can be constructed by varying $\hat{f}$ and A/D. A finite number of equations are established using $\hat{f} \in [0.2, 0.5]$ and $(A/D) \in [0.2, 1.0]$ which is solved for C_1 and C_2 using least-squares. This yields $C_1 = 0.485$ and $C_2 = 0.936$, which gives an average relative difference (over the specified range of $\hat{f}$ and (A/D)) between the excitation coefficient from the two models of 1.8 %. Notice that the amplitude of oscillation is included in the non-linear term of equation (4). This is in general not constant, and is continuously updated as the time domain simulation progresses using the following expression:

$$A = \frac{1}{2} \int_{T_1}^{T_2} |\dot{y}| dt, \tag{8}$$

where T_1 and T_2 are the time of the two latest zero-crossings of the cross-flow velocity, as shown in figure 2.

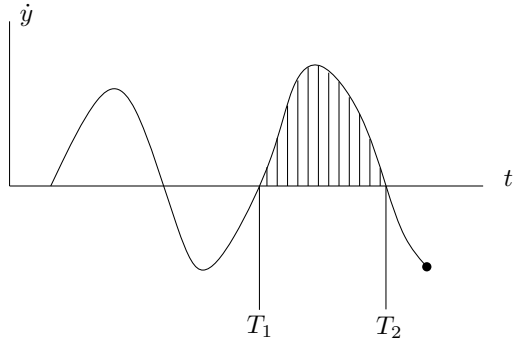

Figure 2: Definition of T_1 and T_2, the integration limits of equation (8).

As indicated in figure 1 the lift force is assumed to act perpendicular to the instantaneous relative velocity vector, and is expressed mathematically as:

$$\vec{F_l} = \frac{1}{2}\rho D C_l |\vec{V}|(\vec{k} \times \vec{V}). \tag{9}$$

The time varying lift coefficient is written as $C_l = C_{l,0}\cos\phi_l$. The first part corresponds to the amplitude of the lift force, and is a function of the non-dimensional oscillation amplitude, i.e. $C_{l,0} = C_{l,0}(A/D)$. Although the amplitude may vary in time, $C_{l,0}$ will be constant during a single oscillation cycle. This means that the short term variability of the vortex shedding process is contained in the second term, ϕ_l, which is termed the instantaneous phase of the lift force. To exemplify the concept of instantaneous phase, consider the special case of a regular sinusoidally varying lift force. Then the lift coefficient is given as $C_l = C_{l,0}\cos(2\pi f t + \varphi)$. This means the instantaneous phase in this particular example is $\phi_l = 2\pi f t + \varphi$ and the time rate of change of the instantaneous phase is $d\phi_l/dt = 2\pi f$. In other words, the time derivative of the instantaneous phase equals the angular frequency if the force signal is sinusoidal. However, the lift force is in general not purely sinusoidal, and may change its instantaneous frequency to obtain lock-in. This must be included in the model, and a synchronization algorithm providing the general behavior of the lift phase is described in the next section.

The values of $C_{l,0}$ as a function of A/D can be calculated if one has knowledge of the cross-flow excitation coefficient. The calculation is based on the assumption that the lift force is completely in phase with the cylinder velocity for the non-dimensional frequency at which the excitation coefficient attains its maximum value. Based on experiments by Gopalkrishnan [29] with an oscillating rigid cylinder, this occurs when $\hat{f} \approx 0.17$. This makes it possible to find the function $C_{l,0}(A/D)$ necessary to have a certain excitation coefficient at $\hat{f} = 0.17$. Note that the lift coefficient in the present context is not a function of frequency, meaning that it is valid for all frequencies even though it is extracted from the excitation coefficient at $\hat{f} = 0.17$. The damping force is also taken into account in the process, as the actual excitation coefficient is a result of the power input from the lift force and the power output due to damping. The excitation coefficient curve currently applied in VIVANA is utilized for the calculation. This curve is based on Gopalkrishnan [29], with some modifications to include experience from flexible beam tests [15]. It should be noted that data from other sources might have been used instead. The utilized excitation coefficient curve is shown in figure 3 together with the resulting lift coefficient curve.

In addition to the lift and damping force, an added mass force is present as a result of cylinder acceleration. The still water potential theory value is used for the added mass coefficient, i.e. $C_a = 1.0$. This means the total fluid force in the cross-flow direction (assuming no in-line motion) can be written:

$$F_{\text{fluid},y} = \underbrace{\frac{1}{2}\rho D|\vec{V}|UC_{l,0}\cos\phi_l}_{\text{lift force, y-component}} \underbrace{-\frac{1}{2}\rho D C_1 U\dot{y} - \frac{1}{2}\rho A C_2|\dot{y}|\dot{y}}_{\text{damping force}} \underbrace{-\frac{\rho\pi D^2}{4}C_a\ddot{y}}_{\text{added mass force}}. \tag{10}$$

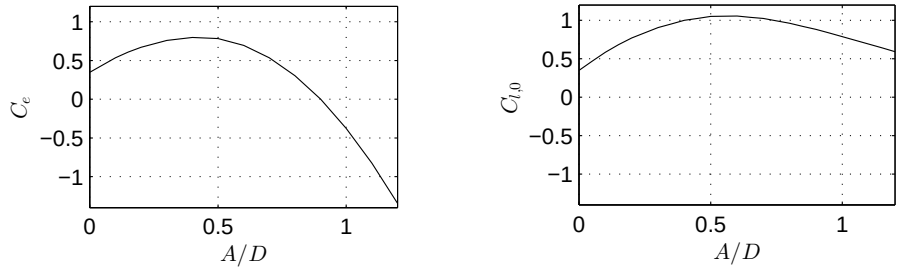

(a) Input C_e at $\hat{f} = 0.17$

(b) Resulting $C_{l,0}$

Figure 3: Input excitation coefficient at $\hat{f} = 0.17$ and resulting $C_{l,0}$ as function of amplitude.

Note that the *total* added mass force is not only the $(\rho\pi D^2/4)C_a\ddot{y}$-term, but also the part of the lift force which is in phase with the cylinder acceleration.

2.3 Synchronization

Synchronization may be described as the adjustment of frequencies or phases in a system of coupled oscillators. This phenomenon is observed in many branches of science, ranging from mechanical systems to biological issues such as the synchronization of neurons in the brain and the flashing of fireflies [30].

Theory used to describe weakly coupled oscillators and their synchronization behavior is presented by Izhikevich and Kuramoto [31]. An important point is that for a dynamical system,

$$\dot{x} = f(x), \quad x \in \mathbb{R}^m, \tag{11}$$

having a periodic orbit, there is a continuous transformation between $x(t)$ and the phase $\phi(t)$ defined on the unit circle. Such a transformation removes the amplitude and preserves the phase of the oscillation. Using this transformation makes it easier to study and describe the synchronization behavior of coupled oscillator networks.

For the present application, it is of interest to describe the synchronization between the cylinder motion and the lift force. It is assumed that the force at a given section is affected only by the motion of the same cylinder strip, which is a common assumption in other VIV prediction tools. It then follows that the span-wise correlation of the lift force is determined by the cylinder motion, i.e. 3-dimensional effects are communicated by the structure alone. Synchronization between force and velocity is necessary in order to get a positive energy transfer from fluid to body. Hence, the cross-flow velocity of the cylinder will be used as the physical quantity which the lift force seeks to synchronize

with. Denoting the instantaneous phase of the cross-flow velocity as $\phi_{\dot{y}}$, the following general form for a lift phase model is assumed valid:

$$\frac{d\phi_l}{dt} = 2\pi f_s + H(\phi_{\dot{y}} - \phi_l), \tag{12}$$

where the function $H(\phi_{\dot{y}} - \phi_l)$ provides the synchronization behavior, as it involves the phase of both lift force and cross-flow velocity. A procedure providing an estimate of the lift phase model is given in the following section.

2.3.1 Lift phase model

Rosenblum et al. [32] describes methods to reveal synchronization between different processes. These are based on applying the Hilbert transform to establish the instantaneous phase of a given signal. It was however found difficult to get reliable results using the Hilbert transform on measured vortex shedding forces. The reason is probably that the Hilbert transform is sensitive to frequency content, and should ideally only be applied to narrow band signals. Therefore, a more indirect approach is used, which is based on available results for the cross-flow excitation coefficient. For a sinusoidal oscillation, $\dot{y} = \omega A \cos(\omega t)$, in lock-in condition, there is a significant force component at the frequency of oscillation, meaning that it is possible to write

$$C_y(t) = C_{y,0} \cos(\omega t - \theta) + \epsilon(t), \tag{13}$$

where $\epsilon(t)$ represents higher order frequency terms and noise. Inserting this in equation (5), the following simple expression for the excitation coefficient is obtained, as $\epsilon(t)$ is uncorrelated with $\cos(\omega t)$:

$$C_e = C_{y,0} \cos\theta. \tag{14}$$

Recall that the lift force in the present model is not necessarily acting in the cross-flow direction. Hence it is incorrect to mix the lift force and the cross-flow force in a general situation, however for small oscillation amplitudes the two will coincide because the angle between the lift force vector, $\vec{F}_l$ and the y-axis is small. In addition, the damping force will be negligible. This means that $C_y = C_l$ as long as the oscillation amplitude is small. It follows that

$$\theta = \phi_{\dot{y}} - \phi_l, \tag{15}$$

for small amplitudes. If it is assumed that $C_{y,0}$ is constant when the amplitude is kept constant (and small), the phase difference between velocity and force is found as a function of the oscillation frequency,

$$\phi_{\dot{y}} - \phi_l = \cos^{-1}\left(\frac{C_e(\omega)}{C_{y,0}}\right) = \cos^{-1}\left(\frac{C_e(\omega)}{C_{e,\max}}\right), \tag{16}$$

where it has been inserted that $C_{y,0} = C_{e,\max}$, reflecting that the excitation coefficients attains its maximum when the velocity and force are completely in phase (i.e. when $\theta = 0$), and that this maximum value must equal the amplitude of the cross-flow force coefficient.

As the main frequency of the lift force is constant and equal to the oscillation frequency when lift and velocity are synchronized, the following statement must be true in the range of frequencies where excitation is positive:

$$\frac{d\phi_l}{dt} = \omega. \tag{17}$$

Utilizing a known excitation coefficient curve, $C_e(\omega)$, and combining equation (16) and (17) makes it possible to construct a point in the $(\phi_{\dot{y}} - \phi_l,\ d\phi_l/dt)$-plane for every ω in the synchronization range, resulting in a graph of the lift phase model. The VIVANA excitation coefficient curve for $A/D = 0.15$ is used for this purpose. As previously stated, this curve is based on experience from a number of tests and is therefore a reasonable choice, although data from other sources might have been used instead. The curve is smoothed to give only one local maximum, ensuring that the derived lift phase model is well defined. Figure 4 shows the original curve, along with the smoothed version. The coefficient is normalized by its maximum value and is shown as a function of $\hat{f} = \omega D/2\pi U$.

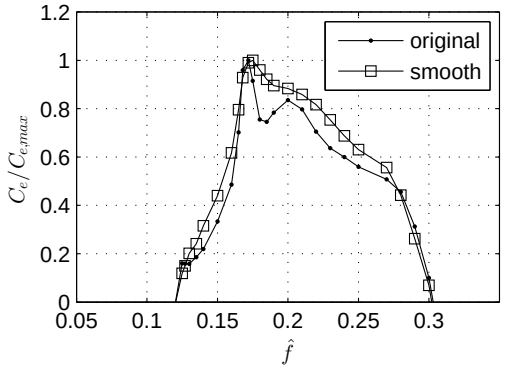

Figure 4: VIVANA excitation coefficient at A/D=0.15, original and smoothed version. The curves are normalized by their maximum values.

The smoothed curve is used to construct the lift phase model based on equations (16) and (17) as previously described. The instantaneous frequency, $d\phi_l/dt$, is normalized by

$\omega_s = 2\pi \mathrm{St}\ U/D$, assuming $\mathrm{St} = 0.2$, and plotted versus the phase difference between cross-flow velocity and lift force, $\phi_{\dot{y}} - \phi_l$. The resulting curve is shown in figure 5. The solid curve is obtained directly from applying equations (16) and (17), which produces results from $-\pi/2$ to $\pi/2$ on the unit circle. It is necessary to have results around the whole unit circle, and the unknown part of the curve is established based on the fact that $d\phi_l/dt$ should be continuous and 2π-periodic. A proposed curve in the unknown domain is shown with a dashed line.

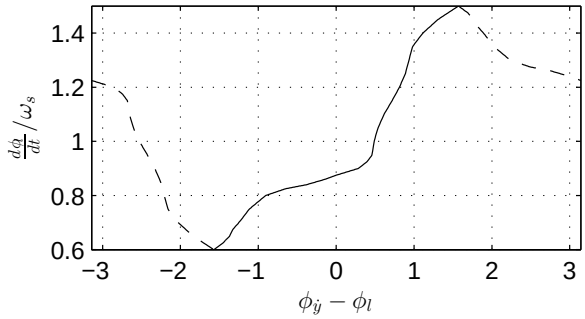

Figure 5: Lift phase model derived from the smoothed C_e curve. The instantaneous frequency of the lift force is normalized by the Strouhal frequency.

A short discussion regarding the interpretation of the lift phase model presented in figure 5 is appropriate at this point. The basis of the model is the fact that the time variability of the cross-flow velocity of the cylinder and the lift force can be described in terms of their instantaneous phases, $\phi_{\dot{y}}$ and ϕ_l. The phase gives a point on the unit circle which rotates with a certain angular velocity, which is defined as the instantaneous angular frequency. With this in mind, the cross-flow velocity and the lift force may be visualized as two individuals running around a field (the unit circle). Synchronization means that the lift force will speed up if the velocity gets too far ahead, and slow down in the opposite case. Referring to figure 5, it is seen that the mean instantaneous frequency of the lift force is approximately the Strouhal frequency, while it can accelerate up to 1.5 this value if the velocity is $\pi/2$ in front of the lift force. It may also slow down to 0.6 times the Strouhal frequency if the velocity is $\pi/2$ behind. In this way, the lift force will continuously update its speed, always trying to match the cross-flow oscillation frequency. However, if the oscillation frequency is higher than $1.5f_s$ or lower than $0.6f_s$, the lift force is unable to synchronize, and will not provide any energy to the oscillation.

2.3.2 Calculating phases

In order to apply the lift phase model, it is necessary to know the instantaneous phase of the cross-flow velocity, $\phi_{\dot{y}}$, and lift force, ϕ_l. The lift force phase is found from its initial

value and the rate of change $d\phi_l/dt$ given by the lift phase model shown in figure 5. The initial value of ϕ_l can in principle be taken arbitrarily, as the motion of the structure will, after a short transient period, determine the time-evolution of ϕ_l. However, for an elastic cylinder, unphysical transient vibrations will occur if $\phi_l(0, z)$ is taken to be uniformly distributed along the length of the cylinder because the lift force then will be fully correlated over the entire structure length at the starting point of the simulation. To avoid this unphysical transient startup, $\phi_l(0, z)$ is assigned independent random values between 0 and 2π.

In contrast to the lift force phase, the phase of the cross-flow velocity must be estimated from the simulated time series. At a given time step in a time domain simulation, one has knowledge of the response up to that particular time step only. This means that methods requiring data for the whole time series, such as the Hilbert transform, are unsuited. Instead, a phase portrait is constructed as shown in figure 6. The position on the x-axis is given by the normalized velocity, while the position on the y-axis is given by the normalized acceleration with a negative sign. The normalization is performed by dividing the current value of $\dot{y}(t)$ and $\ddot{y}(t)$ on the maximum value observed between time $t - t_c$ and t, where t_c is some characteristic time. This procedure is not necessarily optimal, but is considered sufficient and easy to implement. In all simulations presented here, t_c is set to 5 times the vortex-shedding period based on the Strouhal frequency.

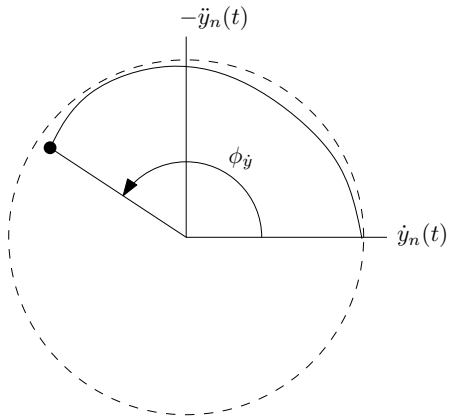

Figure 6: Phase portrait providing the phase of the cross-flow velocity.

3 Numerical results

3.1 Rigid cylinder subjected to forced oscillations

The hydrodynamic force model described in section 2 is used to simulate force time series for a rigid cylinder undergoing sinusoidal cross-flow motions at different frequencies and

amplitudes. In other words, a prescribed cross-flow motion, $y(t) = A\sin(\omega t)$, is used as input to the algorithm, and the hydrodynamic force per unit length is computed. The simulations resemble the experiments by Gopalkrishnan [29], which makes it possible verify the model directly. The Strouhal number is taken to be 0.2, which is known to be approximately true in the subcritical flow regime. All relevant parameters used in the simulations are shown in table 1.

Table 1: Simulation parameters, forced oscillations

U	0.4 m/s
D	0.0254 m
St	0.2
ρ	1000 kg/m^3

For different combinations of $\hat{f} = fD/U$ and A/D, the simulated time histories are post-processed to obtain the component of the cross-flow force in phase with velocity and acceleration respectively. The results are presented in figure 7 as contour plots together with Gopalkrishnan's experimental results. The coefficients have been calculated using the following formulas:

$$C_{y,v} = \lim_{T\to\infty} \frac{2}{T} \int_0^T C_y(t)\cos(\omega t)dt, \tag{18}$$

$$C_{y,a} = -\lim_{T\to\infty} \frac{2}{T} \int_0^T C_y(t)\sin(\omega t)dt, \tag{19}$$

where the integration is performed over a complete number of cycles. The cross-flow force coefficient is evaluated based on the total hydrodynamic force and the undisturbed incoming current velocity:

$$C_y(t) = \frac{F_{\text{fluid},y}(t)}{\frac{1}{2}\rho D U^2}. \tag{20}$$

Looking at the component in phase with velocity (fig. 7), it is seen that the model captures the essence of the underlying physics. The synchronization of the lift force ensures a positive power input to the oscillation at non-dimensional frequencies between approximately 0.13 and 0.3 at small amplitudes. As the amplitude increases, so does the damping, and the net power input drops. At a certain combination of amplitude and frequency, the power input from the lift force balances the damping, and this gives the curve where $C_{y,v} = 0$. This curve is important when predicting free vibrations of a rigid cylinder, as

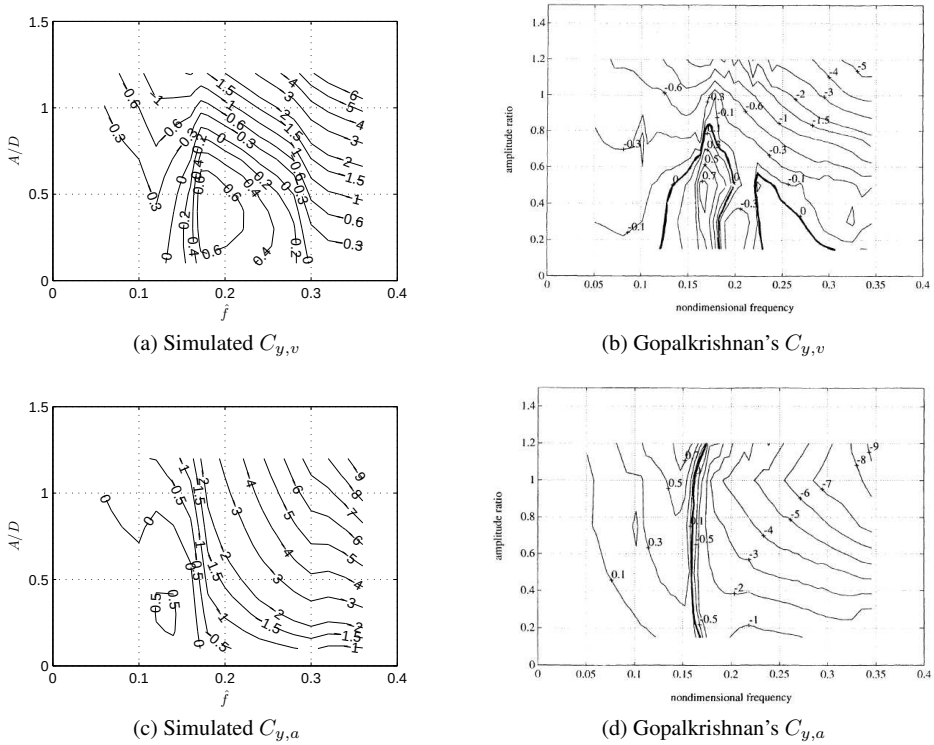

(a) Simulated $C_{y,v}$

(b) Gopalkrishnan's $C_{y,v}$

(c) Simulated $C_{y,a}$

(d) Gopalkrishnan's $C_{y,a}$

Figure 7: Simulated force coefficients (left) compared to experimental results by [29] (right).

it will determine the oscillation amplitude in absence of structural damping. Compared to Gopalkrishnan's results, the simulated zero-curve is quite similar, although the two distinct excitation regions seen in the experiments has been merged together to a single one in the simulated results. This is explained from the fact that the lift phase model is based on the VIVANA excitation coefficients, where the two regions are arranged as one. The behavior outside the positive excitation zone is also realistic, showing intermediate negative values at low $\hat{f}$ and larger negative values at high $\hat{f}$.

Continuing to the component in phase with acceleration, good overall agreement is seen between the simulated and experimental results, although there are some minor discrepancies. Both have an area of relatively low positive values to the left, and a steep slope at $\hat{f} \approx 0.17$. At higher non-dimensional frequencies, the simulated and experimental results show similar behavior, with increasingly negative values as the frequency and amplitude is increased. It is interesting that the component in phase with acceleration comes out this close to the measurements, considering that no information about experimentally measured $C_{y,a}$ or added mass have been used to construct the model. This shows that the

assumptions and simplifications embedded in the model are realistic. In particular, it supports the assumption that the total added mass force consists of the lift force in phase with acceleration and the added mass force due to cylinder acceleration, ref. equation (10).

3.2 Free oscillations of a spring supported rigid cylinder

The hydrodynamic force model (ref. equation (10)) is combined with time integration of the equations of motion to simulate the vibration of a spring supported rigid cylinder free to move in the cross-flow direction. The only degree of freedom is the transverse displacement of the cylinder, and the equation of motion reads:

$$(m + \rho\frac{\pi D^2}{4}C_a)\ddot{y}(t) + ky(t) = F(t), \tag{21}$$

where the external force term $F(t)$ contains the lift and fluid damping force as given in equation (10). The still water added mass term has been moved to the left hand side of the equation. Recall that C_a is constant and equal to 1.0 in all simulations presented in this paper. Equation (21) is solved using the Newmark-β method with standard parameters and a time step corresponding to 100 steps per vortex shedding period (based on the Strouhal frequency). The hydrodynamic force per unit length is evaluated based on the incoming current speed and the cross-flow velocity of the cylinder. An explicit calculation of the hydrodynamic force is made, meaning that velocities from the previous time step are used to calculate the current hydrodynamic force. This is justifiable as the time step is small. The simulation runs for 200 cycles, and the 100 first are discarded before the oscillation amplitude and frequency are extracted. This has been done for reduced velocities $V_r = U/(f_0 D)$ ranging from 2 to 20. The structure is characterized by its diameter, its natural frequency in still water f_0 and the mass ratio $m^* = m/(\rho\pi D^2/4)$ which is given in table 2. No structural damping is included. An experimental study by Govardhan and Williamson [33] is chosen for comparison. The numerical and experimental results are shown in figure 8.

Table 2: Simulation parameters, free oscillations

D	0.0381 m
m^*	1.2 - 10.3
f_0	0.33 Hz
St	0.2
ρ	1000 kg/m^3

As seen in figure 8, the overall agreement is good, and several relevant details are captured by the simulations. For example, high-amplitude vibration is sustained for a longer range of velocities at low mass ratio compared to high mass ratio, even though

the peak amplitude remains the same. The largest response is found at $V_r \approx 6$, where the simulated amplitude reaches $(A/D) = 0.9$. This is slightly lower than seen in the experiments, which is explained from the fact that the present lift coefficient is derived from the excitation coefficient used in VIVANA, which in turn is adapted to experiments with flexible, not rigid cylinders. The simulations do not capture the desynchronization that occurs around $V_r \approx 18$ for the low m^* case, but maintains a moderate amplitude.

Also for the simulated oscillation frequency, the results are generally similar to the experiments. At $V_r = 5$, the oscillation frequency equals the natural frequency in still water. As the velocity is increased further, the frequency remains nearly constant for the heavy cylinder, at least for $V_r < 10$. For the light cylinder, the frequency varies more and is seen to increase almost linearly. The frequency is a compromise between the Strouhal frequency and the natural frequency of the cylinder, which is a result of the synchronization algorithm where the cylinder response affects the frequency of the lift force. For very low reduced velocities, the simulated frequency is somewhat high, suggesting that the present synchronization model may give the lift force a too strong ability to increase its frequency. There are also some discrepancies at very high reduced velocities.

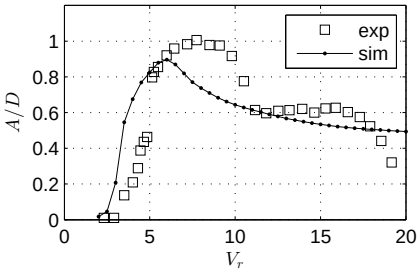

(a) A/D for mass ratio $m^* = 1.2$

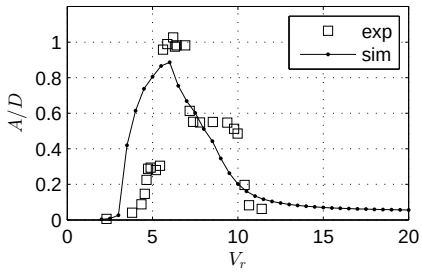

(b) A/D for mass ratio $m^* = 10.3$

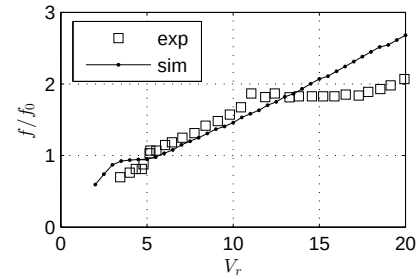

(c) f_{osc}/f_0 for mass ratio $m^* = 1.2$

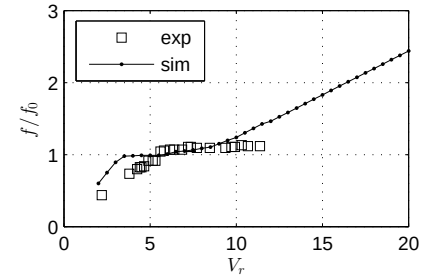

(d) f_{osc}/f_0 for mass ratio $m^* = 10.3$

Figure 8: Amplitude and frequency of oscillation for rigid cylinder, simulated and experimental results (exp. from Govardhan and Williamson [33]).

3.3 Vibrations of a flexible cylinder in shear flow

In this section, the hydrodynamic force model is used in combination with a linear finite element model to calculate response time series for a tensioned, flexible beam exposed to linearly sheared flow. More specifically, the model is used to simulate high mode VIV-tests performed by the Norwegian Deepwater Program (NDP) [34, 35], such that the results may be compared to experiments. The physical properties of the riser model are given in table 3, while an overview of the set up is shown in figure 9. Many different scenarios were investigated in the NDP tests, including bare riser and different configurations of strakes in both uniform and linear sheared flow. Here, only the bare riser in shear flow is considered. In these particular tests, the structure was exposed to different maximum velocities ranging from 0.3 m/s to 2.4 m/s.

Table 3: Physical properties of the NDP riser

L	38 m
D	0.027 m
T	4300 - 4600 N
EI	599 Nm^2
m	0.933 kg/m

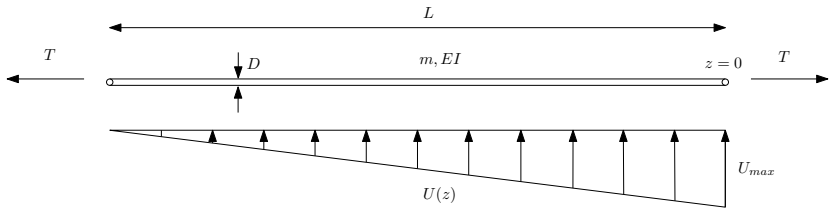

Figure 9: Overview of the NDP shear flow tests.

In the present analysis, the structure is divided into 50 beam elements, with elastic (bending) and initial stress (tension) stiffness. The beam elements have one rotation and translation degree of freedom in each end. Only cross-flow motion is simulated, and hence are the degrees of freedom in the cross-flow plane. A consistent mass formulation is used, and the added mass term $(\rho\pi D^2/4)C_a$ is included in the mass matrix. The experimentally measured structural damping of the riser model (in air) was reported to be 0.4 % of critical or less, which is negligible compared to the hydrodynamic damping. Therefore, no structural damping is included in the simulations. The dynamic equilibrium equation is solved using the Newmark-β method with standard parameters and a time step corresponding to 100 steps per vortex shedding cycle, based on the mean current velocity. As for the rigid

cylinder, the hydrodynamic forces are evaluated based on velocities in the previous time step. The dynamic equilibrium equation reads:

$$\mathbf{M}\ddot{\mathbf{y}}(t) + \mathbf{K}\mathbf{y}(t) = \mathbf{F}(t), \tag{22}$$

where $\mathbf{M}$ is the mass, $\mathbf{K}$ the stiffness matrix and $\mathbf{y}(t)$ a vector containing nodal translations and rotations. The external force vector $\mathbf{F}(t)$ contains lift and damping forces calculated according to the described procedure and transformed into equivalent point forces through multiplication with the element length.

Based on the maximum current velocity, the Reynolds number is in the range of 8000 to 65 000. The relatively large variation could make Reynolds number effects important. Govardhan and Williamson [36] have shown that the response of an elastically mounted cylinder increases along with the Reynolds number, at least for $\mathrm{Re} < 10^5$. A study performed by Swithenbank et al. [37] has shown that this is also the case for long flexible cylinders. This must be a result of either larger lift forces or less damping, which means that the present model should possibly include a factor on one of these forces, accounting for the Reynolds number effect. Another possibility is that the variation is so small that the model performs well over the entire range of Re considered here. The difference between the experimental and simulated results will reveal if such a factor is necessary or not. The Strouhal number is also known to vary as a function of Re, but as the variability is small in the present range, a constant value of 0.19 is used, which is the mean value for $8000 < \mathrm{Re} < 65\,000$ reported by Norberg [23].

Using the model described above, simulations are performed for velocities ranging from 0.3 m/s to 2.4 m/s with a step of 0.1 m/s, giving a total of 22 simulations. Each simulation lasts for 200 vortex shedding cycles based on the mean current velocity. The results are post-processed after removing the first 150 cycles. The dominating cross-flow frequency is extracted at the point of maximum motion and the root-mean-square (r.m.s.) value of the cross-flow displacement along the riser is calculated and plotted. The dominating mode is found by modal analysis [38] of the calculated response, utilizing eigenmodes from the finite element solution. The number of participating modes in the modal analysis is set to 20, and as 51 data points of displacement are available, the modal weights are found using least-squares. The dominating frequency and mode is shown in figure 10 and 11 along with the experimental results from the NDP test. The maximum r.m.s. value of cross-flow displacement along the riser for all current velocities is reported in figure 12, while the entire r.m.s. distribution for cross-flow displacement along the riser for a few selected cases are given in figure 13. Time series plots of the simulated riser response for the same cases are presented in figure 14.

Figure 10-12 indicates that the agreement between the simulations and the experimental results is very good, except for a slight overestimation of the frequency and mode. This could have been improved by lowering the Strouhal number, however justifying this reduction is difficult. Due to inherent experimental errors and the random nature of VIV, it

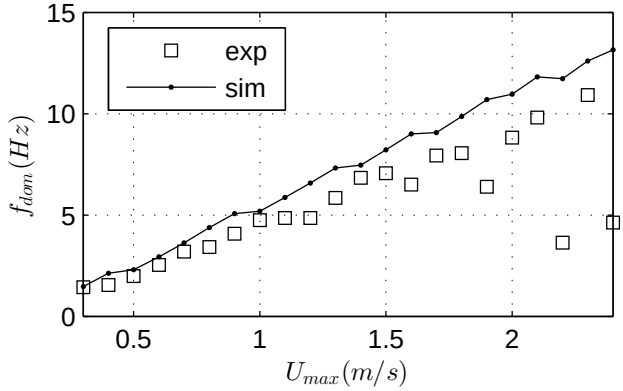

Figure 10: Dominating frequency, cross-flow displacement.

cannot be expected to achieve a perfect match between experiments and simulations. Further uncertainties are introduced by the modal reconstruction utilized in post-processing the experimental data [35]. With this in mind, the agreement in terms of the maximum value of the root-mean-square of the displacement is very good for $U_{\max} > 0.5\mathrm{m/s}$. For the lowest current velocities the simulated response is somewhat high, which may be a result of the Reynolds number effect previously discussed. It is however concluded that the present model produces realistic oscillation amplitudes for $16\,000 < \mathrm{Re} < 65\,000$, without any need for a Reynolds number dependent term. The r.m.s. of the response along the riser as shown in figure 13 shows how the response mostly consists of symmetric standing waves for low current velocities, while traveling waves become more dominating for higher velocities. When traveling waves dominate, the response is clearly largest in the high current velocity region along the structure. All these features are captured by the model. As seen in figure 14, the waves propagate from the high velocity region towards the other end, where standing waves are observed due to reflection at the boundary.

4 Conclusions

A new method for time domain simulation of cross-flow VIV has been presented. The method is based on simple assumptions regarding the physics of the vortex shedding process, and includes a synchronization model which simulates how the instantaneous frequency of the lift force reacts to the structure motion. It is shown through numerical experimentation and comparison with published experimental observations that the method produces realistic results in a variety of situations, including forced and free cross-flow vibrations of a rigid cylinder, and also a flexible cylinder in shear flow. The results indicate that the model is useful for prediction purposes, and since it is formulated in time domain,

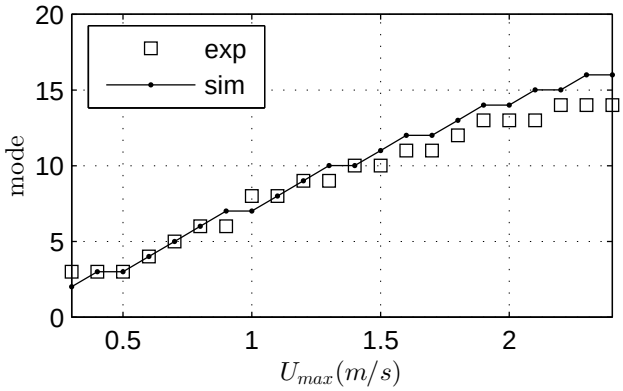

Figure 11: Dominating mode, cross-flow displacement.

it is especially suited for problems involving non-linear structural behavior, or other external loads. When combined with a finite element model of the structure, the method may in principle be used for simulating any type of (circular) cylindrical slender structure in arbitrary flow conditions, as the formulation is completely general with respect to current profile and geometry.

Further work should focus on increased understanding of the model, such as how the response frequency is determined through synchronization between force and motion. This should be fully understood in order to establish an improved synchronization model. Numerical issues such as accuracy versus time step size when using an explicit calculation of forces should also be investigated. When it comes to further enhancement of the model, a natural step would be to include the fluctuating drag force and in-line motion. The synchronization model would have to be modified to take in-line motion into account, such that the model can simulate combined in-line and cross-flow vibrations. The higher order harmonics of force and response should also be looked into. An interesting fact is that the present model produces a significant cross-flow force at 3 times the cross-flow vibration frequency when in-line motion is present. This surely motivates further work on the model, as the 3rd harmonic is an important contributor to fatigue damage. The model includes no restriction on the time variation of the incoming current velocity, meaning that it is possible to simulate VIV in oscillating current or waves. The model performance in such situations should be investigated in the future.

Acknowledgments

The authors are very grateful to the Norwegian Deepwater Program (NDP) for making the results from the Riser High Mode VIV tests available for comparison.

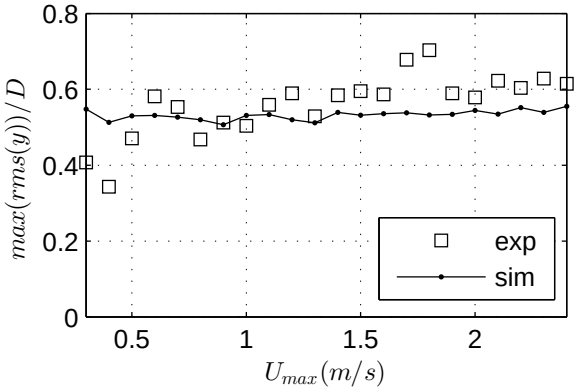

Figure 12: Max of r.m.s. of cross-flow displacement.

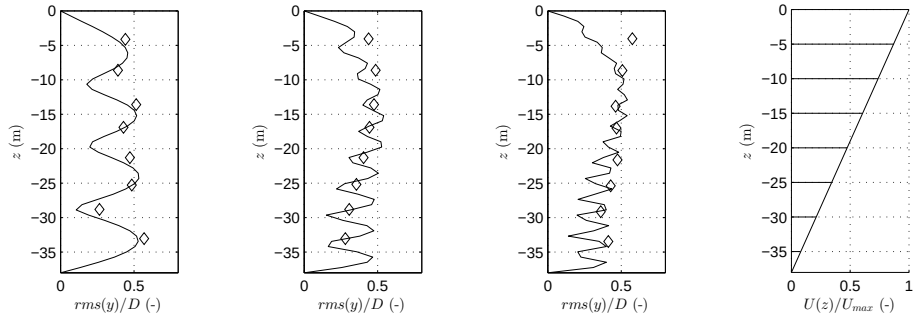

(a) $U_{\max} = 0.6$ m/s (b) $U_{\max} = 1.3$ m/s (c) $U_{\max} = 2.0$ m/s (d) Current profile

Figure 13: Solid lines: r.m.s. of simulated cross-flow response. Diamonds: r.m.s. values from experiments obtained by direct integration of measured accelerations [35].

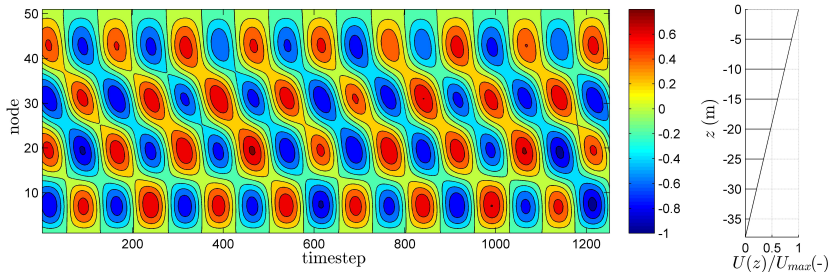

(a) $U_{\max} = 0.6$ m/s

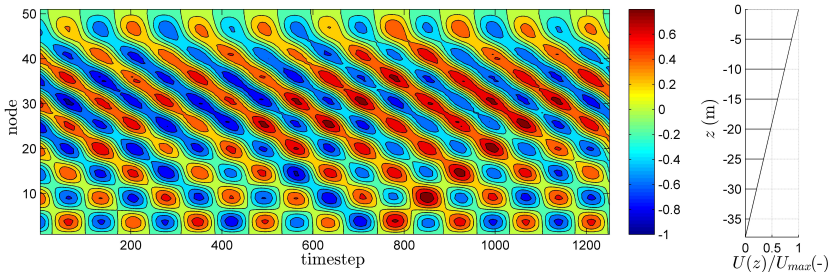

(b) $U_{\max} = 1.3$ m/s

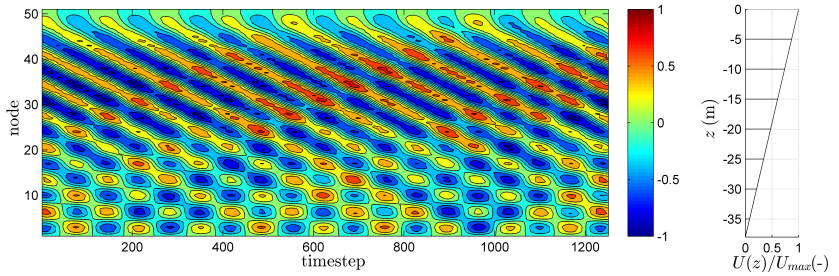

(c) $U_{\max} = 2.0$ m/s

Figure 14: Simulated cross-flow response in time and space. The color represents the normalized cross-flow response, y/D.

References

[1] Bearman PW. Vortex shedding from oscillating bluff bodies. Annual Review of Fluid Mechanics 1984;16(1):195–222.

[2] Sarpkaya T. A critical review of the intrinsic nature of vortex-induced vibrations. Journal of Fluids and Structures 2004;19(4):389 – 447.

[3] Williamson C, Govardhan R. Vortex-induced vibrations. Annual Review of Fluid Mechanics 2004;36(1):413–455.

[4] Wu X, Ge F, Hong Y. A review of recent studies on vortex-induced vibrations of long slender cylinders. Journal of Fluids and Structures 2012;28(0):292 – 308.

[5] Jauvtis N, Williamson C. The effect of two degrees of freedom on vortex-induced vibration at low mass and damping. Journal of Fluid Mechanics 2004;509(6):23–62.

[6] Dahl J, Hover F, Triantafyllou M. Two-degree-of-freedom vortex-induced vibrations using a force assisted apparatus. Journal of Fluids and Structures 2006;22(6):807–818.

[7] Vandiver JK, Swithenbank SB, Jaiswal V, Jhingran V. Fatigue damage from high mode number vortex-induced vibration. In: Proc. 25th OMAE Conf. 2006,.

[8] Modarres-Sadeghi Y, Mukundan H, Dahl J, Hover F, Triantafyllou M. The effect of higher harmonic forces on fatigue life of marine risers. Journal of Sound and Vibration 2010;329(1):43–55.

[9] Modarres-Sadeghi Y, Chasparis F, Triantafyllou M, Tognarelli M, Beynet P. Chaotic response is a generic feature of vortex-induced vibrations of flexible risers. Journal of Sound and Vibration 2011;330(11):2565 – 2579.

[10] Lie H, Ciappi E, Huang S, Hong S, Zhi Z. The Specialist Committee on Vortex induced Vibrations, Final Report and Recommendations to the 26th ITTC. In: Proceedings of the 26th International Towing Tank Conference. Rio de Janeiro, Brazil; 2011, p. 561–574.

[11] Bourguet R, Karniadakis GE, Triantafyllou MS. Vortex-induced vibrations of a long flexible cylinder in shear flow. Journal of Fluid Mechanics 2011;677:342–382.

[12] Facchinetti M, de Langre E, Biolley F. Coupling of structure and wake oscillators in vortex-induced vibrations. Journal of Fluids and Structures 2004;19(2):123 – 140.

[13] Ogink R, Metrikine A. A wake oscillator with frequency dependent coupling for the modeling of vortex-induced vibration. Journal of Sound and Vibration 2010;329(26):5452–5473.

[14] Vandiver JK, Li L. SHEAR7 V4.4 Program Theoretical Manual. Department of Ocean Engineering, Massaccusetts Institute of Technology; 2005.

[15] Larsen CM, Lie H, Passano E, Yttervik R, Wu J, Baarholm G. VIVANA - Theory Manual, Version 3.7. MARINTEK; 2009.

[16] Lie H. A time domain model for simulation of vortex induced vibrations on a cable. In: Proc. Sixth Int. Conf. on Flow Induced Vibrations. London, UK; 1995, p. 455–466.

[17] Finn L, Lambrakos K, Maher J. Time domain prediction of riser VIV. In: Proceedings of the Fourth International Conference on Advances in Riser Technologies. 1999,.

[18] Mainçon P. A wiener-laguerre model of VIV forces given recent cylinder velocities. Mathematical Problems in Engineering 2011;2011.

[19] Venugopal M. Damping and response prediction of a flexible cylinder in a current. Ph.D. thesis; Massachusetts Institute of Technology; 1996.

[20] Bishop R, Hassan A. The lift and drag forces on a circular cylinder in a flowing fluid. Proceedings of the Royal Society of London Series A Mathematical and Physical Sciences 1964;277(1368):32–50.

[21] Sumer BM, Fredsøe J. Hydrodynamics around cylindrical structures; vol. 12. World Scientific Publishing Company; 1997.

[22] Hallam M, Heaf N, Wootton LR. Dynamics of marine structures: Methods of calculating the dynamic response of fixed structures subject to wave and current action. Tech. Rep.; CIRIA Underwater Engineering Group; 1977.

[23] Norberg C. Fluctuating lift on a circular cylinder: review and new measurements. Journal of Fluids and Structures 2003;17(1):57–96.

[24] Khalak A, Williamson C. Motions, forces and mode transitions in vortex-induced vibrations at low mass-damping. Journal of Fluids and Structures 1999;13(7):813–851.

[25] Vikestad K. Multi-frequency response of a cylinder subjected to vortex shedding and support motions. Ph.D. thesis; Norwegian University of Science and Technology, Department of Marine Technology; 1998.

[26] Sarpkaya T. Fluid forces on oscillating cylinders. NASA STI/Recon Technical Report A 1978;78.

[27] Yin D. Experimental and numerical analysis of combined in-line and cross-flow vortex induced vibration. Ph.D. thesis; Norwegian University of Science and Technology, Centre for Ships and Ocean Structures; 2013.

[28] Jhingran VG. Drag amplification and fatigue damage in vortex-induced vibrations. Ph.D. thesis; Massachusetts Institute of Technology; 2008.

[29] Gopalkrishnan R. Vortex-induced forces on oscillating bluff cylinders. Ph.D. thesis; Massachusetts Institute of Technology; 1993.

[30] Mirollo RE, Strogatz SH. Synchronization of pulse-coupled biological oscillators. SIAM Journal on Applied Mathematics 1990;50(6):1645–1662.

[31] Izhikevich EM, Kuramoto Y. Weakly coupled oscillators. In: Encyclopedia of Mathematical Physics; vol. 5. Elsevier; 2006, p. 448–453.

[32] Rosenblum MG, Kurths J, Pikovsky A, Schafer C, Tass P, Abel HH. Synchronization in noisy systems and cardiorespiratory interaction. Engineering in Medicine and Biology Magazine, IEEE 1998;17(6):46–53.

[33] Govardhan R, Williamson C. Modes of vortex formation and frequency response of a freely vibrating cylinder. Journal of Fluid Mechanics 2000;420:85–130.

[34] Braaten H, Lie H. NDP riser high mode VIV tests, main report. Tech. Rep.; Norwegian Marine Technology Research Institute; 2004.

[35] Kristiansen T, Lie H. NDP riser high mode VIV tests, modal analysis. Tech. Rep.; Norwegian Marine Technology Research Institute; 2005.

[36] Govardhan R, Williamson C. Defining the 'modified Griffin plot' in vortex-induced vibration: revealing the effect of Reynolds number using controlled damping. Journal of Fluid Mechanics 2006;561:147–180.

[37] Swithenbank SB, Vandiver JK, Larsen CM, Lie H. Reynolds number dependence of flexible cylinder VIV response data. In: ASME 2008 27th International Conference on Offshore Mechanics and Arctic Engineering. American Society of Mechanical Engineers; 2008, p. 503–511.

[38] Lie H, Kaasen K. Modal analysis of measurements from a large-scale VIV model test of a riser in linearly sheared flow. Journal of Fluids and Structures 2006;22(4):557–575.

Paper II

Fatigue damage from time domain simulation of combined in-line and cross-flow vortex-induced vibrations

Mats J. Thorsen, Svein Sævik and Carl M. Larsen

Department of Marine Technology, Norwegian University of Science and Technology, Trondheim, Norway

Marine Structures, Vol. 41, 2015, pp. 200 – 222

Abstract

A semi-empirical method for time domain simulation of vortex-induced vibrations (VIV) is used to calculate the in-line and cross-flow fatigue damage of a tensioned riser in uniform and sheared flow. Simulations are run for flow velocities ranging from 0.3 m/s to 2.4 m/s, and a detailed comparison with experimental observations is performed. Results are reported in terms of dominating frequency, mode of vibration and mean of r.m.s. of displacement, as well as fatigue damage distribution along the length of the structure and maximum fatigue damage rates for each case. Fatigue damage is calculated by rainflow counting of the strain time series together with an idealized S-N curve with slope $m = 3$. The results show that the model reproduces the measured fatigue damage with a satisfactory level of realism, using a consistent set of parameters. This indicates that the model is usable for calculation of riser VIV fatigue damage in various current conditions, assuming the Reynolds number is in the subcritical range.

Keywords: Vortex-induced vibrations; Fatigue; Simulation; In-line; Cross-flow

1 Introduction

When a circular cylinder is placed in a flowing fluid, flow separation and shedding of vortices result in oscillating lift and drag forces. If the cylinder is elastic these forces will cause structural oscillations, referred to as vortex-induced vibrations (VIV). For slender structures such as marine risers, these vibrations may induce significant dynamic stresses, which in turn can cause rapid accumulation of fatigue damage. Being able to predict the stresses and corresponding fatigue damage caused by VIV is therefore important for the design of safe structures.

Substantial research efforts have been put into increasing the understanding of VIV, as seen in the reviews by Bearman [1, 2], Sarpkaya [3], Williamson and Govardhan [4] and Wu et al. [5]. Due to the complexity of the mathematical models describing viscous fluid flow, experiments have played a central part of this research. This includes experiments with flexibly mounted rigid cylinders [6–8], forced oscillations [9–11] and slender elastic cylinders in various flow conditions [12–14]. At first, experimenters were mainly interested in the cross-flow (transverse) response. Although in-line vibrations were known to occur, these were considered less important due to the smaller amplitude of response. However, Baarholm et al. [15] have shown that the in-line vibrations may be equally important for the fatigue life of risers. VIV of cylinders with two degrees of freedom was studied experimentally by Jauvtis and Williamson [16] and Dahl et al. [17]. An important consequence of the in-line motion is higher harmonic forces in the cross-flow direction. As illustrated by Vandiver et al. [18] and Modarres-Sadeghi et al. [19] the higher harmonics may contribute significantly to the total fatigue damage, and should not be neglected. Another recent finding is that the VIV response of risers continuously alternate between a chaotic and a stationary state [20].

As the direct solution of the equations governing viscous flow is extremely computationally demanding, most available engineering tools are based on empirical relationships. There exist a number of semi-empirical frequency domain tools, such as SHEAR7 [21] and VIVANA [22], which employ similar techniques to calculate the VIV response. In the frequency domain tools, the fluid forces are described through excitation (lift), damping and added mass coefficients which are functions of the amplitude and frequency of response. These coefficients are typically found from experiments with rigid cylinders subjected to forced oscillations.

Although the semi-empirical frequency domain tools are efficient, and quite accurate in some cases [23, 24], these methods have some inherent weaknesses. The formulation requires a linear structural model, and because the hydrodynamic coefficients are functions of the non-dimensional oscillation frequency (or, equivalently, reduced velocity), only constant fluid velocity is allowed. This prohibits the inclusion of non-linear structural effects (such as varying tension) and the study of VIV in non-stationary flows such as waves. It is also difficult to account for the interaction between the response at different frequencies, which may be relevant in cases where the current velocity varies strongly

along the structure.

To dispose of the above mentioned limitations one must perform a step-by-step integration of the equations of motion, i.e. time domain simulation. This would allow for non-linear structural effects, true interaction between competing frequencies, study of VIV in combination with other external disturbances (e.g. soil interaction and top-end motions) and time varying currents or waves. An existing method for time domain simulation of VIV is the wake-oscillator [25]. This method is based on the assumption that the fluid force may be described by a forced Van der Pol oscillator. It is however difficult to find a set of parameters suitable for both forced and free vibrations [26]. Mainçon [27] developed a totally new method for time domain prediction of VIV, training an artificial neural network to predict the instantaneous hydrodynamic force based on a compressed form of the recent velocity history. Although promising, the method has some stability issues.

A novel method for time domain simulation of cross-flow VIV was introduced in [28]. A model for the synchronization between the exciting force and structure motion was derived, and it was shown that this model gives realistic results for forced as well as free vibrations of short rigid cylinders. In combination with a finite element structural model the frequency, amplitude and mode of vibration for a flexible cylinder in linearly sheared current was accurately predicted. In [29], the model was extended to enable simulation of combined cross-flow and in-line vibrations. The purpose of the present paper is to investigate how this model performs with respect to predicting fatigue damage rates for a flexible cylinder in uniform and shear flow. As fatigue damage is the primary concern in connection with VIV, a useful model must provide realistic estimates. This highlights the importance of the present study, as the direct comparison between experiments and simulations provides a basis for evaluating the accuracy of the model.

2 NDP experimental data

Experimental data from the Norwegian Deepwater Programme (NDP) Riser High Mode VIV tests [30] have been used for comparison. In this experimental campaign, a 38 meter long riser model with circular cross section was towed through the Ocean Basin at the Norwegian Marine Technology Research Institute (MARINTEK). The experiments consist of both uniform and sheared flow cases. In the uniform flow cases, the entire structure was exposed to a constant flow velocity U. In the sheared flow cases, the current velocity increased linearly from zero to U along the riser length. The velocity U was varied from 0.3 m/s to 2.4 m/s with steps of 0.1 m/s. Various configurations of strakes were also tested, however only the naked riser results are used here. The physical properties of the riser model are given in table 1.

The uniform flow profile was created by towing the structure in a straight line, while sheared flow was produced by towing one end in circular arc, keeping the other end fixed. The riser was equipped with strain gauges and accelerometers measuring the in-line strain

Table 1: Physical properties of the NDP riser

Length (L)	38 m
Diameter (D)	0.027 m
Mean tension (T)	4000 - 6000 N
Bending stiffness (EI)	599 Nm^2
Mass per unit length (m)	0.933 kg/m

at 40 locations, the cross-flow strain at 24 locations and the acceleration (in-line and cross-flow) at 8 locations along the length of the model. A pretension of approximately 4000 N was applied before the experiment started, and the actual tension during towing was measured by force transducers mounted at the riser ends.

3 Hydrodynamic force model

When a circular cylinder is exposed to an incoming fluid flow, the boundary layer separates from the cylinder surface and rolls up into a vortex on either side of the cylinder [31]. For Reynolds numbers larger than 40, the vortices become unstable, causing alternating vortex shedding. The shedding frequency is given in non-dimensional form as the Strouhal number, $\mathrm{St} = f_s D/U$, where f_s is the frequency, D the cylinder diameter and U the velocity of the incoming flow. For a stationary cylinder in uniform flow, St is close to 0.2 for subcritical Reynolds numbers. However, the presence of shear flow causes the Strouhal number to vary along the cylinder length, as the vortex shedding takes place in spanwise cells with constant frequency over each cell [32]. Furthermore, a flexible cylinder affects the flow such that the vortex shedding may lock-on to the frequency of vibration. This effect may cause the vortex shedding frequency to deviate from the expected Strouhal frequency. In experiments with a flexible riser in uniform flow, St was found to vary from 0.14 to 0.18, based on the observed frequency of vibration [33].

The model developed in [28] and [29] is used to calculate the dynamic lift and drag forces in the simulations presented here. This semi-empirical model provides the hydrodynamic force per unit length on a cylindrical cross section based on the motion of the same cross-section, corresponding to a strip-theory approach. It is hence implicitly assumed that the motion of the structure determines the 3-dimensional behavior of the flow. It should be noted that the empirical parameters are based on data from subcritical Reynolds numbers. The coordinate system is defined in figure 1, where the x-axis is determined by the direction of the incoming flow. The origin is placed at the static equilibrium position of the cylinder, such that x and y represents the cylinder displacement in the in-line and cross-flow direction. The present formulation includes some minor modifications compared to the original model. Firstly, the incoming fluid velocity is used instead of relative velocity when calculating excitation forces. Secondly, the magnitude of the in-line excitation force

is established by physical instead of pure empirical considerations.

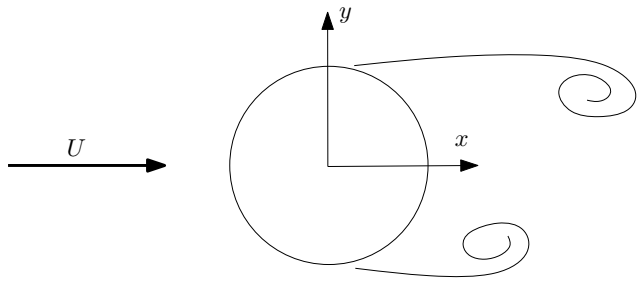

Figure 1: Coordinate system definition

3.1 Cross-flow force

It is assumed that the fluid forces may be decomposed into three components; excitation, damping and added mass. The excitation force is associated with the fluctuating pressure field due to vortex-shedding, and the cross-flow component is expressed as:

$$F_{\mathrm{exc},y} = \frac{1}{2}\rho D C_v U^2 \cos\phi_{\mathrm{exc},y}, \tag{1}$$

where ρ is the fluid density, D the cylinder diameter, C_v an empirical coefficient which is a function of the cross-flow amplitude of vibration A_y (see figure 2) and $\phi_{\mathrm{exc},y}$ is the instantaneous phase of the force. In case of a sinusoidal force of constant frequency f, the instantaneous phase can be written as $\phi_{\mathrm{exc},y} = 2\pi f t + \theta$, where θ is the phase at $t = 0$. Such a representation could have been used for a stationary cylinder, where the vortex-shedding frequency is given by the relation $f_s = \mathrm{St}U/D$ [31], where St is the Strouhal number. It is however well known [34] that cylinder motion will strongly influence the flow, and the vortex-shedding frequency may synchronize with the frequency of motion. This effect is included through an equation for the synchronization of the instantaneous phase of the exciting force:

$$\frac{d\phi_{\mathrm{exc},y}}{dt} = H(\phi_{\dot{y}} - \phi_{\mathrm{exc},y}). \tag{2}$$

Equation (2) is used to calculate the rate of change of $\phi_{\mathrm{exc},y}$, which is called the instantaneous angular frequency of the exciting force. The instantaneous phase of the cross-flow velocity of the cylinder is denoted $\phi_{\dot{y}}$, and it is assumed that $d\phi_{\mathrm{exc},y}/dt$ is a function of the phase difference between the cross-flow cylinder velocity and the exciting force. The reason why cylinder velocity is used as the quantity which the force seeks to synchronize

with, is that the force must be in phase with the velocity in order to provide energy to the oscillation. In [28] it was shown how the function $H(\phi_{\dot{y}} - \phi_{\mathrm{exc},y})$ is found from data for the cross-flow force component in phase with velocity. The resulting function is shown in figure 3, normalized by the Strouhal angular frequency $\omega_s = 2\pi \mathrm{St} U/D$, using $\mathrm{St} = 0.2$.

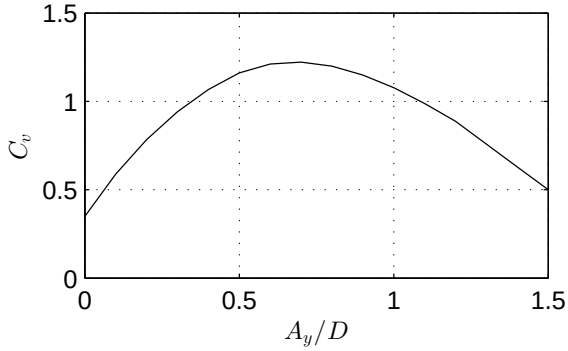

Figure 2: Excitation force coefficient, $C_v(A_y/D)$.

It is elucidating to visualize the synchronization process as two individuals running around the unit circle. Imagine $\phi_{\dot{y}}$ is moving with an arbitrary angular velocity, while $\phi_{\mathrm{exc},y}$ attempts to synchronize. Intuitively, this means the phase of the force must speed up if it gets behind, or slow down if it gets ahead. This is exactly what the function $H(\phi_{\dot{y}} - \phi_{\mathrm{exc},y})$ does. As seen in figure 3, the instantaneous frequency of the force will be reduced to a minimum of 0.6 times the Strouhal frequency when the cylinder velocity is $\pi/2$ behind, or increased to a maximum of 1.5 times this value if the cylinder velocity is $\pi/2$ ahead. If the frequency of motion is outside this range, the exciting force is unable to synchronize, and cannot transfer any energy to the oscillation.

There will be fluid resistance, or damping, as the cylinder moves through the water. By definition, this force will always extract energy from the oscillation. In addition, an added mass force is present as a result of the cylinder acceleration. The damping and added mass forces are modeled as in [28], which means the total hydrodynamic force in the cross-flow direction is calculated as:

$$F_{\mathrm{fluid},y} = \underbrace{\frac{1}{2}\rho D C_v U^2 \cos\phi_{\mathrm{exc},y}}_{\text{excitation}} \underbrace{-\frac{1}{2}\rho D C_{y1} U \dot{y} - \frac{1}{2}\rho A_y C_{y2} |\dot{y}| \dot{y}}_{\text{damping}} \underbrace{-\frac{\rho \pi D^2}{4} C_{ay} \ddot{y}}_{\text{added mass}}, \tag{3}$$

where $C_{y1} = 0.485$, $C_{y2} = 0.936$ is used in all simulations. This particular choice of damping coefficients provides approximately the same energy extracted per cycle as the model by Venugopal [35], which is based on a number of experiments in still water as well

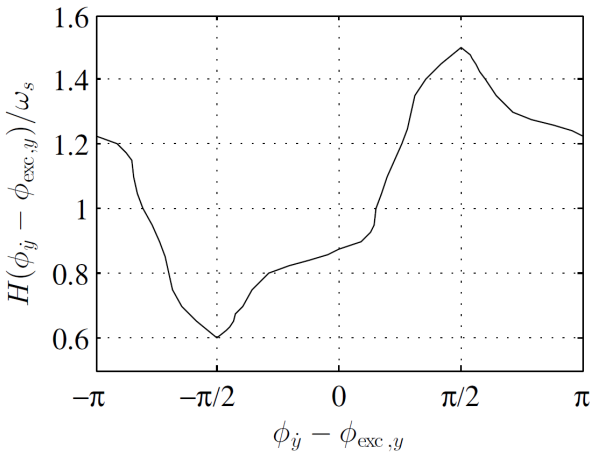

Figure 3: Normalized instantaneous angular frequency of the cross-flow excitation force as a function of the phase difference between cross-flow cylinder velocity and excitation force.

as low and high reduced velocities. The still water potential theory value of $C_{ay} = 1.0$ is used for the added mass coefficient.

3.2 In-line force

In the model presented here, the in-line excitation force is a direct result of cross-flow motion. This means the model is only applicable in cases with combined cross-flow and in-line vibrations. Pure in-line VIV is known to occur at low reduced velocities [36], and the model should not be applied in such cases. The starting point for deducing an expression for the in-line excitation force is the fact that the excitation forces in the in-line and cross-flow direction are both components of the same force vector $\vec{F}_{\text{exc}}$, as illustrated in figure 4. A simplifying assumption is introduced, namely that $\vec{F}_{\text{exc}}$ acts perpendicular to the relative velocity vector, $\vec{V} = (U - \dot{x})\vec{i} - \dot{y}\vec{j}$, where $\vec{i}$ and $\vec{j}$ are unit vectors in the x- and y-direction. The rationale behind this assumption is the fact that, for a stationary cylinder, the oscillating drag force is small compared to the lift [31]. Thereby, the resultant excitation force is approximately normal to the incoming flow. When the cylinder is moving, the incoming flow velocity is replaced by the relative fluid velocity felt by the cylinder, and the force is thereby assumed normal to the relative velocity. This assumption will not hold in the limiting case of a fixed cylinder, because the small oscillating drag force is neglected. To simplify the derivation further, it is also assumed that the cylinder velocity in the x-direction is much smaller than U. For equation (1) to hold under these assumptions, $\vec{F}_{\text{exc}}$ must be given as:

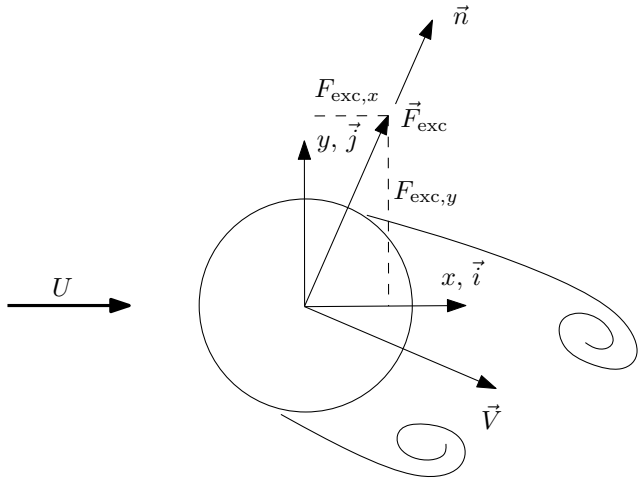

Figure 4: Excitation force with in-line and cross-flow components. Also shown are the unit vectors and relative velocity between fluid and cylinder

$$\vec{F}_{\mathrm{exc}} = \frac{1}{2}\rho D C_v U |\vec{V}| \cos\phi_{\mathrm{exc},y} \vec{n}, \tag{4}$$

where $\vec{n}$ is a unit vector normal to the relative velocity as shown in figure 4. This result is used to find the component in the in-line direction:

$$F_{\mathrm{exc},x} = \vec{F}_{\mathrm{exc}} \cdot \vec{i} = \frac{1}{2}\rho D C_v U |\vec{V}| \cos\phi_{\mathrm{exc},y} \frac{\dot{y}}{|\vec{V}|} = \frac{1}{2}\rho D C_v U \dot{y} \cos\phi_{\mathrm{exc},y}. \tag{5}$$

When force and motion are synchronized, the frequency is constant and we may write $\phi_{\mathrm{exc},y} = \omega t$ and $\dot{y} = \dot{y}_0 \cos(\omega t + \theta)$. Inserting this in equation (5) and applying a trigonometric identity yields:

$$F_{\mathrm{exc},x} = \frac{1}{2}\rho D C_v U \dot{y}_0 \cos(\omega t + \theta)\cos\omega t \tag{6}$$

$$= \frac{1}{2}\rho D C_v U \dot{y}_0 \Big(\frac{1}{2}\cos(2\omega t + \theta) + \frac{1}{2}\cos\theta\Big). \tag{7}$$

The first term in the parenthesis is oscillating with twice the cross-flow frequency. This is as expected, based on experimental observations as well as physical considerations. The second term is constant, and will be neglected in the following, as we are presently not interested in the mean drag force. The appearance of a constant term is however interesting,

and it is believed to be one of the sources to the experimentally observed amplification of drag forces for oscillating cylinders. The dynamic in-line excitation force is thus expressed as:

$$F_{\text{exc},x} = \frac{1}{4}\rho D C_v U \dot{y}_0 \cos\left(2\omega t + \theta\right) = \frac{1}{4}\rho D C_v U \dot{y}_0 \cos\phi_{\text{exc},x}. \tag{8}$$

As for cross-flow, the in-line force must be able to vary its instantaneous frequency to synchronize with the motion. Simultaneously, the relationship $d\phi_{\text{exc},x}/dt = 2d\phi_{\text{exc},y}/dt$ must be satisfied for the in-line and cross-flow excitation frequencies. However, direct use of this relationship makes it impossible for the in-line force to synchronize with the motion. Instead, the frequency relationship is satisfied approximately, i.e. $d\phi_{\text{exc},x}/dt \approx 2d\phi_{\text{exc},y}/dt$. The following equation is used to describe the synchronization of the in-line excitation force:

$$\frac{d\phi_{\text{exc},x}}{dt} = 2\frac{d\phi_{\text{exc},y}}{dt}\big(1 + \alpha\sin\left(\phi_{\dot{x}} - \phi_{\text{exc},x}\right)\big), \tag{9}$$

where α is a small positive number and $\phi_{\dot{x}}$ is the phase of the in-line velocity of the cylinder. The above formulation allows the in-line excitation force to increase or decrease its instantaneous frequency slightly to synchronize with the in-line cylinder velocity, while ensuring that

$$2(1-\alpha)\frac{d\phi_{\text{exc},y}}{dt} \leq \frac{d\phi_{\text{exc},x}}{dt} \leq 2(1+\alpha)\frac{d\phi_{\text{exc},y}}{dt}, \tag{10}$$

which shows that the frequency relationship is satisfied approximately as $\alpha \ll 1$. In the numerical simulations, α is set to 0.02.

The in-line fluid damping and added mass force is expressed on the same form as for cross-flow, and the total in-line fluid force is thereby computed as:

$$F_{\text{fluid},x} = \underbrace{\frac{1}{4}\rho D C_v U \dot{y}_0 \cos\phi_{\text{exc},x}}_{\text{excitation}} \underbrace{-\frac{1}{2}\rho D C_{x1} U\dot{x} - \frac{1}{2}\rho A_x C_{x2}|\dot{x}|\dot{x}}_{\text{damping}} \underbrace{-\frac{\rho\pi D^2}{4}C_{ax}\ddot{x}}_{\text{added mass}}, \tag{11}$$

where A_x is the amplitude of the in-line displacement. The coefficients are set to $C_{x1} = 0.507$ and $C_{x2} = 0.936$, which yields good agreement with the in-line damping model by Venugopal [35]. Obviously, $C_{x2} = C_{y2}$ as in-line and cross-flow motion is equivalent in case of still water. As for cross flow, the potential theory result is used for the in-line added mass, i.e. $C_{ax} = 1.0$.

4 Numerical model

4.1 Finite element model

A numerical model of the NDP riser is established based on the previously described hydrodynamic force model and a finite element model of the structure. Classical Euler-Bernoulli beam theory is assumed to be applicable. The structure is divided into 100 finite elements with 4 degrees of freedom, corresponding to cubic interpolation of the lateral displacements. Contributions from bending and initial stress (tension) are included in the element stiffness matrices, using the mean tensile force measured in each test. The mass matrix is assembled using a consistent mass formulation, including the added mass term $C_a \rho \pi D^2/4$ ($C_a = 1$). The small static displacements due to gravity and mean drag are neglected. Linear structural behavior is assumed, which means the in-line and cross-flow displacements are uncoupled from a structural point of view (although the external forces are strongly coupled). Hence, for both in-line and cross-flow displacements, the dynamic equilibrium equation for the structural system reads:

$$\mathbf{M}\ddot{\mathbf{r}}(t) + \mathbf{C}\dot{\mathbf{r}}(t) + \mathbf{K}\mathbf{r}(t) = \mathbf{F}(t), \tag{12}$$

where $\mathbf{M}$ is the mass, $\mathbf{C}$ the structural damping, $\mathbf{K}$ the stiffness matrix and $\mathbf{r}$(t) a vector containing the nodal displacements (i.e. rotations and translations). The external force vector $\mathbf{F}(t)$ represents the hydrodynamic forces in the in-line or cross-flow direction (depending on which direction we are looking at), and contains the fluid excitation and damping forces calculated according to the described procedure (see equations (3) and (11)). The forces are evaluated at every finite element node, i.e. at 99 positions along the length and transformed into equivalent point forces by multiplication with the element length. The structural damping (in air) was reported to be less than 0.4 % of critical [30], which is negligible compared to the hydrodynamic damping. Nevertheless, some structural damping is included to increase the stability of the solution. The structural damping matrix is represented as $\mathbf{C} = \alpha_1 \mathbf{M} + \alpha_2 \mathbf{K}$, using $\alpha_1 = 10^{-2}$ and $\alpha_2 = 10^{-4}$.

The analysis is a time integration procedure where the response is calculated step-by-step based on previous results (displacements, velocities and accelerations) and the present hydrodynamic load. The dynamic equilibrium equation is solved using the Newmark-β method with $\gamma = 0.5$ and $\beta = 0.25$. The length of the time-step is set to $h = D/(20U)$, corresponding to approximately 100 steps per oscillation cycle. As the time-step is small, the hydrodynamic forces are found using the velocity and acceleration of the structure at the previous time-step.

Each simulation lasts for 200 oscillation cycles, and the first 100 are removed prior to post-processing to remove any transient effects. The curvature is taken as the second derivative of the calculated displacement (d^2x/dz^2 for in-line curvature and d^2y/dz^2 for cross-flow) and the strain at the outer fiber is found by multiplying the curvature with the radius of the riser cross-section. At time $t = 0$, the instantaneous phases of the exciting

forces (i.e. $\phi_{\text{exc},x}(0,z)$ and $\phi_{\text{exc},y}(0,z)$) are assigned independent random values between 0 and 2π.

4.2 Amplitudes and phases

As seen in section 3, the hydrodynamic forces depend on the amplitude of vibration. The amplitude will vary along the structure, and in general also in time. Therefore, it is continuously extracted from the calculated response at every node as the simulation progresses. For a narrow-banded signal, the amplitude may be taken as half the distance traveled between two succeeding turning points. The turning points are characterized by zero-crossings of the velocity. With this in mind, the following expression is used to estimate the amplitude of vibration:

$$A_y = \frac{1}{2}\int_{t_1}^{t_2} |\dot{y}| dt, \tag{13}$$

where t_1 and t_2 are the time at the two most recent zero-crossings of the velocity. The same procedure is used to find the in-line amplitude.

The synchronization models (ref. equation (2) and (9)) require the phase of the cross-flow and in-line velocity of the cross-section. This is found using the phase portrait concept. In the phase portrait, the position on the horizontal axis is given by the normalized velocity and the position on the vertical axis by the normalized acceleration with negative sign. Now, the instantaneous phase equals the angle between the present position and the horizontal axis as illustrated in figure 5. The normalization consists of dividing the velocity (or acceleration) on the maximum value observed, i.e. $\dot{x}_n(t) = \dot{x}(t)/\max(\dot{x}(t_i), t_i \in [0,t])$. The same procedure is used to find the cross-flow phase.

4.3 Adjusting the vortex shedding frequency for Reynolds number effects

Although the Strouhal number for fixed cylinders is known to be almost constant for $300 < \text{Re} < 3 \times 10^5$ [31], there is a slight reduction as Re is increased from 10^3 to 10^5 (see e.g. [37]). This effect is also found in experiments with flexible cylinders [38] through a reduction in the non-dimensional frequency, $\hat{f} = f_{\text{osc}} D/U$, where f_{osc} is the frequency of oscillation. As the stress level is proportional to the square of the excited mode number (assuming a single mode dominates the response), it follows that the fatigue life is extremely sensitive to the excited mode. It is therefore important that the present numerical model produces the correct frequency of excitation, taking the Reynolds number dependency into account.

In the numerical model, the instantaneous frequency of the cross-flow excitation force is given by equation (2). The function $H(\phi_{\dot{y}} - \phi_{\text{exc},y})$ was originally obtained from the VIVANA database [22], [28]. To improve the model, this function is now multiplied with a Reynolds number dependent factor, meaning we use $d\phi_{\text{exc},y}/dt = C_f(\text{Re})H(\phi_{\dot{y}} - \phi_{\text{exc},y})$

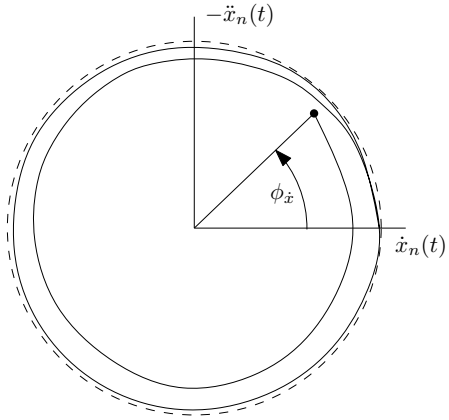

Figure 5: In-line velocity phase portrait.

to calculate the instantaneous frequency of the cross-flow excitation force. A curve for $C_f(\mathrm{Re})$ is established using the numerical model and comparison with the experimental data. The data for uniform flow is utilized, as the Reynolds number is constant along the length of the riser in these tests. For each experiment, the simulated dominating frequency is compared to the measured dominating frequency [39], and C_f is varied until the two values coincide. The result for each Reynolds number is shown in figure 6, along with a simple linear regression fit. Based on these calculations, C_f is found to be nearly constant over the whole range of Re considered, although a slight reduction is seen. The linear curve is used for evaluating C_f in all simulations reported in the remaining part of this paper.

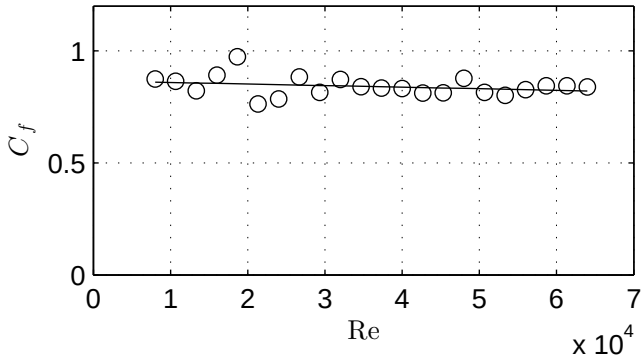

Figure 6: C_f as a function of Reynolds number based on comparison of simulated and measured dominating frequency.

5 Fatigue analysis

Fatigue damage is calculated using Miner-Palmgren summation:

$$D = \sum_{i=1}^{k} \frac{1}{N(S_i)}, \tag{14}$$

where $N(S_i)$ is the number of cycles to failure at a stress amplitude S_i, and the summation is done over all cycles in the sample time series. The number of cycles to failure for a given stress level is found from an idealized S-N curve, $N(S) = S^{-m}$. According to [40], $m = 3$ in seawater under free corrosion conditions, and this value is adopted here. For irregular time series, the rainflow counting method is considered the most accurate way of establishing stress ranges from a sample [41], and the WAFO Matlab toolbox [42] is used for this purpose. As stress is a linear function of strain, the fatigue analysis is simply carried out on the strain time series. For the measured cross-flow strain, rainflow counting is carried out on the original and a filtered version of the signal, where higher harmonics have been removed. The idea of the filtering is to isolate the fatigue damage from fundamental frequency strain and compare this to the total damage. The filtering is performed as follows: The frequency spectrum is established by Fourier transformation. The fundamental frequency f_1 is found by visual inspection, and all Fourier components above $2f_1$ are removed. The signal is then tranformed back to time domain. A typical result of the filtering process is shown in figure 7, where the filtered signal is compared to the original.

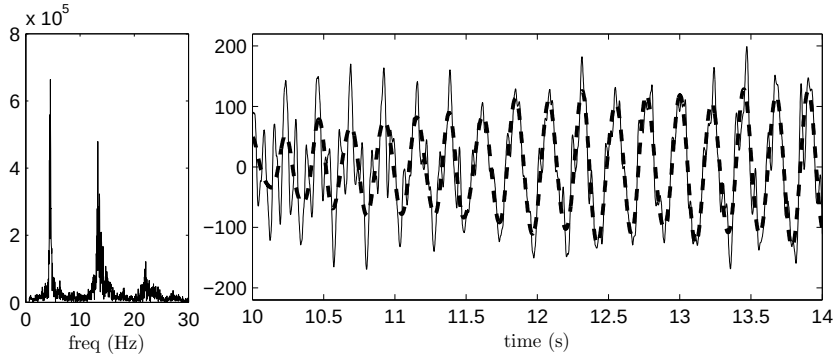

Figure 7: Fourier spectrum of measured strain (left) and original and filtered strain time series (right).

Each experiment consists of an initial transient phase, a period of fully developed VIV and a decay period as the towing velocity is reduced. Only the fully developed period is

of interest here, and the initial and decay periods are removed prior to any data analysis (e.g. filtering and rainflow counting). A nominal time window is established based on the time when full towing speed is reached and the time when the speed starts to drop. The actual time window used in the analyses is taken as the last 2/3 of the nominal.

6 Results and discussion

6.1 Uniform flow

Results for the uniform flow cases are presented first. The dominating frequency and mode in the experiments were found based on measured strains and accelerations [39]. For the simulations, the dominating frequency is found from the peak in the frequency spectrum at the position of max displacement. For a tensioned beam the modes are sinusoids, and the mode number corresponds to the number of half-waves along the riser. The dominating mode is found by modal analysis [43] of the simulated response, using modeshapes from the finite element model. This is done for all current velocities, and the results are reported and compared to the measurements in figure 8 and 9. The simulated frequency is seen to be very accurate for in-line as well as cross-flow, indicating that the in-line synchronization model is good. The dominating mode is also in good agreement, especially for cross-flow. Note that both the experimental and simulated response consists of multiple modes, and in some cases two adjacent modes may be almost equal in strength. Hence, a difference of ± 1 between simulation and experiment is a natural result of the inherent stochastic variations. With this in mind, the simulated cross-flow mode is very good, while the in-line mode is in general slightly high. One possible explanation for this is that the in-line added mass is not taken correctly into account, and that the actual added mass in the in-line direction is lower. A reduction in added mass would result in higher natural frequencies, hence the observed excitation frequency would activate a lower mode.

As a measure of the amplitude of response, the mean along the riser of the r.m.s. of the displacement time series is used:

$$\bar{y}_{rms} = \frac{1}{L}\int_0^L \left(\sqrt{\frac{1}{T}\int_0^T y(t,z)^2 \, dt} \right) dz. \tag{15}$$

This is done for both in-line and cross-flow and the results are compared to experiments in figure 10. It is found that the simulated cross-flow response is somewhat large, on average 27 % higher than measured. This may be related to the fact that important parameters in the simulations, such as Strouhal number and excitation force coefficient are constant, while in reality random variations occur. Such disturbances are likely to decrease the overall response, and this effect is not included in the simulations. Experimenting with random parameters in the hydrodynamic force model would be interesting in the future.

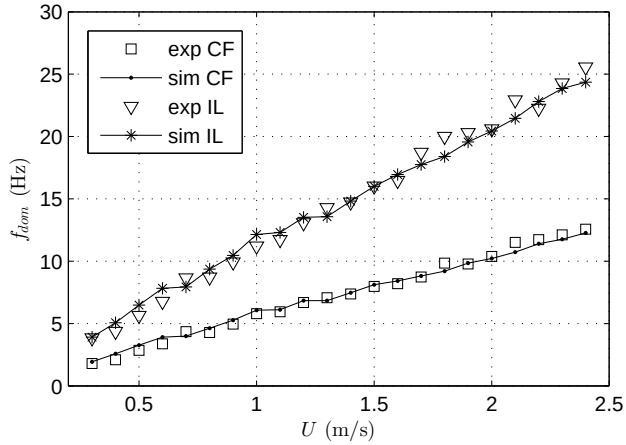

Figure 8: Dominating frequency in uniform flow from experiments and simulations.

In addition, the presence of higher harmonics may reduce the amplitude of the fundamental frequency response, which is also not taken into account in the simulations. The predicted amplitude of the in-line response is seen to be very accurate, which strengthens the assumptions regarding the source of the in-line excitation force (section 3.2).

As described in section 5, fatigue damage is calculated based on rainflow counting of the strain time series from simulations and experiments. Hence, for every simulation, the distribution of fatigue damage rate along the riser is established. In figure 11, results for the cases $U = 0.8$ m/s, $U = 1.5$ m/s and $U = 2.3$ m/s are compared to the fatigue damage caused by the actual measured strains. Compared to measurements, the predicted fatigue damage due to cross-flow vibrations is realistic, while the predicted in-line damage is too large. This is likely due to the error in the predicted in-line mode. For example, for $U = 1.5$ m/s the measured dominating mode is 17 while the predicted is 19. Hence one will expect the associated predicted strain to be $(19/17)^2 \approx 1.25$ times larger, which yields a maximum fatigue damage that is $1.25^3 \approx 1.95$ times higher than observed. This number is in reasonable agreement with the ratio between predicted and measured in-line fatigue damage for this case. When it comes to the variation of the fatigue rate along the riser, the calculations show harmonic variations with distinct peaks and troughs, while the measured fatigue rate is more irregular. This indicates that the vibrations are in reality non-stationary, such that the fatigue damage is dispersed over a larger area. Non-stationary VIV has been reported by various researchers [20], [44]. This apparently random behavior is not captured by the model, but may be included in the future, for instance by introducing random fluctuations in the coefficients. Another interesting observation is that the fatigue rate in some cases have a maximum value close to one end of the riser, with significantly lower fatigue rates at the other end (see e.g. figure 11b and 11c). This behavior is also

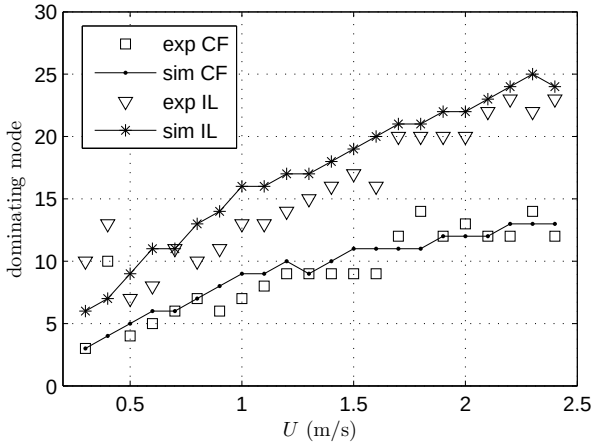

Figure 9: Dominating mode in uniform flow from experiments and simulations.

seen in the simulations, even though the incoming current and boundary conditions are symmetric.

Of particular interest is the maximum fatigue damage rate along the riser. This is extracted from every simulation and compared to the corresponding measured value in figures 12 (cross-flow) and 13 (in-line). For the measured cross-flow strain, the analysis is carried out on the total signals as well as a low-pass filtered version, i.e. with higher harmonics removed. Hence, the low-pass filtered signals contains only the fundamental frequency component. This makes it possible to compare the fundamental frequency fatigue damage to the total damage, thereby revealing the importance of the higher harmonics. The difference between the total and the fundamental frequency damage is explored more thoroughly in section 6.4. Looking at figure 12 it is however seen that the higher harmonics are important, and the fundamental frequency damage is in some cases below 20 % of the total.

For all current velocities, the prediction bias is calculated as:

$$\text{bias} = \frac{\text{simulated maximum fatigue damage rate}}{\text{measured maximum fatigue damage rate}}. \tag{16}$$

The average bias for the cross-flow fatigue damage in uniform flow is 0.72, meaning there is a general tendency to under-predict the fatigue damage. Considering the complexity of the flow, including higher harmonic forces, and the simplifications introduced in the present model, the result is considered satisfactory.

It is interesting that the predicted maximum cross-flow fatigue damage is so close to the measured, even though no higher harmonics are included in the simulations. As

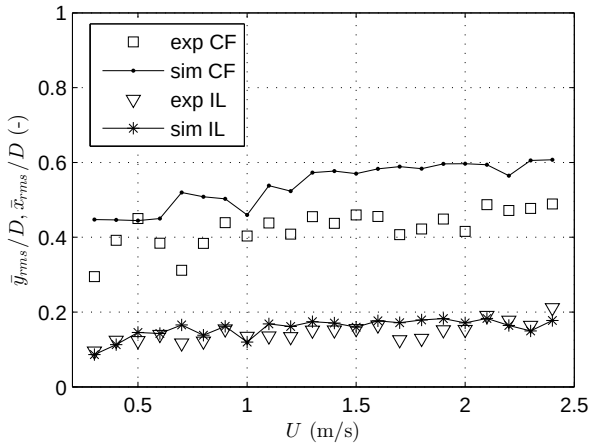

Figure 10: Mean of r.m.s. of displacement for uniform flow, normalized by diameter.

seen in figure 12, the predicted damage is much closer to the total than the fundamental frequency damage. A possible explanation follows: The magnitude of the hydrodynamic forces depends on the kinetic energy density in the incoming current. When more energy is transferred to higher harmonic vibrations, it is likely that less energy will be found at the fundamental frequency response, as the energy density in the incoming flow remains the same. This would result in more irregular vibrations, but the values of the largest maxima and lowest minima (e.g. for strain) may remain virtually the same as if all energy were concentrated at the fundamental frequency. The present model assumes that all the energy goes into the fundamental frequency force, hence it over-predicts the associated fundamental frequency response and under-predicts (does not predict) the higher harmonics. By direct comparison of time series of simulated and total measured strain (see figure 14) it is illustrated how the model still predicts the strain ranges quite accurately.

Moving on to the maximum predicted in-line fatigue damage rate in uniform flow (see figure 13), this is found to be reasonably realistic and in some cases quite accurate. However, the maximum in-line fatigue damage in uniform flow is on average over-predicted by a factor of 2.44. As the frequency and amplitude of the in-line response is very accurate (ref. figure 8 and 10), this is mainly due to the over-prediction of the dominating mode, as previously discussed.

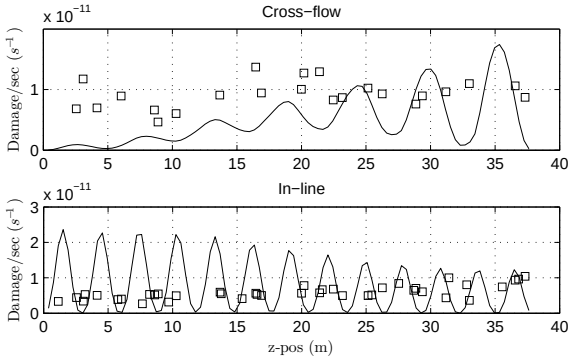

(a) $U = 0.8$ m/s

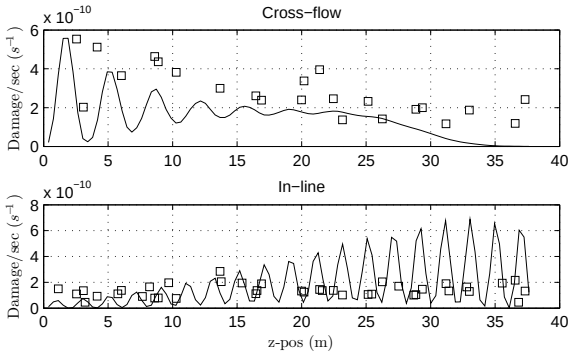

(b) $U = 1.5$ m/s

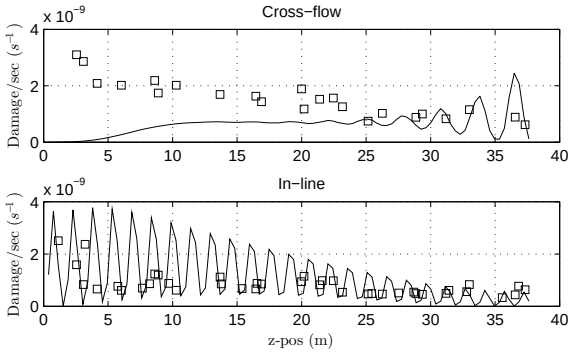

(c) $U = 2.3$ m/s

Figure 11: Predicted and measured fatigue damage rate along riser for three uniform flow cases. The solid lines are from simulations, while squares are from measurements.

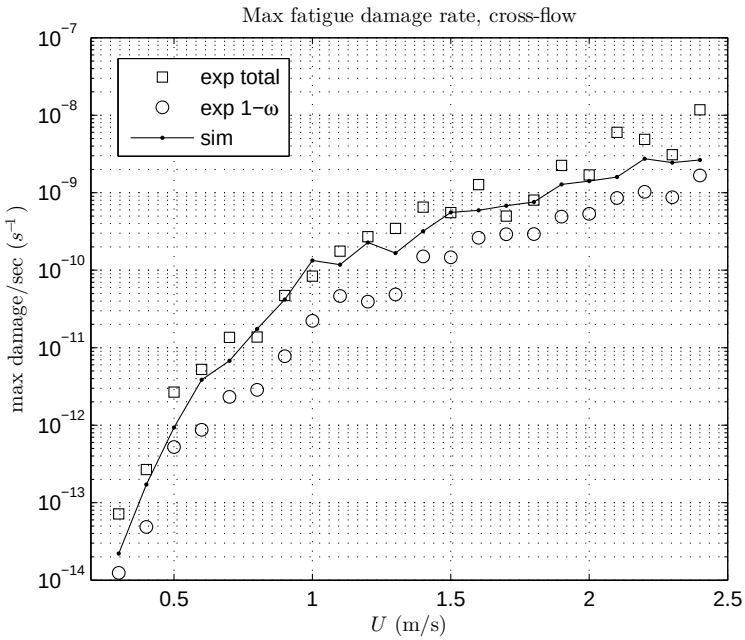

Figure 12: Comparison between predicted and measured maximum fatigue damage rate due to cross-flow vibrations in uniform flow. For the experiments, the fatigue damage is calculated based on the total strain signal (squares), and with higher harmonics removed (circles). The solid line represents the simulations.

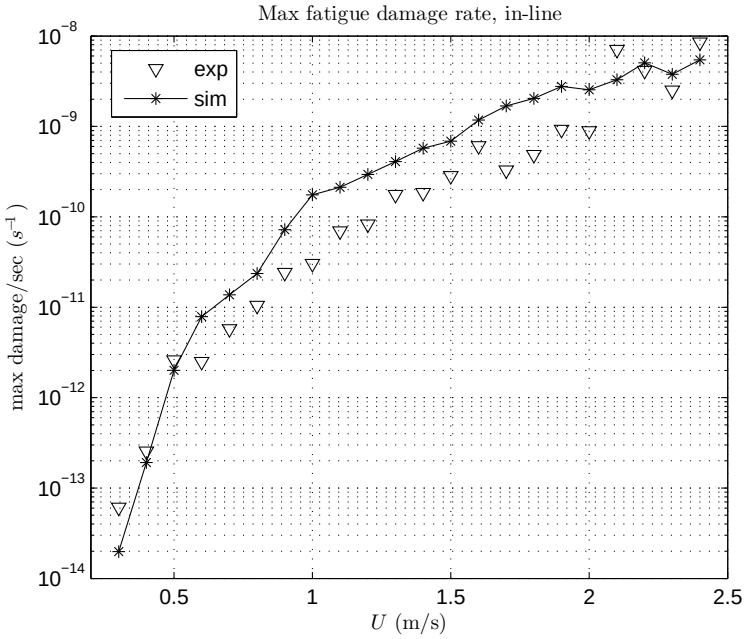

Figure 13: Comparison between predicted (solid line) and measured (triangles) maximum fatigue damage rate due to in-line vibrations in uniform flow.

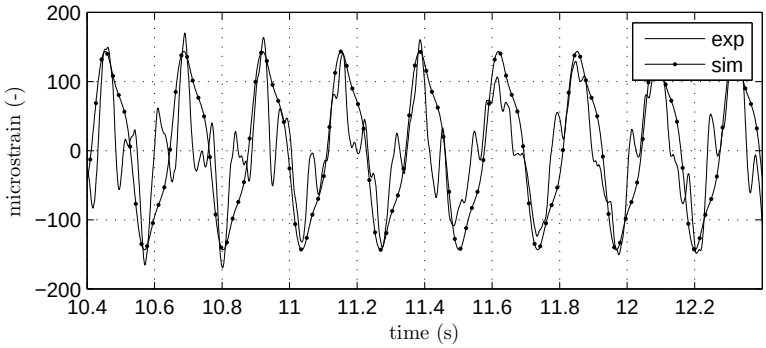

Figure 14: Direct comparison of simulated and measured cross-flow strain. Results are for uniform flow with $U = 0.8$ m/s at the position of maximum fatigue damage.

6.2 Shear flow

Results for the shear flow cases are presented on the same form as for uniform flow. It should be noted that the parameters in the numerical model are exactly the same as for the uniform flow simulations. The only differences are in the current profile and the mean tension of the riser. The dominating frequency for the various velocities is given in figure 15. The measured frequencies are more irregular compared to uniform flow, and in some cases, such as $U = 2.2\ \mathrm{m/s}$, the observed frequency is abnormally low. Setting these exceptional observations aside, the predicted frequencies compare very well with the experimental results.

Moving on to the dominating mode (figure 16), this is seen to be accurately predicted both for in-line and cross-flow, although small differences are found due to random variations in the multi-mode response. The predictions are in this case better than for uniform flow, particularly for the in-line mode which was generally over-predicted in uniform flow. This means the natural frequencies of the structure are more accurate for the shear flow simulations. The main uncertainties in the natural frequencies lie in the added mass, which points to the conclusion that using potential theory added mass in the in-line direction ($C_{ax} = 1$) is more correct in sheared than uniform flow.

The mean of the r.m.s. of the cross-flow and in-line displacement are again used for evaluating the predicted amplitude of vibration. This is reported and compared to the experimental results in figure 17. As seen, the average r.m.s. of the cross-flow displacement is realistic, although slightly low. The magnitude of the simulated in-line displacements compares well with measurements.

Figure 18 shows the how the simulated fatigue damage rate varies along the length of the riser for the three selected cases, $U = 0.8\ \mathrm{m/s}$, $U = 1.5\ \mathrm{m/s}$ and $U = 2.3\ \mathrm{m/s}$. The results are in reasonable agreement with measurements, and the predicted cross-flow fatigue damage corresponds accurately to the measured for $U = 0.8\ \mathrm{m/s}$ and $U = 2.3\ \mathrm{m/s}$, while being slightly low for $U = 1.5\ \mathrm{m/s}$. The predicted in-line fatigue damage is in some cases too high and in others too low. The variations along the riser show similar features as in the uniform flow case, i.e. the calculations are more regular than the measurements. This is likely due to the previously discussed non-stationary behavior, which occurs in reality, but is not captured by the model. It is seen that the cross-flow fatigue rate is significantly influenced by traveling waves, both in the calculations and the measurements, particularly in the region with high current velocity (maximum is at $z = 38\mathrm{m}$). The point of maximum fatigue damage is typically found close to the middle, slightly towards the high velocity region.

The maximum simulated fatigue damage rate along the riser is plotted as a function of the current velocity and compared to experiments in figures 19 (cross-flow) and 20 (in-line). Again, the cross-flow fatigue analysis for the experimental results is performed on both the original and filtered strain signals as described in section 5. The results show that the higher harmonics are less important in sheared than in uniform flow. The prediction

bias (as defined in equation (16)) is found to be on average 0.91 for cross-flow. This is better than for uniform flow, and is explained from the fact that the higher harmonics are less important in shear flow.

The maximum in-line fatigue damage rate is presented in figure 20 and the average prediction bias is in this case 1.34. The in-line fatigue damage is in most cases slightly over-predicted, but is significantly under-predicted for the lowest flow velocities. This is probably because the dominating in-line mode is surprisingly high in the low-velocity tests (see figure 16).

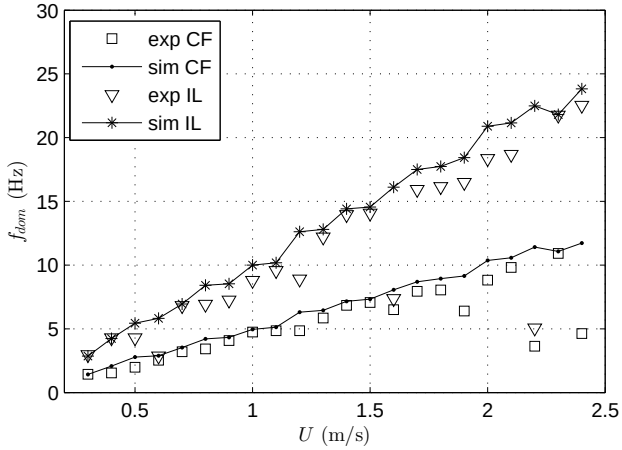

Figure 15: Dominating frequency in shear flow from experiments and simulations.

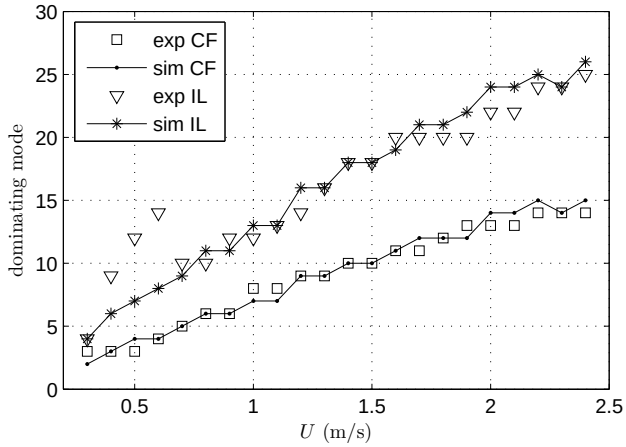

Figure 16: Dominating mode in shear flow from experiments and simulations.

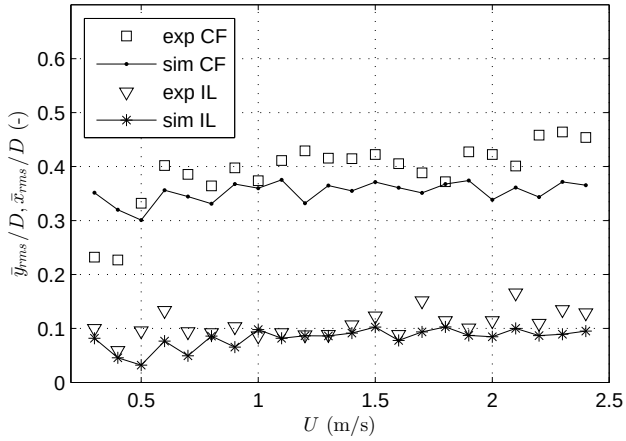

Figure 17: Mean of r.m.s. of displacement for shear flow.

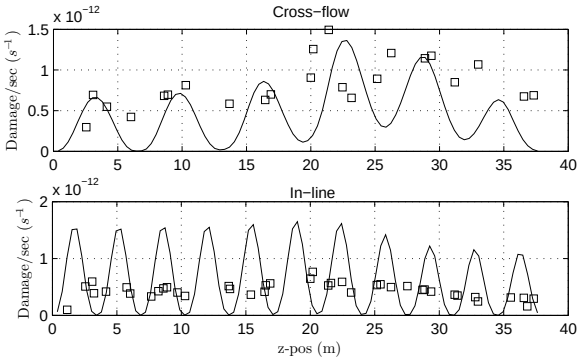

(a) $U = 0.8$ m/s

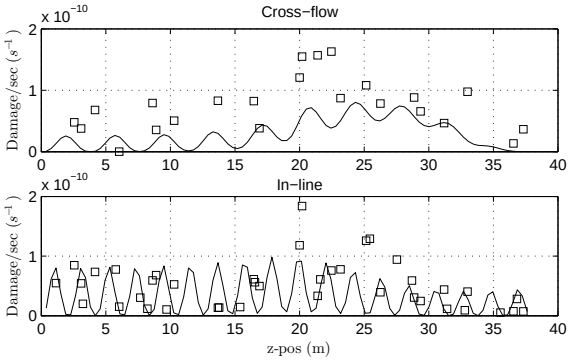

(b) $U = 1.5$ m/s

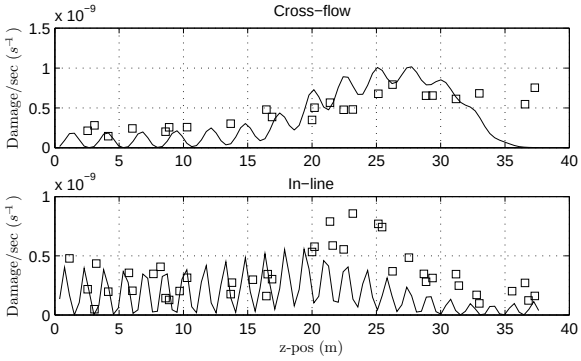

(c) $U = 2.3$ m/s

Figure 18: Predicted and measured fatigue damage rate along riser for three sheared flow cases. The solid lines are from simulations, while squares are from measurements.

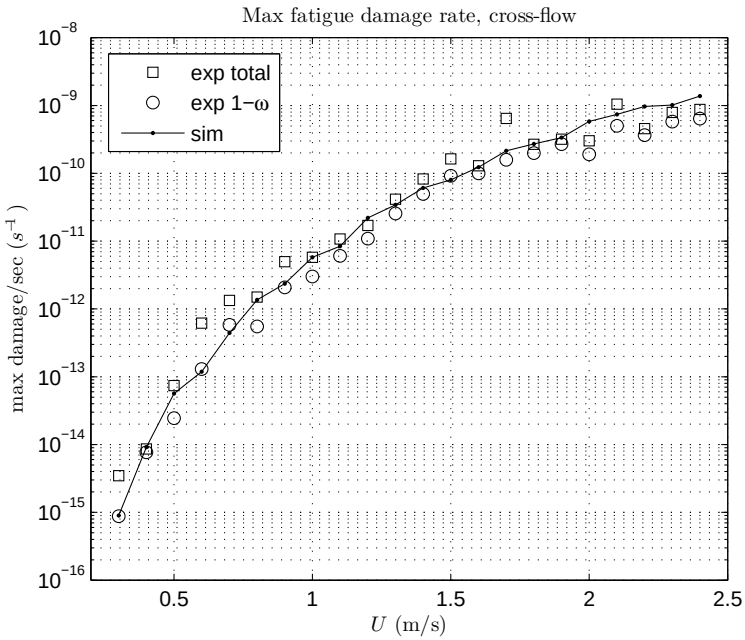

Figure 19: Comparison between predicted and measured maximum fatigue damage rate due to cross-flow vibrations in shear flow. For the experiments, the fatigue damage is calculated based on the total strain signal (squares), and with higher harmonics removed (circles). The solid line represents the simulations.

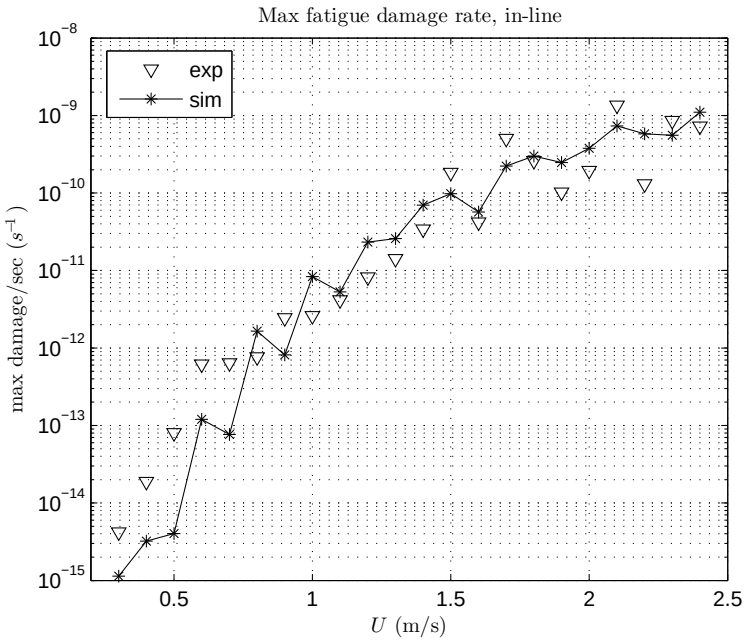

Figure 20: Comparison between predicted (solid line) and measured (triangles) maximum fatigue damage rate due to in-line vibrations in shear flow.

6.3 Assessment of model prediction accuracy

It was established in the preceding sections that the maximum cross-flow fatigue damage is on average slightly under-predicted, while the in-line damage is over-predicted. Due to stochastic variations, individual prediction may still be either above or below. The accuracy of individual predictions (and the associated randomness) is shown graphically in figure 21, which shows the predicted versus the measured maximum fatigue damage rate. If the model was perfect, all points would lie on the straight line. A point above the line indicates that the fatigue damage is over-predicted, while a point below corresponds to an under-prediction.

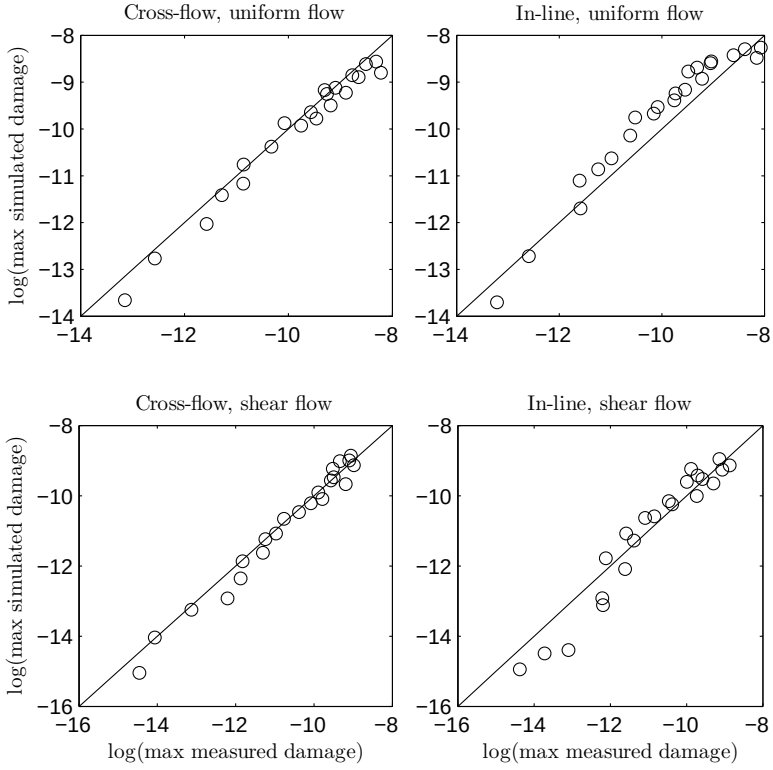

Figure 21: Simulated versus measured maximum fatigue damage rate (in-line and cross-flow) in uniform and shear flow.

The prediction bias for the maximum fatigue damage rate was defined in equation (16), and has been calculated for every simulation. The quality of predictions are different

for cross-flow and in-line as well as sheared and uniform flow, and these groups will therefore be treated separately. To obtain a conservative estimate for a given simulation, the predicted fatigue damage can be multiplied with a safety factor, $\gamma = 1/B$, where B is the prediction bias. It is difficult to provide general guidelines on what safety factor to use based on the available data, however, using the safety factor associated with the most nonconservative prediction (i.e. $\gamma_{max} = 1/B_{min}$) yields a conservative result in 21 out of the 22 cases. Hence, adopting the safety factor γ_{max} is expected to give conservative results with a probability of 95.5 %. The median of the safety factors within each group is also of interest, and is assigned the symbol $\tilde{\gamma}$. This is associated with an equal number of over- and under-predictions, and can therefore be interpreted as an optimum safety factor for realistic predictions. The maximum and median safety factor for each group are presented in table 2.

Table 2: Safety factors necessary for conservative prediction of the maximum fatigue damage in 95.5 % (γ_{max}) and 50 % ($\tilde{\gamma}$) of the cases, for the various groups.

	Uniform flow		Shear flow	
	Cross-flow	In-line	Cross-flow	In-line
γ_{max}	4.42	3.08	5.20	19.84
$\tilde{\gamma}$	1.53	0.42	1.15	0.83

The fact that the cross-flow fatigue is on average under-predicted is reflected in the median safety factor, as this is larger than 1 for both current conditions. The median safety factor is less than 1 for in-line fatigue, due to the overall tendency to over-predict this. Furthermore, it is seen that the shear flow simulations are on average more accurate than the uniform flow simulations. It should however be pointed out that the maximum safety factor is larger in sheared than uniform flow, meaning that the worst shear flow prediction is less accurate than the worst uniform flow prediction. For the cross-flow fatigue damage, the maximum safety factors are 4.42 and 5.20, which is reasonable compared to results obtained with state-of-the-art software used by the industry [45]. Moving on to γ_{max} for in-line fatigue, the uniform flow result is consistent with the others, while the shear flow safety factor is significantly larger. The simulation requiring a safety factor of 19.84 is the shear flow case with $U = 0.5$ m/s, which was considerably less accurate than the other predictions, as seen in figure 20. Looking back at figure 17, it is observed that the predicted mean r.m.s. in-line displacement was in this case less than half the measured, which explains the large error in fatigue rate for this case. Future research should attempt to find out why the in-line amplitude is significantly under-predicted in some cases. A possible solution is to increase the value of α in equation (9), but this is not considered in the present paper.

6.4 Observations on the importance of higher harmonics

This section focuses on some interesting findings in the NDP experimental data. The maximum cross-flow fatigue damage rate found by rainflow counting of the fundamental frequency strain (i.e. with higher harmonics filtered out) is denoted D_1. Similarly, the maximum cross-flow fatigue damage rate found by rainflow counting of the *original* strain signals is denoted D_{tot}. The ratio D_1/D_{tot} is calculated for every current velocity, and the results are shown in figure 22a (uniform flow) and 22b (shear flow). In the absence of higher harmonic components, D_1 and D_{tot} are equal, and the ratio is one. On the other hand, if higher harmonics are very important compared to the fundamental frequency component, the ratio approaches zero.

As seen in figure 22a, the importance of the higher harmonics in uniform flow are rather stable, and the ratio D_1/D_{tot} is usually around 0.2, meaning that the contribution from fundamental frequency strain is approximately 20 %. Moving on to the results for shear flow (figure 22b), something quite different is seen. At low velocities, D_1/D_{tot} is close to 0.2, however, the ratio clearly rises when the current velocity is increased. At $U = 2.0\,\mathrm{m/s}$, the fundamental frequency fatigue damage is around 80 % of the total. This shows that in sheared flow, the higher harmonics become less important (with respect to fatigue) as the velocity is increased.

The observed differences can be explained by a gradual change from tension- to bending-dominated vibrations. The tensioned riser behaves like a string for the lower modes, meaning that the natural frequencies increase linearly with mode, n. For higher modes, the bending stiffness dominates, and the natural frequencies are proportional to n^2. Also, the riser tension increases together with current velocity as a result of drag forces. These forces are significantly higher in uniform than sheared flow, which means the bending stiffness is more important in shear flow. The higher harmonics are usually dominated by a frequency 3 times higher than the fundamental frequency, and if the natural frequencies increase linearly with mode (as for a tension-dominated riser), the mode excited by the higher harmonic forces will be $n_h = 3n_1$, where n_1 is the mode excited by the fundamental frequency forces. However, for a bending dominated riser, the higher harmonic mode will be $n_h = \sqrt{3}n_1$. Hence, the ratio n_1/n_h is larger for bending- than tension-dominated risers, which may explain the observed differences. At present, this is only a hypothesis, and more research is necessary to conclude whether or not the ratio between tension and bending stiffness is important for the higher harmonic stress.

The observed differences may also be related to the flow around the structure. The reduced velocity, $V_r = U/(fD)$, is known to be of critical importance to the flow. In uniform flow (assuming mono-frequency response), this is constant along the riser length, while in sheared flow it will vary from zero in one end to a maximum value in the other. It is possible that the higher harmonic components are less pronounced in low reduced velocities, either because the higher harmonic exciting force is diminished, or because the high frequency damping is larger. This does however not explain why the ratio D_1/D_{tot}

varies so strongly in sheared current when the velocity is changed.

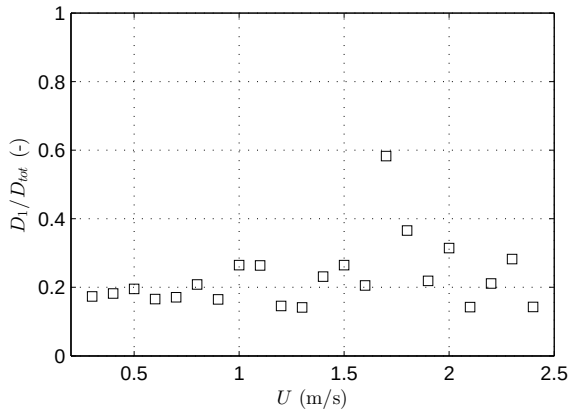

(a) Uniform flow

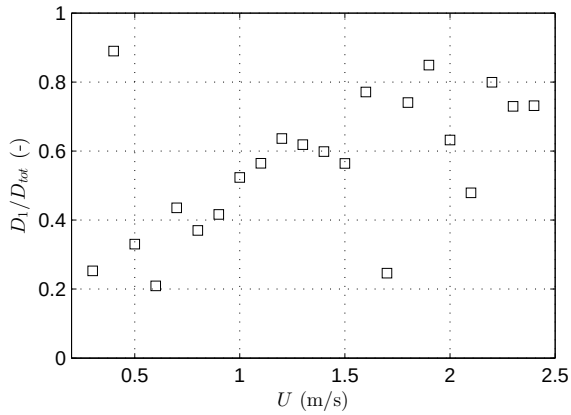

(b) Shear flow

Figure 22: Ratio of maximum fundamental frequency fatigue damage to maximum total fatigue damage, D_1/D_{tot}, from measured cross-flow strain.

7 Conclusions

Fatigue damage due to vortex-induced vibrations have been numerically predicted, and a detailed comparison with experimental observations have been performed. This is the first time this numerical model, which includes both in-line and cross-flow vibrations, has been used for fatigue damage calculations. Results obtained by rainflow counting of

simulated and measured strain time series show that the model is capable of reproducing the actual fatigue damage with satisfactory accuracy through time domain simulation of hydrodynamic forces and structural response. Some discrepancies are seen, which must be expected due to the chaotic nature of VIV and the simplifications embedded in the model. Riser fatigue damage in uniform and shear flow have been calculated for current velocities ranging from 0.3 m/s to 2.4 m/s, and the fact that a constant set of parameters have been used for all simulations indicates that the hydrodynamic force model is applicable to arbitrary (planar) current profiles and structural configurations, assuming that the Reynolds number is within the subcritical range and the cross-section is circular. The accuracy of individual predictions has been assessed, and safety factors necessary to ensure conservative predictions in 50 % and 95.5 % of the cases have been given. This is mainly to illustrate the accuracy of the method, but also serves as an indication of the uncertainties associated with VIV. When it comes to computational cost, the running-time for a 200 cycle simulation (i.e. 20 000 time steps) is approximately 20 seconds on a standard lap-top. All calculations are performed with the software MATLAB.

Some observations on the importance of higher harmonics have also been made. Based on strain signals from experiments, it is found that the fatigue damage contribution from fundamental frequency and higher harmonic strain are almost constant in uniform flow, while the relative importance of the fundamental frequency contribution increases together with current velocity in the shear flow cases. A possible explanation which should be investigated in the future is related to the characteristic behavior of natural frequencies for tension- versus bending-dominated risers.

Acknowledgments

The authors are very grateful to the Norwegian Deepwater Programme (NDP) Riser and Mooring Project for making the results from the Riser High Mode VIV tests available.

References

[1] Bearman PW. Circular cylinder wakes and vortex-induced vibrations. Journal of Fluids and Structures 2011;27(5–6):648 – 658.

[2] Bearman PW. Vortex shedding from oscillating bluff bodies. Annual Review of Fluid Mechanics 1984;16(1):195–222.

[3] Sarpkaya T. A critical review of the intrinsic nature of vortex-induced vibrations. Journal of Fluids and Structures 2004;19(4):389 – 447.

[4] Williamson C, Govardhan R. Vortex-induced vibrations. Annual Review of Fluid Mechanics 2004;36(1):413–455.

[5] Wu X, Ge F, Hong Y. A review of recent studies on vortex-induced vibrations of long slender cylinders. Journal of Fluids and Structures 2012;28(0):292 – 308.

[6] Sarpkaya T. Hydrodynamic damping, flow-induced oscillations, and biharmonic response. Journal of offshore Mechanics and Arctic engineering 1995;117(4):232–238.

[7] Vikestad K. Multi-frequency response of a cylinder subjected to vortex shedding and support motions. Ph.D. thesis; Norwegian University of Science and Technology, Department of Marine Technology; 1998.

[8] Govardhan R, Williamson C. Modes of vortex formation and frequency response of a freely vibrating cylinder. Journal of Fluid Mechanics 2000;420:85–130.

[9] Sarpkaya T. Fluid forces on oscillating cylinders. NASA STI/Recon Technical Report A 1978;78.

[10] Moe G, Wu ZJ. The lift force on a cylinder vibrating in a current. Journal of Offshore Mechanics and Arctic Engineering 1990;112(4):297–303.

[11] Yin D. Experimental and numerical analysis of combined in-line and cross-flow vortex induced vibration. Ph.D. thesis; Norwegian University of Science and Technology, Centre for Ships and Ocean Structures; 2013.

[12] Vandiver JK. Dimensionless parameters important to the prediction of vortex-induced vibration of long, flexible cylinders in ocean currents. Journal of Fluids and Structures 1993;7(5):423 – 455.

[13] Chaplin J, Bearman P, Huera Huarte F, Pattenden R. Laboratory measurements of vortex-induced vibrations of a vertical tension riser in a stepped current. Journal of Fluids and Structures 2005;21(1):3–24.

[14] Huera-Huarte F, Bangash Z, González L. Towing tank experiments on the vortex-induced vibrations of low mass ratio long flexible cylinders. Journal of Fluids and Structures 2014;48(0):81 – 92.

[15] Baarholm GS, Larsen CM, Lie H. On fatigue damage accumulation from in-line and cross-flow vortex-induced vibrations on risers. Journal of Fluids and Structures 2006;22(1):109–127.

[16] Jauvtis N, Williamson C. The effect of two degrees of freedom on vortex-induced vibration at low mass and damping. Journal of Fluid Mechanics 2004;509(6):23–62.

[17] Dahl J, Hover F, Triantafyllou M. Two-degree-of-freedom vortex-induced vibrations using a force assisted apparatus. Journal of Fluids and Structures 2006;22(6):807–818.

[18] Vandiver JK, Swithenbank SB, Jaiswal V, Jhingran V. Fatigue damage from high mode number vortex-induced vibration. In: Proc. 25th OMAE Conf. 2006,.

[19] Modarres-Sadeghi Y, Mukundan H, Dahl J, Hover F, Triantafyllou M. The effect of higher harmonic forces on fatigue life of marine risers. Journal of Sound and Vibration 2010;329(1):43–55.

[20] Modarres-Sadeghi Y, Chasparis F, Triantafyllou M, Tognarelli M, Beynet P. Chaotic response is a generic feature of vortex-induced vibrations of flexible risers. Journal of Sound and Vibration 2011;330(11):2565 – 2579.

[21] Vandiver JK, Li L. SHEAR7 V4.4 Program Theoretical Manual; 2005.

[22] Larsen CM, Lie H, Passano E, Yttervik R, Wu J, Baarholm G. VIVANA - Theory Manual, Version 3.7; 2009.

[23] Chaplin J, Bearman P, Cheng Y, Fontaine E, Graham J, Herfjord K, et al. Blind predictions of laboratory measurements of vortex-induced vibrations of a tension riser. Journal of Fluids and Structures 2005;21(1):25–40.

[24] Passano E, Larsen CM, Lie H. Comparison of calculated in-line vortex induced vibrations to model tests. In: ASME 2012 31st International Conference on Ocean, Offshore and Arctic Engineering. American Society of Mechanical Engineers; 2012, p. 705–712.

[25] Facchinetti M, de Langre E, Biolley F. Coupling of structure and wake oscillators in vortex-induced vibrations. Journal of Fluids and Structures 2004;19(2):123 – 140.

[26] Ogink R, Metrikine A. A wake oscillator with frequency dependent coupling for the modeling of vortex-induced vibration. Journal of Sound and Vibration 2010;329(26):5452–5473.

[27] Mainçon P. A Wiener-Laguerre Model of VIV Forces Given Recent Cylinder Velocities. Mathematical Problems in Engineering 2011;2011.

[28] Thorsen MJ, Sævik S, Larsen CM. A simplified method for time domain simulation of cross-flow vortex-induced vibrations. Journal of Fluids and Structures 2014;49(0):135 – 148.

[29] Thorsen MJ, Sævik S, Larsen CM. Time domain simulation of cross-flow and in-line vortex-induced vibrations. In: Proceedings of the 9th International Conference on Structural Dynamics, EURODYN. 2014,.

[30] Braaten H, Lie H. NDP riser high mode VIV tests, main report. Tech. Rep.; Norwegian Marine Technology Research Institute; Trondheim, Norway; 2004.

[31] Sumer BM, Fredsøe J. Hydrodynamics around cylindrical structures; vol. 12. World Scientific Publishing Company; 1997.

[32] Griffin OM. Vortex shedding from bluff bodies in a shear flow: a review. Journal of Fluids Engineering 1985;107(3):298–306.

[33] Li L, Fu S, Yang J, Ren T, Wang X. Experimental investigation on vortex-induced vibration of risers with staggered buoyancy. In: ASME 2011 30th International Conference on Ocean, Offshore and Arctic Engineering. American Society of Mechanical Engineers; 2011, p. 51–59.

[34] Bishop R, Hassan A. The lift and drag forces on a circular cylinder oscillating in a flowing fluid. Proceedings of the Royal Society of London Series A Mathematical and Physical Sciences 1964;277(1368):51–75.

[35] Venugopal M. Damping and response prediction of a flexible cylinder in a current. Ph.D. thesis; Massachusetts Institute of Technology; 1996.

[36] King R, Prosser M, Johns D. On vortex excitation of model piles in water. Journal of Sound and Vibration 1973;29(2):169 – 188.

[37] Norberg C. Fluctuating lift on a circular cylinder: review and new measurements. Journal of Fluids and Structures 2003;17(1):57–96.

[38] Swithenbank SB, Vandiver JK, Larsen CM, Lie H. Reynolds number dependence of flexible

cylinder VIV response data. In: ASME 2008 27th International Conference on Offshore Mechanics and Arctic Engineering. American Society of Mechanical Engineers; 2008, p. 503–511.

[39] Kristiansen T, Lie H. NDP riser high mode VIV tests, modal analysis. Tech. Rep.; Norwegian Marine Technology Research Institute; Trondheim, Norway; 2005.

[40] NORSOK Standard . Design of Steel Structures, Annex C - Fatigue Strength Analysis. Tech. Rep.; Norwegian Technology Standards Institution; 1998.

[41] Watson P, Dabell B. Cycle counting and fatigue damage. In: Statistical aspects of fatigue testing: papers presented at a symposium of the Society of Environmental Engineers, Warwick, UK. 1975,.

[42] Brodtkorb PA, Johannesson P, Lindgren G, Rychlik I, Rydén J, Sjö E, et al. Wafo—a matlab toolbox for analysis of random waves and loads. In: Proceedings of the 10th international offshore and polar engineering conference; vol. 3. 2000, p. 343–350.

[43] Lie H, Kaasen K. Modal analysis of measurements from a large-scale VIV model test of a riser in linearly sheared flow. Journal of Fluids and Structures 2006;22(4):557–575.

[44] Larsen CM, Zhao Z, Lie H. Frequency components of vortex induced vibrations in sheared current. In: ASME 2012 31st International Conference on Ocean, Offshore and Arctic Engineering. 2012,.

[45] Tognarelli M, Fontaine E, Beynet P, Santosa M, Marcollo H. Reliability-based factors of safety for vortex induced vibration fatigue using field measurements. Journal of Offshore Mechanics and Arctic Engineering 2013;135(4).

PAPER II

Paper III

Time domain simulation of vortex-induced vibrations in stationary and oscillating flows

Mats J. Thorsen, Svein Sævik and Carl M. Larsen

Department of Marine Technology, Norwegian University of Science and Technology, Trondheim, Norway

Journal of Fluids and Structures, Vol. 61, 2016, pp. 1 – 19

Abstract

This paper focuses on the further development of a previously published semi-empirical method for time domain simulation of vortex-induced vibrations (VIV). A new hydrodynamic damping formulation is given, and the necessary coefficients are found from experimental data. It is shown that the new model predicts the observed hydrodynamic damping in still water and for cross-flow oscillations in stationary incoming flow with high accuracy. Next, the excitation force model, which is one component of the total hydrodynamic force model, is optimized by simulating the VIV response of an elastic cylinder in a series of experiments with stationary flow. The optimization is performed by repeating the simulations until the best possible agreement with the experiments is found. The optimized model is then applied to simulate the cross-flow VIV of an elastic cylinder in oscillating flow, without introducing any changes to the hydrodynamic force modeling. By comparison with experiment, it is shown that the model predicts the frequency content, mode and amplitude of vibration with a high level of realism, and the amplitude modulations occurring at high Keulegan-Carpenter numbers are well captured. The model is also utilized to investigate the effect of increasing the maximum reduced velocity and the mass ratio of the elastic cylinder in oscillating flow. Simulations show that complex response patterns with multiple modes and frequencies appear when the maximum reduced velocity is increased. If, however, the mass ratio is increased by a factor of 5, a single mode dominates. This illustrates that, in oscillating flows, the mass ratio is important in determining the mode participation at high maximum reduced velocities.

Keywords: Vortex-induced vibrations; Elastic cylinders; Oscillating flow; Time domain; Simulation

1 Introduction

Slender structures such as pipelines and risers experience vortex-induced vibrations (VIV) when exposed to external fluid flow [1]. The vibrations are a result of the fluctuating lift and drag forces associated with flow separation and vortex shedding. Depending on the incoming flow and structural properties, significant dynamic stress may occur, causing fatigue damage accumulation which over time may lead to structural failure. Understanding and being able to predict VIV in realistic environmental conditions is therefore important to ensure the safety of slender structures.

A considerable amount of work has been done to increase the understanding of VIV, as reflected in the reviews by Sarpkaya [2], Williamson and Govardhan [3], Bearman [4] and Wu et al. [5]. As the equations of motion governing viscous flow are difficult to solve, experiments have been the most important source of new insight. Examples of typical experiments are free vibration of elastically mounted rigid cylinders [6–9] and cylinders undergoing forced motions [10–14]. Experiments with long flexible structures have also been performed, both under controlled laboratory conditions [15–17] and in field environments [18, 19]. These experiments focused on various flow situations such as uniform, sheared and stepped current, and in all cases the incoming flow was essentially stationary, i.e. constant in time.

In some situations, the relative current velocity may be non-stationary, either due to movement of the structure or oscillations in the incoming flow itself. For example, a riser connected to a floating platform will oscillate as a result of the wave-induced motions of the floater. The relative flow velocity caused by the riser moving back and forth in the water may cause vortex shedding and VIV if the motion amplitude is sufficiently large. VIV of an elastic cylinder in oscillating flow was studied experimentally by Fu et al. [20]. They found that the structure vibrated significantly due to vortex shedding, and noted some important differences compared to stationary flow VIV. For instance, they observed a characteristic developing process with vibrations continuously building up and dying out. VIV of spring mounted rigid cylinders in oscillating flow has previously been studied by several researchers such as Sarpkaya [21] and Sumer and Fredsøe [22].

In light of these experimental studies, and the fact that oscillating flows are relevant in several practical applications, the need for a mathematical model able to predict VIV in oscillating flows becomes evident. One possibility is to solve the Navier-Stokes equations numerically, but the required computational effort is generally large. The semi-empirical frequency domain methods VIVA [23], SHEAR7 [24] and VIVANA [25] are more efficient, but can only predict VIV in stationary flows. As illustrated by Chang and Isherwood [26], the wake-oscillator can be used to simulate VIV in time domain for unsteady flow situations, but no comparison with experiment was included in this study. Liao [27] was able to predict VIV in unsteady flow based on a relationship between an equivalent reduced damping and the resulting vibration amplitude. Recently, Resvanis [28] proposed a dimensionless parameter which can be used to determine if the response in unsteady flow

will be similar to the response in steady flow.

An alternative method for simulating VIV in time domain was proposed by Thorsen et al. [29]. In this semi-empirical method, the fluid forces are calculated based on the incoming flow velocity and the motion of the cross-section. The special feature is how synchronization between the vortex shedding and cylinder motion is taken into account. It has been shown that the model provides realistic results for several different cases, including flexible cylinders in uniform, sheared and stepped current [30, 31]. The formulation includes no restriction on the time variability of the incoming flow velocity, which means it is theoretically suited for simulating VIV in oscillating flows. With this in mind, the outline of the present paper is as follows: Firstly, the original model [29] is slightly modified to improve the prediction accuracy in stationary flows. Secondly, the improved model is used to simulate a flexible cylinder in oscillating flow. The experiment by Fu et al. [20] is used for comparison, allowing for direct assessment of the prediction accuracy. Finally, the model is used to explore the effect of changing certain key parameters. For instance, the reduced velocity is increased beyond what was considered in the actual experiment, resulting in the appearance of complex vibration patterns.

2 Time domain VIV model

2.1 Hydrodynamic force model

A stationary cylinder in an incoming undisturbed flow is subjected to time varying forces. The force component parallel to the flow is called drag, while the perpendicular component is named lift. Due to the vortex shedding process, the lift force oscillates with a frequency $f_s = \mathrm{St}U/D$ called the Strouhal frequency, where D is the cylinder diameter and U is the velocity of the flow. The Strouhal number St is generally a function of the Reynolds number and the surface roughness of the cylinder, but in the subcritical Reynolds number range, St is nearly constant and close to 0.2 [32]. If the cylinder is flexible, it will vibrate as a result of the oscillating fluid forces, and the movement of the cylinder alters the surrounding flow and the corresponding fluid forces. One of the most important effects is that the vortex shedding may synchronize with the cylinder motion, such that the frequency of the lift force deviates from the expected Strouhal frequency. In addition, there will be fluid resistance (damping) and added mass effects due to the velocity and acceleration of the cylinder.

The hydrodynamic force model used here was first presented by Thorsen et al. [29]. Some minor modifications were introduced [31], providing the starting point for the present paper. In these previous studies, hydrodynamic damping was modeled using a linear and quadratic term, and the empirical coefficients were found by minimizing the difference between this model and the model given by Venugopal [33]. Although this was quite successful, a tendency to over-predict the cross-flow vibration amplitude in uniform flow and under-predict it in linearly sheared flow was seen [31], which indicates that the model

can still be improved. With this in mind, a new damping model is developed here, using actual measurements to adjust the empirical coefficients. As the total energy transfer between fluid and structure is determined from the energy delivered by the vortex shedding process and the energy subtracted by the hydrodynamic damping, altering the damping model will require a change in the excitation model to ensure that the net power transfer is physically correct. This is addressed further in section 3.

It should be pointed out that the new developments described in this section are based on data from experiments performed in stationary incoming flow. Hence, the model is directly tuned to accurately predict vortex-induced vibrations in stationary flows. As there are no mathematical restrictions on the time-variability of the incoming flow, it is straightforward to apply the model in oscillating flows as well. However, an oscillating flow will introduce some physical changes which are not taken into account in the model. Most importantly, the flow meeting the cylinder is no longer undisturbed, but contains previously shed vortices. In this context, an interesting question is: Can VIV in oscillating flows be predicted based on data from stationary flow VIV? An attempt to answer this question is made in section 4.

2.1.1 Cross-flow hydrodynamic force

Hydrodynamic damping of circular cylinders has been extensively studied, see e.g. Sarpkaya [34]. For the present application, trying to develop a model which reproduces the true damping exactly in every situation would be disadvantageous, because such a model would be very complicated, and perhaps unrealizable without resorting to direct numerical simulation of the Navier-Stokes equations. A pragmatic point of view is therefore adopted, trying to find a damping model which is sufficiently accurate to represent the energy extraction in vortex-induced vibrations, while being applicable in a computationally efficient time domain simulation.

Consider a cylinder cross-section with diameter D in an incoming undisturbed flow of velocity U and density ρ. Let the x-axis point in the direction of the flow, and the y-axis in the direction normal to the flow, as seen in figure 1. The origin is positioned at the center of the undisturbed cylinder, such that y corresponds to the cross-flow displacement away from the position of static equilibrium. In the previous papers on this model, hydrodynamic damping was modeled using a linear and quadratic term. However, the accuracy is found to increase if the linear term is dropped, and the cross-flow hydrodynamic damping force per unit length is now expressed as

$$F_{d,y} = -\frac{1}{2}\rho D C_{d,y} |\dot{y}| \dot{y}, \tag{1}$$

where $\dot{y}$ is the cross-flow velocity of the cylinder. A crucial step is to find an appropriate $C_{d,y}$. If $U = 0$, the problem reduces to an oscillating cylinder in still water, which with respect to the damping force is equivalent to a fixed cylinder in an oscillating flow. This

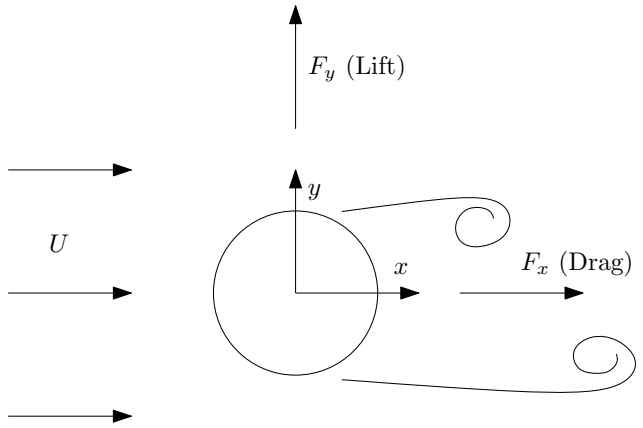

Figure 1: Cylinder with incoming flow and coordinate system definition.

case has been studied by Sarpkaya [35], and it is found that $C_{d,y}$ depends strongly on the Keulegan-Carpenter number (KC), i.e. the ratio between the oscillation amplitude and the cylinder diameter. For simplicity, it is assumed that the damping coefficient can be expressed as a linear function of y_0/D over the relevant range, i.e. $C_{d,y} = a_0 + a_1 y_0/D$, where y_0 is the cross-flow amplitude of vibration.

To find the appropriate values of a_0 and a_1, experimental data is necessary. Vikestad [36] reports results from decay tests in still-water which is used here. In that paper, the damping force was expressed as a linear function of velocity, i.e. $F_{d,y} = -c\dot{y}$, and the damping coefficient was given as a function of y_0/D, meaning that $c = c(y_0/D)$. Because of the differences in formulation, these results cannot be used directly in the present quadratic damping model. However, the damping coefficients given by Vikestad [36] reflects the experimentally measured energy loss. Therefore, the strategy used to find the damping parameters a_0 and a_1 is to minimize the difference between the predicted energy loss (based on equation (1)) and the energy loss observed in experiment. The average power extracted by the damping force over one oscillation period is used as a measure of energy loss. This can be expressed as:

$$\overline{\dot{W}}_{d,y} = \frac{1}{T}\int_0^T F_{d,y}\,\dot{y}\,dt, \tag{2}$$

where $T = 2\pi/\omega$ is the period. Inserting the damping force from equation (1) using $C_{d,y} = a_0 + a_1 y_0/D$ and $\dot{y} = \omega y_0 \cos\omega t$, the following result is obtained:

$$\overline{\dot{W}}_{d,y} = -\frac{1}{2T}\rho D(a_0 + a_1\frac{y_0}{D})\int_0^T |\dot{y}|\dot{y}^2 dt = -\frac{8}{12\pi}\rho D(a_0 + a_1\frac{y_0}{D})\omega^3 y_0^3. \tag{3}$$

Using the linear damping formulation (as Vikestad [36] did) in equation (2) gives

$$\overline{\dot{W}}_{d,y} = -\frac{1}{T}\int_0^T c\dot{y}^2 dt = -\frac{1}{2}c\omega^2 y_0^2. \tag{4}$$

To summarize, equation (3) gives the average extracted power predicted by the present damping model, while equation (4) gives the average extracted power measured by Vikestad [36]. Ideally, these should be equal for all oscillation amplitudes. The method of least squares is used to find the values of a_0 and a_1 that minimize the sum of the square differences, resulting in $a_0 = 0.31$ and $a_1 = 0.89$. The power loss based on Vikestad's measurements and the present model is shown in figure 2. The results from the old damping model [29] is also shown, and it is seen that the new model provides much better agreement with the experiment. The value of a_0 and a_1 reported here is expected to be valid in other cases as well, provided that the flow regime is the same. The Reynolds number for the oscillating cylinder in still-water can be expressed as $\dot{y}_{\max}D/\nu$, where $\dot{y}_{\max}$ is the maximum cylinder velocity and ν is the kinematic viscosity. In the experiments [36], this was between 0 and 10 000 approximately. The amplitude ratio y_0/D was varied between 0 and 0.6 (see figure 2). For significantly larger vibration amplitudes, the present damping model will not be accurate.

To investigate the performance when $U \neq 0$, the model is used to simulate the hydrodynamic damping force on a cylinder oscillating in the cross-flow direction with frequency f at a reduced velocity, $U_r = U/(fD)$ of 3 and 10, which is below and above the positive excitation zone respectively. The resulting lift coefficient in phase with cylinder velocity is compared to forced vibration experiments by Morse and Williamson [12] in figure 3. It is seen that the agreement between the model and experiments is very good, which is somewhat surprising due to the absence of the incoming flow velocity in the model. It is also seen that the new formulation gives a much better description of the hydrodynamic damping than the old model [29]. Based on the results in figures 2 and 3 it is concluded that equation (1) combined with $C_{d,y} = 0.31 + 0.89y_0/D$ yields a good approximation of the hydrodynamic damping in still water as well as for cross-flow motion at low and high reduced velocities. It should be emphasized that the comparison shown in figure 3 is for non-lock-in cases only, meaning that for the reduced velocities shown, the vortex shedding is uncorrelated with the motion. These cases where selected specifically because of this, such that the damping model can be tested separately. For lock-in cases, the vortex shedding force (called excitation force in the present paper) must be taken into account.

The cross-flow excitation and added mass force is modeled according to Thorsen et al. [31], and the total cross-flow hydrodynamic force (i.e. the final hydrodynamic force model), is thereby given as:

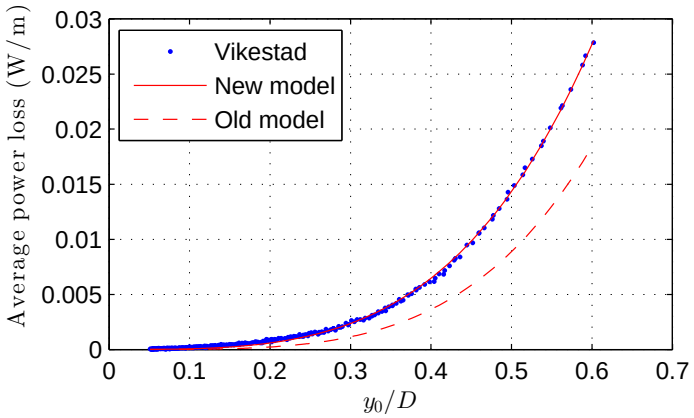

Figure 2: Average power loss (in Watts per unit length of cylinder) due to hydrodynamic damping in still water as a function of non-dimensional vibration amplitude y_0/D. The dots represent the measurements from still-water decay tests (performed by Vikestad [36]) and the solid line is the present model. The power loss predicted by the old damping model [29] is shown with a dashed line.

$$F_y = \underbrace{\frac{1}{2}\rho D U^2 C_v \cos\phi_{\mathrm{exc},y}}_{\text{excitation}} - \underbrace{\frac{1}{2}\rho D C_{d,y}|\dot{y}|\dot{y}}_{\text{damping}} - \underbrace{\rho\frac{\pi D^2}{4}\ddot{y}}_{\text{added mass}}. \tag{5}$$

It is assumed that the potential theory added mass term can be used to describe the force due to cylinder acceleration. However, the *total* hydrodynamic inertia force is the potential theory added mass plus the part of the excitation force which is in phase with the cylinder acceleration. The latter generally depends on the vibration frequency and amplitude, and the effective added mass is therefore not constant. The magnitude of the excitation force is determined by the dimensionless coefficient C_v, which is a function of the cross-flow amplitude ratio, y_0/D. The fluctuations of the excitation force due to the vortex shedding process is taken into account through the time variability of the phase $\phi_{\mathrm{exc},y}$, which is coupled to the motion of the cylinder through the equation:

$$\frac{d\phi_{\mathrm{exc},y}}{dt} = H(\phi_{\dot{y}} - \phi_{\mathrm{exc},y}). \tag{6}$$

Here, $\phi_{\dot{y}}$ is the instantaneous phase of the cylinder's cross-flow velocity, and H is the instantaneous angular frequency of the excitation force, which is a function of $\phi_{\dot{y}} - \phi_{\mathrm{exc},y}$, i.e. the phase difference between the velocity and the excitation force itself. Equation

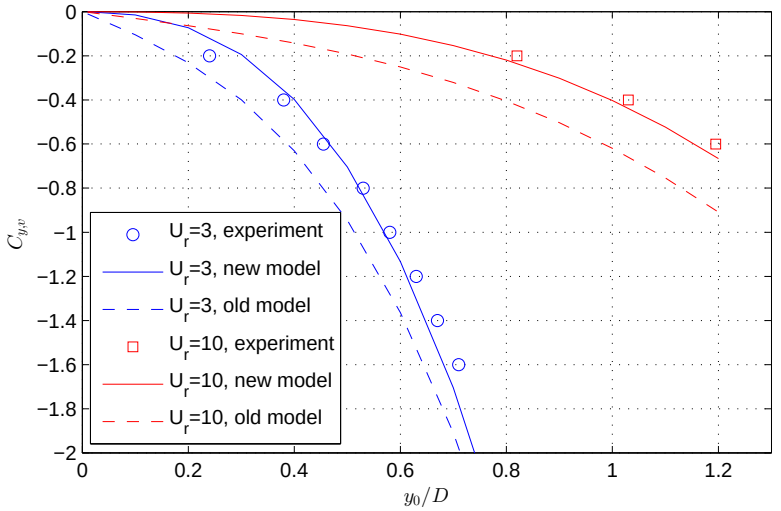

Figure 3: Lift coefficient in phase with cylinder velocity as a function of y_0/D. The circles and squares are from experiments by Morse and Williamson [12], with $U_r = 3$ and $U_r = 10$ respectively. The corresponding values predicted by the present damping model are shown with solid lines, and the results obtained with the old damping model are shown with dashed lines.

(6) allows the frequency of the force to vary such that the force may synchronize with the velocity of the cylinder, provided that the frequency of motion is within the right range. The function H was first given by Thorsen et al. [29]. The database from the VIV analysis tool VIVANA [25] was used to find this function, but data from forced vibration experiments could also have been used. The function was slightly adjusted for increased performance [31], and this version is also used here. It is shown in figure 4 in non-dimensional frequency form, $\hat{f} = HD/(2\pi U)$. It is seen that the non-dimensional frequency of the excitation force may vary between approximately 0.1 and 0.26, which means that synchronization between the excitation force and motion can occur only if the frequency of motion is within this range.

2.2 Structural model

The elastic cylinder is modeled using finite elements. An example structural model and coordinate system definition is shown in figure 5. Only cross-flow (y-direction) displacements are considered, and the structure is modeled using linear beam elements based on classical beam theory. The stiffening effect from tension is included, such that the element stiffness matrix consists of an elastic (bending) and an initial stress (tension) contribution. The element mass matrix is established using a consistent mass formulation, including

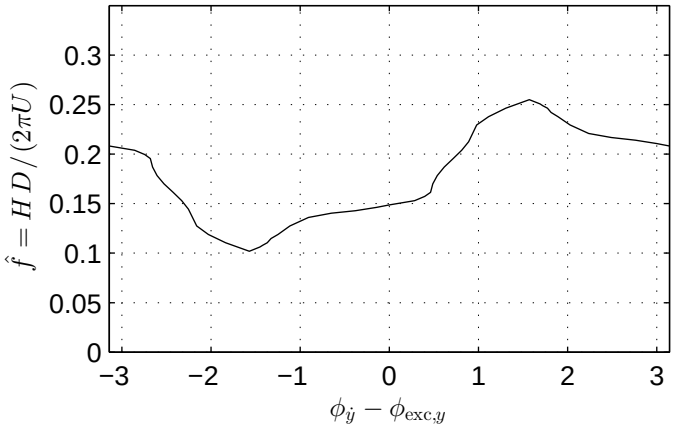

Figure 4: Non-dimensional frequency of the excitation force as a function of the phase difference between the cross-flow velocity and the excitation force.

both the structural and the hydrodynamic added mass term $0.25\rho\pi D^2$ (see equation 5). Assembling the element contributions, the equation of motion for the structural system reads

$$\mathbf{M}\ddot{\mathbf{r}} + \mathbf{C}\dot{\mathbf{r}} + \mathbf{K}\mathbf{r} = \mathbf{F} \tag{7}$$

where $\mathbf{M}$ is the mass, $\mathbf{C}$ is (structural) damping, $\mathbf{K}$ is stiffness, $\mathbf{F}$ is the hydrodynamic force vector and $\mathbf{r}$ is the structural degrees of freedom. The vector $\mathbf{F}$ is established by evaluating the hydrodynamic force per unit length at the individual nodes (as described in section 2.1, see equation (5)). Note that the added mass term is included in the mass matrix, and not in $\mathbf{F}$. As the hydrodynamic force at any node is calculated based on the local flow velocity and the velocity and acceleration of the node, there is no hydrodynamic coupling in the longitudinal direction. This corresponds to a strip-theory approach, where the 3-dimensional effects are determined by the motion of the structure. Equation (7) is solved step by step in time domain using the Newmark-β method with coefficients $\gamma = 0.5$ and $\beta = 0.25$ [37]. This choice of parameters leads to zero numerical damping and constant average acceleration during each time step. The time step length corresponds to 100 steps per oscillation cycle, based on the expected vibration frequency. This is found to be sufficient, as increasing the resolution to 200 steps per cycle gives a change of less than 0.1 % in the dominating frequency and root-mean-square of the displacement. The number of finite elements is 100 for the simulations presented in section 3 and 30 in section 4. Convergence is checked by doubling the number of elements, which gives a change of less than 0.1 % in the dominating frequency and the root-mean-square of the

displacement.

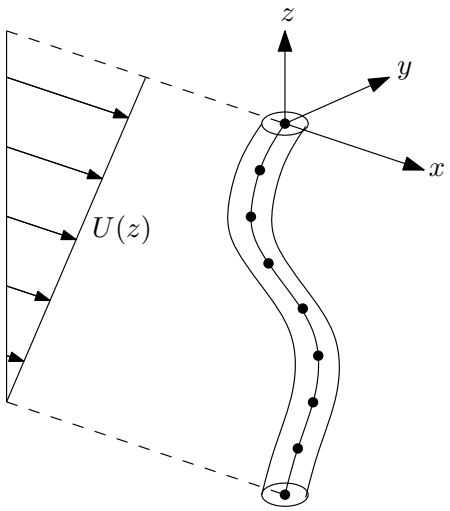

Figure 5: Example of finite element model showing the coordinate system definition and incoming current.

2.3 Amplitude estimation

The hydrodynamic excitation and damping forces depend on the amplitude of vibration. This will generally vary along the structure and in time, and must be extracted from the simulated response as the solution progresses. The vibration amplitude at any node is initially calculated as:

$$y_0 = \frac{1}{2}\int_{t_1}^{t_2} |\dot{y}| dt, \tag{8}$$

where $\dot{y}$ is the cross-flow velocity of the node, and t_1 and t_2 is the time of the two previous zero-crossings of $\dot{y}$. The rationale behind equation (8) is that the cylinder travels a distance of $2y_0$ in the cross-flow direction between each zero-crossing of $\dot{y}$, assuming that the vibration signal is narrow-banded. A problem with this method is that the amplitude (at a given node) is not a smooth function of time. It can only be updated when a zero-crossing of the velocity occurs, and remains constant between zero-crossings. The sudden change occurring when y_0 is updated may in turn cause a spurious impulse load on the structure, as the hydrodynamic forces change. To overcome this numerical problem, a smoothed amplitude y_0^* is calculated according to the following differential equation:

$$\frac{dy_0^*}{dt} = k_a(y_0 - y_0^*), \tag{9}$$

using $y_0^*(0) = 0$. According to equation (9), if y_0^* is different from y_0, then y_0^* will change such that the difference decreases, and y_0^* will thereby converge to y_0 over time. The rate of change is proportional to the difference between y_0 and y_0^* along with a factor, k_a, which determines how rapidly the smoothed amplitude is allowed to change. Hence, y_0^* will be a smoothed version of y_0. The smoothed amplitude is then used to evaluate the hydrodynamic coefficients, ensuring that the resulting forces along the structure are smooth, continuous functions of time. In this paper, the value of k_a is taken as $0.1/\Delta t$, where Δt is the time step length. This means that the change in y_0^* over one time step is $\Delta y_0^* = (dy_0^*/dt)\Delta t = 0.1(y_0 - y_0^*)$, which was found to be reasonable by numerical experimentation. When selecting a value for k_a one must keep in mind that the amplitude should not be smoothed too much (such that variations are missed), or too little (such that spurious impulse loads occur).

3 Optimizing hydrodynamic excitation force model

In the present hydrodynamic force model, the magnitude of the cross-flow excitation force depends on the dimensionless coefficient C_v, which is a function of the amplitude ratio y_0/D. In the previous papers [29–31], this function was found using the excitation coefficient from the VIVANA database [25]. However, a better approach may be to directly utilize data from experiments. Therefore, the strategy used here is to simulate the vortex-induced response of an elastic cylinder in a series of experiments and modify $C_v(y_0/D)$ until the agreement between the simulations and experiments is as good as possible. For this purpose, data from the Norwegian Deepwater Programme (NDP) Riser High Mode VIV tests [16, 38] is utilized. In this experimental campaign, a 38 meter long riser model was towed through the Ocean Basin Laboratory at the Norwegian Marine Technology Research Institute (MARINTEK). The riser was tested in both uniform and sheared flow, where the effective current velocity increased linearly from zero to maximum along the riser length. The maximum velocity was varied from 0.3 m/s to 2.4 m/s. The physical properties of the riser model are given in table 1. The riser was equipped with strain gauges measuring the cross-flow strain at 24 locations along the model, and these measurements are used for comparison with the present model. The riser was connected to a towing rig with universal joints in both ends, which allows for free rotation. Accordingly, the boundary conditions of the present model are zero translation and free rotation in both ends.

It is important to recall that the actual vortex-induced response consists of a fundamental frequency component, as well as higher harmonic frequencies [19, 39]. As the model includes only the fundamental frequency response, the higher harmonic components in

Table 1: Physical properties of the NDP riser

Length (L)	38 m
Diameter (D)	0.027 m
Mean tension (T)	4000-6000 N
Bending stiffness (EI)	599 Nm^2
Mass per unit length (m)	0.933 kg/m

the experimental data are removed by filtering, such that the simulations are compared to the measured fundamental frequency response only. An example of the measured cross-flow strain before and after removing the higher harmonic components is shown in figure 6. To quantify the prediction error for a given measurement, the maximum value of the root-mean-square (r.m.s.) of strain in each test is used. Thereby, the prediction error for a specific test is

$$e_i = \hat{\sigma}_{\max,i} - \sigma_{\max,i}, \tag{10}$$

where $\sigma_{\max,i}$ is the maximum r.m.s. of the fundamental frequency strain in test number i, and $\hat{\sigma}_{\max,i}$ is the corresponding prediction.

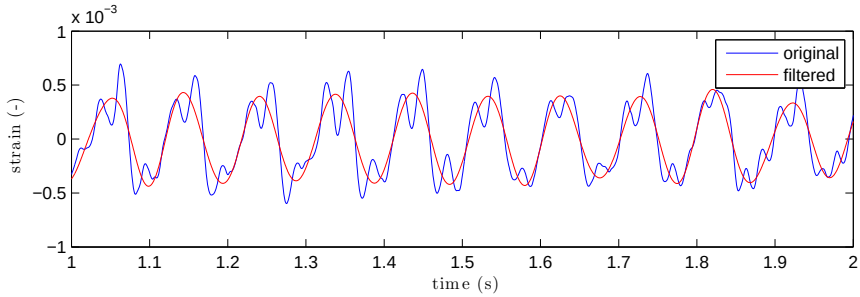

Figure 6: Example of measured strain before and after removal of higher harmonic components. The time series is from a uniform flow test with $U = 2.0$ m/s, measured at the position of maximum r.m.s. strain.

To find the best possible $C_v(y_0/D)$, the curve is parametrized such that the problem is reduced to finding the optimal set of parameters. The parameters are the coordinates of the maximum point (p_1) and the zero-crossing point (p_2). Between the specified points, the curve is described by second order polynomials. It is also assumed that $C_v(y_0/D)$ is either positive or zero (not negative). An optimization task may then be formulated, where the goal is to minimize the sum of the square errors, $\sum e_i^2$. This is done by simulating all the NDP test cases (22 uniform and 22 sheared flow tests), and systematically varying

the coordinates of p_1 and p_2 until the minimum error sum is found. The MATLAB implementation of the Nelder-Mead simplex method [40] is used to search for the optimal parameters. The curve which is found to provide the minimum prediction error is shown in figure 7. This curve reflects the strength of the vortex shedding force, which generally depends on the Reynolds number, and the optimized curve presented here is therefore only valid in the range of Re which was seen in the NDP experiments, i.e. between 8000 and 65 000. The predicted maximum r.m.s. of the cross-flow strain in the NDP tests obtained using the optimized $C_v(y_0/D)$ is compared to the measurements in figure 8a (uniform flow) and 8b (sheared flow). The maximum r.m.s. of the measured total strain (including higher harmonics) is also shown for comparison.

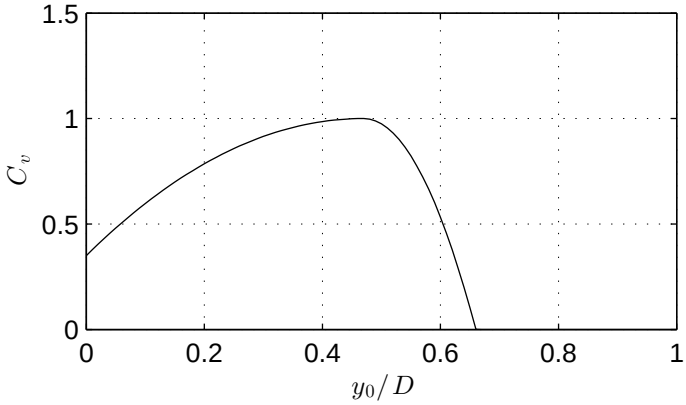

Figure 7: Optimal C_v as a function of y_0/D.

With reference to figures 8a and 8b it is evident that the model is not perfect, even though an optimal excitation curve has been applied. The optimization of $C_v(y_0/D)$ was performed considering 44 cases simultaneously, but the resulting curve is not necessarily the best for each case. This suggests that the underlying physical process may be viewed as stochastic, such that the optimal excitation curve found here represents an average, or expected value of $C_v(y_0/D)$. However, considering the simple formulation of the model and the complicated problem at hand, the overall agreement is satisfactory. To illustrate more thoroughly how the model performs, the r.m.s. of the cross-flow strain along the riser is shown for three selected cases in figure 9 (uniform flow) and 10 (sheared flow). The spectrum of the measured and simulated strain (at the location of the maximum r.m.s. of strain) is also shown. It is seen that the measurements contain higher harmonics around 3 times the fundamental frequency. These are not included in the model, but the fundamental frequency is predicted with good accuracy. The lack of higher harmonics in the model means that the total strain ranges are under-estimated, which is seen in figure 9 and 10. As a result of this, safety factors must be applied if e.g. fatigue damage is to be predicted. The

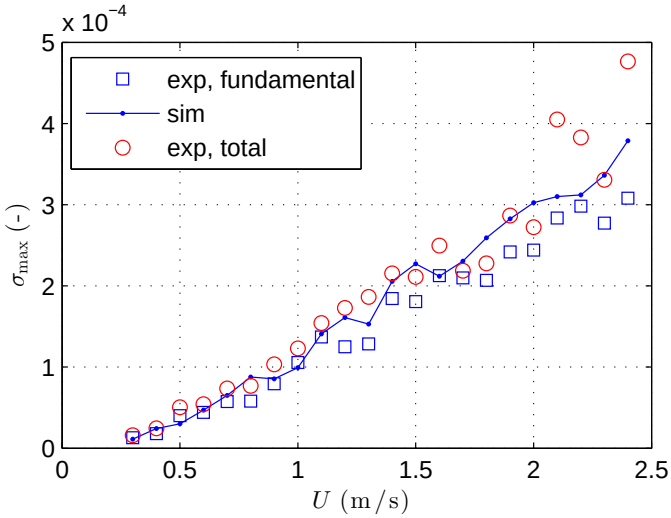

(a) Uniform flow

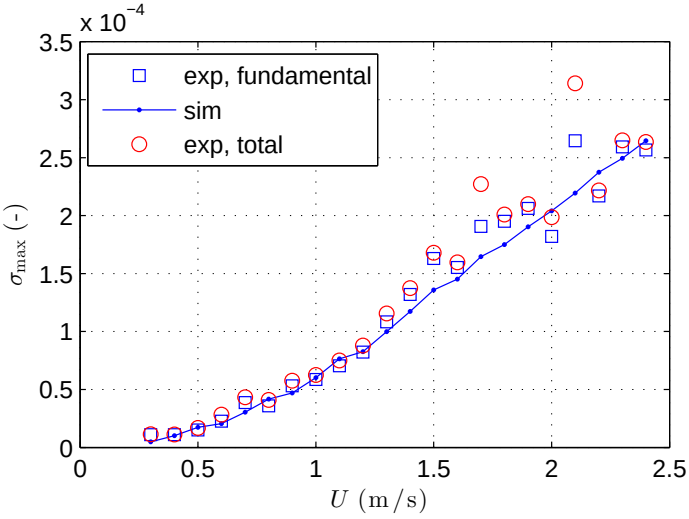

(b) Sheared flow

Figure 8: Maximum r.m.s. of cross-flow strain for all NDP cases, shown as a function of the incoming flow velocity (for shear flow, U is the maximum flow velocity). The results based on measured total strain are shown as circles and those based on fundamental frequency strain as squares. The simulated results are shown as dots connected with a solid line.

ratio between the fundamental frequency fatigue damage and the total damage has been discussed in detail by Thorsen et al. [31]. It is also seen that the predicted r.m.s. of strain is not always accurate at every point along the riser. VIV of risers is chaotic [41], which means it is impossible to predict the motion at every point with absolute certainty. However, quantities such as the average or maximum strain along the whole riser are easier to predict. For example, in the three uniform flow cases shown in figure 9, the maximum r.m.s. strain is 75 %, 94 % and 124 % of the corresponding test result (comparing with the fundamental frequency strain), and this level of accuracy is comparable to existing VIV analysis tools [42]. An interesting effect is that even in the uniform flow cases, where the boundary conditions and the incoming flow is symmetric, the VIV response is not symmetric. Typically, the strain is larger in one end than the other, which is also seen in the simulations.

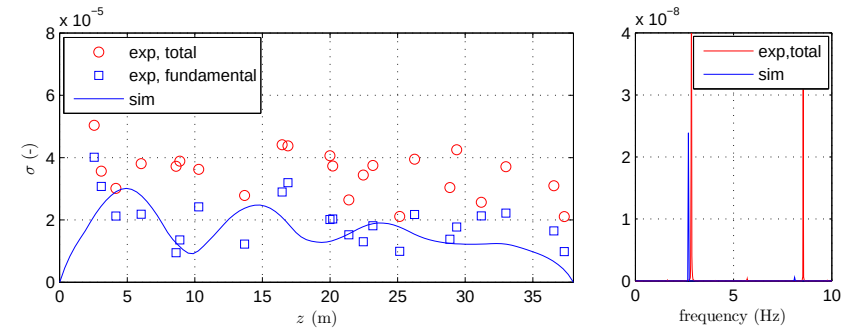

(a) $U = 0.5$ m/s

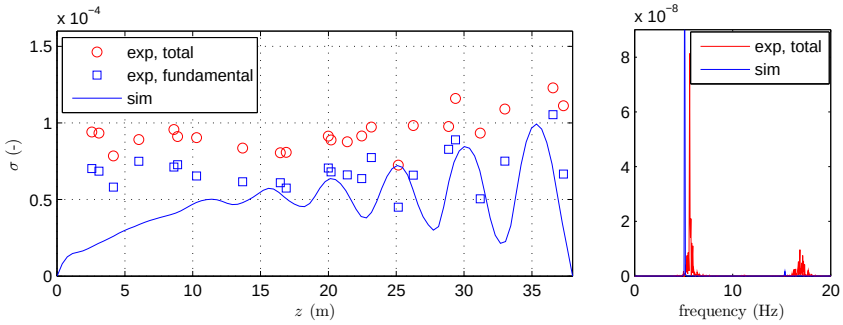

(b) $U = 1.0$ m/s

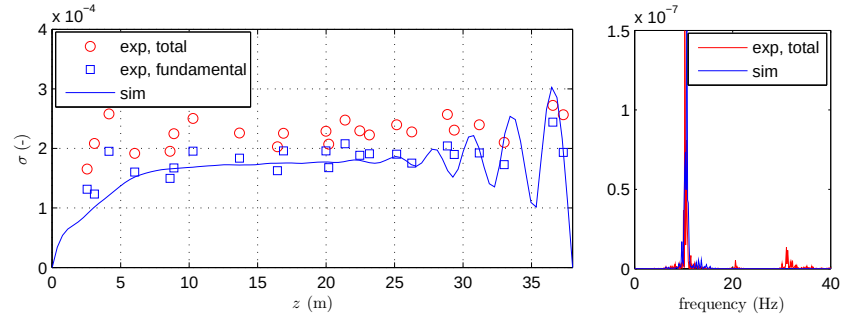

(c) $U = 2.0$ m/s

Figure 9: Uniform flow results: To the left is the r.m.s. of cross-flow strain along the riser for three different cases. Red circles: total measured strain, blue squares: measured fundamental frequency strain, solid line: strain from simulation. To the right is the power spectrum of cross-flow strain at the location of maximum r.m.s. strain. Red is measured and blue is simulated. Note that the location of maximum strain is not necessarily the same in simulation and experiment.

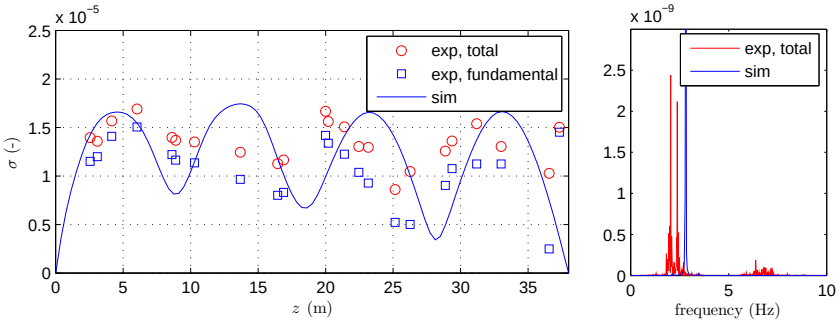

(a) $U = 0.5$ m/s

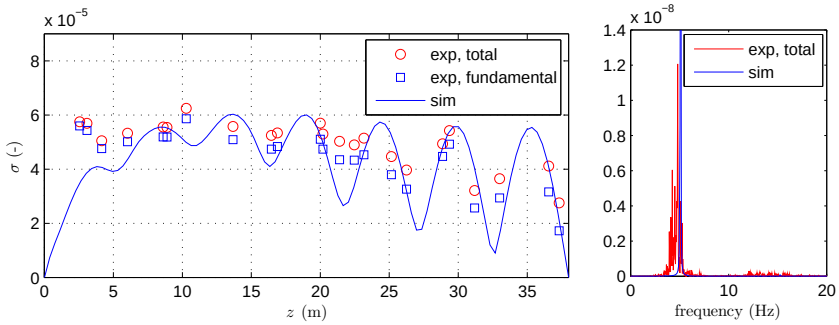

(b) $U = 1.0$ m/s

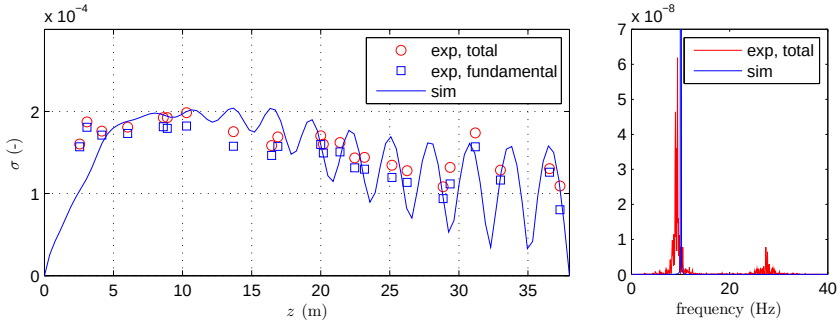

(c) $U = 2.0$ m/s

Figure 10: Sheared flow results: To the left is the r.m.s. of cross-flow strain along the riser for three different cases. Red circles: total measured strain, blue squares: measured fundamental frequency strain, solid line: strain from simulation. To the right is the power spectrum of cross-flow strain at the location of maximum r.m.s. strain. Red is measured and blue is simulated. Note that the location of maximum strain is not necessarily the same in simulation and experiment.

4 Flexible cylinder in oscillating flow

4.1 Overview

An experimental investigation of VIV in oscillating flow was performed by Fu et al. [20]. These experiments were conducted in the ocean basin at Shanghai Jiao Tong University (SJTU), and consisted of a flexible cylinder being towed horizontally with a prescribed oscillating motion. The oscillation amplitude and period was varied, such that the cylinder experienced oscillating flow with different combinations of KC numbers and maximum reduced velocities, $U_{r,\max}$. Denoting the amplitude of the prescribed oscillating motion as A_m, the KC number may be defined as

$$\mathrm{KC} = \frac{U_{\max} T}{D} = \frac{2\pi A_m}{D}, \tag{11}$$

where $U_{\max}$ is the maximum velocity of the incoming oscillating flow and T is the corresponding period. The maximum reduced velocity may then be expressed as

$$U_{r,\max} = \frac{U_{\max}}{f_1 D} = \frac{2\pi A_m}{T f_1 D} = \frac{\mathrm{KC}}{T f_1}, \tag{12}$$

where f_1 is the lowest natural frequency of the cylinder in still water. Key properties of the test cylinder are given in table 2, and a simplified overview of the experimental set up is shown in figure 11. At both ends, the cylinder was attached to universal joints, allowing free rotation around the x- and y-axis (ref. figure 5). A large number of cases were included in the experiments, with KC numbers between 26 and 178 and maximum reduced velocities between 4 and 7.9. The model was equipped with strain gauges measuring the cross-flow strain at 7 equally spaced positions along the length. As only lower modes (mode 1-2) were excited, the number of measuring points are sufficient to perform modal reconstruction of the displacements, as described by e.g. Lie and Kaasen [43]. The Reynolds number in these experiments was close to 10^4, which is within the range of the NDP tests used to optimize the simulation model.

4.2 Simulation and comparison with experiment

To test how the present simulation model performs at predicting VIV in oscillating flows, the model is used to recreate the SJTU experiments. Some simplifications are introduced: The small displacements due to mean drag and weight are neglected (the actual displacement due to mean drag is estimated to less than 1% of the cylinder length). Furthermore, the oscillatory motion is transformed to an oscillating incoming current, meaning that the boundary conditions of the model is zero displacement (but free rotation) at both ends. This is possible because the inertial forces associated with the oscillatory motion are small

Table 2: Physical properties of the test cylinder

Length, L	4 m
Diameter, D	0.024 m
Mass per unit length, m	0.69 kg/m
Mass ratio, $m/(0.25\rho\pi D^2)$	1.53
Bending stiffness, EI	10.5 Nm^2
Pretension, T	500 N
Structural damping (in air)	1.5 %

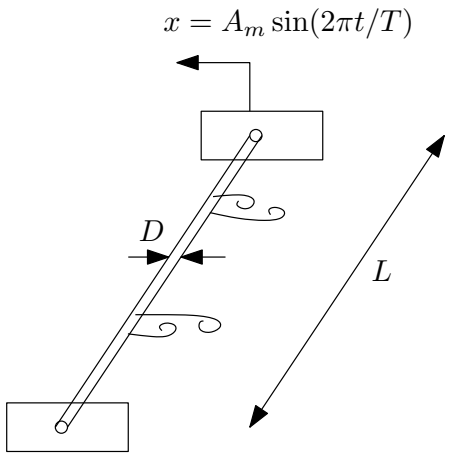

Figure 11: Simplified overview of the SJTU experimental set up.

compared to the vortex-induced forces. In addition, the small fluctuations in tension are neglected and a constant $T = 500$ N is used. Recall that the model was tuned to stationary flow measurements, and no changes in the hydrodynamic modeling are introduced. The results will therefore clearly show whether or not it is reasonable to predict VIV in oscillating flow based on data from stationary flow VIV.

To investigate the model performance at different KC numbers and reduced velocities, four cases are considered as shown in table 3. In Case 1 and 2 the KC number is low, meaning the cylinder travels a relatively short distance in one direction, before it turns back into its own wake. Hence it is expected that previously shed vortices are still present in the wake, which will affect the lift force on the cylinder. Also, the number of generated vortices per flow period is low. In case 3 and 4 the KC number is increased to 178. In these cases, the cylinder travels significantly longer between each flow reversal, meaning the situation is more similar to a steady flow. In addition, different values of the reduced velocity are considered. The higher value ($U_r = 6.5$) corresponds to the point where

the maximum vibration amplitude is expected, based on stationary flow observations (see e.g. Sumer and Fredsøe [44]). The lower value is included to see how the model performs when the lock-in situation is less perfect.

Table 3: Test cases used for comparison.

Case No.	A_m	T	KC	$U_{r,\max}$
1	0.12 m	2.5 s	31.4	4.7
2	0.12 m	1.8 s	31.4	6.5
3	0.68 m	16.5 s	178	4.0
4	0.68 m	10.2 s	178	6.5

The simulation results are shown in figures 12-15 together with the corresponding experimental results. Starting with case 1, it is seen that the cylinder vibrates at mode 1, i.e. one half-wave along the cylinder span. The measured response consists mainly of a single dominating frequency component at approximately 2.5 Hz, but lower frequencies are also present, causing the overall response to appear slightly irregular. A possible explanation for these irregularities is that previously shed vortices are still present in the incoming flow, causing disturbances in the lift force. The simulated response is more regular, but the dominating frequency and amplitude is well captured. Due to the low KC number, there is not much time for the vibration amplitude to diminish between periods with high flow velocity. Therefore, the response appears almost stationary, which is also seen in the simulation.

For case 2, the response is similar to case 1, but the amplitude is larger as a result of the increased reduced velocity. As the reduced velocity is close to the ideal value for synchronization between the vortex shedding and the natural frequency of the structure, the measured response is more regular than in case 1, and contains essentially only a single frequency component around 2.8 Hz. This is also seen in the simulations, which reproduces both the amplitude and frequency with good accuracy. Again, the response is almost stationary in time, as the flow velocity increases to a level sufficiently high for positive power transfer between the fluid and structure, before the vibration amplitude has decreased notably.

Moving on to case 3, the effect of increasing the KC number is clearly illustrated. The flow velocity now changes slowly compared to the vibration frequency, causing the amplitude to decay significantly during periods of low incoming flow velocity. This is seen both in the experiment and the simulation. The frequency and amplitude are rather accurately predicted, although the amplitude is slightly larger than measured. The building-up and dying-out effect is realistically reproduced in the simulations.

In case 4, the KC number is the same as for case 3, but the maximum reduced velocity is closer to the point of maximum vibration amplitude. This means the incoming flow velocity is large enough to cause positive excitation a larger fraction of the time. It is

seen that as the flow velocity increases, the vibration amplitude builds up rapidly, before a maximum value is reached. The vibration continues at this constant amplitude for some time, before the flow velocity reduces to a level where vortex shedding no longer can excite the structure. The ongoing process of "building-up", "lock-in" and "dying out" was described by Fu et al. [20], and is clearly seen in both the experiment and simulation. An interesting feature is that the amplitude builds up faster than it decays, which is also captured by the model.

To summarize the comparison in figures 12-15, it has been shown that the model is able to predict cross-flow VIV of a flexible cylinder for KC numbers 31 and 178. For $\mathrm{KC} = 31$, the number of vortex shedding periods between flow reversals is low, approximately 3. Hence, one would expect the incoming flow to be significantly disturbed by previously shed vortices. It is therefore somewhat surprising that the simulations are seen to reproduce the observed behavior quite accurately, even though the hydrodynamic force model was initially adjusted according to data from stationary flow VIV experiments. This suggests that the effect of the disturbed incoming flow is small (at least for the KC numbers considered here), and that the relevant hydrodynamic forces can be found using the same mathematical description as in stationary flows, if the time variability of the incoming flow velocity is taken properly into account.

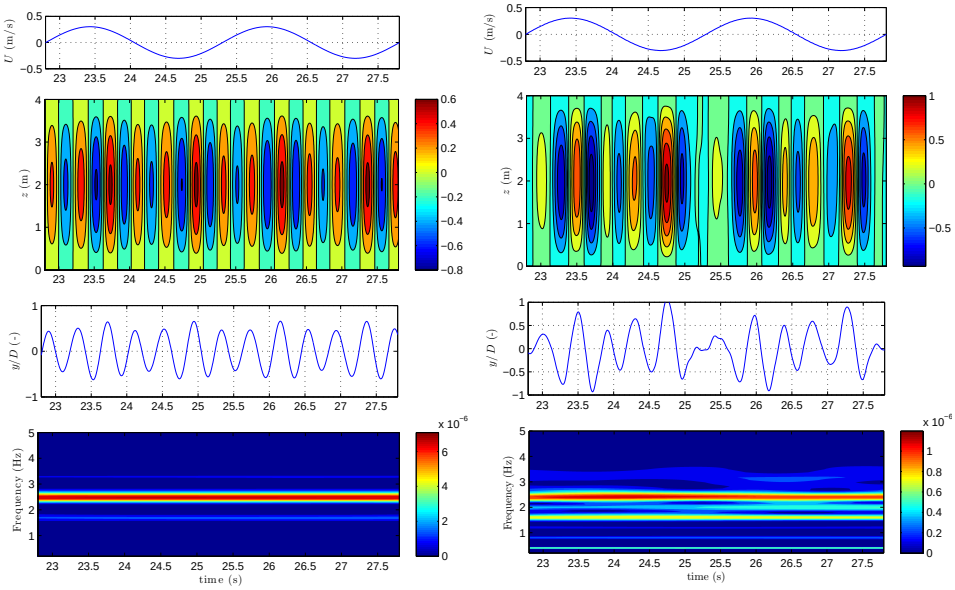

(a) Simulation (b) Experiment

Figure 12: Case 1 results. The top row shows the incoming current velocity U as a function of time. The row below shows the normalized cross-flow displacement y/D in time and space. The next row shows y/D at the mid-span, i.e. at $z = 2$ m. At the bottom is a wavelet contour plot of the vibration energy at the mid-span, showing the frequency content over time.

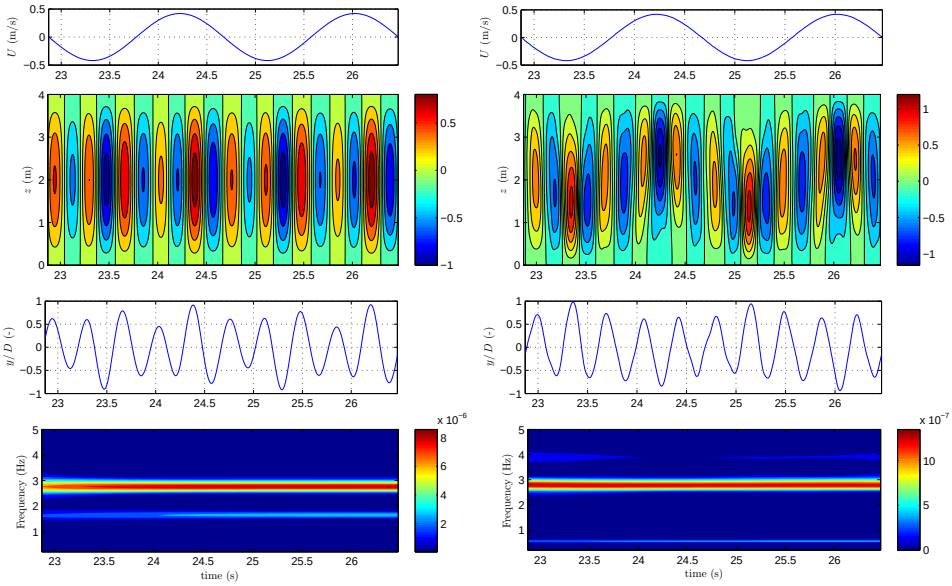

(a) Simulation (b) Experiment

Figure 13: Case 2 results. The top row shows the incoming current velocity U as a function of time. The row below shows the normalized cross-flow displacement y/D in time and space. The next row shows y/D at the mid-span, i.e. at $z = 2$ m. At the bottom is a wavelet contour plot of the vibration energy at the mid-span, showing the frequency content over time.

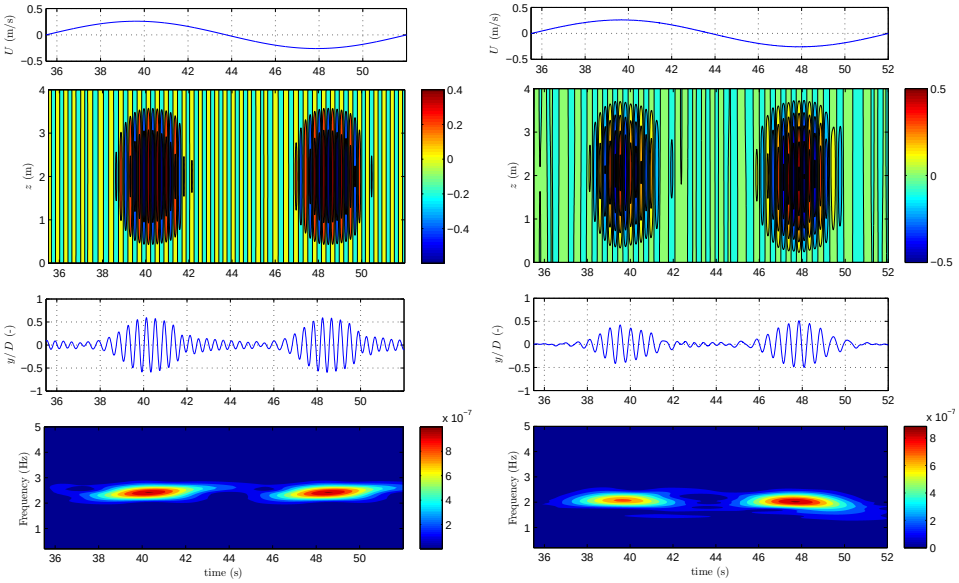

(a) Simulation (b) Experiment

Figure 14: Case 3 results. The top row shows the incoming current velocity U as a function of time. The row below shows the normalized cross-flow displacement y/D in time and space. The next row shows y/D at the mid-span, i.e. at $z = 2$ m. At the bottom is a wavelet contour plot of the vibration energy at the mid-span, showing the frequency content over time.

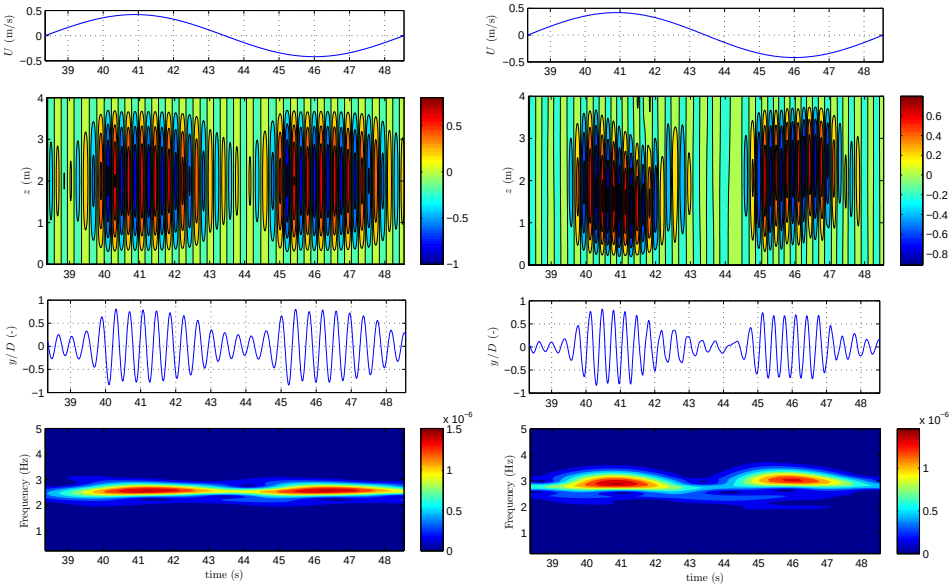

(a) Simulation (b) Experiment

Figure 15: Case 4 results. The top row shows the incoming current velocity U as a function of time. The row below shows the normalized cross-flow displacement y/D in time and space. The next row shows y/D at the mid-span, i.e. at $z = 2$ m. At the bottom is a wavelet contour plot of the vibration energy at the mid-span, showing the frequency content over time.

4.3 Effect of reduced velocity and mass ratio

The comparison in the previous section indicates that the hydrodynamic force model includes the most relevant physical effects, and it is therefore fair to assume that this remains true when external parameters such as incoming flow velocity and structural mass are changed. In the experiments by Fu et al. [20], the magnitude of the relative flow velocity was such that mainly the first natural mode of the structure was excited by vortex shedding (some participation of mode 2 was also seen). Increasing the velocity further could reveal some interesting phenomena. For instance, if the maximum flow velocity corresponds to excitation of a high mode, then a number of lower modes may be excited before the maximum flow velocity is reached. In such cases it is not clear what the response will look like, and the present model is utilized to investigate this.

4.3.1 Example 1: High reduced velocity

The KC number and other parameters are the same as in the previously shown case 3 and 4, except the maximum reduced velocity, which is increased to $U_{r,\max} = 32$ to excite higher modes of vibration. Before moving on to the simulation results, it is illustrated how the expected excitation frequency varies with time, due to the oscillating flow velocity. A simple way to estimate the excitation frequency would be to assume a constant non-dimensional frequency, and according to experiments [45], the energy transfer is largest around $\hat{f} = fD/U \approx 0.17$. Hence, the expected vibration frequency can be found from the instantaneous flow velocity as $f(t) = 0.17|U(t)|/D$. This is shown in figure 16, where the 5 first natural frequencies of the structure (in still water) are shown with dashed lines. As the flow velocity increases, it is seen that the expected vibration frequency passes the three lowest natural frequencies, and finally exceeds the fourth before it starts reducing. Hence one would expect the response to consist of modes 1-4.

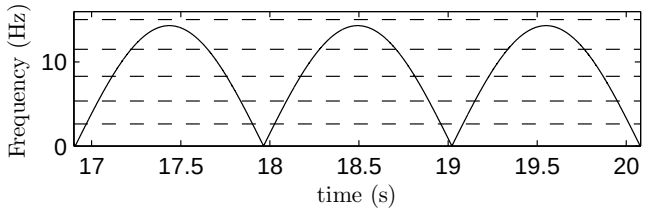

Figure 16: Expected vibration frequency, $f = 0.17|U|/D$, as a function of time (solid line). The dashed lines are the first 5 natural frequencies of the cylinder.

The simulation results are shown in figure 17. The complex pattern resulting from the continuously changing mode and frequency is easily seen. The modal weight factors $w_n(t)$ for the first 5 modes are also shown, giving a clearer picture of how the dominating

mode varies with time. The modal weights are related to the cross-flow displacement through the following equation:

$$y(z,t) = \sum_{n=1}^{\infty} w_n(t)\psi_n(z) = \sum_{n=1}^{\infty} w_n(t)\sin(n\pi z/L). \tag{13}$$

As seen in figure 17, mode 1 dominates in periods of low flow velocity. When the velocity increases, a transition to mode 3 is seen, before mode 4 finally takes over. When the velocity has decreased sufficiently, mode 3 and 4 dies out, and mode 1 starts to dominate once more. It is also seen that each oscillation cycle (from one flow reversal to the next) is slightly different from the previous, meaning the response is not periodic. Because the duration of one flow cycle is short relative to the first natural frequency, the response at mode 1 does not have time to decay significantly, even when the flow velocity is too high to excite this mode. Hence, the response in periods with high flow velocity is a superposition of the previously activated mode 1 together with mode 3 or 4 which is currently being excited. This causes the maximum cross-flow displacement to become somewhat larger than in the previously considered cases containing only mode 1. It is somewhat surprising that mode 2 never dominates the response, but with reference to the modal weights shown in figure 17, it is seen that mode 2 is clearly present. The reason why mode 2 is weaker than the others may be related to the time it takes for the mode to change, and also that the higher modes (3 and 4) are associated with a higher flow velocity, and are thus more energetic. As the flow velocity increases, there is only a short time interval where the expected vibration frequency is close to the second natural frequency, and if the structure does not change from mode 1 to 2 inside this interval, it is more likely to jump to mode 3. In addition, the excitation force gets stronger when the flow velocity increases, hence favoring mode 3 over mode 2.

4.3.2 Example 2: High reduced velocity combined with high mass ratio

The mass ratio $m^* = m/(0.25\rho\pi D^2)$ of the cylinder studied by Fu et al. [20] was 1.53. As mass ratio is identified as one of the dimensionless parameters important to the VIV response of cylinders in stationary flow [3], it is of interest to investigate how this parameter affects VIV in oscillating flows. With this in mind, another simulation is performed, where the mass of the cylinder is increased by a factor of 5. This gives a mass ratio of 7.65, corresponding to a solid steel cylinder in water. The KC number and maximum reduced velocity are kept the same as in example 1, meaning that the flow may still potentially excite modes 1-4, as illustrated in figure 16 (although the numerical values of the frequencies are changed due to the increased mass).

The simulation results are shown in figure 18. In comparison to the low mass ratio case, the response appears less complicated. The cross-flow displacement is almost single-moded with mode 3 clearly dominating. The amplitude varies only slightly, with

maximum values occurring around the time of maximum flow velocity, and minimum values when U is close to zero. The frequency content as seen in the wavelet contour plot is nearly constant in time, with the energy concentrated around 4.7 Hz, which is close to the 3rd natural frequency. The maximum vibration amplitude is smaller than in the previous example, and the maximum y/D is approximately 0.7. These results, and particularly the differences between example 1 and 2 can be qualitatively explained as follows. Due to the increased mass and inertia, the cylinder is more resistant to change in the vibration state, and therefore continues at the same mode and frequency even when this is no longer being excited by vortex shedding. Furthermore, as the vibration frequency is almost constant, there will be periods of time when the vortex shedding is unable to synchronize with the cylinder motion, and the energy transfer from fluid to structure will hence be reduced compared to example 1. This explains why the maximum vibration amplitude is smaller for the high mass ratio case.

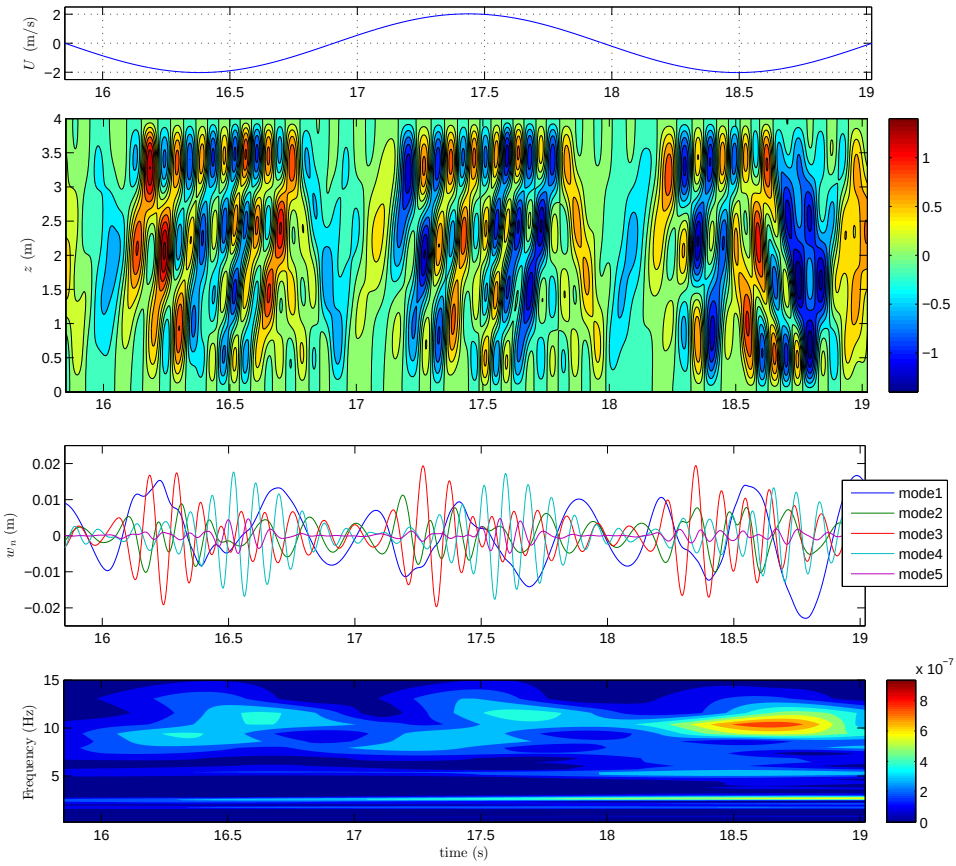

Figure 17: Simulation results for example 1. At the top: incoming flow velocity U as a function of time. Below is a contour plot of the normalized cross-flow displacement y/D in time and space. The next figure shows the modal weight factors, $w_n(t)$, for mode 1 to 5. At the bottom is the wavelet contour plot of the energy-density of the cross-flow displacement at $z = 0.5$ m.

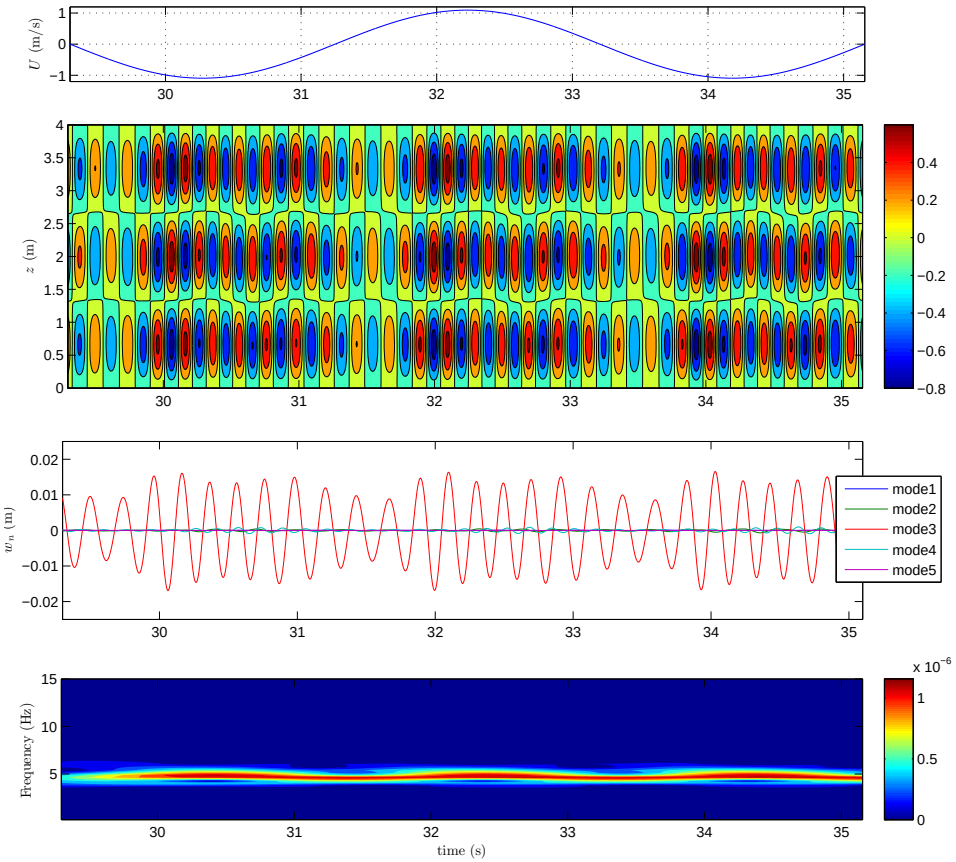

Figure 18: Simulation results for example 2. At the top: incoming flow velocity U as a function of time. Below is a contour plot of the normalized cross-flow displacement y/D in time and space. The next figure shows the modal weight factors, $w_n(t)$, for mode 1 to 5. At the bottom is the wavelet contour plot of the energy-density of the cross-flow displacement at $z = 0.5$ m.

5 Conclusions

The hydrodynamic force model developed by Thorsen et al. [29] has been improved by introducing a new damping formulation, with parameters obtained from experimental data. It is demonstrated that the predicted damping corresponds well with actual measurements in still water and for cross-flow oscillations in stationary flow at low and high reduced velocity. Furthermore, the excitation force model is optimized through comparison with a series of tests with a flexible cylinder in uniform and sheared flow. In these tests, the incoming flow was stationary, meaning that no information from VIV in oscillating flow was used to construct the hydrodynamic force model.

The optimized model was used to simulate the cross-flow VIV of an elastic cylinder in oscillating flow at different KC numbers and maximum reduced velocities. Comparison with experiments shows that the model provides realistic results in terms of important characteristics such as frequency content, mode and amplitude of vibration. For high KC numbers, the vibrations continuously build up and die out, which is well captured by the simulations. This indicates that the relevant hydrodynamic forces in oscillating flow can be found from empirical relationships obtained from experiments in stationary flow, at least for the KC numbers considered in this study (31 and 178).

The model was also used to investigate the effect of increasing the maximum reduced velocity and mass ratio of the flexible cylinder. When $U_{r,\max} = 32$ and $m^* = 1.53$, the dominating mode and frequency changes continuously as the vortex shedding excites different natural frequencies depending on the velocity of the incoming flow. This results in the appearance of a complex response pattern. In contrast, when the mass ratio is increased by a factor of 5, the response is almost stationary with a single dominating mode. A possible explanation is that the heavy cylinder is more resistant to change in the vibration state due to the larger inertia.

Acknowledgments

The authors would like to thank Statoil for permission to use the data from the oscillating flow experiments performed at Shanghai Jiao Tong University. We are also very grateful to the Norwegian Deepwater Programme (NDP) Riser and Mooring Project for permission to use the Riser High Mode VIV test data. Finally, we would like to thank Jungao Wang for sharing his experience on VIV in oscillating flows and Jie Wu for providing help with the wavelet analysis.

References

[1] Blevins RD. Flow-Induced Vibration. 2 ed.; Van Nostrand Reinhold; 1990.

[2] Sarpkaya T. A critical review of the intrinsic nature of vortex-induced vibrations. Journal of Fluids and Structures 2004;19(4):389 – 447.

[3] Williamson C, Govardhan R. Vortex-induced vibrations. Annual Review of Fluid Mechanics 2004;36(1):413–455.

[4] Bearman PW. Circular cylinder wakes and vortex-induced vibrations. Journal of Fluids and Structures 2011;27(5–6):648 – 658.

[5] Wu X, Ge F, Hong Y. A review of recent studies on vortex-induced vibrations of long slender cylinders. Journal of Fluids and Structures 2012;28(0):292 – 308.

[6] Feng C. The measurement of vortex induced effects in flow past stationary and oscillating circular and D-section cylinders. Master's thesis; University of British Columbia; 1968.

[7] Vikestad K. Multi-frequency response of a cylinder subjected to vortex shedding and support motions. Ph.D. thesis; Norwegian University of Science and Technology, Department of Marine Technology; Trondheim, Norway; 1998.

[8] Govardhan R, Williamson C. Modes of vortex formation and frequency response of a freely vibrating cylinder. Journal of Fluid Mechanics 2000;420:85–130.

[9] Jauvtis N, Williamson C. The effect of two degrees of freedom on vortex-induced vibration at low mass and damping. Journal of Fluid Mechanics 2004;509(6):23–62.

[10] Sarpkaya T. Fluid forces on oscillating cylinders. NASA STI/Recon Technical Report A 1978;78.

[11] Moe G, Wu ZJ. The lift force on a cylinder vibrating in a current. Journal of Offshore Mechanics and Arctic Engineering 1990;112(4):297–303.

[12] Morse T, Williamson C. Prediction of vortex-induced vibration response by employing controlled motion. Journal of Fluid Mechanics 2009;634:5–39.

[13] Aglen IM, Larsen CM. Importance of added mass for the interaction between IL and CF vibrations of free spanning pipelines. In: ASME 2011 30th International Conference on Ocean, Offshore and Arctic Engineering. American Society of Mechanical Engineers; 2011, p. 545–556.

[14] Yin D, Larsen CM. Forced motion experiments with measured motions from flexible beam tests under uniform and sheared flows. In: ASME 2012 31st International Conference on Ocean, Offshore and Arctic Engineering. American Society of Mechanical Engineers; 2012, p. 573–581.

[15] Chaplin J, Bearman P, Huera Huarte F, Pattenden R. Laboratory measurements of vortex-induced vibrations of a vertical tension riser in a stepped current. Journal of Fluids and Structures 2005;21(1):3–24.

[16] Trim A, Braaten H, Lie H, Tognarelli M. Experimental investigation of vortex-induced vibration of long marine risers. Journal of Fluids and Structures 2005;21(3):335–361.

[17] Huera-Huarte F, Bangash Z, González L. Towing tank experiments on the vortex-induced vibrations of low mass ratio long flexible cylinders. Journal of Fluids and Structures 2014;48:81–92.

[18] Huse E, Kleiven G, Nielsen F, et al. Large scale model testing of deep sea risers. In: Offshore Technology Conference. 1998,.

[19] Vandiver JK, Swithenbank SB, Jaiswal V, Jhingran V. Fatigue damage from high mode number vortex-induced vibration. In: Proc. 25th OMAE Conf. 2006,.

[20] Fu S, Wang J, Baarholm R, Wu J, Larsen C. Features of vortex-induced vibration in oscillatory flow. Journal of Offshore Mechanics and Arctic Engineering 2014;136(1).

[21] Sarpkaya T. Lateral oscillations of smooth and sand-roughened cylinders in harmonic flow. Mechanics of Wave-Induced Forces on Cylinders (ed TL Shaw), Pitman, London 1979;:421–435.

[22] Sumer B, Fredsøe J. Transverse vibrations of an elastically mounted cylinder exposed to an oscillating flow. Journal of Offshore Mechanics and Arctic Engineering 1988;110(4):387–394.

[23] Triantafyllou M, Triantafyllou G, Tein Y, Ambrose BD, et al. Pragmatic riser VIV analysis. In: Offshore Technology Conference. 1999,.

[24] Vandiver JK, Li L. SHEAR7 V4.4 Program Theoretical Manual; 2005.

[25] Larsen CM, Lie H, Passano E, Yttervik R, Wu J, Baarholm G. VIVANA - Theory Manual, Version 3.7; 2009.

[26] Chang SHM, Isherwood M, et al. Vortex-induced vibrations of steel catenary risers and steel offloading lines due to platform heave motions. In: Offshore Technology Conference. Offshore Technology Conference; 2003,.

[27] Liao JC. Vortex-induced vibration of slender structures in unsteady flow. Ph.D. thesis; Massachusetts Institute of Technology; 2001.

[28] Resvanis TL. Vortex-induced vibration of flexible cylinders in time-varying flows. Ph.D. thesis; Massachusetts Institute of Technology; 2014.

[29] Thorsen MJ, Sævik S, Larsen CM. A simplified method for time domain simulation of cross-flow vortex-induced vibrations. Journal of Fluids and Structures 2014;49:135 – 148.

[30] Thorsen MJ, Sævik S, Larsen CM. Time domain simulation of cross-flow and in-line vortex-induced vibrations. In: Proceedings of EURODYN 2014. Porto, Portugal; 2014,.

[31] Thorsen MJ, Sævik S, Larsen CM. Fatigue damage from time domain simulation of combined in-line and cross-flow vortex-induced vibrations. Marine Structures 2015;41:200–222.

[32] Norberg C. Fluctuating lift on a circular cylinder: review and new measurements. Journal of Fluids and Structures 2003;17(1):57–96.

[33] Venugopal M. Damping and response prediction of a flexible cylinder in a current. Ph.D. thesis; Massachusetts Institute of Technology; 1996.

[34] Sarpkaya T. Wave forces on offshore structures. Cambridge University Press; 2010.

[35] Sarpkaya T. Force on a circular cylinder in viscous oscillatory flow at low keulegan—carpenter numbers. Journal of Fluid Mechanics 1986;165:61–71.

[36] Vikestad K, Larsen CM, Vandiver JK, et al. Norwegian deepwater program: damping of vortex-induced vibrations. In: Offshore Technology Conference. Offshore Technology Conference; 2000,.

[37] Newmark NM. A method of computation for structural dynamics. Journal of the Engineering

Mechanics Division 1959;85(3):67–94.

[38] Braaten H, Lie H. NDP riser high mode VIV tests, main report. Tech. Rep.; Norwegian Marine Technology Research Institute; Trondheim, Norway; 2004.

[39] Modarres-Sadeghi Y, Mukundan H, Dahl J, Hover F, Triantafyllou M. The effect of higher harmonic forces on fatigue life of marine risers. Journal of Sound and Vibration 2010;329(1):43–55.

[40] Lagarias JC, Reeds JA, Wright MH, Wright PE. Convergence properties of the Nelder–Mead simplex method in low dimensions. SIAM Journal on optimization 1998;9(1):112–147.

[41] Modarres-Sadeghi Y, Chasparis F, Triantafyllou M, Tognarelli M, Beynet P. Chaotic response is a generic feature of vortex-induced vibrations of flexible risers. Journal of Sound and Vibration 2011;330(11):2565 – 2579.

[42] Chaplin J, Bearman P, Cheng Y, Fontaine E, Graham J, Herfjord K, et al. Blind predictions of laboratory measurements of vortex-induced vibrations of a tension riser. Journal of Fluids and Structures 2005;21(1):25–40.

[43] Lie H, Kaasen K. Modal analysis of measurements from a large-scale VIV model test of a riser in linearly sheared flow. Journal of Fluids and Structures 2006;22(4):557–575.

[44] Sumer BM, Fredsøe J. Hydrodynamics around cylindrical structures; vol. 12. World Scientific Publishing Company; 1997.

[45] Gopalkrishnan R. Vortex-induced forces on oscillating bluff cylinders. Ph.D. thesis; Massachusetts Institute of Technology; 1993.

PAPER III

Paper IV

Non-linear time domain analysis of cross-flow vortex-induced vibrations

Mats J. Thorsen, Svein Sævik and Carl M. Larsen

Department of Marine Technology, Norwegian University of Science and Technology, Trondheim, Norway

Submitted for journal publication, 2016

Abstract

A previously proposed hydrodynamic load model for time domain simulation of cross-flow vortex-induced vibrations (VIV) is modified and combined with Morison's equation. The resulting model includes added mass, drag and a cross-flow vortex shedding force which is able to synchronize with the cylinder motion within a specified range of non-dimensional frequencies. It is demonstrated that the hydrodynamic load model provides a realistic representation of the cross-flow energy transfer and added mass for different values of the non-dimensional frequency and amplitude. Furthermore, it gives a reasonable approximation of the experimentally observed drag amplification. The load model is combined with a non-linear finite element model to predict the cross-flow VIV of a steel catenary riser in two different conditions: VIV due to a stationary uniform flow and VIV caused by periodic oscillation of the riser top end. In the latter case, the prescribed motion leads to an oscillating relative flow around the riser, causing an irregular response. The simulation results are compared to experimental measurements, and it is found that the model provides highly realistic results, although some discrepancies are seen.

Keywords: Vortex-induced vibrations; Dynamic time domain analysis; Nonlinear finite element model

1 Introduction

Elastic cylinders in fluid flow experience structural oscillations caused by vortex shedding, known as vortex-induced vibrations (VIV) [1]. The classic example is the elastically mounted rigid cylinder in a steady incoming flow, free to oscillate in the cross-flow direction [2]. In the offshore industry however, one is typically concerned with VIV of long slender structures such as risers and free spanning pipelines. Here, the VIV response may consist of several higher modes, in-line and cross-flow oscillations, and a combination of traveling and standing waves [3]. In addition, the incoming undisturbed flow may vary along the cylinder span.

To accurately predict riser VIV, two things must be in place. The first is a mathematical model that, given the hydrodynamic forces acting on the structure, can accurately predict the structural response. Secondly, one must be able to calculate the hydrodynamic forces along the structure, which will depend on the motion of the riser. The first part of the problem can be handled using the finite element method (FEM). If non-linear FEM is utilized, potentially important effects such as large displacements, time-varying geometric stiffness and changing boundary conditions may also be dealt with. The second part of the problem is possible to solve using computational fluid dynamics [4], but the necessary computer resources are large. Therefore, alternative semi-empirical methods have been developed, such as VIVANA, VIVA and SHEAR7 [5–7]. These are based on hydrodynamic coefficients measured in experiments, which is combined with a structural model to predict the VIV response in the frequency domain. Because the analysis is performed in the frequency domain, these methods require a linear structural model and stationary conditions (i.e. constant current velocity in time).

The limitations of the frequency domain methods prohibit realistic modeling of some problems. As an example, consider a steel catenary riser (SCR) suspended from a floating platform. The top end will be subjected to wave induced motions, which will cause the riser tension, and hence the geometric stiffness, to vary with time. Close to the bottom, a segment of the riser will go in and out of contact with the seabed, causing time-varying boundary conditions. If the wave induced motions are sufficiently large, vortex shedding will initiate due to the relative oscillatory flow [8]. Hence, the VIV response can be stationary in some parts (due to current) while in other parts it may be intermittent (due to relative oscillatory flow). In addition, internal slug flow may also cause riser vibrations [9], which will interact with the VIV response. To capture all these effects, a non-linear time domain analysis is required.

Several models exists which can be used to simulate VIV in time domain. One such model is the wake-oscillator, which is based on the assumption that the lift coefficient can be described by a forced Van der Pol oscillator. This idea was first suggested by Bishop and Hassan [10], and has been modified by many others since then (see e.g. [11] for a review). Such models have been used in a large number of studies, for instance to investigate the behavior of flexible structures with geometric nonlinearities [12]. However,

it is difficult to find a consistent set of wake-oscillator parameters suitable for both forced and free vibrations. [13]. Other time domain models have been developed by Lie [14], Finn et al. [15], Mainçon [16] and Xue et al. [17].

An alternative semi-empirical model for time domain simulation of VIV has been under development by Thorsen et al. [18–22], and the present paper is a continuation of this work. In combination with a finite element model, it has been shown that the model can be used to predict VIV of elastic cylinders in various current conditions, including oscillating flow. In these previous studies, the structural model was linear, and the mean in-line drag force was not included. The purpose of the present paper is to introduce a non-linear finite element model (including non-linear soil contact) for the structure, and to include the mean in-line drag forces (and the associated displacements). This should enable highly realistic prediction of the dynamic response of risers and other slender structures due to ocean currents in combination with prescribed oscillatory motions and possibly other loads (ocean waves are not considered here). To illustrate the applicability of the proposed model, it is utilized to simulate the cross-flow VIV of an SCR in two different conditions. The first is VIV due to a stationary incoming uniform flow. Secondly, VIV caused by periodic oscillation of the riser top end is considered. The results are compared to experiments.

2 Hydrodynamic load modeling

2.1 Morison's equation

This paper considers the dynamic response of slender circular structures exposed to currents. In addition, the structure can have velocities and accelerations induced by other loads or prescribed motions. A strip theory approach is used, such that the hydrodynamic force on a cylinder cross-section is calculated from velocities and accelerations at the same cross-section only. The relevant velocity vectors and coordinate system for computing the hydrodynamic force on a cylinder segment is shown in figure 1. The relative flow velocity is $\mathbf{v} = \mathbf{u} - \dot{\mathbf{x}}$, where $\mathbf{u}$ is the incoming flow velocity and $\dot{\mathbf{x}}$ is the velocity of the cylinder cross-section. The relative flow is not necessarily perpendicular to the cylinder, and $\mathbf{v}$ is therefore decomposed into a tangential component $\mathbf{v}_t$ and a normal component $\mathbf{v}_n$. Similarly, the normal component of the flow and structure acceleration is denoted $\dot{\mathbf{u}}_n$ and $\ddot{\mathbf{x}}_n$ respectively. The hydrodynamic drag and inertia forces (per unit length) on a cylinder cross-section is described using the generalized Morison's equation:

$$\mathbf{F}_n = C_M \rho \frac{\pi D^2}{4} \dot{\mathbf{u}}_n - (C_M - 1)\rho \frac{\pi D^2}{4} \ddot{\mathbf{x}}_n + \frac{1}{2}\rho D C_D |\mathbf{v}_n| \mathbf{v}_n. \tag{1}$$

Here, ρ is the water density and D is the cylinder diameter. C_M and C_D are the inertia and drag coefficients in the normal direction, which depend on a number of parameters

(see e.g. [23]). Note that equation (1) only gives forces normal to the cylinder, and any tangential forces are neglected.

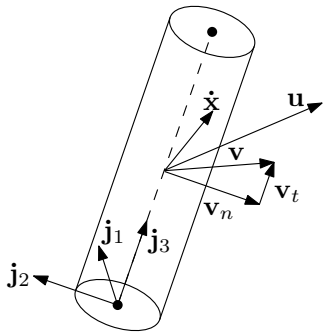

Figure 1: A cylinder segment with local coordinate system and velocity vectors.

2.2 Vortex shedding

A cylinder in a current will be excited by vortex shedding, even if the incoming flow is steady [24]. The flow separates from the cylinder surface and rolls up into vortices on either side, which for Reynolds numbers larger than 40 are unstable, causing alternating vortex shedding and the formation of a vortex street. For a stationary cylinder in a steady flow with velocity U, the vortex shedding frequency is given as $f_s = \mathrm{St}U/D$, where St is the Strouhal number. This depends on the Reynolds number and the cylinder surface roughness, but in the subcritical Reynolds number range, St is fairly constant and close to 0.2. [25]. The fluctuating pressure field associated with the vortex shedding causes oscillating forces both in the direction of the flow (drag) and perpendicular to the flow (lift). In the case of an elastic cylinder, the vortex shedding forces will cause structural vibrations, which in turn alters the surrounding flow and the hydrodynamic forces. An important interaction effect is that the vortex shedding frequency may deviate from the Strouhal frequency (i.e. the frequency for a stationary cylinder), and lock on to the frequency of motion. The synchronization between the cylinder motion and vortex shedding has been experimentally observed and discussed by several researchers, for instance Williamson and Roshko [26].

To represent the vortex shedding forces, a simple empirical model is applied. The present model is based on the work by Thorsen et al. [18–22], with some modifications. The main reason for modifying the model is that the drag term in Morison's equation will cause damping of vibrations. To illustrate this, consider as an example a cylinder in an incoming steady flow, U. Let the y-axis point in the direction perpendicular to the flow and assume the cylinder is oscillating in the cross-flow direction with a velocity $\dot{y}$, as

shown in figure 2. Taking only the drag term from equation (1) into account, the cross-flow component of the drag force is:

$$F_y = -\frac{1}{2}\rho D C_D |\mathbf{v}_n|^2 \sin\theta = -\frac{1}{2}\rho D C_D |\mathbf{v}_n| \dot{y}$$
$$= -\frac{1}{2}\rho D C_D \sqrt{U^2 + \dot{y}^2}\,\dot{y}. \tag{2}$$

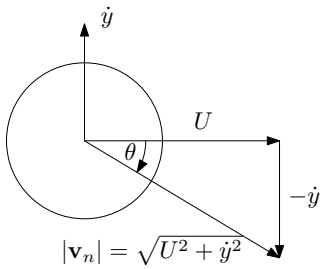

Figure 2: A cylinder in an incoming flow, moving in the cross-flow direction with velocity $\dot{y}$.

It is seen from equation (2) that the cross-flow component of the drag force is always in the direction opposite of the cross-flow cylinder velocity, and will therefore cause damping of vibrations. The previous investigations by Thorsen et al. [18–22] did not include drag forces, and hydrodynamic damping was introduced by a separate damping model. This damping model is not applicable in the present work, because damping is already included through the drag term in Morison's equation. The question is then if the drag term in Morison's equation is able to represent damping of vortex-induced vibrations? For the sake of simplicity, it will be assumed in the following that this is true. Although it is easy to criticize this assumption, one should remember that it is the net flow of energy between the fluid and structure which is important. This is determined by the power-in from vortex excitation minus the power-out from damping (drag in this case). Therefore, the properties of the damping model is not necessarily important, it is only required that the sum of excitation and damping is correct.

Based on [18], the vortex shedding force on a cylinder strip is expressed as:

$$\mathbf{F}_{\text{exc}} = \frac{1}{2}\rho D C_v |\mathbf{v}_n| (\mathbf{j}_3 \times \mathbf{v}_n) \cos\phi_{\text{exc}}. \tag{3}$$

The force given by equation (3) is perpendicular to $\mathbf{v}_n$ and $\mathbf{j}_3$ (see figure 1), which means that $\mathbf{F}_{\text{exc}}$ points in the direction normal to the relative flow velocity. The magnitude of the force is determined by a dimensionless coefficient, C_v, and the oscillatory behavior is taken into account through the time varying instantaneous phase ϕ_{exc}. Note that a fluctuating drag force (i.e. an excitation force parallel to $\mathbf{v}_n$) is generally also present. This force

will cause in-line vibrations of the cylinder, but these are significantly smaller than the cross-flow vibrations [27]. In the present research, focus will be on cross-flow vibrations, and the fluctuating drag is neglected.

As the vortex shedding force oscillates, the phase ϕ_{exc} changes continuously, and goes from 0 to 2π in one complete cycle. If the frequency of the force was some constant f_{exc}, the rate of change of the phase angle would be $\dot{\phi}_{\text{exc}} = 2\pi f_{\text{exc}}$. This is however not the case, as the frequency is influenced by, and will in some cases synchronize with the cylinder motion. A synchronization model was presented by Thorsen et al. [18], where the instantaneous frequency of the excitation force was expressed as a function of the phase difference between the cylinder cross-flow velocity and the force itself. This type of model is also adopted here, but for simplicity and efficiency in the numerical calculations, the non-dimensional frequency curve is now described analytically as:

$$\hat{f}_{exc} = \hat{f}_0 + \Delta\hat{f}\sin(\phi_{\dot{y}_{\text{rel}}} - \phi_{\text{exc}}) = \hat{f}_0 + \Delta\hat{f}\sin\theta. \tag{4}$$

This type of synchronization model is known as the Kuramoto model, which was originally used to study collective synchronization in large systems of oscillators [28]. In the present context, $\phi_{\dot{y}_{\text{rel}}}$ is the instantaneous phase of the relative cross-flow velocity of the cylinder (to be defined in section 2.2.1), and $\theta = \phi_{\dot{y}_{\text{rel}}} - \phi_{\text{exc}}$ is the phase difference between the relative cross-flow cylinder velocity and the vortex excitation force. $\hat{f}_0$ corresponds to the non-dimensional frequency at the center of the synchronization range, while $\Delta\hat{f}$ describes how much the vortex shedding frequency is allowed to deviate from $\hat{f}_0$. This means that the vortex shedding will synchronize with the cylinder motion for non-dimensional frequencies between $\hat{f}_0 - \Delta\hat{f}$ and $\hat{f}_0 + \Delta\hat{f}$. The present synchronization model is compared to the curve previously used by [22] in figure 3. The parameters in the model is taken as $\hat{f}_0 = 0.18$ and $\Delta\hat{f} = 0.08$, as these values give approximately the same synchronization range as the previously used curve, i.e. from $\hat{f} = 0.10$ to $\hat{f} = 0.26$. When the non-dimensional excitation frequency is found, the rate of change of ϕ_{exc} is computed as:

$$\dot{\phi}_{\text{exc}} = 2\pi f_{\text{exc}} = \frac{2\pi|\mathbf{v}_n|}{D}\hat{f}_{\text{exc}}. \tag{5}$$

The idea behind the synchronization model is that the phase difference $\phi_{\dot{y}_{\text{rel}}} - \phi_{\text{exc}}$ gives information about who is "leading" the oscillation. For example, if the phase difference is positive, the cylinder velocity is ahead, which means the excitation force must increase its frequency to catch up.

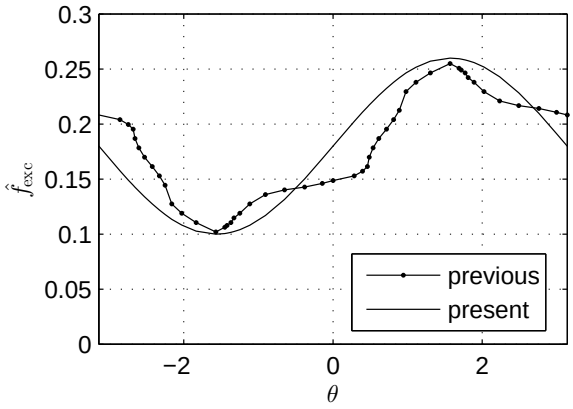

Figure 3: Non-dimensional frequency of the excitation force as a function of the phase difference between the relative cross-flow cylinder velocity and the vortex excitation force. The present analytical model is shown together with the previously used curve [22].

2.2.1 Computing the phase of the relative cross-flow cylinder velocity

The instantaneous phase of the relative cross-flow velocity of the cylinder strip appears in equation (4), and must be computed for every time step of the simulation (and for every cylinder strip/element in the model). The relative cross-flow cylinder velocity is defined as:

$$\dot{y}_{\text{rel}} = \dot{\mathbf{x}} \cdot \mathbf{n}, \tag{6}$$

where $\mathbf{n}$ is a unit vector normal to $\mathbf{v}_n$, which is found as

$$\mathbf{n} = \frac{\mathbf{j}_3 \times \mathbf{v}_n}{|\mathbf{v}_n|}. \tag{7}$$

Similarly, the relative cross-flow cylinder acceleration is found as

$$\ddot{y}_{\text{rel}} = \ddot{\mathbf{x}} \cdot \mathbf{n}. \tag{8}$$

The phase of $\dot{y}_{\text{rel}}$ is calculated using the phase portrait concept [18]. This can be visualized by plotting the normalized relative cross-flow velocity on a horizontal axis and the normalized relative cross-flow acceleration with a negative sign on a vertical axis, as shown in figure 4. The velocities/accelerations are normalized by their respective root

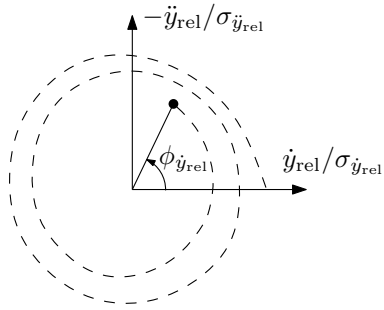

Figure 4: The phase diagram illustrates how the instantaneous phase of the relative cross-flow velocity is found.

mean square (r.m.s.) values. For generality, the r.m.s. is allowed to vary with time and is hence calculated over a finite interval backwards in time. Let n_m be the number of time steps in the interval, such that $T_m = (n_m - 1)\Delta t$ is the length of the interval. Then, the r.m.s. of $\dot{y}_{\mathrm{rel}}$ at time t_i may be found from the following expression:

$$\sigma_{\dot{y}_{\mathrm{rel}}}(t_i) = \sqrt{\frac{1}{n_m} \sum_{j=i-n_m+1}^{i} (\dot{y}_{\mathrm{rel}}(t_j))^2}, \tag{9}$$

Because computing the sum in equation (9) every time step would be time consuming, a more efficient approximate method is used. By splitting the sum in two parts, the r.m.s. can be written as:

$$\sigma_{\dot{y}_{\mathrm{rel}}}(t_i) = \sqrt{\frac{1}{n_m} \sum_{j=i-n_m+1}^{i-1} (\dot{y}_{\mathrm{rel}}(t_j))^2 + \frac{1}{n_m}(\dot{y}_{\mathrm{rel}}(t_i))^2}. \tag{10}$$

By introducing the approximation

$$\sum_{j=i-n_m+1}^{i-1} (\dot{y}_{\mathrm{rel}}(t_j))^2 \approx (n_m - 1)(\sigma_{\dot{y}_{\mathrm{rel}}}(t_{i-1}))^2, \tag{11}$$

the new r.m.s. value can be calculated from the previous, in combination with the new relative velocity:

$$\sigma_{\dot{y}_{\mathrm{rel}}}(t_i) \approx \sqrt{\frac{n_m - 1}{n_m}(\sigma_{\dot{y}_{\mathrm{rel}}}(t_{i-1}))^2 + \frac{1}{n_m}(\dot{y}_{\mathrm{rel}}(t_i))^2}. \tag{12}$$

To verify that the approximate expression (12) provides satisfactory accuracy, a test is performed where the time varying r.m.s. of a given time series are compared to the exact result (i.e. calculated by performing the sum over all the data points in the time interval). The results are shown in figure 5. The time series is taken from a simulation with the present model. It is seen that the curves calculated using the approximate expression follow the exact results closely, and it is concluded that the approximate expression provides sufficient accuracy.

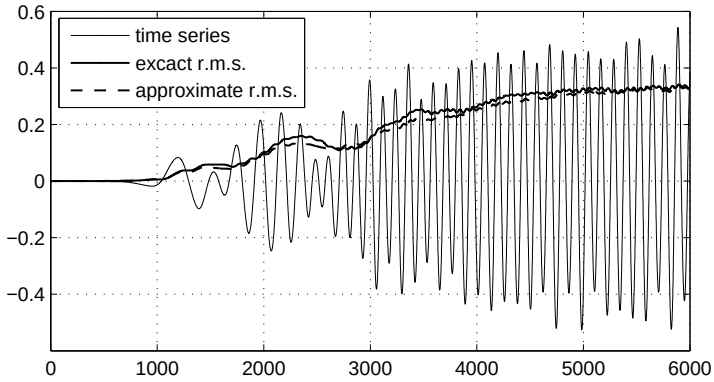

Figure 5: Comparison between the exact and approximate expression for the moving r.m.s. of a time series. In this example, $n_m = 500$.

2.3 Total hydrodynamic force

To summarize the above, the total hydrodynamic force per unit length on a cylinder section is given as the sum of equation (1) and (3):

$$\begin{aligned}\mathbf{F} = C_M\rho\frac{\pi D^2}{4}\dot{\mathbf{u}}_n - (C_M-1)\rho\frac{\pi D^2}{4}\ddot{\mathbf{x}}_n + \frac{1}{2}\rho D C_D|\mathbf{v}_n|\mathbf{v}_n \\ + \frac{1}{2}\rho D C_v|\mathbf{v}_n|(\mathbf{j}_3\times\mathbf{v}_n)\cos\phi_{\text{exc}}.\end{aligned} \tag{13}$$

The above equation is referred to as "the hydrodynamic force model". The first term is the force due to water particle acceleration, the second term is added mass, the third term is drag and the last is due to vortex shedding.

3 Testing the hydrodynamic force model

3.1 Introduction

As the proposed hydrodynamic force model is semi-empirical, it is important to test its predictive capabilities. To accurately predict VIV, it is necessary to have a good description of the energy transfer (between the fluid and the oscillating cylinder) and the added mass variations. The mean drag force is also of interest due to its role in determining the static deflection and tension in a slender structure such as a riser. It should be kept in mind that the goal of this research has been to develop a model which is as simple as possible, but still able to include the most important effects. Although it is certainly desirable to include every physical effect, it is recognized that reaching such a goal would probably require a very complex model. Because of this, it is assumed here that the hydrodynamic coefficients C_M, C_D and C_v (ref. equation (13)) can be considered constant when the Reynolds number is constant. In other words, the coefficients do not depend on e.g. the VIV frequency or amplitude. This is in contrast to the previous work by Thorsen et al. [18–22], where C_v was a function of y_0/D (but not frequency). However, the Reynolds number dependency must be accounted for, which is discussed in section 5. In the following, some basic examples are used to demonstrate that the model provides reasonable results compared to experimental observations, and also how the choice of C_v influences the results.

3.2 Energy transfer

The energy transfer between the fluid and structure during VIV is important to the response amplitude. A useful dimensionless measure of the cross-flow energy transfer is the lift coefficient in phase with the cylinder velocity, defined as:

$$C_{y,v} = \lim_{T\to\infty} \frac{2}{T} \int_0^T C_y(t) \cos(\omega t) dt, \tag{14}$$

where $C_y(t) = F_y/(0.5\rho DU^2)$ is the (total) lift coefficient. Here it has been assumed that the cross-flow displacement of the cylinder is $y = y_0 \sin(\omega t)$. If there is no in-line motion and the incoming flow velocity is U, the cross-flow hydrodynamic force is according to the present model:

$$F_y = \frac{1}{2}\rho D C_v \sqrt{U^2 + \dot{y}^2} U \cos\phi_{\text{exc}} - \frac{1}{2}\rho D C_D \sqrt{U^2 + \dot{y}^2}\dot{y} - (C_M - 1)\rho \frac{\pi D^2}{4}\ddot{y}. \tag{15}$$

To investigate the performance of the model, simulations have been performed, where a rigid cylinder is oscillated in the cross-flow direction with different y_0/D and $\hat{f} = fD/U = \omega D/(2\pi U)$. The resulting lift coefficient in phase with cylinder velocity is

shown in figure 6. For these simulations, $C_D = C_v = 1.2$ and $C_M = 2$. Note however that the inertia force is always out of phase with $\dot{y}$, and does not contribute to $C_{y,v}$. It is seen that for small amplitudes, $C_{y,v}$ is positive between approximately $\hat{f} = 0.1$ and $\hat{f} = 0.26$. In the present model, the range of positive excitation is determined by the parameters $\hat{f}_0$ and $\Delta\hat{f}$ (ref. equation (4)). When the amplitude increases, so does the energy loss due to drag, and $C_{y,v}$ drops. The excitation zone extends up to a maximum of $y_0/D \approx 0.8$. Above this level, $C_{y,v}$ is negative, which means that vibrations will be damped. To demonstrate how the choice of C_v affects the results, the above simulations are repeated with $C_v = 1.0$ and $C_v = 1.4$. The zero excitation curve (i.e. $C_{y,v} = 0$) for the different realizations are shown and compared to the experimental results by Gopalkrishnan [29] in figure 7. Clearly, an increase in C_v causes the positive excitation region to extend upwards to higher amplitude. However, the frequency range for synchronization remains unchanged.

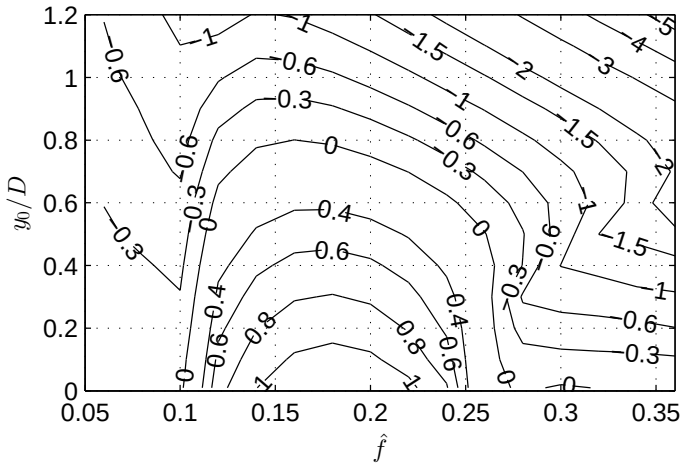

Figure 6: Lift coefficient in phase with cylinder velocity predicted by the model, using $C_D = C_v = 1.2$.

3.3 Added mass

The added mass is a measure of the hydrodynamic force component in phase with the acceleration of the cylinder. The added mass is especially important in VIV, as experiments have shown that the VIV response occurs at a true natural frequency when the added mass is taken into account [30]. This means that the oscillation frequency can be calculated if the added mass is known, and this fact is utilized in other VIV prediction tools such as VIVANA [5]. Solving for the unknown vibration frequency is however not straight forward because the added mass depends on both y_0/D and $\hat{f}$. Using the present

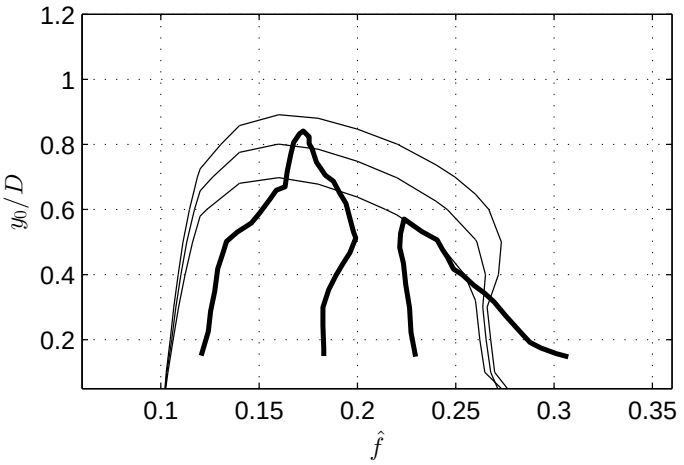

Figure 7: The curve corresponding to zero energy transfer, i.e. $C_{y,v} = 0$, calculated using $C_v = 1.0$ (the smallest region), $C_v = 1.2$ (the intermediate region) and $C_v = 1.4$ (the largest region). The thick curve is from experiments by Gopalkrishnan [29].

method, this problem is circumvented because the response is computed directly in the time domain, without any prior knowledge of the vibration frequency. With reference to equation (13), there are two terms contributing to the total added mass: the added mass term from Morison's equation, and the vortex shedding force. The latter may be partially in phase with the cylinder acceleration (the actual phase difference will be determined by the synchronization model, ref. equation (4)), and will influence the total added mass. The added mass is usually expressed as a dimensionless coefficient $C_a = M_a/(0.25\rho\pi D^2)$, where M_a is the total added mass of the cylinder. When the time series of the force and acceleration are known (from experiment or simulation), the added mass coefficient may be found as:

$$C_a = -\frac{8}{\rho\pi D^2\omega^4 y_0^2} \lim_{T\to\infty} \frac{1}{T} \int_0^T F_y(t)\ddot{y}(t)dt. \tag{16}$$

The added mass predicted by the present model was found by simulating a rigid cylinder with a prescribed cross-flow oscillation, using different y_0/D and $\hat{f}$, and the results are shown in figure 8. It is seen that the model predicts positive added mass for non-dimensional frequencies higher than 0.15 approximately, while for lower frequencies, the added mass is negative. This is in agreement with the observations made by Gopalkrishnan [29]. However, the model predicts large negative values of added mass when both the frequency and amplitude is low, and this is not seen in experiments. This discrepancy may

be unimportant, because the resulting added mass force is small when the frequency and amplitude is small. To investigate this further, the model is used to simulate the cross-flow VIV of a spring mounted cylinder, which means solving the 1-DOF dynamic equilibrium equation:

$$m\ddot{y} + c\dot{y} + ky = F_y(t), \tag{17}$$

where m is the cylinder (structural) mass per unit length, c is the structural damping and k is the spring stiffness. The mass ratio is set to $m/(0.25\rho\pi D^2) = 1.66$ and the damping ratio (in air) to 0.1 %, which is the same as in the free vibration experiment performed by Vikestad [30]. A number of simulations are run, with increasing reduced velocity, $U_r = U/(f_0 D)$, where f_0 is the natural frequency of the cylinder in still water. For each simulation, the transient is removed before the total added mass coefficient are computed according to equation (16). The results are shown and compared to Vikestad's in figure 9. It is seen that the model predicts the total added mass coefficient with a very high accuracy for $U_r > 5$. As cross-flow VIV is known to initiate around $U_r = 4$, the results indicate that the model predicts the correct added mass over the most important range of reduced velocities.

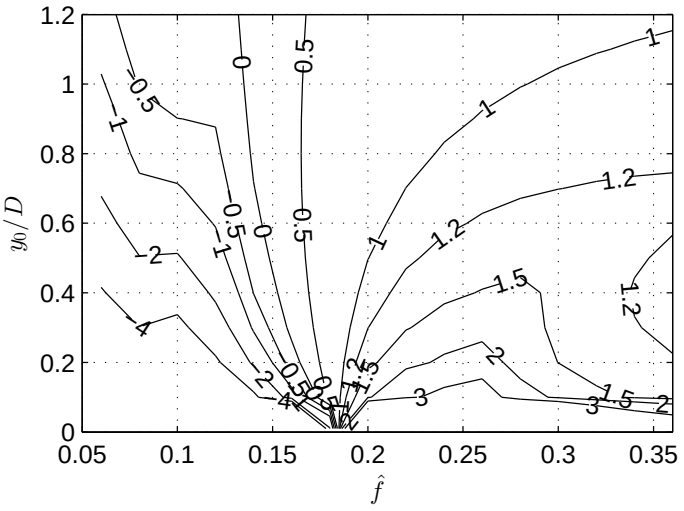

Figure 8: Added mass coefficient predicted by the model, using $C_D = C_v = 1.2$ and $C_M = 2$.

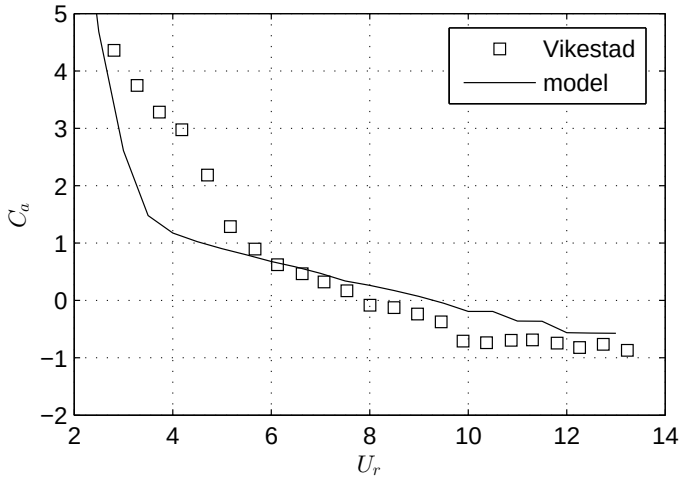

Figure 9: Added mass coefficient for free cross-flow vibration of spring mounted cylinder. The dotted line is predicted by the model, using $C_D = C_v = 1.2$ and $C_M = 2$, while the squares are from the experiments by Vikestad [30].

3.4 Amplitude and phase of lift coefficient

The preceding sections focused on the lift coefficient components in phase with the cylinder velocity and acceleration. However, the lift coefficient may also be expressed in terms of its total magnitude and a phase angle. This approach was used by Carberry et al. [31] , who expressed the total lift force as:

$$F_y = \frac{1}{2}\rho D U^2 C_L \sin(2\pi f t + \phi_{\text{lift}}). \tag{18}$$

The cross-flow displacement was taken as $y = y_0 \sin(2\pi f t)$, such that ϕ_{lift} is the phase angle between the cross-flow displacement of the cylinder and the lift force component at the frequency of oscillation. Carberry et al. presents how the phase angle and total lift coefficient varies with the oscillation frequency at a constant $y_0/D = 0.5$, and compares their result to those of Sarpkaya [32], Gopalkrishnan [29], Mercier [33] and Staubli [34]. The purpose here is to investigate how the present hydrodynamic load model predicts the total lift coefficient and phase angle compared to all these experiments. To do this, simulation of forced cross-flow vibration is performed as previously. The initial transient is removed, and the lift coefficient in phase with the cylinder velocity is calculated according to equation (14). Similarly, the component in phase with the cylinder displacement is found as:

$$C_{y,d} = \lim_{T\to\infty} \frac{2}{T} \int_0^T C_y(t) \sin(\omega t) dt. \tag{19}$$

The total lift coefficient is then found as $C_L = \sqrt{C_{y,v}^2 + C_{y,d}^2}$ and the phase angle is found from $\tan \phi_{\text{lift}} = C_{y,v}/C_{y,d}$. The results are plotted and compared to the mentioned experiments in figure 10 and 11, where the frequency of vibration has been normalized by the Strouhal frequency. From figure 10, it is seen that there is a transition in the phase angle as the oscillation frequency approaches the Strouhal frequency. When the oscillation frequency is low, ϕ_{lift} is approximately $225°$, and for high frequencies the phase angle is close to zero. Looking at the experimental results, the change in phase angle happens quite suddenly around $f/f_s = 0.8$, while the model predicts a smoother transition, beginning around $f/f_s = 0.6$. Moving on to figure 11, the magnitude of the lift coefficient is small for the lower frequencies. This is because the vortex shedding force is not synchronized with the cylinder motion. In addition, the cross-flow component of the drag force is small. As the frequency is increased towards f_s, synchronization causes C_L to rise. When the frequency is increased further, the drag and added mass forces increase, causing very high values of C_L. Taking the scatter in the experimental results into account, the present model gives a good approximation of how the phase angle and the total lift coefficient changes as the oscillation frequency is varied around the Strouhal frequency.

3.5 Mean drag

For a cylinder oscillating with a cross-flow motion $y = y_0 \sin \omega t$, the force per unit length in the flow direction may generally be expressed as $F_x = \bar{F}_x + \tilde{F}_x$, where $\bar{F}_x$ is the mean and $\tilde{F}_x$ is the fluctuating drag. The magnitude of the mean drag is usually given as a dimensionless mean drag coefficient, defined as:

$$\bar{C}_D = \frac{\bar{F}_x}{0.5\rho D U^2}. \tag{20}$$

According to the present model, the in-line component of the hydrodynamic force is in this situation (from equation (13)):

$$F_x = \frac{1}{2}\rho D C_D \sqrt{U^2 + \dot{y}^2} U + \frac{1}{2}\rho D C_v \sqrt{U^2 + \dot{y}^2} \dot{y} \cos \phi_{\text{exc}}. \tag{21}$$

The first term in the above equation is the in-line component of the drag force in Morison's equation, and it is seen that this term increases with the cross-flow velocity. The second term is due to the vortex shedding force, which is also seen to increase with the cross-flow velocity. However, the mean value of the second term will be zero if $\cos \phi_{\text{exc}}$ is

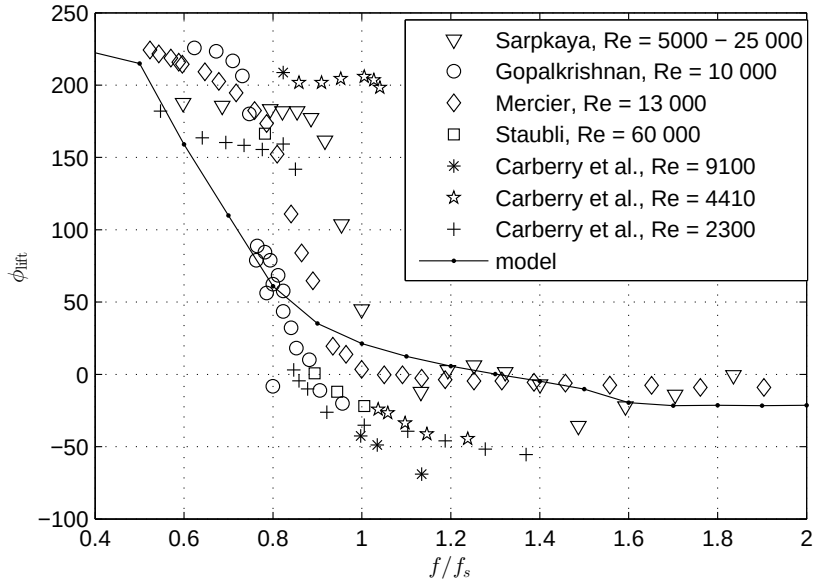

Figure 10: Phase angle between the total lift force and the cross-flow cylinder displacement as a function of frequency at $y_0/D = 0.5$. The solid line is predicted by the model using $C_D = C_v = 1.2$ and $C_M = 2$, while the symbols represent the experiments by Sarpkaya [32], Gopalkrishnan [29], Mercier [33], Staubli [34] and Carberry et al. [31]. The experimental data was taken from [31].

uncorrelated with $\dot{y}$. In other words, the vortex shedding force only contributes to the mean drag if it is synchronized with the cylinder velocity.

The mean drag coefficient predicted by the present model was found by simulating a rigid cylinder with a prescribed cross-flow oscillation, using different y_0/D and $\hat{f}$, and the results are shown in figure 12. In this example, $C_D = C_v = 1.2$. This value of C_D agrees with that of a stationary cylinder at $\mathrm{Re} \approx 10\ 000$. With reference to figure 12, it is seen that the mean drag is essentially equal to 1.2 for small amplitudes and/or frequencies. This is because the cylinder velocity is small compared to the incoming flow, which means that $\bar{C}_D \to C_D$, according to equation (21). When y_0/D or $\hat{f}$ is increased, so does the mean drag, and for cases where both y_0/D and $\hat{f}$ are large, $\bar{C}_D$ can reach very high values. This behavior is also seen in experiments, and figure 13 shows a comparison between the simulated results and experimental observations by Gopalkrishnan [29] for $y_0/D = 0.75$.

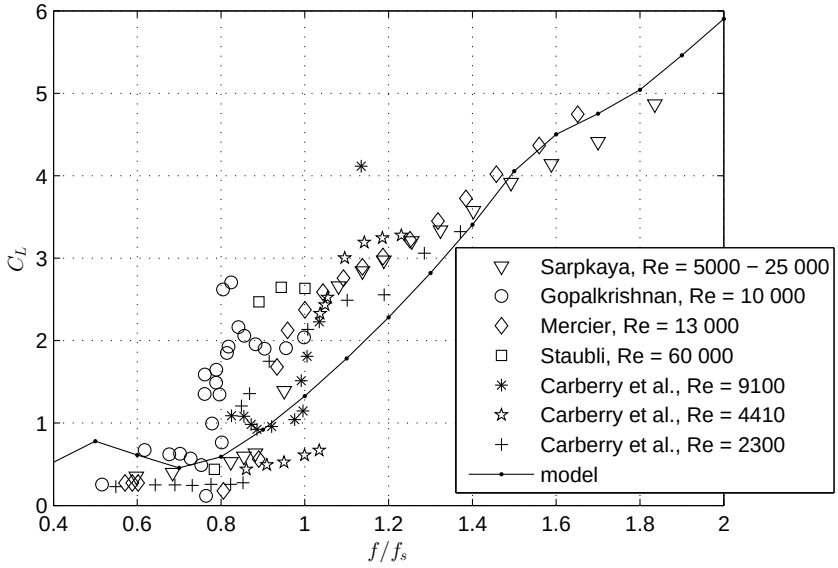

Figure 11: Total lift coefficient amplitude as a function of frequency at $y_0/D = 0.5$. The solid line is predicted by the model using $C_D = C_v = 1.2$ and $C_M = 2$, while the symbols represent the experiments by Sarpkaya [32], Gopalkrishnan [29], Mercier [33], Staubli [34] and Carberry et al. [31]. The experimental data was taken from [31].

3.6 Summary

Some of the most important points illustrated above is summarized as follows:

i) The energy transferred to the vibrating cylinder (quantified through the lift coefficient in phase with the cylinder velocity) depends on C_D and C_v. The drag coefficient determines the damping, which increases together with the vibration amplitude and frequency. With reference to figure 6, the drag force has an impact on $C_{y,v}$ for all values of y_0/D and $\hat{f}$. The vortex shedding force on the other hand, only affects $C_{y,v}$ in the region where the vortex shedding is synchronized with the cylinder motion. Increasing C_v extends the positive excitation region to higher amplitudes. For an elastically mounted rigid cylinder, stable oscillations occur when $C_{y,v} = 0$ (neglecting structural damping). This means that if the model is to predict the correct free vibration amplitude, C_v should be chosen so that $C_{y,v} = 0$ at the correct y_0/D.

ii) The total added mass coefficient predicted by the model is a result of the added mass term in Morison's equation and the vortex shedding force. The first term gives

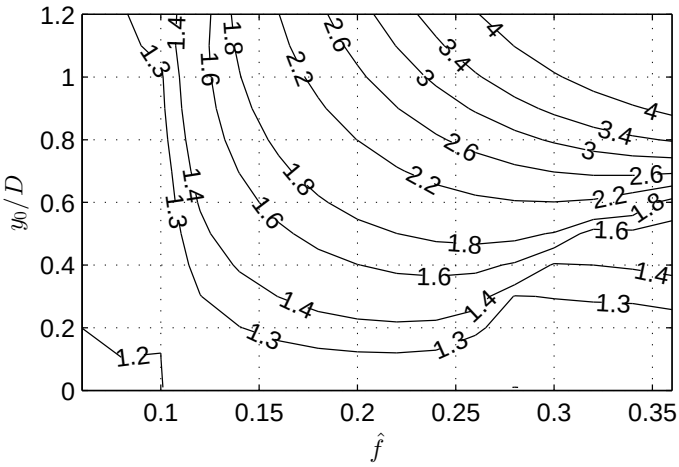

Figure 12: Mean drag coefficient predicted by the model, using $C_D = C_v = 1.2$.

a constant contribution equal to $C_a = C_M - 1$, while the latter will vary depending on the phase difference between the vortex shedding force and the cylinder acceleration.

iii) The mean drag coefficient $\bar{C}_D$ depends on both C_D and C_v. When the cylinder is stationary, $\bar{C}_D = C_D$, and C_D should be chosen accordingly. When the cylinder vibrates, two effects contribute to increasing the mean drag. Firstly, the average relative velocity increases. Secondly, the vortex shedding force has a component in the direction of the flow which will have a non-zero mean value when the vortex shedding is synchronized with the cylinder motion.

iv) Although this has not been considered here, the parameters $\hat{f}_0$ and $\Delta\hat{f}$ in equation 4 can be changed, thereby altering the synchronization range of the vortex shedding force.

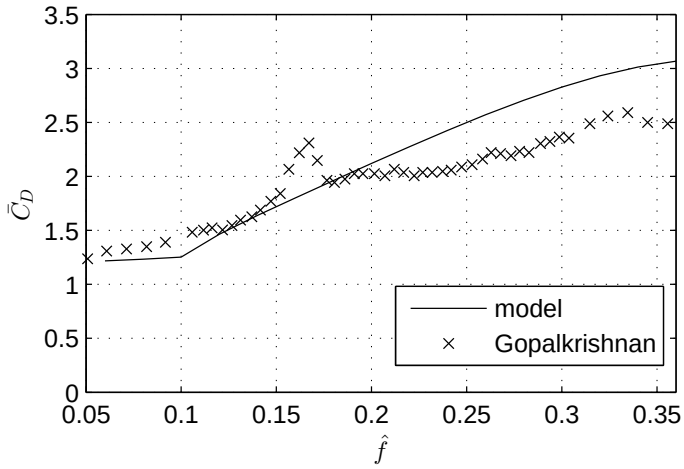

Figure 13: Mean drag coefficient for $y_0/D = 0.75$. The solid line are predicted by the model using $C_D = C_v = 1.2$, while the crosses are from experiments by Gopalkrishnan [29].

4 Structure modeling and dynamic analysis

The hydrodynamic force model has been implemented into the finite element software Simla [35], which is a tool developed for pipe-laying analyses including very large deformations, non-linear material behavior and contact. 2-node 3 dimensional beam elements are used, with 3 translational and 3 rotational degrees of freedom at each node. The beam element is based on classical theory for slender beams, assuming planes normal to the neutral axis to remain plane, as well as neglecting shear deformations due to lateral loads and lateral contraction due to axial elongation. In addition, the strains are assumed to be small. A corotational formulation is used to account for large displacements and rotations. Based on the principle of virtual work on incremental form, the element stiffness matrix contains contributions from geometric and material stiffness. The geometric contribution is the influence of axial force on the lateral stiffness of the beam. The nonlinear dynamic analysis in Simla is based on the incremental equation of motion, which is solved in time domain using the HHT-α method [36].

5 Results

5.1 Case 1: SCR in uniform current

Wang et al. [8] performed model tests to study VIV on steel catenary risers (SCRs). In these experiments, the top end of a truncated SCR model was suspended from a towing carriage, while the lower end was resting on an fake seabed made of aluminium. The

riser was terminated in both ends with universal couplings, which were moment-free and torsion restricted. Strain sensors were installed at 25 equidistant points to measure the dynamic response. Important physical properties of the model riser are given in table 1. The experimental campaign consisted of two parts: Uniform current VIV and heave induced VIV. Uniform current was obtained by moving the top end and the seabed with a constant speed (on tracks).

Table 1: Properties of the riser model [8].

Riser length	23.71 m
Depth	9 m
Horizontal length	21.0425 m
Outer diameter	0.024 m
Mass per length (dry)	0.69 kg/m
Bending stiffness (EI)	10.5 Nm^2
Tensile stiffness (EA)	$6.66 \cdot 10^5$ N

The experimental campaign contained cases with current velocities ranging from 0.1 to 0.5 m/s. However, due to the restricted track length, the test duration was relatively short for the high velocity cases. With this in mind, a case with a current velocity of 0.2 m/s is chosen for the present comparison. The current direction is in the riser plane, as indicated in figure 14, which means that the VIV motion is mainly out of the riser plane (i.e. the cross-flow direction). As previously stated, this study focuses on the prediction of cross-flow VIV, and for this reason only the cross-flow strains are analyzed. Figure 15 shows the dynamic part of the measured cross-flow strain from the experiment by Wang et al. [8]. Note that the strain sensors were mounted at a diameter $D = 19.5$ mm, and the measured values have been adjusted to show the strain at the outer surface ($D = 24$ mm). The initial transient has been removed, and the data in figure 15 is from the time window with fully developed VIV. Waves are seen traveling towards the bottom end (which is located at $x = 0$), and the vibration pattern is relatively stationary, although some irregularities are seen. It is also quite clear that a single frequency dominates.

A finite element model of the SCR is established using the previously described software, Simla. The SCR is discretized into 500 beam elements (a convergence test was performed by doubling the number of elements). An initial static analysis is performed, including weight, buoyancy and a prescribed top-end displacement in the x-direction to obtain the desired static configuration. The FE model after the completion of the static analysis is seen in figure 14. Seabed contact is modeled using nonlinear springs with a vertical stiffness of 1 (kN/m)/m in compression. This is very stiff compared to the SCR, and represents a nearly rigid surface. The seabed spring stiffness in tension is zero, which means the SCR is allowed to lift freely from the seabed. When a node of the SCR is in contact with the seabed, it will also experience friction forces in the axial and lateral

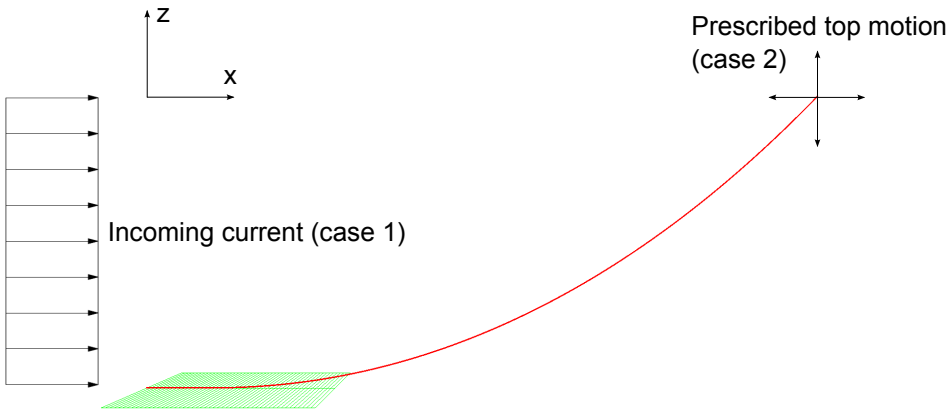

Figure 14: Finite element model in the static configuration.

directions, which will restrain the riser from sliding until the friction force exceeds the vertical contact force multiplied by a friction coefficient. In the analysis, the seabed-riser friction coefficient is set to 0.2. The exact number is not known, but 0.2 is a reasonable value for plastic and aluminium in water. For the dynamic analysis, a time step of 0.005 s is applied, which was found to be sufficient (i.e. reducing the time step gave no change in the results).

The hydrodynamic forces are calculated according to the described model (equation (13)). The Reynolds number for the case considered here is approximately 3 000, based on the maximum normal flow velocity. Swithenbank et al. [37] have shown that the VIV response amplitude for flexible cylinders depends on the Reynolds number, and this must be kept in mind when choosing a value for C_v. As stated in section 3, a suitable strategy would be to choose C_v such that the maximum amplitude of the positive excitation zone (i.e. the region where $C_{y,v}$ is positive) is correct, compared to experiments. For $\mathrm{Re} = 10\ 000$, the maximum y_0/D which gives positive excitation is approximately 0.85, according to Gopalkrishnan [29]. Based on [37], the maximum amplitude at $Re = 3\ 000$ is reduced to 60% compared to $Re = 10\ 000$. Assuming that the maximum response amplitude for a flexible cylinder is linearly related to the maximum y_0/D of the positive excitation zone, it follows that the positive excitation zone extends up to $y_0/D = 0.85 \cdot 0.6 \approx 0.5$ for $\mathrm{Re} = 3\,000$. This corresponds to $C_v = 0.7$ (found by plotting figure 6 using different values for C_v), which is used in the subsequent simulations. The drag and inertia coefficients are set to $C_D = 1.2$ and $C_M = 2$.

The dynamic cross-flow strain from the simulation is shown in figure 16. Compared to the experimental results, the same type of traveling waves are seen. 7 distinctive peaks are seen along the riser span, while in the experimental results, there are only 6 peaks. This indicates that the predicted mode of vibration is one number higher than in the ex-

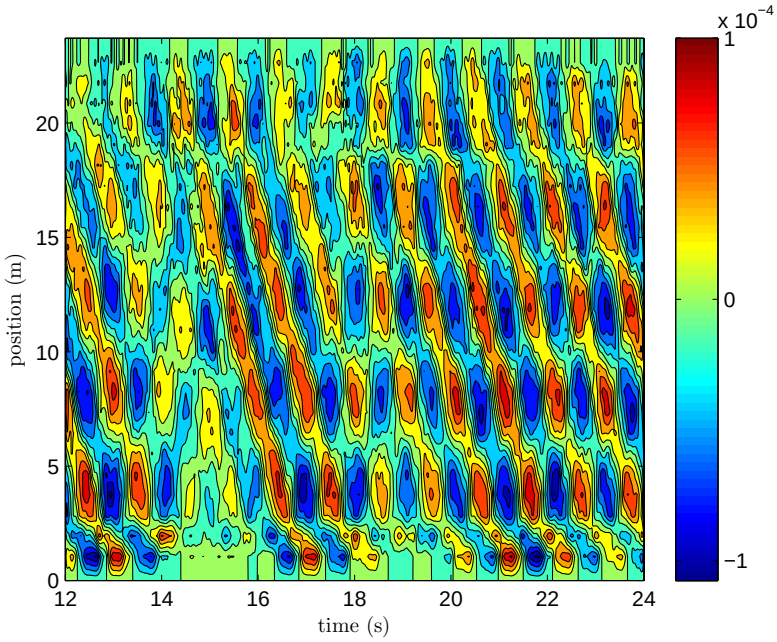

Figure 15: From experiment by Wang et al. [8] (constant uniform flow): Dynamic cross-flow strain along the riser as a function of time.

periment, which may be caused by a mismatch in the added mass. This is however a small error, and some uncertainty in the predicted mode must be expected. Furthermore, the predicted vibration pattern is more regular than in the experiment, which is also unsurprising, due to the simplifications embedded in the model. The magnitude of the predicted strains are compared to the experimental results in figure 17, in terms of the r.m.s. of the dynamic cross-flow strain along the riser. The agreement along the riser span is reasonable, although some discrepancies are seen. The maximum r.m.s. of strain predicted by the model is 99.6 % of the experimentally observed value. However, the point of maximum strain in the simulation is not the same as in the experiment. The power spectrum of the strain signals from the experiment and simulation are shown and compared in figure 18. It is seen that the dominating frequencies are almost exactly the same, although the predicted spectrum is slightly more narrow-banded.

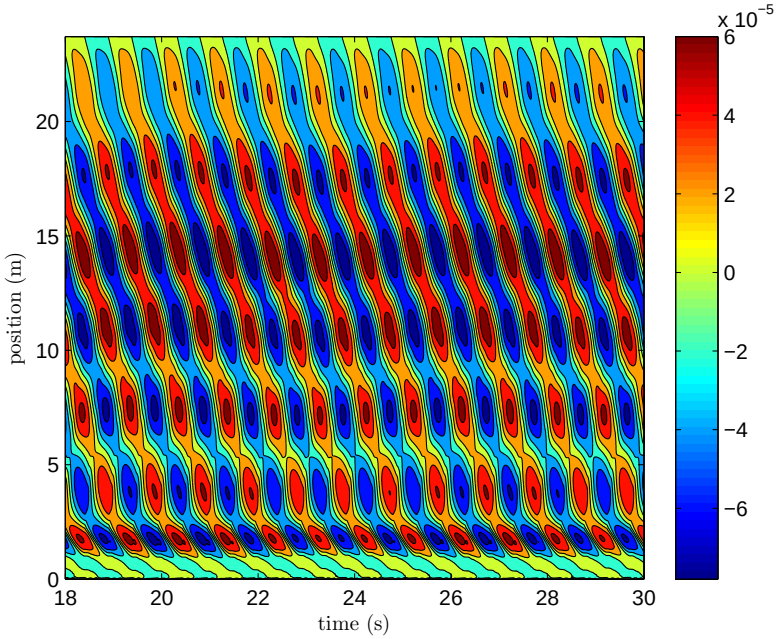

Figure 16: From simulation (constant uniform flow): Dynamic cross-flow strain along the riser as a function of time.

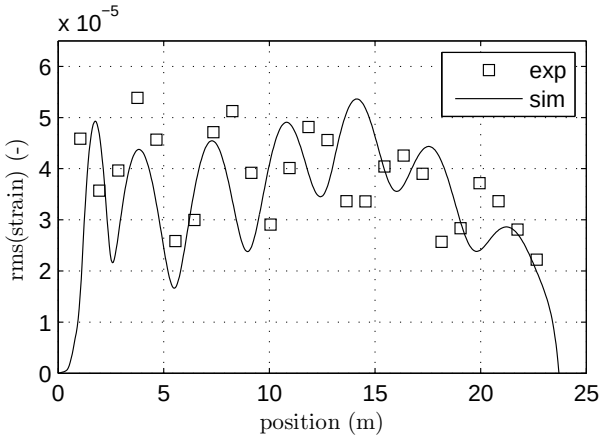

Figure 17: Comparison between predicted (solid line) and measured (squares) r.m.s. of dynamic cross-flow strain along the riser (constant uniform flow).

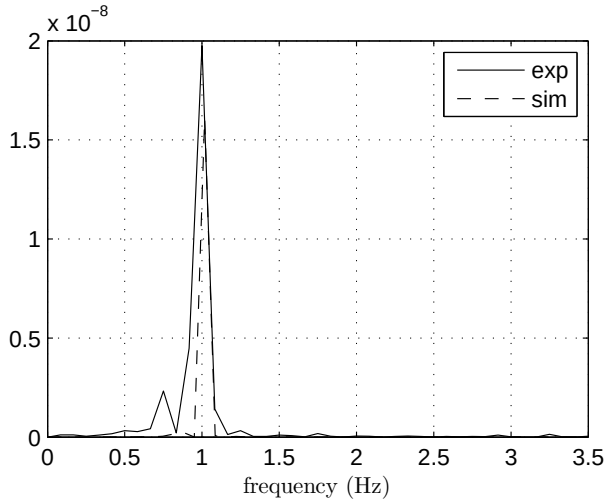

Figure 18: Frequency spectrum of dynamic cross-flow strain from simulation and experiment (constant uniform flow) 8.25 meters from the lower end.

5.2 Case 2: Heave induced VIV of SCR

Wang et al. [8] used the same experimental set up to study heave induced VIV, caused by a forced oscillating movement of the upper end of the riser, as indicated in figure 14. The SCR model was oscillating in still water, and the relative velocity between the riser and the surrounding water caused vortex shedding and VIV. The cross-flow strains measured in the test are shown in figure 19 together with the x (horizontal) and z (vertical) displacement of the top point. Note that the strain signal has been band-pass filtered to remove high-frequency noise and the low-frequency component associated with the heave motion. The top-end motion is approximately sinusoidal with a period of 5.96 s. Compared to the constant current case, the VIV response appears more irregular, which is expected due to the relative oscillating flow. Although the spatial resolution is limited, it is possible to see how the touch-down point of the SCR (located close to $x = 0$) is moving as the lower end of the riser lifts up and falls down towards the bottom repeatedly.

The r.m.s. of the in-plane velocity (i.e. the relative flow velocity causing VIV) along the riser according to the simulation model is shown in figure 20. When the flow velocity varies both in time and space, there is no unique Reynolds number, which can make it difficult to choose a single value for C_v. However, the maximum of the r.m.s. of the in-plane velocity may be a reasonable choice for a characteristic velocity. From figure 20, this is found to be 0.16 m/s, which means the Reynolds number is approximately 4 000. This is slightly larger than in the preceding case, and based on [37], the maximum response is expected to be around 70 % of the value at $\mathrm{Re} = 10\,000$. Following the same way of thinking as for the previous case, this means that $C_v = 0.8$ approximately, and this value is adopted in the simulations. As in the previous case, $C_D = 1.2$ and $C_M = 2$. Apart from the boundary conditions at the top, the structural model is also the same as before.

The cross-flow bending strains found from the simulation are shown in figure 21, together with the x (horizontal) and z (vertical) displacement of the top end node. The prescribed motion of the top node is exactly the same as measured in the experiment. The predicted vibration pattern looks qualitatively similar to the experimental results, and consists of irregular traveling waves. It is seen that the peak close to the touch-down point moves back and forth due to the variation in bottom contact. The predicted r.m.s. of the cross-flow strains are compared to the experiment in figure 22, and the comparison shows that the magnitude of the strain is somewhat over-predicted for the lower part and under-predicted for the upper half. Compared to the experiment, the maximum r.m.s. of strain predicted by the model is 6 % too high. To get a better understanding of the frequency content in the response, the measured and predicted cross-flow strain at a point 8.25 meters from the lower end are shown in figure 23 and 24 together with a wavelet plot of the strain signals. The wavelet plot shows the frequency content as a function of time, and from figure 23 it is seen that the dominating frequency in the experiment is close to 1 Hz. Less pronounced frequencies are seen at all times, both below and above the dominating ones. It is also noted that the amplitude in the experiment is relatively small

at $t = 30$ s, but increases around $t = 36$ s for some unknown reason. The amplitude of the predicted strain shown in figure 24 is more stable. The predicted dominating frequency is also close to 1 Hz, and other frequency components are present at lower and higher frequencies, as in the experiment.

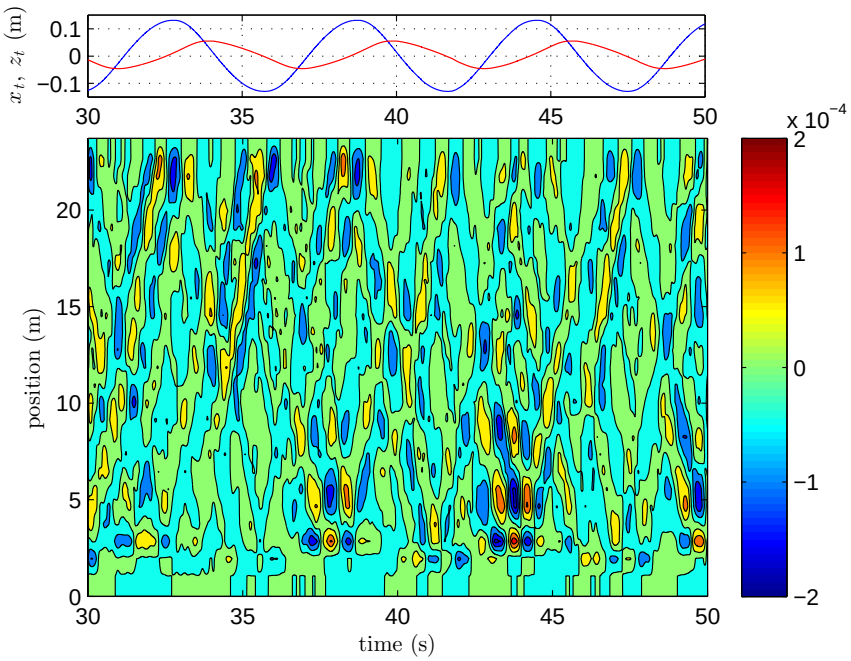

Figure 19: From experiment by Wang et al. [8] (heave induced VIV): Dynamic cross-flow strain along the riser as a function of time. The top figure shows the x (red) and z (blue) displacement of the riser's upper end. Note that the strain signal has been band-pass filtered to remove high-frequency noise and the low-frequency component associated with the heave motion.

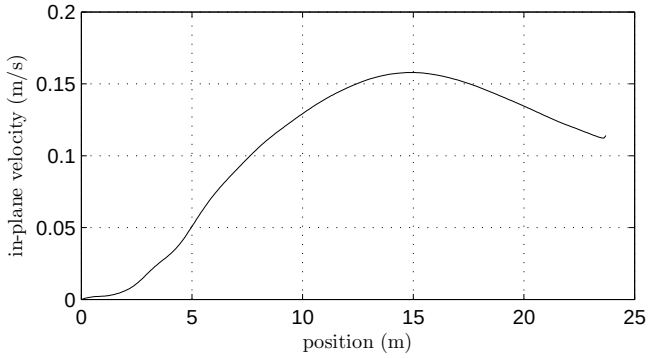

Figure 20: R.m.s. of riser in-plane velocity (calculated).

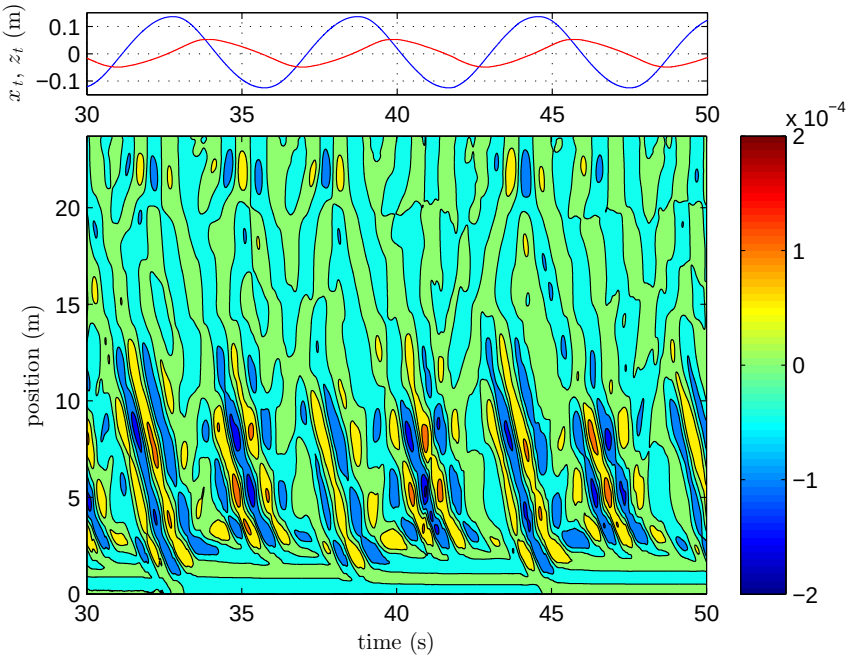

Figure 21: From simulation (heave induced VIV): Dynamic cross-flow strain along the riser as a function of time. The top figure shows the x (red) and z (blue) displacement of the riser's upper end.

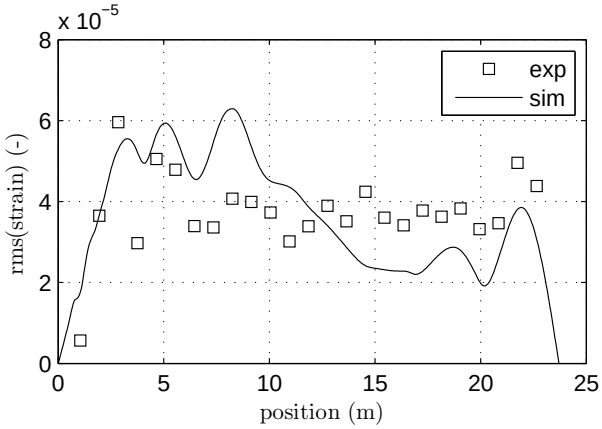

Figure 22: Comparison between predicted (solid line) and measured (squares) r.m.s. of dynamic cross-flow strain along the riser (heave induced VIV).

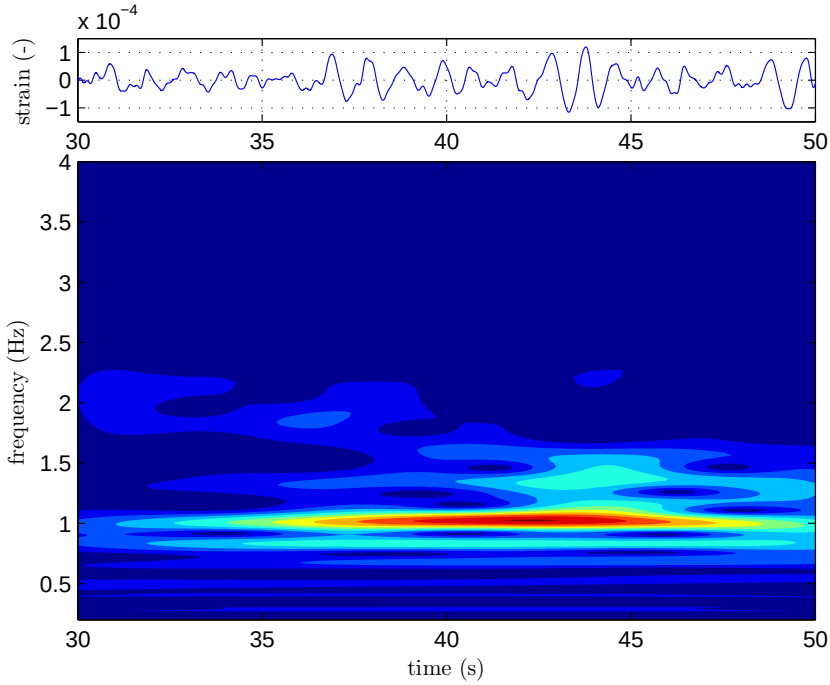

Figure 23: From experiment by Wang et al. [8] (heave induced VIV): The top figure shows the dynamic cross-flow strain 8.25 meters from the lower end. The bottom figure shows the wavelet contour plot of the strain signal.

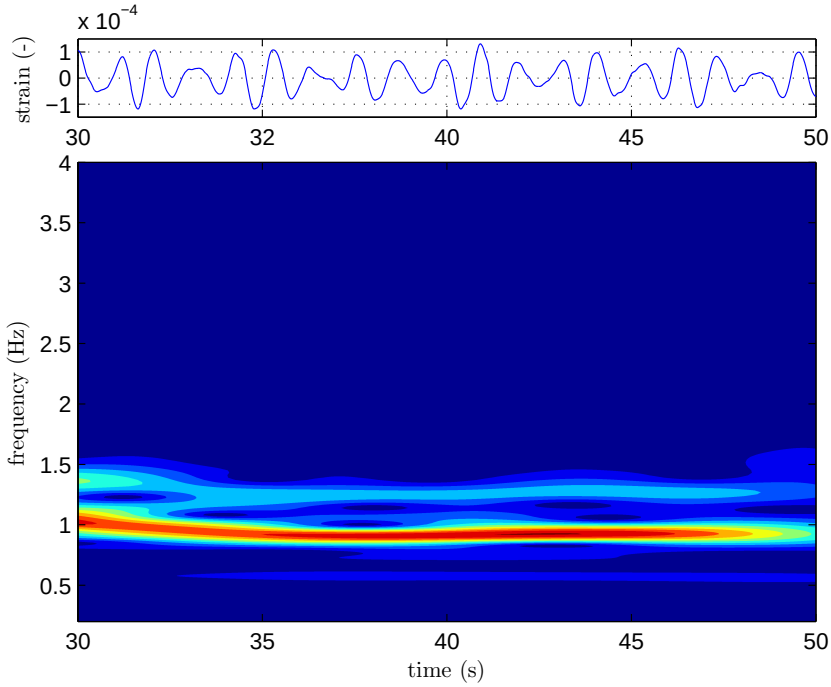

Figure 24: From simulation (heave induced VIV): The top figure shows the dynamic cross-flow strain 8.25 meters from the lower end. The bottom figure shows the wavelet contour plot of the strain signal.

6 Conclusions

A method for time domain analysis of cross-flow VIV of slender structures exposed to currents and prescribed motions has been presented, which is able to account for non-linear structural effects such as large displacements and time varying contact conditions. The hydrodynamic loading is computed based on Morison's equation and a semi-empirical formulation of the cross-flow vortex shedding force [18]. It is shown that the model provides a realistic description of the cross-flow energy transfer and added mass as well as the experimentally observed drag amplification, using constant hydrodynamic coefficients. Next, the combined hydrodynamic and structural model is applied to simulate VIV of the model scale SCR tested by Wang et al. [8]. Two different conditions are considered, namely uniform stationary current and heave induced VIV. In the first case, the response is almost stationary with a single dominating frequency. Both the magnitude and the frequency content of the dynamic cross-flow strain is accurately predicted by the model. In the second case, the relative fluid velocity is oscillating, due to the sinusoidal motion prescribed at the top end of the riser. This causes an irregular response pattern with multiple frequencies and varying amplitudes. Similar behavior is seen in the simulation and the experiment, and the dominating frequency and the r.m.s. of strain is quite accurately captured. This indicates that the present hydrodynamic load model provides a good approximation of the relevant loads, which makes it possible to simulate riser VIV with a high degree of realism, when combined with a non-linear finite element program.

Acknowledgments

The authors gratefully acknowledge Statoil for permission to use the data from the experiments performed at Shanghai Jiao Tong University. We would also like to thank Elizabeth Passano, Jie Wu, Decao Jin, Shixiao Fu and Halvor Lie at MARINTEK for contributing with valuable discussions regarding VIV in general, as well as sharing their knowledge about the SCR experiment.

References

[1] Blevins RD. Flow-Induced Vibration. 2 ed.; Van Nostrand Reinhold; 1990.

[2] Feng C. The measurement of vortex induced effects in flow past stationary and oscillating circular and D-section cylinders. Master's thesis; University of British Columbia; 1968.

[3] Vandiver JK, Jaiswal V, Jhingran V. Insights on vortex-induced, traveling waves on long risers. Journal of Fluids and Structures 2009;25(4):641–653.

[4] Bourguet R, Karniadakis GE, Triantafyllou MS. Vortex-induced vibrations of a long flexible cylinder in shear flow. Journal of Fluid Mechanics 2011;677:342–382.

[5] Larsen CM, Lie H, Passano E, Yttervik R, Wu J, Baarholm G. VIVANA - Theory Manual, Version 3.7. MARINTEK; 2009.

[6] Triantafyllou M, Triantafyllou G, Tein Y, Ambrose BD, et al. Pragmatic riser VIV analysis. In: Offshore Technology Conference. 1999,.

[7] Vandiver JK, Li L. SHEAR7 V4.4 Program Theoretical Manual. Department of Ocean Engineering, Massaccusetts Institute of Technology; 2005.

[8] Wang J, Fu S, Baarholm R, Wu J, Larsen CM. Fatigue damage of a steel catenary riser from vortex-induced vibration caused by vessel motions. Marine Structures 2014;39:131–156.

[9] Ortega A, Rivera A, Nydal OJ, Larsen CM. On the dynamic response of flexible risers caused by internal slug flow. In: ASME 2012 31st International Conference on Ocean, Offshore and Arctic Engineering. American Society of Mechanical Engineers; 2012, p. 647–656.

[10] Bishop R, Hassan A. The lift and drag forces on a circular cylinder oscillating in a flowing fluid. Proceedings of the Royal Society of London Series A Mathematical and Physical Sciences 1964;277(1368):51–75.

[11] Gabbai R, Benaroya H. An overview of modeling and experiments of vortex-induced vibration of circular cylinders. Journal of Sound and Vibration 2005;282(3):575–616.

[12] Srinil N. Multi-mode interactions in vortex-induced vibrations of flexible curved/straight structures with geometric nonlinearities. Journal of Fluids and Structures 2010;26(7):1098–1122.

[13] Ogink R, Metrikine A. A wake oscillator with frequency dependent coupling for the modeling of vortex-induced vibration. Journal of Sound and Vibration 2010;329(26):5452–5473.

[14] Lie H. A time domain model for simulation of vortex induced vibrations on a cable. In: Proc. Sixth Int. Conf. on Flow Induced Vibrations. London, UK; 1995, p. 455–466.

[15] Finn L, Lambrakos K, Maher J. Time domain prediction of riser VIV. In: Proceedings of the Fourth International Conference on Advances in Riser Technologies. 1999,.

[16] Mainçon P. A Wiener-Laguerre Model of VIV Forces Given Recent Cylinder Velocities. Mathematical Problems in Engineering 2011;2011.

[17] Xue H, Wang K, Tang W. A practical approach to predicting cross-flow and in-line VIV response for deepwater risers. Applied Ocean Research 2015;52:92 – 101.

[18] Thorsen MJ, Sævik S, Larsen CM. A simplified method for time domain simulation of cross-flow vortex-induced vibrations. Journal of Fluids and Structures 2014;49:135–148.

[19] Thorsen MJ, Sævik S, Larsen CM. Time domain simulation of cross-flow and in-line vortex-induced vibrations. In: Proceedings of EURODYN 2014. Porto, Portugal; 2014,.

[20] Thorsen MJ, Sævik S, Larsen CM. Fatigue damage from time domain simulation of combined in-line and cross-flow vortex-induced vibrations. Marine Structures 2015;41:200–222.

[21] Thorsen MJ, Sævik S, Larsen CM. Time domain simulation of vortex-induced vibrations based on phase-coupled oscillator synchronization. In: ASME 2015 34th International Conference on Ocean, Offshore and Arctic Engineering. American Society of Mechanical Engineers; 2015,.

[22] Thorsen MJ, Sævik S, Larsen CM. Time domain simulation of vortex-induced vibrations in stationary and oscillating flows. Journal of Fluids and Structures 2016;61:1 – 19.

[23] Faltinsen O. Sea loads on ships and offshore structures; vol. 1. Cambridge university press; 1993.

[24] Sumer BM, Fredsøe J. Hydrodynamics around cylindrical structures; vol. 12. World Scientific Publishing Company; 1997.

[25] Norberg C. Fluctuating lift on a circular cylinder: review and new measurements. Journal of Fluids and Structures 2003;17(1):57–96.

[26] Williamson C, Roshko A. Vortex formation in the wake of an oscillating cylinder. Journal of Fluids and Structures 1988;2(4):355–381.

[27] Jauvtis N, Williamson C. The effect of two degrees of freedom on vortex-induced vibration at low mass and damping. Journal of Fluid Mechanics 2004;509(6):23–62.

[28] Strogatz SH. From Kuramoto to Crawford: exploring the onset of synchronization in populations of coupled oscillators. Physica D: Nonlinear Phenomena 2000;143(1–4):1 – 20.

[29] Gopalkrishnan R. Vortex-induced forces on oscillating bluff cylinders. Ph.D. thesis; Massachusetts Institute of Technology; 1993.

[30] Vikestad K. Multi-frequency response of a cylinder subjected to vortex shedding and support motions. Ph.D. thesis; Norwegian University of Science and Technology, Department of Marine Technology; Trondheim, Norway; 1998.

[31] Carberry J, Sheridan J, Rockwell D. Controlled oscillations of a cylinder: forces and wake modes. Journal of Fluid Mechanics 2005;538:31–69.

[32] Sarpkaya T. Hydrodynamic damping, flow-induced oscillations, and biharmonic response. Journal of offshore Mechanics and Arctic engineering 1995;117(4):232–238.

[33] Mercier JA. Large amplitude oscillations of a circular cylinder in a low-speed stream. Stevens Institute of Technology, PhD 1973;.

[34] Staubli T. Calculation of the vibration of an elastically mounted cylinder using experimental data from forced oscillation. Journal of Fluids Engineering 1983;105(2):225–229.

[35] Sævik S. SIMLA Theory Manual; 2008.

[36] Hilber HM, Hughes TJ, Taylor RL. Improved numerical dissipation for time integration algorithms in structural dynamics. Earthquake Engineering & Structural Dynamics 1977;5(3):283–292.

[37] Swithenbank SB, Vandiver JK, Larsen CM, Lie H. Reynolds number dependence of flexible cylinder VIV response data. In: ASME 2008 27th International Conference on Offshore Mechanics and Arctic Engineering. American Society of Mechanical Engineers; 2008, p. 503–511.

Previous PhD theses published at the Departement of Marine Technology
(earlier: Faculty of Marine Technology)
NORWEGIAN UNIVERSITY OF SCIENCE AND TECHNOLOGY

Report No.	Author	Title
	Kavlie, Dag	Optimization of Plane Elastic Grillages, 1967
	Hansen, Hans R.	Man-Machine Communication and Data-Storage Methods in Ship Structural Design, 1971
	Gisvold, Kaare M.	A Method for non-linear mixed -integer programming and its Application to Design Problems, 1971
	Lund, Sverre	Tanker Frame Optimalization by means of SUMT-Transformation and Behaviour Models, 1971
	Vinje, Tor	On Vibration of Spherical Shells Interacting with Fluid, 1972
	Lorentz, Jan D.	Tank Arrangement for Crude Oil Carriers in Accordance with the new Anti-Pollution Regulations, 1975
	Carlsen, Carl A.	Computer-Aided Design of Tanker Structures, 1975
	Larsen, Carl M.	Static and Dynamic Analysis of Offshore Pipelines during Installation, 1976
UR-79-01	Brigt Hatlestad, MK	The finite element method used in a fatigue evaluation of fixed offshore platforms. (Dr.Ing. Thesis)
UR-79-02	Erik Pettersen, MK	Analysis and design of cellular structures. (Dr.Ing. Thesis)
UR-79-03	Sverre Valsgård, MK	Finite difference and finite element methods applied to nonlinear analysis of plated structures. (Dr.Ing. Thesis)
UR-79-04	Nils T. Nordsve, MK	Finite element collapse analysis of structural members considering imperfections and stresses due to fabrication. (Dr.Ing. Thesis)
UR-79-05	Ivar J. Fylling, MK	Analysis of towline forces in ocean towing systems. (Dr.Ing. Thesis)
UR-80-06	Nils Sandsmark, MM	Analysis of Stationary and Transient Heat Conduction by the Use of the Finite Element Method. (Dr.Ing. Thesis)
UR-80-09	Sverre Haver, MK	Analysis of uncertainties related to the stochastic modeling of ocean waves. (Dr.Ing. Thesis)
UR-81-15	Odland, Jonas	On the Strength of welded Ring stiffened cylindrical Shells primarily subjected to axial Compression
UR-82-17	Engesvik, Knut	Analysis of Uncertainties in the fatigue Capacity of

		Welded Joints
UR-82-18	Rye, Henrik	Ocean wave groups
UR-83-30	Eide, Oddvar Inge	On Cumulative Fatigue Damage in Steel Welded Joints
UR-83-33	Mo, Olav	Stochastic Time Domain Analysis of Slender Offshore Structures
UR-83-34	Amdahl, Jørgen	Energy absorption in Ship-platform impacts
UR-84-37	Mørch, Morten	Motions and mooring forces of semi submersibles as determined by full-scale measurements and theoretical analysis
UR-84-38	Soares, C. Guedes	Probabilistic models for load effects in ship structures
UR-84-39	Aarsnes, Jan V.	Current forces on ships
UR-84-40	Czujko, Jerzy	Collapse Analysis of Plates subjected to Biaxial Compression and Lateral Load
UR-85-46	Alf G. Engseth, MK	Finite element collapse analysis of tubular steel offshore structures. (Dr.Ing. Thesis)
UR-86-47	Dengody Sheshappa, MP	A Computer Design Model for Optimizing Fishing Vessel Designs Based on Techno-Economic Analysis. (Dr.Ing. Thesis)
UR-86-48	Vidar Aanesland, MH	A Theoretical and Numerical Study of Ship Wave Resistance. (Dr.Ing. Thesis)
UR-86-49	Heinz-Joachim Wessel, MK	Fracture Mechanics Analysis of Crack Growth in Plate Girders. (Dr.Ing. Thesis)
UR-86-50	Jon Taby, MK	Ultimate and Post-ultimate Strength of Dented Tubular Members. (Dr.Ing. Thesis)
UR-86-51	Walter Lian, MH	A Numerical Study of Two-Dimensional Separated Flow Past Bluff Bodies at Moderate KC-Numbers. (Dr.Ing. Thesis)
UR-86-52	Bjørn Sortland, MH	Force Measurements in Oscillating Flow on Ship Sections and Circular Cylinders in a U-Tube Water Tank. (Dr.Ing. Thesis)
UR-86-53	Kurt Strand, MM	A System Dynamic Approach to One-dimensional Fluid Flow. (Dr.Ing. Thesis)
UR-86-54	Arne Edvin Løken, MH	Three Dimensional Second Order Hydrodynamic Effects on Ocean Structures in Waves. (Dr.Ing. Thesis)
UR-86-55	Sigurd Falch, MH	A Numerical Study of Slamming of Two-Dimensional Bodies. (Dr.Ing. Thesis)
UR-87-56	Arne Braathen, MH	Application of a Vortex Tracking Method to the Prediction of Roll Damping of a Two-Dimension Floating Body. (Dr.Ing. Thesis)

UR-87-57	Bernt Leira, MK	Gaussian Vector Processes for Reliability Analysis involving Wave-Induced Load Effects. (Dr.Ing. Thesis)
UR-87-58	Magnus Småvik, MM	Thermal Load and Process Characteristics in a Two-Stroke Diesel Engine with Thermal Barriers (in Norwegian). (Dr.Ing. Thesis)
MTA-88-59	Bernt Arild Bremdal, MP	An Investigation of Marine Installation Processes – A Knowledge - Based Planning Approach. (Dr.Ing. Thesis)
MTA-88-60	Xu Jun, MK	Non-linear Dynamic Analysis of Space-framed Offshore Structures. (Dr.Ing. Thesis)
MTA-89-61	Gang Miao, MH	Hydrodynamic Forces and Dynamic Responses of Circular Cylinders in Wave Zones. (Dr.Ing. Thesis)
MTA-89-62	Martin Greenhow, MH	Linear and Non-Linear Studies of Waves and Floating Bodies. Part I and Part II. (Dr.Techn. Thesis)
MTA-89-63	Chang Li, MH	Force Coefficients of Spheres and Cubes in Oscillatory Flow with and without Current. (Dr.Ing. Thesis
MTA-89-64	Hu Ying, MP	A Study of Marketing and Design in Development of Marine Transport Systems. (Dr.Ing. Thesis)
MTA-89-65	Arild Jæger, MH	Seakeeping, Dynamic Stability and Performance of a Wedge Shaped Planing Hull. (Dr.Ing. Thesis)
MTA-89-66	Chan Siu Hung, MM	The dynamic characteristics of tilting-pad bearings
MTA-89-67	Kim Wikstrøm, MP	Analysis av projekteringen for ett offshore projekt. (Licenciat-avhandling)
MTA-89-68	Jiao Guoyang, MK	Reliability Analysis of Crack Growth under Random Loading, considering Model Updating. (Dr.Ing. Thesis)
MTA-89-69	Arnt Olufsen, MK	Uncertainty and Reliability Analysis of Fixed Offshore Structures. (Dr.Ing. Thesis)
MTA-89-70	Wu Yu-Lin, MR	System Reliability Analyses of Offshore Structures using improved Truss and Beam Models. (Dr.Ing. Thesis)
MTA-90-71	Jan Roger Hoff, MH	Three-dimensional Green function of a vessel with forward speed in waves. (Dr.Ing. Thesis)
MTA-90-72	Rong Zhao, MH	Slow-Drift Motions of a Moored Two-Dimensional Body in Irregular Waves. (Dr.Ing. Thesis)
MTA-90-73	Atle Minsaas, MP	Economical Risk Analysis. (Dr.Ing. Thesis)
MTA-90-74	Knut-Aril Farnes, MK	Long-term Statistics of Response in Non-linear Marine Structures. (Dr.Ing. Thesis)
MTA-90-75	Torbjørn Sotberg, MK	Application of Reliability Methods for Safety Assessment of Submarine Pipelines. (Dr.Ing.

		Thesis)
MTA-90-76	Zeuthen, Steffen, MP	SEAMAID. A computational model of the design process in a constraint-based logic programming environment. An example from the offshore domain. (Dr.Ing. Thesis)
MTA-91-77	Haagensen, Sven, MM	Fuel Dependant Cyclic Variability in a Spark Ignition Engine - An Optical Approach. (Dr.Ing. Thesis)
MTA-91-78	Løland, Geir, MH	Current forces on and flow through fish farms. (Dr.Ing. Thesis)
MTA-91-79	Hoen, Christopher, MK	System Identification of Structures Excited by Stochastic Load Processes. (Dr.Ing. Thesis)
MTA-91-80	Haugen, Stein, MK	Probabilistic Evaluation of Frequency of Collision between Ships and Offshore Platforms. (Dr.Ing. Thesis)
MTA-91-81	Sødahl, Nils, MK	Methods for Design and Analysis of Flexible Risers. (Dr.Ing. Thesis)
MTA-91-82	Ormberg, Harald, MK	Non-linear Response Analysis of Floating Fish Farm Systems. (Dr.Ing. Thesis)
MTA-91-83	Marley, Mark J., MK	Time Variant Reliability under Fatigue Degradation. (Dr.Ing. Thesis)
MTA-91-84	Krokstad, Jørgen R., MH	Second-order Loads in Multidirectional Seas. (Dr.Ing. Thesis)
MTA-91-85	Molteberg, Gunnar A., MM	The Application of System Identification Techniques to Performance Monitoring of Four Stroke Turbocharged Diesel Engines. (Dr.Ing. Thesis)
MTA-92-86	Mørch, Hans Jørgen Bjelke, MH	Aspects of Hydrofoil Design: with Emphasis on Hydrofoil Interaction in Calm Water. (Dr.Ing. Thesis)
MTA-92-87	Chan Siu Hung, MM	Nonlinear Analysis of Rotordynamic Instabilities in Highspeed Turbomachinery. (Dr.Ing. Thesis)
MTA-92-88	Bessason, Bjarni, MK	Assessment of Earthquake Loading and Response of Seismically Isolated Bridges. (Dr.Ing. Thesis)
MTA-92-89	Langli, Geir, MP	Improving Operational Safety through exploitation of Design Knowledge - an investigation of offshore platform safety. (Dr.Ing. Thesis)
MTA-92-90	Sævik, Svein, MK	On Stresses and Fatigue in Flexible Pipes. (Dr.Ing. Thesis)
MTA-92-91	Ask, Tor Ø., MM	Ignition and Flame Growth in Lean Gas-Air Mixtures. An Experimental Study with a Schlieren System. (Dr.Ing. Thesis)
MTA-86-92	Hessen, Gunnar, MK	Fracture Mechanics Analysis of Stiffened Tubular Members. (Dr.Ing. Thesis)

MTA-93-93	Steinebach, Christian, MM	Knowledge Based Systems for Diagnosis of Rotating Machinery. (Dr.Ing. Thesis)
MTA-93-94	Dalane, Jan Inge, MK	System Reliability in Design and Maintenance of Fixed Offshore Structures. (Dr.Ing. Thesis)
MTA-93-95	Steen, Sverre, MH	Cobblestone Effect on SES. (Dr.Ing. Thesis)
MTA-93-96	Karunakaran, Daniel, MK	Nonlinear Dynamic Response and Reliability Analysis of Drag-dominated Offshore Platforms. (Dr.Ing. Thesis)
MTA-93-97	Hagen, Arnulf, MP	The Framework of a Design Process Language. (Dr.Ing. Thesis)
MTA-93-98	Nordrik, Rune, MM	Investigation of Spark Ignition and Autoignition in Methane and Air Using Computational Fluid Dynamics and Chemical Reaction Kinetics. A Numerical Study of Ignition Processes in Internal Combustion Engines. (Dr.Ing. Thesis)
MTA-94-99	Passano, Elizabeth, MK	Efficient Analysis of Nonlinear Slender Marine Structures. (Dr.Ing. Thesis)
MTA-94-100	Kvålsvold, Jan, MH	Hydroelastic Modelling of Wetdeck Slamming on Multihull Vessels. (Dr.Ing. Thesis)
MTA-94-102	Bech, Sidsel M., MK	Experimental and Numerical Determination of Stiffness and Strength of GRP/PVC Sandwich Structures. (Dr.Ing. Thesis)
MTA-95-103	Paulsen, Hallvard, MM	A Study of Transient Jet and Spray using a Schlieren Method and Digital Image Processing. (Dr.Ing. Thesis)
MTA-95-104	Hovde, Geir Olav, MK	Fatigue and Overload Reliability of Offshore Structural Systems, Considering the Effect of Inspection and Repair. (Dr.Ing. Thesis)
MTA-95-105	Wang, Xiaozhi, MK	Reliability Analysis of Production Ships with Emphasis on Load Combination and Ultimate Strength. (Dr.Ing. Thesis)
MTA-95-106	Ulstein, Tore, MH	Nonlinear Effects of a Flexible Stern Seal Bag on Cobblestone Oscillations of an SES. (Dr.Ing. Thesis)
MTA-95-107	Solaas, Frøydis, MH	Analytical and Numerical Studies of Sloshing in Tanks. (Dr.Ing. Thesis)
MTA-95-108	Hellan, Øyvind, MK	Nonlinear Pushover and Cyclic Analyses in Ultimate Limit State Design and Reassessment of Tubular Steel Offshore Structures. (Dr.Ing. Thesis)
MTA-95-109	Hermundstad, Ole A., MK	Theoretical and Experimental Hydroelastic Analysis of High Speed Vessels. (Dr.Ing. Thesis)
MTA-96-110	Bratland, Anne K., MH	Wave-Current Interaction Effects on Large-Volume Bodies in Water of Finite Depth. (Dr.Ing. Thesis)
MTA-96-111	Herfjord, Kjell, MH	A Study of Two-dimensional Separated Flow by a Combination of the Finite Element Method and

		Navier-Stokes Equations. (Dr.Ing. Thesis)
MTA-96-112	Æsøy, Vilmar, MM	Hot Surface Assisted Compression Ignition in a Direct Injection Natural Gas Engine. (Dr.Ing. Thesis)
MTA-96-113	Eknes, Monika L., MK	Escalation Scenarios Initiated by Gas Explosions on Offshore Installations. (Dr.Ing. Thesis)
MTA-96-114	Erikstad, Stein O., MP	A Decision Support Model for Preliminary Ship Design. (Dr.Ing. Thesis)
MTA-96-115	Pedersen, Egil, MH	A Nautical Study of Towed Marine Seismic Streamer Cable Configurations. (Dr.Ing. Thesis)
MTA-97-116	Moksnes, Paul O., MM	Modelling Two-Phase Thermo-Fluid Systems Using Bond Graphs. (Dr.Ing. Thesis)
MTA-97-117	Halse, Karl H., MK	On Vortex Shedding and Prediction of Vortex-Induced Vibrations of Circular Cylinders. (Dr.Ing. Thesis)
MTA-97-118	Igland, Ragnar T., MK	Reliability Analysis of Pipelines during Laying, considering Ultimate Strength under Combined Loads. (Dr.Ing. Thesis)
MTA-97-119	Pedersen, Hans-P., MP	Levendefiskteknologi for fiskefartøy. (Dr.Ing. Thesis)
MTA-98-120	Vikestad, Kyrre, MK	Multi-Frequency Response of a Cylinder Subjected to Vortex Shedding and Support Motions. (Dr.Ing. Thesis)
MTA-98-121	Azadi, Mohammad R. E., MK	Analysis of Static and Dynamic Pile-Soil-Jacket Behaviour. (Dr.Ing. Thesis)
MTA-98-122	Ulltang, Terje, MP	A Communication Model for Product Information. (Dr.Ing. Thesis)
MTA-98-123	Torbergsen, Erik, MM	Impeller/Diffuser Interaction Forces in Centrifugal Pumps. (Dr.Ing. Thesis)
MTA-98-124	Hansen, Edmond, MH	A Discrete Element Model to Study Marginal Ice Zone Dynamics and the Behaviour of Vessels Moored in Broken Ice. (Dr.Ing. Thesis)
MTA-98-125	Videiro, Paulo M., MK	Reliability Based Design of Marine Structures. (Dr.Ing. Thesis)
MTA-99-126	Mainçon, Philippe, MK	Fatigue Reliability of Long Welds Application to Titanium Risers. (Dr.Ing. Thesis)
MTA-99-127	Haugen, Elin M., MH	Hydroelastic Analysis of Slamming on Stiffened Plates with Application to Catamaran Wetdecks. (Dr.Ing. Thesis)
MTA-99-128	Langhelle, Nina K., MK	Experimental Validation and Calibration of Nonlinear Finite Element Models for Use in Design of Aluminium Structures Exposed to Fire. (Dr.Ing. Thesis)
MTA-99-	Berstad, Are J., MK	Calculation of Fatigue Damage in Ship Structures.

129		(Dr.Ing. Thesis)
MTA-99-130	Andersen, Trond M., MM	Short Term Maintenance Planning. (Dr.Ing. Thesis)
MTA-99-131	Tveiten, Bård Wathne, MK	Fatigue Assessment of Welded Aluminium Ship Details. (Dr.Ing. Thesis)
MTA-99-132	Søreide, Fredrik, MP	Applications of underwater technology in deep water archaeology. Principles and practice. (Dr.Ing. Thesis)
MTA-99-133	Tønnessen, Rune, MH	A Finite Element Method Applied to Unsteady Viscous Flow Around 2D Blunt Bodies With Sharp Corners. (Dr.Ing. Thesis)
MTA-99-134	Elvekrok, Dag R., MP	Engineering Integration in Field Development Projects in the Norwegian Oil and Gas Industry. The Supplier Management of Norne. (Dr.Ing. Thesis)
MTA-99-135	Fagerholt, Kjetil, MP	Optimeringsbaserte Metoder for Ruteplanlegging innen skipsfart. (Dr.Ing. Thesis)
MTA-99-136	Bysveen, Marie, MM	Visualization in Two Directions on a Dynamic Combustion Rig for Studies of Fuel Quality. (Dr.Ing. Thesis)
MTA-2000-137	Storteig, Eskild, MM	Dynamic characteristics and leakage performance of liquid annular seals in centrifugal pumps. (Dr.Ing. Thesis)
MTA-2000-138	Sagli, Gro, MK	Model uncertainty and simplified estimates of long term extremes of hull girder loads in ships. (Dr.Ing. Thesis)
MTA-2000-139	Tronstad, Harald, MK	Nonlinear analysis and design of cable net structures like fishing gear based on the finite element method. (Dr.Ing. Thesis)
MTA-2000-140	Kroneberg, André, MP	Innovation in shipping by using scenarios. (Dr.Ing. Thesis)
MTA-2000-141	Haslum, Herbjørn Alf, MH	Simplified methods applied to nonlinear motion of spar platforms. (Dr.Ing. Thesis)
MTA-2001-142	Samdal, Ole Johan, MM	Modelling of Degradation Mechanisms and Stressor Interaction on Static Mechanical Equipment Residual Lifetime. (Dr.Ing. Thesis)
MTA-2001-143	Baarholm, Rolf Jarle, MH	Theoretical and experimental studies of wave impact underneath decks of offshore platforms. (Dr.Ing. Thesis)
MTA-2001-144	Wang, Lihua, MK	Probabilistic Analysis of Nonlinear Wave-induced Loads on Ships. (Dr.Ing. Thesis)
MTA-2001-145	Kristensen, Odd H. Holt, MK	Ultimate Capacity of Aluminium Plates under Multiple Loads, Considering HAZ Properties. (Dr.Ing. Thesis)
MTA-2001-146	Greco, Marilena, MH	A Two-Dimensional Study of Green-Water

		Loading. (Dr.Ing. Thesis)
MTA-2001-147	Heggelund, Svein E., MK	Calculation of Global Design Loads and Load Effects in Large High Speed Catamarans. (Dr.Ing. Thesis)
MTA-2001-148	Babalola, Olusegun T., MK	Fatigue Strength of Titanium Risers – Defect Sensitivity. (Dr.Ing. Thesis)
MTA-2001-149	Mohammed, Abuu K., MK	Nonlinear Shell Finite Elements for Ultimate Strength and Collapse Analysis of Ship Structures. (Dr.Ing. Thesis)
MTA-2002-150	Holmedal, Lars E., MH	Wave-current interactions in the vicinity of the sea bed. (Dr.Ing. Thesis)
MTA-2002-151	Rognebakke, Olav F., MH	Sloshing in rectangular tanks and interaction with ship motions. (Dr.Ing. Thesis)
MTA-2002-152	Lader, Pål Furset, MH	Geometry and Kinematics of Breaking Waves. (Dr.Ing. Thesis)
MTA-2002-153	Yang, Qinzheng, MH	Wash and wave resistance of ships in finite water depth. (Dr.Ing. Thesis)
MTA-2002-154	Melhus, Øyvin, MM	Utilization of VOC in Diesel Engines. Ignition and combustion of VOC released by crude oil tankers. (Dr.Ing. Thesis)
MTA-2002-155	Ronæss, Marit, MH	Wave Induced Motions of Two Ships Advancing on Parallel Course. (Dr.Ing. Thesis)
MTA-2002-156	Økland, Ole D., MK	Numerical and experimental investigation of whipping in twin hull vessels exposed to severe wet deck slamming. (Dr.Ing. Thesis)
MTA-2002-157	Ge, Chunhua, MK	Global Hydroelastic Response of Catamarans due to Wet Deck Slamming. (Dr.Ing. Thesis)
MTA-2002-158	Byklum, Eirik, MK	Nonlinear Shell Finite Elements for Ultimate Strength and Collapse Analysis of Ship Structures. (Dr.Ing. Thesis)
IMT-2003-1	Chen, Haibo, MK	Probabilistic Evaluation of FPSO-Tanker Collision in Tandem Offloading Operation. (Dr.Ing. Thesis)
IMT-2003-2	Skaugset, Kjetil Bjørn, MK	On the Suppression of Vortex Induced Vibrations of Circular Cylinders by Radial Water Jets. (Dr.Ing. Thesis)
IMT-2003-3	Chezhian, Muthu	Three-Dimensional Analysis of Slamming. (Dr.Ing. Thesis)
IMT-2003-4	Buhaug, Øyvind	Deposit Formation on Cylinder Liner Surfaces in Medium Speed Engines. (Dr.Ing. Thesis)
IMT-2003-5	Tregde, Vidar	Aspects of Ship Design: Optimization of Aft Hull with Inverse Geometry Design. (Dr.Ing. Thesis)
IMT-	Wist, Hanne Therese	Statistical Properties of Successive Ocean Wave

2003-6		Parameters. (Dr.Ing. Thesis)
IMT-2004-7	Ransau, Samuel	Numerical Methods for Flows with Evolving Interfaces. (Dr.Ing. Thesis)
IMT-2004-8	Soma, Torkel	Blue-Chip or Sub-Standard. A data interrogation approach of identity safety characteristics of shipping organization. (Dr.Ing. Thesis)
IMT-2004-9	Ersdal, Svein	An experimental study of hydrodynamic forces on cylinders and cables in near axial flow. (Dr.Ing. Thesis)
IMT-2005-10	Brodtkorb, Per Andreas	The Probability of Occurrence of Dangerous Wave Situations at Sea. (Dr.Ing. Thesis)
IMT-2005-11	Yttervik, Rune	Ocean current variability in relation to offshore engineering. (Dr.Ing. Thesis)
IMT-2005-12	Fredheim, Arne	Current Forces on Net-Structures. (Dr.Ing. Thesis)
IMT-2005-13	Heggernes, Kjetil	Flow around marine structures. (Dr.Ing. Thesis
IMT-2005-14	Fouques, Sebastien	Lagrangian Modelling of Ocean Surface Waves and Synthetic Aperture Radar Wave Measurements. (Dr.Ing. Thesis)
IMT-2006-15	Holm, Håvard	Numerical calculation of viscous free surface flow around marine structures. (Dr.Ing. Thesis)
IMT-2006-16	Bjørheim, Lars G.	Failure Assessment of Long Through Thickness Fatigue Cracks in Ship Hulls. (Dr.Ing. Thesis)
IMT-2006-17	Hansson, Lisbeth	Safety Management for Prevention of Occupational Accidents. (Dr.Ing. Thesis)
IMT-2006-18	Zhu, Xinying	Application of the CIP Method to Strongly Nonlinear Wave-Body Interaction Problems. (Dr.Ing. Thesis)
IMT-2006-19	Reite, Karl Johan	Modelling and Control of Trawl Systems. (Dr.Ing. Thesis)
IMT-2006-20	Smogeli, Øyvind Notland	Control of Marine Propellers. From Normal to Extreme Conditions. (Dr.Ing. Thesis)
IMT-2007-21	Storhaug, Gaute	Experimental Investigation of Wave Induced Vibrations and Their Effect on the Fatigue Loading of Ships. (Dr.Ing. Thesis)
IMT-2007-22	Sun, Hui	A Boundary Element Method Applied to Strongly Nonlinear Wave-Body Interaction Problems. (PhD Thesis, CeSOS)
IMT-2007-23	Rustad, Anne Marthine	Modelling and Control of Top Tensioned Risers. (PhD Thesis, CeSOS)
IMT-2007-24	Johansen, Vegar	Modelling flexible slender system for real-time simulations and control applications
IMT-2007-25	Wroldsen, Anders Sunde	Modelling and control of tensegrity structures.

		(PhD Thesis, CeSOS)
IMT-2007-26	Aronsen, Kristoffer Høye	An experimental investigation of in-line and combined inline and cross flow vortex induced vibrations. (Dr. avhandling, IMT)
IMT-2007-27	Gao, Zhen	Stochastic Response Analysis of Mooring Systems with Emphasis on Frequency-domain Analysis of Fatigue due to Wide-band Response Processes (PhD Thesis, CeSOS)
IMT-2007-28	Thorstensen, Tom Anders	Lifetime Profit Modelling of Ageing Systems Utilizing Information about Technical Condition. (Dr.ing. thesis, IMT)
IMT-2008-29	Refsnes, Jon Erling Gorset	Nonlinear Model-Based Control of Slender Body AUVs (PhD Thesis, IMT)
IMT-2008-30	Berntsen, Per Ivar B.	Structural Reliability Based Position Mooring. (PhD-Thesis, IMT)
IMT-2008-31	Ye, Naiquan	Fatigue Assessment of Aluminium Welded Box-stiffener Joints in Ships (Dr.ing. thesis, IMT)
IMT-2008-32	Radan, Damir	Integrated Control of Marine Electrical Power Systems. (PhD-Thesis, IMT)
IMT-2008-33	Thomassen, Paul	Methods for Dynamic Response Analysis and Fatigue Life Estimation of Floating Fish Cages. (Dr.ing. thesis, IMT)
IMT-2008-34	Pákozdi, Csaba	A Smoothed Particle Hydrodynamics Study of Two-dimensional Nonlinear Sloshing in Rectangular Tanks. (Dr.ing.thesis, IMT/ CeSOS)
IMT-2007-35	Grytøyr, Guttorm	A Higher-Order Boundary Element Method and Applications to Marine Hydrodynamics. (Dr.ing.thesis, IMT)
IMT-2008-36	Drummen, Ingo	Experimental and Numerical Investigation of Nonlinear Wave-Induced Load Effects in Containerships considering Hydroelasticity. (PhD thesis, CeSOS)
IMT-2008-37	Skejic, Renato	Maneuvering and Seakeeping of a Singel Ship and of Two Ships in Interaction. (PhD-Thesis, CeSOS)
IMT-2008-38	Harlem, Alf	An Age-Based Replacement Model for Repairable Systems with Attention to High-Speed Marine Diesel Engines. (PhD-Thesis, IMT)
IMT-2008-39	Alsos, Hagbart S.	Ship Grounding. Analysis of Ductile Fracture, Bottom Damage and Hull Girder Response. (PhD-thesis, IMT)
IMT-2008-40	Graczyk, Mateusz	Experimental Investigation of Sloshing Loading and Load Effects in Membrane LNG Tanks Subjected to Random Excitation. (PhD-thesis, CeSOS)
IMT-2008-41	Taghipour, Reza	Efficient Prediction of Dynamic Response for Flexible amd Multi-body Marine Structures. (PhD-

		thesis, CeSOS)
IMT-2008-42	Ruth, Eivind	Propulsion control and thrust allocation on marine vessels. (PhD thesis, CeSOS)
IMT-2008-43	Nystad, Bent Helge	Technical Condition Indexes and Remaining Useful Life of Aggregated Systems. PhD thesis, IMT
IMT-2008-44	Soni, Prashant Kumar	Hydrodynamic Coefficients for Vortex Induced Vibrations of Flexible Beams, PhD thesis, CeSOS
IMT-2009-45	Amlashi, Hadi K.K.	Ultimate Strength and Reliability-based Design of Ship Hulls with Emphasis on Combined Global and Local Loads. PhD Thesis, IMT
IMT-2009-46	Pedersen, Tom Arne	Bond Graph Modelling of Marine Power Systems. PhD Thesis, IMT
IMT-2009-47	Kristiansen, Trygve	Two-Dimensional Numerical and Experimental Studies of Piston-Mode Resonance. PhD-Thesis, CeSOS
IMT-2009-48	Ong, Muk Chen	Applications of a Standard High Reynolds Number Model and a Stochastic Scour Prediction Model for Marine Structures. PhD-thesis, IMT
IMT-2009-49	Hong, Lin	Simplified Analysis and Design of Ships subjected to Collision and Grounding. PhD-thesis, IMT
IMT-2009-50	Koushan, Kamran	Vortex Induced Vibrations of Free Span Pipelines, PhD thesis, IMT
IMT-2009-51	Korsvik, Jarl Eirik	Heuristic Methods for Ship Routing and Scheduling. PhD-thesis, IMT
IMT-2009-52	Lee, Jihoon	Experimental Investigation and Numerical in Analyzing the Ocean Current Displacement of Longlines. Ph.d.-Thesis, IMT.
IMT-2009-53	Vestbøstad, Tone Gran	A Numerical Study of Wave-in-Deck Impact usin a Two-Dimensional Constrained Interpolation Profile Method, Ph.d.thesis, CeSOS.
IMT-2009-54	Bruun, Kristine	Bond Graph Modelling of Fuel Cells for Marine Power Plants. Ph.d.-thesis, IMT
IMT 2009-55	Holstad, Anders	Numerical Investigation of Turbulence in a Sekwed Three-Dimensional Channel Flow, Ph.d.-thesis, IMT.
IMT 2009-56	Ayala-Uraga, Efren	Reliability-Based Assessment of Deteriorating Ship-shaped Offshore Structures, Ph.d.-thesis, IMT
IMT 2009-57	Kong, Xiangjun	A Numerical Study of a Damaged Ship in Beam Sea Waves. Ph.d.-thesis, IMT/CeSOS.
IMT 2010-58	Kristiansen, David	Wave Induced Effects on Floaters of Aquaculture Plants, Ph.d.-thesis, CeSOS.

IMT 2010-59	Ludvigsen, Martin	An ROV-Toolbox for Optical and Acoustic Scientific Seabed Investigation. Ph.d.-thesis IMT.
IMT 2010-60	Hals, Jørgen	Modelling and Phase Control of Wave-Energy Converters. Ph.d.thesis, CeSOS.
IMT 2010- 61	Shu, Zhi	Uncertainty Assessment of Wave Loads and Ultimate Strength of Tankers and Bulk Carriers in a Reliability Framework. Ph.d. Thesis, IMT/ CeSOS
IMT 2010-62	Shao, Yanlin	Numerical Potential-Flow Studies on Weakly-Nonlinear Wave-Body Interactions with/without Small Forward Speed, Ph.d.thesis,CeSOS.
IMT 2010-63	Califano, Andrea	Dynamic Loads on Marine Propellers due to Intermittent Ventilation. Ph.d.thesis, IMT.
IMT 2010-64	El Khoury, George	Numerical Simulations of Massively Separated Turbulent Flows, Ph.d.-thesis, IMT
IMT 2010-65	Seim, Knut Sponheim	Mixing Process in Dense Overflows with Emphasis on the Faroe Bank Channel Overflow. Ph.d.thesis, IMT
IMT 2010-66	Jia, Huirong	Structural Analysis of Intect and Damaged Ships in a Collission Risk Analysis Perspective. Ph.d.thesis CeSoS.
IMT 2010-67	Jiao, Linlin	Wave-Induced Effects on a Pontoon-type Very Large Floating Structures (VLFS). Ph.D.-thesis, CeSOS.
IMT 2010-68	Abrahamsen, Bjørn Christian	Sloshing Induced Tank Roof with Entrapped Air Pocket. Ph.d.thesis, CeSOS.
IMT 2011-69	Karimirad, Madjid	Stochastic Dynamic Response Analysis of Spar-Type Wind Turbines with Catenary or Taut Mooring Systems. Ph.d.-thesis, CeSOS.
IMT - 2011-70	Erlend Meland	Condition Monitoring of Safety Critical Valves. Ph.d.-thesis, IMT.
IMT – 2011-71	Yang, Limin	Stochastic Dynamic System Analysis of Wave Energy Converter with Hydraulic Power Take-Off, with Particular Reference to Wear Damage Analysis, Ph.d. Thesis, CeSOS.
IMT – 2011-72	Visscher, Jan	Application of Particla Image Velocimetry on Turbulent Marine Flows, Ph.d.Thesis, IMT.
IMT – 2011-73	Su, Biao	Numerical Predictions of Global and Local Ice Loads on Ships. Ph.d.Thesis, CeSOS.
IMT – 2011-74	Liu, Zhenhui	Analytical and Numerical Analysis of Iceberg Collision with Ship Structures. Ph.d.Thesis, IMT.
IMT – 2011-75	Aarsæther, Karl Gunnar	Modeling and Analysis of Ship Traffic by Observation and Numerical Simulation. Ph.d.Thesis, IMT.

Imt – 2011-76	Wu, Jie	Hydrodynamic Force Identification from Stochastic Vortex Induced Vibration Experiments with Slender Beams. Ph.d.Thesis, IMT.
Imt – 2011-77	Amini, Hamid	Azimuth Propulsors in Off-design Conditions. Ph.d.Thesis, IMT.
IMT – 2011-78	Nguyen, Tan-Hoi	Toward a System of Real-Time Prediction and Monitoring of Bottom Damage Conditions During Ship Grounding. Ph.d.thesis, IMT.
IMT- 2011-79	Tavakoli, Mohammad T.	Assessment of Oil Spill in Ship Collision and Grounding, Ph.d.thesis, IMT.
IMT- 2011-80	Guo, Bingjie	Numerical and Experimental Investigation of Added Resistance in Waves. Ph.d.Thesis, IMT.
IMT- 2011-81	Chen, Qiaofeng	Ultimate Strength of Aluminium Panels, considering HAZ Effects, IMT
IMT- 2012-82	Kota, Ravikiran S.	Wave Loads on Decks of Offshore Structures in Random Seas, CeSOS.
IMT- 2012-83	Sten, Ronny	Dynamic Simulation of Deep Water Drilling Risers with Heave Compensating System, IMT.
IMT- 2012-84	Berle, Øyvind	Risk and resilience in global maritime supply chains, IMT.
IMT- 2012-85	Fang, Shaoji	Fault Tolerant Position Mooring Control Based on Structural Reliability, CeSOS.
IMT- 2012-86	You, Jikun	Numerical studies on wave forces and moored ship motions in intermediate and shallow water, CeSOS.
IMT- 2012-87	Xiang ,Xu	Maneuvering of two interacting ships in waves, CeSOS
IMT- 2012-88	Dong, Wenbin	Time-domain fatigue response and reliability analysis of offshore wind turbines with emphasis on welded tubular joints and gear components, CeSOS
IMT- 2012-89	Zhu, Suji	Investigation of Wave-Induced Nonlinear Load Effects in Open Ships considering Hull Girder Vibrations in Bending and Torsion, CeSOS
IMT- 2012-90	Zhou, Li	Numerical and Experimental Investigation of Station-keeping in Level Ice, CeSOS
IMT- 2012-91	Ushakov, Sergey	Particulate matter emission characteristics from diesel enignes operating on conventional and alternative marine fuels, IMT
IMT- 2013-1	Yin, Decao	Experimental and Numerical Analysis of Combined In-line and Cross-flow Vortex Induced Vibrations, CeSOS

IMT-2013-2	Kurniawan, Adi	Modelling and geometry optimisation of wave energy converters, CeSOS
IMT-2013-3	Al Ryati, Nabil	Technical condition indexes doe auxiliary marine diesel engines, IMT
IMT-2013-4	Firoozkoohi, Reza	Experimental, numerical and analytical investigation of the effect of screens on sloshing, CeSOS
IMT-2013-5	Ommani, Babak	Potential-Flow Predictions of a Semi-Displacement Vessel Including Applications to Calm Water Broaching, CeSOS
IMT-2013-6	Xing, Yihan	Modelling and analysis of the gearbox in a floating spar-type wind turbine, CeSOS
IMT-7-2013	Balland, Océane	Optimization models for reducing air emissions from ships, IMT
IMT-8-2013	Yang, Dan	Transitional wake flow behind an inclined flat plate-----Computation and analysis, IMT
IMT-9-2013	Abdillah, Suyuthi	Prediction of Extreme Loads and Fatigue Damage for a Ship Hull due to Ice Action, IMT
IMT-10-2013	Ramìrez, Pedro Agustìn Pèrez	Ageing management and life extension of technical systems- Concepts and methods applied to oil and gas facilities, IMT
IMT-11-2013	Chuang, Zhenju	Experimental and Numerical Investigation of Speed Loss due to Seakeeping and Maneuvering. IMT
IMT-12-2013	Etemaddar, Mahmoud	Load and Response Analysis of Wind Turbines under Atmospheric Icing and Controller System Faults with Emphasis on Spar Type Floating Wind Turbines, IMT
IMT-13-2013	Lindstad, Haakon	Strategies and measures for reducing maritime CO2 emissons, IMT
IMT-14-2013	Haris, Sabril	Damage interaction analysis of ship collisions, IMT
IMT-15-2013	Shainee, Mohamed	Conceptual Design, Numerical and Experimental Investigation of a SPM Cage Concept for Offshore Mariculture, IMT
IMT-16-2013	Gansel, Lars	Flow past porous cylinders and effects of biofouling and fish behavior on the flow in and around Atlantic salmon net cages, IMT
IMT-17-2013	Gaspar, Henrique	Handling Aspects of Complexity in Conceptual Ship Design, IMT
IMT-18-2013	Thys, Maxime	Theoretical and Experimental Investigation of a Free Running Fishing Vessel at Small Frequency of Encounter, CeSOS
IMT-19-2013	Aglen, Ida	VIV in Free Spanning Pipelines, CeSOS

IMT-1-2014	Song, An	Theoretical and experimental studies of wave diffraction and radiation loads on a horizontally submerged perforated plate, CeSOS
IMT-2-2014	Rogne, Øyvind Ygre	Numerical and Experimental Investigation of a Hinged 5-body Wave Energy Converter, CeSOS
IMT-3-2014	Dai, Lijuan	Safe and efficient operation and maintenance of offshore wind farms ,IMT
IMT-4-2014	Bachynski, Erin Elizabeth	Design and Dynamic Analysis of Tension Leg Platform Wind Turbines, CeSOS
IMT-5-2014	Wang, Jingbo	Water Entry of Freefall Wedged – Wedge motions and Cavity Dynamics, CeSOS
IMT-6-2014	Kim, Ekaterina	Experimental and numerical studies related to the coupled behavior of ice mass and steel structures during accidental collisions, IMT
IMT-7-2014	Tan, Xiang	Numerical investigation of ship's continuous- mode icebreaking in leverl ice, CeSOS
IMT-8-2014	Muliawan, Made Jaya	Design and Analysis of Combined Floating Wave and Wind Power Facilities, with Emphasis on Extreme Load Effects of the Mooring System, CeSOS
IMT-9-2014	Jiang, Zhiyu	Long-term response analysis of wind turbines with an emphasis on fault and shutdown conditions, IMT
IMT-10-2014	Dukan, Fredrik	ROV Motion Control Systems, IMT
IMT-11-2014	Grimsmo, Nils I.	Dynamic simulations of hydraulic cylinder for heave compensation of deep water drilling risers, IMT
IMT-12-2014	Kvittem, Marit I.	Modelling and response analysis for fatigue design of a semisubmersible wind turbine, CeSOS
IMT-13-2014	Akhtar, Juned	The Effects of Human Fatigue on Risk at Sea, IMT
IMT-14-2014	Syahroni, Nur	Fatigue Assessment of Welded Joints Taking into Account Effects of Residual Stress, IMT
IMT-1-2015	Bøckmann, Eirik	Wave Propulsion of ships, IMT
IMT-2-2015	Wang, Kai	Modelling and dynamic analysis of a semi-submersible floating vertical axis wind turbine, CeSOS
IMT-3-2015	Fredriksen, Arnt Gunvald	A numerical and experimental study of a two-dimensional body with moonpool in waves and current, CeSOS
IMT-4-2015	Jose Patricio Gallardo Canabes	Numerical studies of viscous flow around bluff bodies, IMT

IMT-5-2015	Vegard Longva	Formulation and application of finite element techniques for slender marine structures subjected to contact interactions, IMT
IMT-6-2015	Jacobus De Vaal	Aerodynamic modelling of floating wind turbines, CeSOS
IMT-7-2015	Fachri Nasution	Fatigue Performance of Copper Power Conductors, IMT
IMT-8-2015	Oleh I Karpa	Development of bivariate extreme value distributions for applications in marine technology,CeSOS
IMT-9-2015	Daniel de Almeida Fernandes	An output feedback motion control system for ROVs, AMOS
IMT-10-2015	Bo Zhao	Particle Filter for Fault Diagnosis: Application to Dynamic Positioning Vessel and Underwater Robotics, CeSOS
IMT-11-2015	Wenting Zhu	Impact of emission allocation in maritime transportation, IMT
IMT-12-2015	Amir Rasekhi Nejad	Dynamic Analysis and Design of Gearboxes in Offshore Wind Turbines in a Structural Reliability Perspective, CeSOS
IMT-13-2015	Arturo Jesùs Ortega Malca	Dynamic Response of Flexibles Risers due to Unsteady Slug Flow, CeSOS
IMT-14-2015	Dagfinn Husjord	Guidance and decision-support system for safe navigation of ships operating in close proximity, IMT
IMT-15-2015	Anirban Bhattacharyya	Ducted Propellers: Behaviour in Waves and Scale Effects, IMT
IMT-16-2015	Qin Zhang	Image Processing for Ice Parameter Identification in Ice Management, IMT
IMT-1-2016	Vincentius Rumawas	Human Factors in Ship Design and Operation: An Experiential Learning, IMT
IMT-2-2016	Martin Storheim	Structural response in ship-platform and ship-ice collisions, IMT
IMT-3-2016	Mia Abrahamsen Prsic	Numerical Simulations of the Flow around single and Tandem Circular Cylinders Close to a Plane Wall, IMT
IMT-4-2016	Tufan Arslan	Large-eddy simulations of cross-flow around ship sections, IMT

IMT-5-2016	Pierre Yves-Henry	Parametrisation of aquatic vegetation in hydraulic and coastal research,IMT
IMT-6-2016	Lin Li	Dynamic Analysis of the Instalation of Monopiles for Offshore Wind Turbines, CeSOS
IMT-7-2016	Øivind Kåre Kjerstad	Dynamic Positioning of Marine Vessels in Ice, IMT
IMT-8-2016	Xiaopeng Wu	Numerical Analysis of Anchor Handling and Fish Trawling Operations in a Safety Perspective, CeSOS
IMT-9-2016	Zhengshun Cheng	Integrated Dynamic Analysis of Floating Vertical Axis Wind Turbines, CeSOS
IMT-10-2016	Ling Wan	Experimental and Numerical Study of a Combined Offshore Wind and Wave Energy Converter Concept
IMT-11-2016	Wei Chai	Stochastic dynamic analysis and reliability evaluation of the roll motion for ships in random seas, CeSOS
IMT-12-2016	Øyvind Selnes Patricksson	Decision support for conceptual ship design with focus on a changing life cycle and future uncertainty, IMT
IMT-13-2016	Mats Jørgen Thorsen	Time domain analysis of vortex-induced vibrations, IMT